SCIENCE

JOURNAL OF RESEARCH

OF THE U.S. GEOLOGICAL SURVEY

JANUARY–FEBRUARY 1977
VOLUME 5, NUMBER 1

UICC LIBRARY
JAN 19 1977
DOCUMENTS

Scientific notes and summaries of investigations in geology, hydrology, and related fields

U.S. DEPARTMENT OF THE INTERIOR

U.S.
DEPOSITORY

UNITED STATES DEPARTMENT OF THE INTERIOR
THOMAS S. KLEPPE, Secretary
GEOLOGICAL SURVEY
V. E. McKelvey, Director

For sale by Superintendent of Documents, U.S. Government Printing Office, Washington, DC 20402. Annual subscription rate, $18.90 (plus $4.75 for foreign mailing). Make check or money order payable to Superintendent of Documents. Send all subscription inquiries and address changes to Superintendent of Documents at above address.

Purchase single copy ($3.15) from Branch of Distribution, U.S. Geological Survey, 1200 South Eads Street, Arlington, VA 22202. Make check or money order payable to U.S. Geological Survey.

Library of Congress Catalog-card No. 72-600241.

The Journal of Research is published every 2 months by the U.S. Geological Survey. It contains papers by members of the Geological Survey and their professional colleagues on geologic, hydrologic, topographic, and other scientific and technical subjects.

Correspondence and inquiries concerning the Journal (other than subscription inquiries and address changes) should be directed to Anna Orellana, Managing Editor, Journal of Research, Publications Division, U.S. Geological Survey, 321 National Center, Reston, VA 22092.

Papers for the Journal should be submitted through regular Division publication channels.

The Secretary of the Interior has determined that the publication of this periodical is necessary in the transaction of the public business required by law of this Department. Use of funds for printing this periodical has been approved by the Director of the Office of Management and Budget through June 30, 1980.

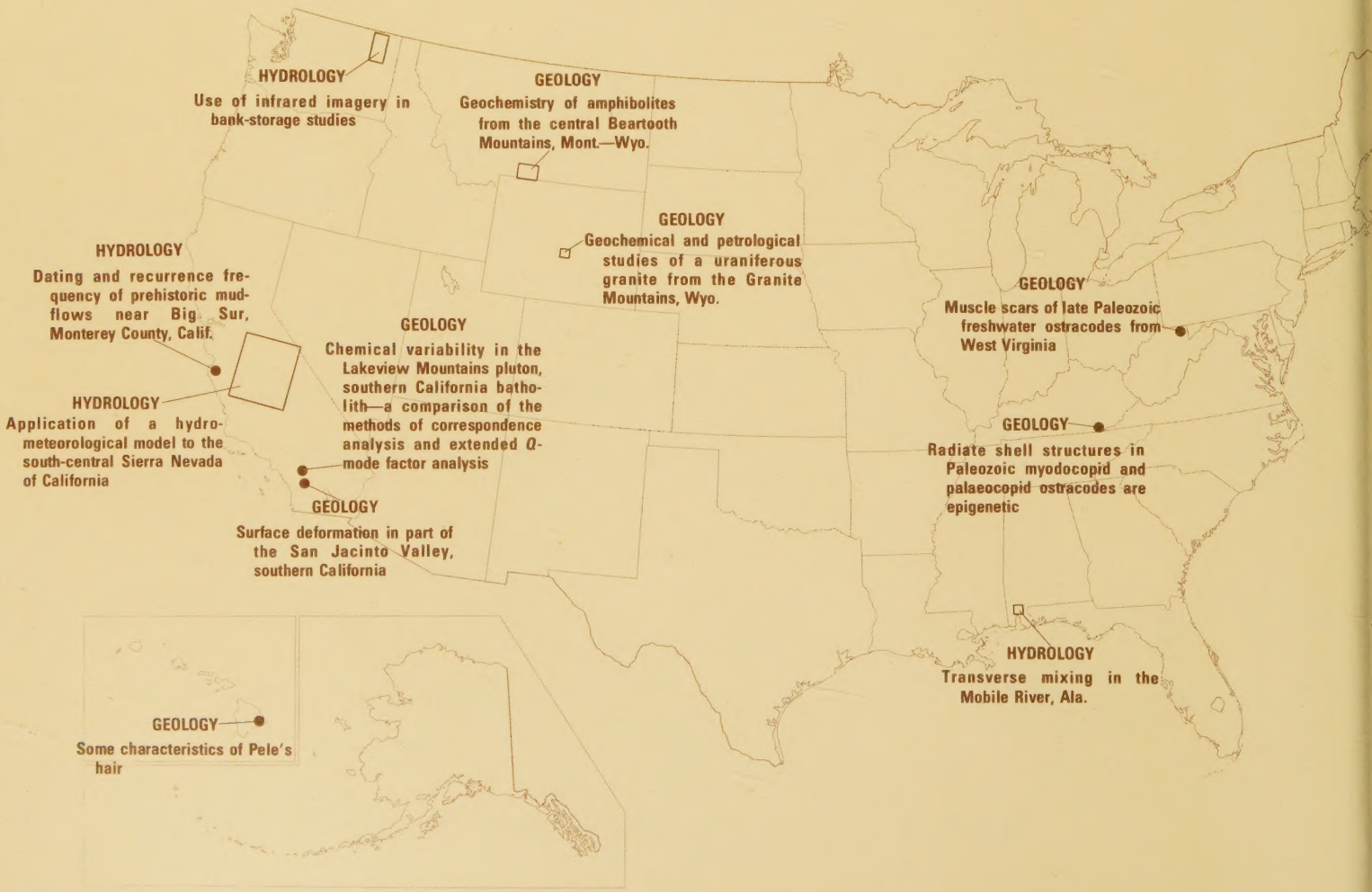
HYDROLOGY
Use of infrared imagery in bank-storage studies
GEOLOGY
Geochemistry of amphibolites from the central Beartooth Mountains, Mont.—Wyo.
GEOLOGY
Geochemical and petrological studies of a uraniferous granite from the Granite Mountains, Wyo.
HYDROLOGY
Dating and recurrence frequency of prehistoric mudflows near Big Sur, Monterey County, Calif.
GEOLOGY
Chemical variability in the Lakeview Mountains pluton, southern California batholith—a comparison of the methods of correspondence analysis and extended Q-mode factor analysis
HYDROLOGY
Application of a hydrometeorological model to the south-central Sierra Nevada of California
GEOLOGY
Surface deformation in part of the San Jacinto Valley, southern California
GEOLOGY
Muscle scars of late Paleozoic freshwater ostracodes from West Virginia
GEOLOGY
Radiate shell structures in Paleozoic myodocopid and palaeocopid ostracodes are epigenetic
HYDROLOGY
Transverse mixing in the Mobile River, Ala.
GEOLOGY
Some characteristics of Pele's hair

GEOGRAPHIC INDEX TO ARTICLES

See "Contents" for articles concerning areas outside the United States and articles without geographic orientation.

JOURNAL OF RESEARCH

of the

U.S. Geological Survey

Vol. 5 No. 1 Jan.–Feb. 1977

CONTENTS

SI units and U.S. customary equivalents II

HYDROLOGIC STUDIES

Use of infrared imagery in bank-storage studies ..... *T. H. Thompson* 1
Transverse mixing in the Mobile River, Ala ..... *William Meyer* 11
Dating and recurrence frequency of prehistoric mudflows near Big Sur, Monterey County, Calif ..... *L. E. Jackson, Jr.* 17
Application of a hydrometeorological model to the south-central Sierra Nevada of California ..... *W. V. Tangborn and L. A. Rasmussen* 33

GEOLOGIC STUDIES

Procedure for estimating the temperature of a hot-water component in a mixed water by using a plot of dissolved silica versus enthalpy ..... *A. H. Truesdell and R. O. Fournier* 49
Geochemistry of amphibolites from the central Beartooth Mountains, Mont.-Wyo ..... *T. J. Armbrustmacher and F. S. Simons* 53
Geochemical and petrological studies of a uraniferous granite from the Granite Mountains, Wyo ..... *J. S. Stuckless, C. M. Bunker, C. A. Bush, W. P. Doering, and J. H. Scott* 61
A comparison of some analytical techniques for determining uranium, thorium, and potassium in granitic rocks ..... *J. S. Stuckless, H. T. Millard, Jr., C. M. Bunker, I. T. Nkomo, J. N. Rosholt, C. A. Bush, Claude Huffman, Jr., and R. L. Keil* 83
Some characteristics of Pele's hair ..... *W. A. Duffield, E. K. Gibson, Jr., and G. H. Heiken* 93
Chemical variability in the Lakeview Mountains pluton, southern California batholith—a comparison of the methods of correspondence analysis and extended *Q*-mode factor analysis ..... *A. T. Miesch and D. M. Morton* 103
Surface deformation in part of the San Jacinto Valley, southern California ..... *D. M. Morton* 117
Radiate shell structures in Paleozoic myodocopid and palaeocopid ostracodes are epigenetic ..... *I. G. Sohn* 125
Muscle scars of late Paleozoic freshwater ostracodes from West Virginia ..... *I. G. Sohn* 135

Recent publications of the U.S. Geological Survey ..... Inside of back cover

SI UNITS AND U.S. CUSTOMARY EQUIVALENTS

[SI, International System of Units, a modernized metric system of measurement. All values have been rounded to four significant digits except 0.01 bar, which is the exact equivalent of 1 kPa. Use of hectare (ha) as an alternative name for square hectometer (hm^2) is restricted to measurement of land or water areas. Use of liter (L) as a special name for cubic decimeter (dm^3) is restricted to the measurement of liquids and gases; no prefix other than milli should be used with liter. Metric ton (t) as a name for megagram (Mg) should be restricted to commercial usage, and no prefixes should be used with it. Note that the style of $meter^2$ rather than square meter has been used for convenience in finding units in this table. Where the units are spelled out in text, Survey style is to use square meter]

SI unit		U.S. customary equivalent	
Length			
millimeter (mm)	=	0.039 37	inch (in)
meter (m)	=	3.281	feet (ft)
	=	1.094	yards (yd)
kilometer (km)	=	0.621 4	mile (mi)
	=	0.540 0	mile, nautical (nmi)
Area			
$centimeter^2$ (cm^2)	=	0.155 0	$inch^2$ (in^2)
$meter^2$ (m^2)	=	10.76	$feet^2$ (ft^2)
	=	1.196	$yards^2$ (yd^2)
	=	0.000 247 1	acre
$hectometer^2$ (hm^2)	=	2.471	acres
	=	0.003 861	section (640 acres or 1 mi^2)
$kilometer^2$ (km^2)	=	0.386 1	$mile^2$ (mi^2)
Volume			
$centimeter^3$ (cm^3)	=	0.061 02	$inch^3$ (in^3)
$decimeter^3$ (dm^3)	=	61.02	$inches^3$ (in^3)
	=	2.113	pints (pt)
	=	1.057	quarts (qt)
	=	0.264 2	gallon (gal)
	=	0.035 31	$foot^3$ (ft^3)
$meter^3$ (m^3)	=	35.31	$feet^3$ (ft^3)
	=	1.308	$yards^3$ (yd^3)
	=	264.2	gallons (gal)
	=	6.290	barrels (bbl) (petroleum, 1 bbl=42 gal)
	=	0.000 810 7	acre-foot (acre-ft)
$hectometer^3$ (hm^3)	=	810.7	acre-feet (acre-ft)
$kilometer^3$ (km^3)	=	0.239 9	$mile^3$ (mi^3)
Volume per unit time (includes flow)			
$decimeter^3$ per second (dm^3/s)	=	0.035 31	$foot^3$ per second (ft^3/s)
	=	2.119	$feet^3$ per minute (ft^3/min)
	=	15.85	gallons per minute (gal/min)
	=	543.4	barrels per day (bbl/d) (petroleum, 1 bbl=42 gal)
$meter^3$ per second (m^3/s)	=	35.31	$feet^3$ per second (ft^3/s)
	=	15 850	gallons per minute (gal/min)
Mass			
gram (g)	=	0.035 27	ounce avoirdupois (oz avdp)
kilogram (kg)	=	2.205	pounds avoirdupois (lb avdp)
megagram (Mg)	=	1.102	tons, short (2 000 lb)
	=	0.984 2	ton, long (2 240 lb)
Mass per unit volume (includes density)			
kilogram per $meter^3$ (kg/m^3)	=	0.062 43	pound per $foot^3$ (lb/ft^3)
Pressure			
kilopascal (kPa)	=	0.145 0	pound-force per $inch^2$ (lbf/in^2)
	=	0.009 869	atmosphere, standard (atm)
	=	0.01	bar
	=	0.296 1	inch of mercury at 60°F (in Hg)
Temperature			
temp kelvin (K)	=	[temp deg Fahrenheit (°F)+459.67]/1.8	
temp deg Celsius (°C)	=	[temp deg Fahrenheit (°F)−32]/1.8	

Any use of trade names and trademarks in this publication is for descriptive purposes only and does not constitute endorsement by the U.S. Geological Survey.

Jour. Research U.S. Geol. Survey
Vol. 5, No. 1, Jan.–Feb. 1977, p. 1–10

USE OF INFRARED IMAGERY IN BANK-STORAGE STUDIES

By T. H. THOMPSON, Menlo Park, Calif.

Work done in cooperation with Bonneville Power Administration

Abstract.—The use of thermal infrared imagery as a reconnaissance tool to identify bank seepage was investigated at Franklin D. Roosevelt Lake in northeastern Washington. The banks of the lake are generally composed of glacial lacustrine sediments deposited when the Cordilleran ice sheet dammed the Columbia River at least three times during the Pleistocene. The existence of a significant amount of bank storage was suspected. An airborne scanner having a spectral coverage of 8.5 to 11 micrometres and continuous filmstrip output was used in two test flights of March 27 and April 24, 1973. These flights were made during the reservoir drawdown when groundwater flow was from the banks to the reservoir and the ground water was warmer than the lake. The imagery shows temperatures in the lake ranging from 5° to 13°C. The lighter tones of the imagery show lake circulation patterns and extensive areas of bank seepage, spring discharge, stream inflow, and subsurface discharge whch are all distinguishable from the darker tones of the colder lake surface. Bank seepage and ground-water discharge generally are evident where unconsolidated glacial sediment rather than bedrock is present.

Within the last decade airborne thermal infrared (IR) detectors have been recognized as a valuable reconnaissance tool for hydrologic investigations. By sensing surface-temperature differences from the air, many hydrologic phenomena can be detected rapidly and at less cost than by ground survey. When aerial IR imagery is obtained in conjunction with surface-temperature measurements, synoptic surface temperatures can be determined. The technique permits recognition of hydrologic features such as lake or ocean circulation patterns, sea-ice dynamics, thermal plumes, spring discharges, and areas of ground-water discharge which are difficult to detect at the surface.

The use of thermal IR imagery for the detection of ground-water discharge has been described by numerous investigators including Fischer, Davis, and Sousa (1966), Lee (1969), Hunn and Cherry (1969), Pluhowski, (1972), and Wood (1972). This study was undertaken to determine if airborne thermal IR imagery could be used to locate areas of ground-water discharge to Franklin D. Roosevelt Lake and to relate such areas to the geology of the lakeshore area. A significant amount of bank storage (greater than 4 percent of usable storage) is believed to exist in the glacial sediments adjacent to the reservoir.

Franklin D. Roosevelt Lake (hereafter referred to as the lake) is located in northeastern Washington (fig. 1) and was created by the construction of Grand Coulee Dam, completed in 1941. It extends 233 river kilometres from Grand Coulee Dam to the international boundary. The lake has a total capacity of 1.179×10^{10} cubic metres (m^3) and a usable storage of 6.453×10^9

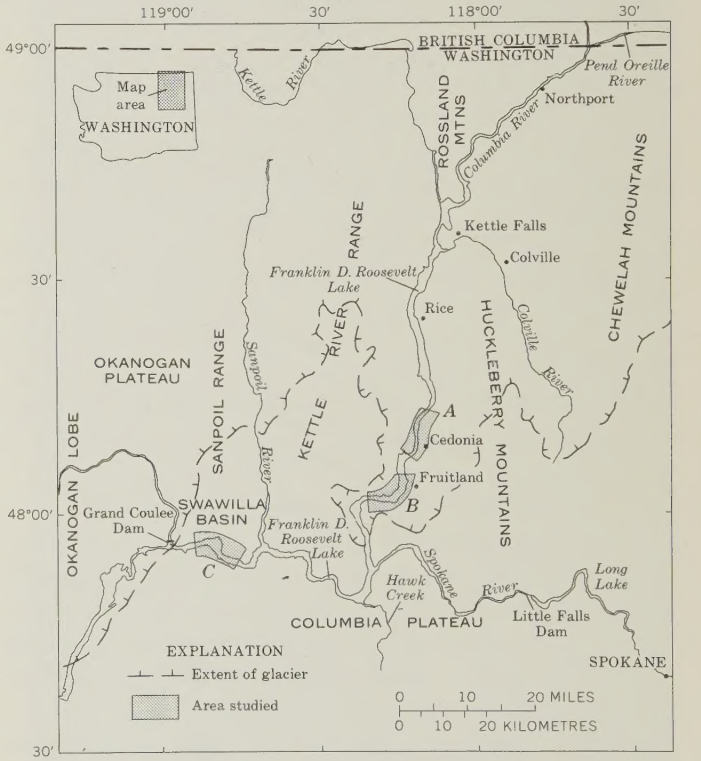

FIGURE 1.—Index map of Columbia River valley of northeastern Washington showing areas of detailed study and maximum southern extent of glacial ice during Pinedale Glaciation.

m^3 between its normal operating elevations of 368 and 393 m above mean sea level.

This investigation is part of a long-term project in the Pacific Northwest to determine the potential for and physical characteristics of bank storage at reservoirs in the Federal Columbia River Power System. Bank storage is defined by Lohman and others (1972, p. 12) as the amount of storage change in an aquifer resulting from a change in stage of an adjacent surface-water body such as a reservoir or river. An understanding of the flow characteristics and total volume of bank storage can be used to increase the efficiency of operation of the reservoirs in this integrated power system. Projected flow from bank storage during drawdown can be incorporated into reservoir operation plans. Thus, such data can (indirectly) result in increased power sales from the same physical facilities.

After the existence of bank storage is identified by thermal IR imagery and other reconnaissance techniques, such as an observation-well network adjacent to the lake, a quantitative determination of bank-storage volumes will be made. A water-budget analysis and mathematical model will be made for the lake as was done at Hungry Horse Reservoir in northwestern Montana (Simons and Rorabaugh, 1971; Thompson, 1974).

Acknowledgments.—This study is part of the continuing program of hydrologic investigations in the Columbia River basin undertaken by the U.S. Geological Survey in cooperation with the Bonneville Power Administration. The author wishes to acknowledge F. A. Limpert, Head, Hydrology Section, Bonneville Power Administration, in the development of the bank-storage project, and W. D. Simons, U.S. Geological Survey, Menlo Park, Calif., for coordinating the remote-sensing activities. The author is grateful to Arnold Boettcher, U.S. Geological Survey, Helena, Mont., for the assistance in imagery interpretation.

PHYSIOGRAPHIC AND GEOLOGIC SETTING

The lake lies within two different physiographic subdivisions. The southern part of the lake, including the Spokane River arm, is bounded on the south by the nearly flat Columbia Plateau. The northern part of the lake lies within the mountainous highlands in the south-trending Columbia River valley.

From the upstream end of the lake at the international boundary, the Columbia River flows southwest in a broad valley between the Rossland Mountains to the northwest and the Chewelah Mountains to the southeast (fig. 1). The Kettle and Colville Rivers join the Columbia River at the southern tip of the Rossland Mountains. From there the Columbia River flows south between the Kettle River Range to the west and the Huckleberry Mountains to the east. The bedrock of the mountain highland exposed along the 160 km of valley walls is composed principally of limestone, marble, quartzite, schist, gneiss, and granite of Paleozoic and Mesozoic ages (Pardee, 1918; Weaver, 1920; Mills, 1969).

The Spokane River arm of the lake begins just below Little Falls Dam and extends northwestward 47 km to the confluence with the Columbia. The Columbia turns westward a few miles below the confluence and follows a sinuous west-northwest course to Grand Coulee Dam 74 km downstream. The westward course of the Spokane and Columbia Rivers is a result of a blocking of the south-flowing rivers by a massive lava plateau in Miocene time. Bedrock formations on the south of the Spokane arm and Columbia River are principally lava flows of the Columbia Plateau while on the north they are granite rocks of the Colville batholith (Jones and others, 1961).

About 90 percent of the 1,060 km of shoreline of the lake is bordered by sediments of Pleistocene age (Jones and others, 1961, p. 5). According to Richmond, Fryxell, Neff, and Weis (1965) and a summary of their work by Anderson (1969, p. 12–15), the deposits exposed in the lake area indicate five separate advances of the Cordilleran ice sheet. The Okanogan lobe formed an ice dam across the ancestral Columbia River at approximately the same location as Grand Coulee Dam at least three different times (fig. 1).

The unconsolidated deposits of Pleistocene age consist of locally well-sorted deltaic deposits, outwash, flood gravel, glacial-lake silt and clay, till, and landslide debris. According to Jones, Embody, and Peterson (1961, p. 4) 25 to 50 percent of the fill in the Columbia River valley is sand and gravel in the reach from Kettle Falls to about 30 km below Grand Coulee Dam.

Drillers' logs from 37 wells tapping the glacial deposits at various points along the shoreline of the lake indicate large variations in sediment type, both vertically and horizontally, as would be expected from the depositional history previously described. Published geologic data for most of the area does not differentiate the various Pleistocene sediment types.

Hydrologic Characteristics of Geologic Units

The water-bearing characteristics of the bedrock and sedimentary deposits adjacent to the lake are discussed by Anderson (1969, p. 15–19). He subdivides bedrock into three subgroups: (1) basaltic rocks, (2) limestone, and (3) granite and miscellaneous metamorphic rocks. The basalt and the granite and miscellaneous rocks have little water-yielding potential except at isolated locations. North of Kettle Falls,

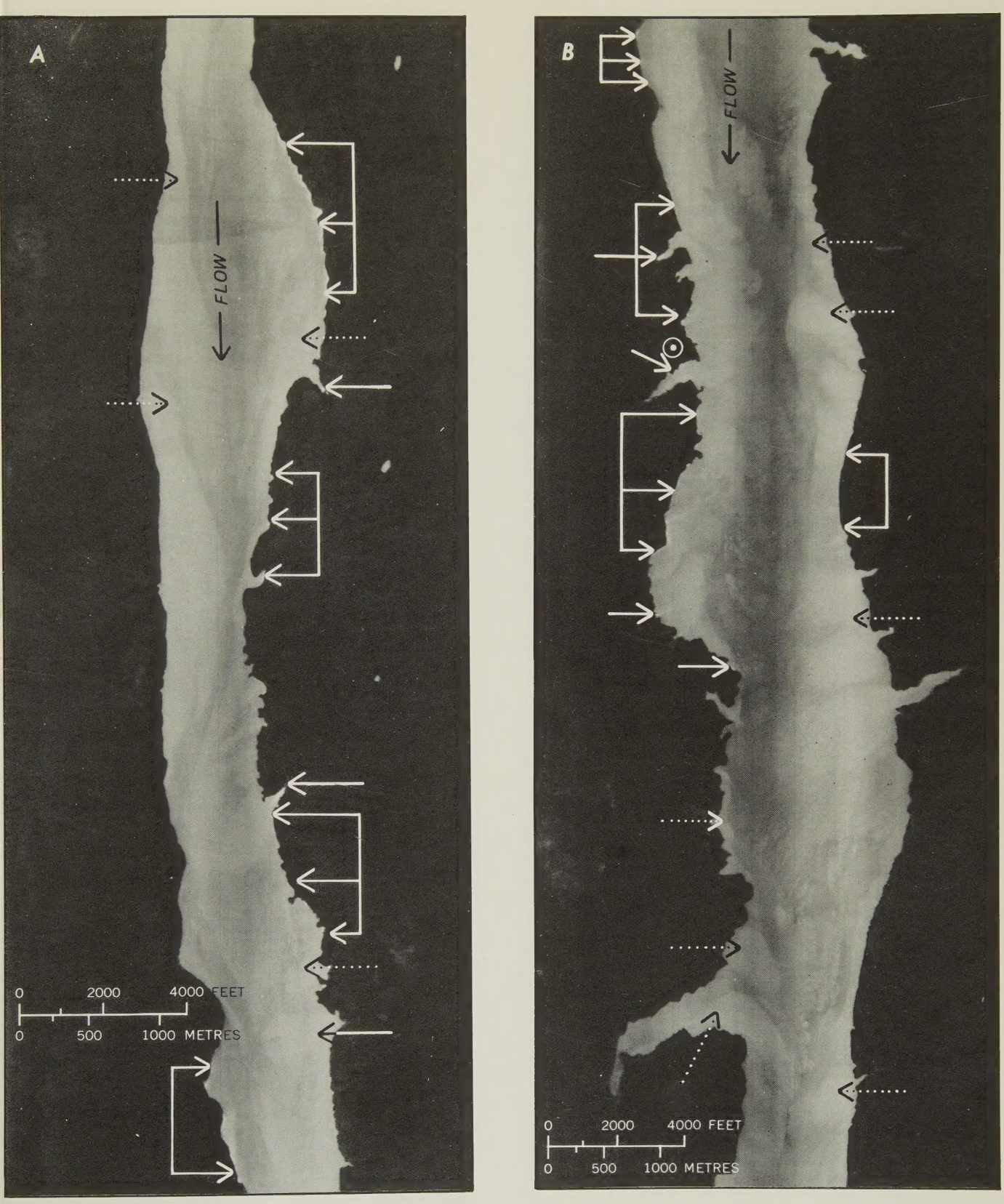

FIGURE 2.—Imagery obtained March 27, 1973, of Franklin D. Roosevelt Lake, showing ground-water discharge to the reservoir. Solid arrows, bank seepage and springs; dotted arrows, subsurface discharge; circle, observation well. *A*, Near Cedonia; approximate scale, 1:40,000. *B*, Near Fruitland; approximate scale 1:50,000.

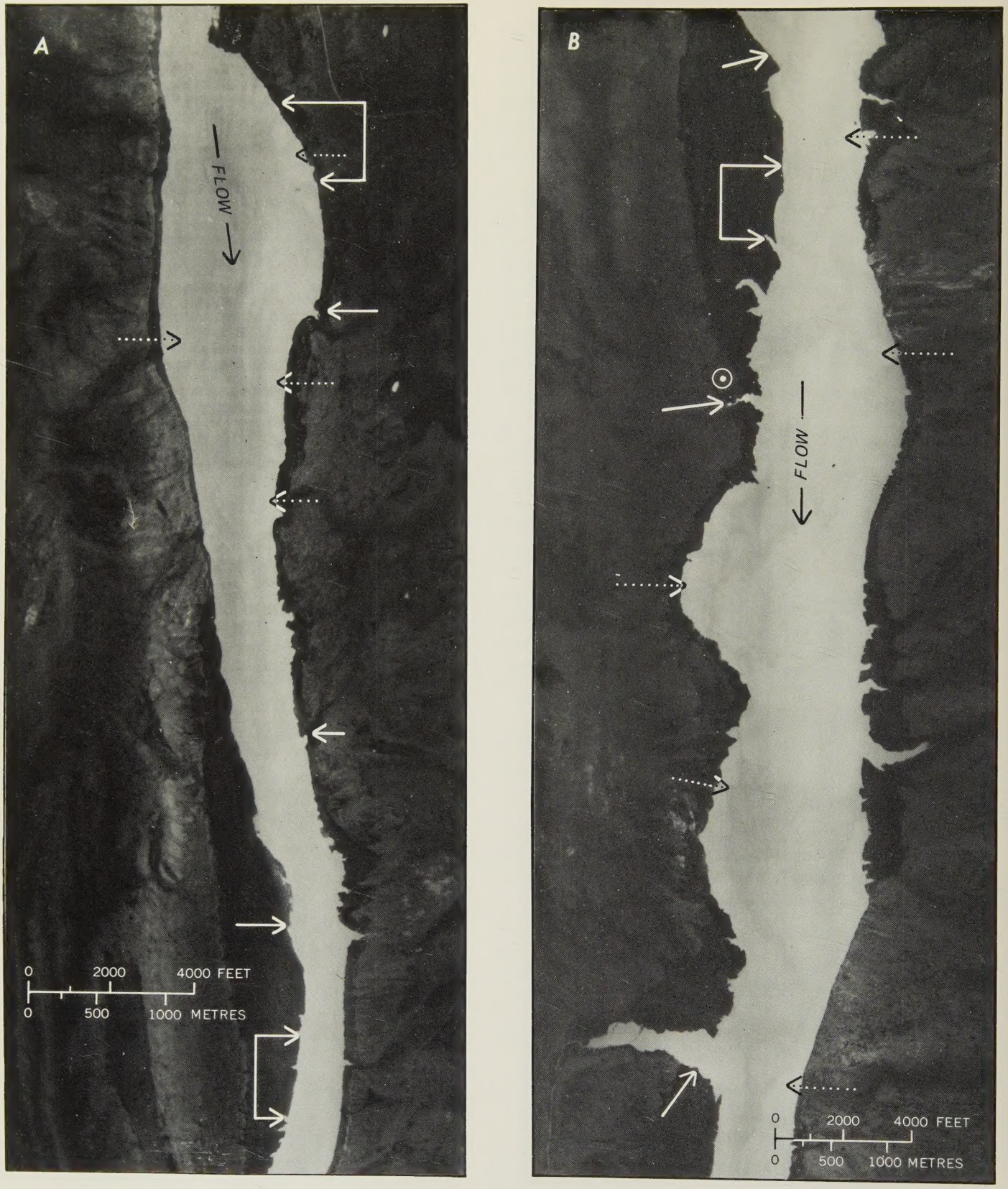

FIGURE 3.—Imagery obtained April 24, 1973, of Franklin D. Roosevelt Lake, showing ground-water discharge to the reservoir. Solid arrows, bank seepage and springs; dotted arrows, subsurface discharge; circle, observation well. *A*, Near Cedonia; approximate scale, 1:40,000. *B*, Near Fruitland; approximate scale, 1:50,000. *C*, At Swawilla Basin, about 8 km upstream from Grand Coulee Dam; approximate scale, 1:43,000.

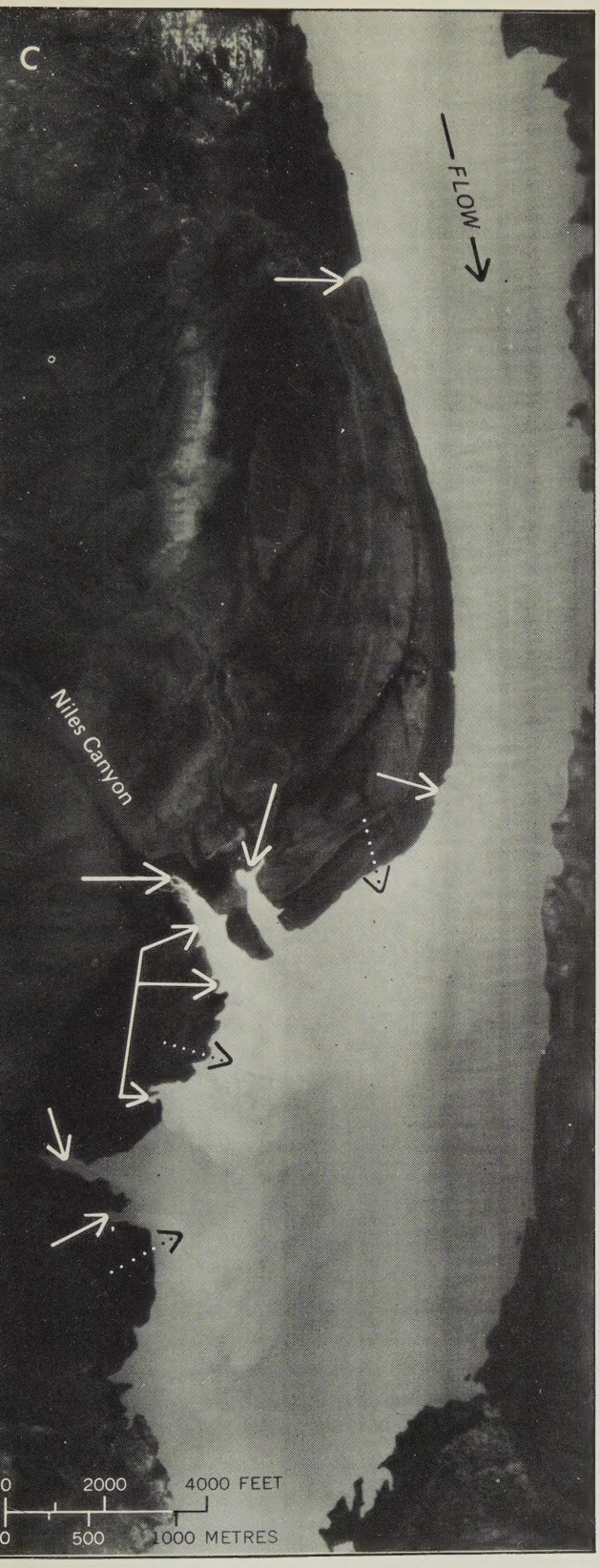

FIGURE 3.—Continued.

water may occur in the limestone which crops out in several areas adjacent to the reservoir.

In the area bordering the lake, most of the ground water is available from the unconsolidated deposits of Pleistocene age (Anderson, 1969, p. 15). The well-sorted deltaic deposits and glacial outwash, where free of silt and clay, yield large volumes of water while the glacial-lake silt and clay deposits are generally too fine grained to yield water. The till generally has a low permeability and the landslide debris is variable in its water-yielding capabilities.

DISCUSSION OF IMAGERY

Water vapor, carbon dioxide, and ozone in the atmosphere absorb most terrestrial radiation. However, the atmosphere is nearly transparent to radiation in the ranges 3 to 5 and 8 to 13 μm (micrometres). These ranges are commonly known as the atmospheric windows. The tonal contrast recorded by IR scanners in these radiation bands is directly related to surface-temperature differences.

The approximate locations and extent of imagery presented in this report are shown in figure 1. The distortion of the lake in the imagery is a result of the irregular flightpath which followed the course of the reservoir.

Equipment

The aerial thermal IR scanner used in this study is owned and operated by the U.S. Forest Service, Boise, Idaho. The scanner, manufactured by Texas Instruments Co. (type RS–7), is cooled by a closed-cycle cooler aboard the aircraft and has a spectral coverage from 3 to 4.1 μm and 8.5 to 11 μm. It has a 120° total field of view and operates at 200 scan lines per second. The scanner has two black-body calibration sources. The display is on a continuous rectilinearized filmstrip exposed by a high resolution cathode-ray tube, and the film is processed in near real time aboard the aircraft.

Flights

Two recording flights were made in 1973 during the winter-spring reservoir drawdown. Both flights were made during predawn hours to eliminate the effects of solar heating and reflectance and during cloudless conditions to eliminate absorption of energy by clouds. Only the 8.5- to 11-μm spectral range was used during these flights. The first flight covering approximately 80 km of the lake from Hawk Creek to a point 10 km north of Rice, Wash., was made on March 27. The lake elevation was 379 m.

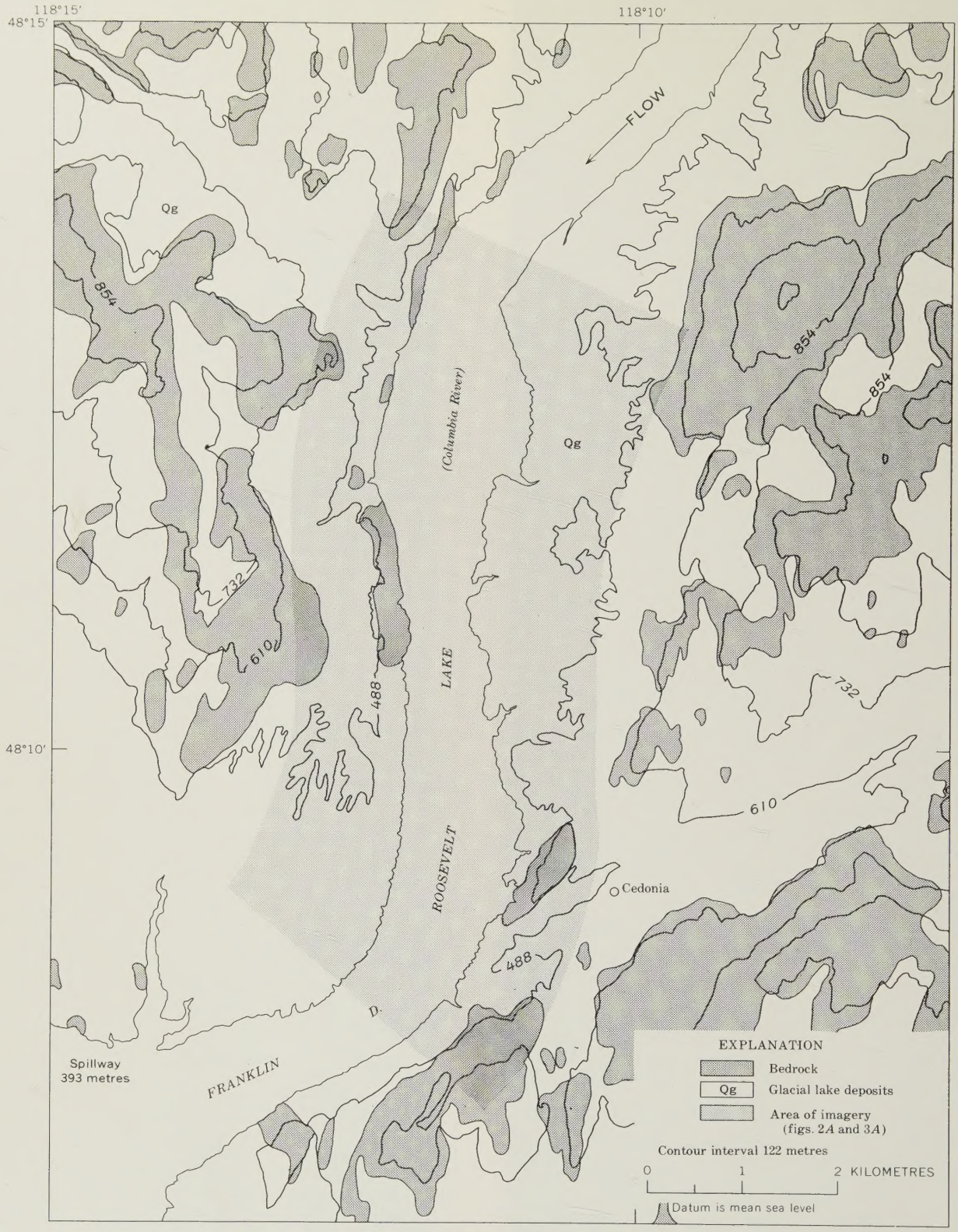

FIGURE 4.—Sketch showing glacial deposits and bedrock and approximate extent of imagery near Cedonia, Wash. Geology from Becraft (1966).

The second flight was made on April 24, 1973, and the imagery covered the entire lake to the international boundary and the Spokane River arm to Little Falls Dam. The lake was at an elevation of 369 m.

Flight of March 27, 1973

Parts of the imagery recorded on March 27 in the vicinity of Cedonia and Fruitland are shown in figure 2. During the 10 days prior to the flight, the lake was being drawn down at a rate of 0.415 m/d (metre per day). Water was flowing from bank storage to the lake as springs and diffuse bank seepage. The water level in an observation well adjacent to the lake near Fruitland (circle in fig. 2*B*) declined an average of 0.323 m/d for the period March 17–26, 1973.

In the imagery, light areas indicate warm surfaces, whereas the dark areas are cold. Ground-water temperatures measured in wells adjacent to the reservoir ranged from 10° to 13°C. Lake temperatures ranged from 5° to 12°C, while small streams tributary to the lake averaged about 5°C. Minimum air and ground-surface temperatures around the reservoir on March 27 averaged 2°C. Based upon the known temperatures, the scanner was calibrated on March 27 (fig. 2) to record white for greater than 12°C to black for temperatures less than 2°C. Temperatures between 12° and 2°C range in the imagery from very light gray to very dark gray.

Indications of ground-water discharge into the reservoir are discernible on the imagery of March 1973 due to the difference in temperature between the ground water (13°C) and the lake (5°C). The solid arrows in figure 2 point to more intense light-toned areas where diffuse bank seepage and large springs discharge to the lake. A stream flowing to the lake can be seen in the lower left corner of figure 2*B*. The less intense light plumes fanning out from shore (dotted arrows) are likely to be the result of subsurface discharge of ground water due to the higher hydraulic head onshore. The water level in the observation well (fig. 2) on March 27 was 2.15 m higher than the lake level. However, the temperatures recorded in the imagery are for the top few millimetres of surface, and positive identification of subsurface flow is not possible.

Lake circulation patterns that generally trend downstream can also be seen in the imagery. The circulation is due to the lake being drawn down, to wind, and to flow to the lake. The net change in the content of the lake during drawdown was $-1{,}250$ m^3/s (cubic metres per second) on March 27.

Flight of April 24, 1973

Parts of the imagery recorded on April 24 near Cedonia, near Fruitland, and 8 km upstream from Grand Coulee Dam are shown in figure 3. The areas shown in figure 3*A* and *B* near Cedonia and Fruitland are approximately the same as those shown in figure 2*A* and *B*. The lake was being drawn down at the average rate of 0.250 m/d for the 10 days prior to the April 24 flight, and water continued to flow from bank storage to the lake.

River temperatures at the international boundary gaging station, Columbia River at Northport, during the week prior to the April 24 flight ranged from 7° to 7.5°C. The temperature of the Spokane River at Long Lake, which flows to the lake, ranged from 6° to 10.5°C during the same period. No lake or ground-water temperatures were obtained prior to the April 24 flight.

Since little change in ground-water temperature is likely to occur in 28 days, it was assumed that temperatures remained at about 10° to 12°C. Minimum air and surface temperatures around the reservoir averaged 1°C on April 24. In the imagery the white areas are equal to or greater than 10°C, where ground water is discharging at or above the lake surface. The black surfaces on shore are 2°C or less. The gray surfaces on the lake range from 6° to 10°C.

In figure 3, the solid arrows point to the light-toned areas where bank seepage and springs flow to the lake. The water level in the observation well (fig. 3*B*) was 4.58 m higher than the lake level on April 24 and was declining at an average rate of 0.210 m/d. Plumes of subsurface discharge (dotted arrows) are also visible, particularly in figure 3*C* at the mouth of Niles Canyon. Here the subsurface flow is probably larger due to the higher permeability of the outwash gravels in the canyon and deltaic deposits at the canyon mouth.

The bank seepage in the April 24 imagery appears less intense and less extensive than in that of March 27 when *A* and *B* of figure 3 are compared with *A* and *B* of figure 2. This difference could be due to a higher rate of dewatering of the banks in March when the lake drawdown rate was 0.415 m/d compared with the rate in April that averaged 0.250 m/d. Also, the bank seepage may appear less intense because of less contrast between ground-water and lake temperatures.

Indications of bank seepage on some parts of the filmstrip are obscured by light streaks on the film caused by electronic noise in the recording system. By use of simultaneous magnetic-tape recording of the sensor signal and later computer processing of the tape, the streaks could possibly be eliminated while the contrasts

of the imagery patterns would be increased (A. J. Boettcher, written commun., 1972).

RELATIONSHIP BETWEEN SEEPAGE AND GEOLOGY

Maps showing the approximate extent of bedrock and glacial lake deposits based upon the geology by Becraft (1966), Campbell and Raup (1964), and Pardee (1918) near Cedonia, near Fruitland, and 8 km upstream from Grand Coulee Dam are shown in figures 4, 5, and 6, respectively. The bedrock units are not differentiated. The approximate extent of the corresponding imagery is also shown on the maps. When the maps are compared with the imagery, areas of extensive glacial lake deposits are seen to be areas where bank seepage is generally prevalent. Conversely, there is little indication of bank seepage in areas where the bedrock is exposed along the lake's shoreline. Discharge varies greatly in the areas of glacial deposits, probably due to the variable nature of the sediments. Since the glacial deposits are undifferentiated in the geologic maps, further study is needed to verify this supposition.

SUMMARY AND CONCLUSIONS

The thermal imagery recorded in March and April 1974 shows water temperature differences that range from 5° to 12°C in Franklin D. Roosevelt Lake. Lake circulation patterns and areas of bank seepage, spring discharge, stream inflow, and subsurface discharge are all discernible as tonal contrasts in the imagery. The areas of bank seepage and subsurface ground-water discharge generally occur in areas where glacial sediments rather than bedrock are present.

Aerial thermal IR imagery can be used as a relatively inexpensive reconnaissance technique to determine areas for further investigations of bank-storage potential. The flights must be made when the reservoir is being drawn down and when there is a detectable difference between ground-water and lake temperatures.

Aerial thermal IR imagery is particularly useful as a reconnaissance tool in the Pacific Northwest because periods of reservoir drawdown and maximum bank seepage occur during late winter and early spring.

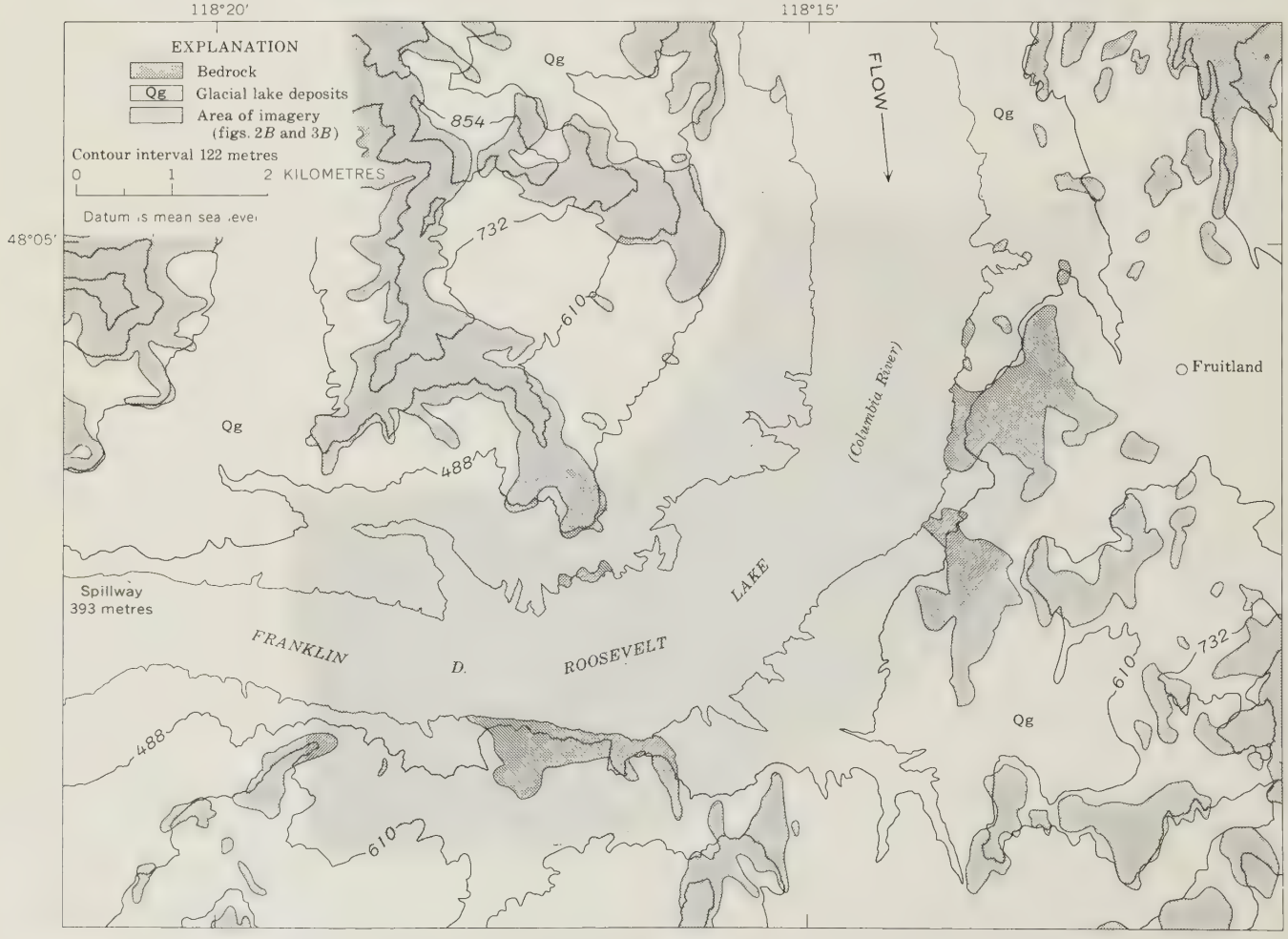

FIGURE 5.—Sketch showing glacial deposits and bedrock and approximate extent of imagery near Fruitland, Wash. Geology from Campbell and Raup (1964).

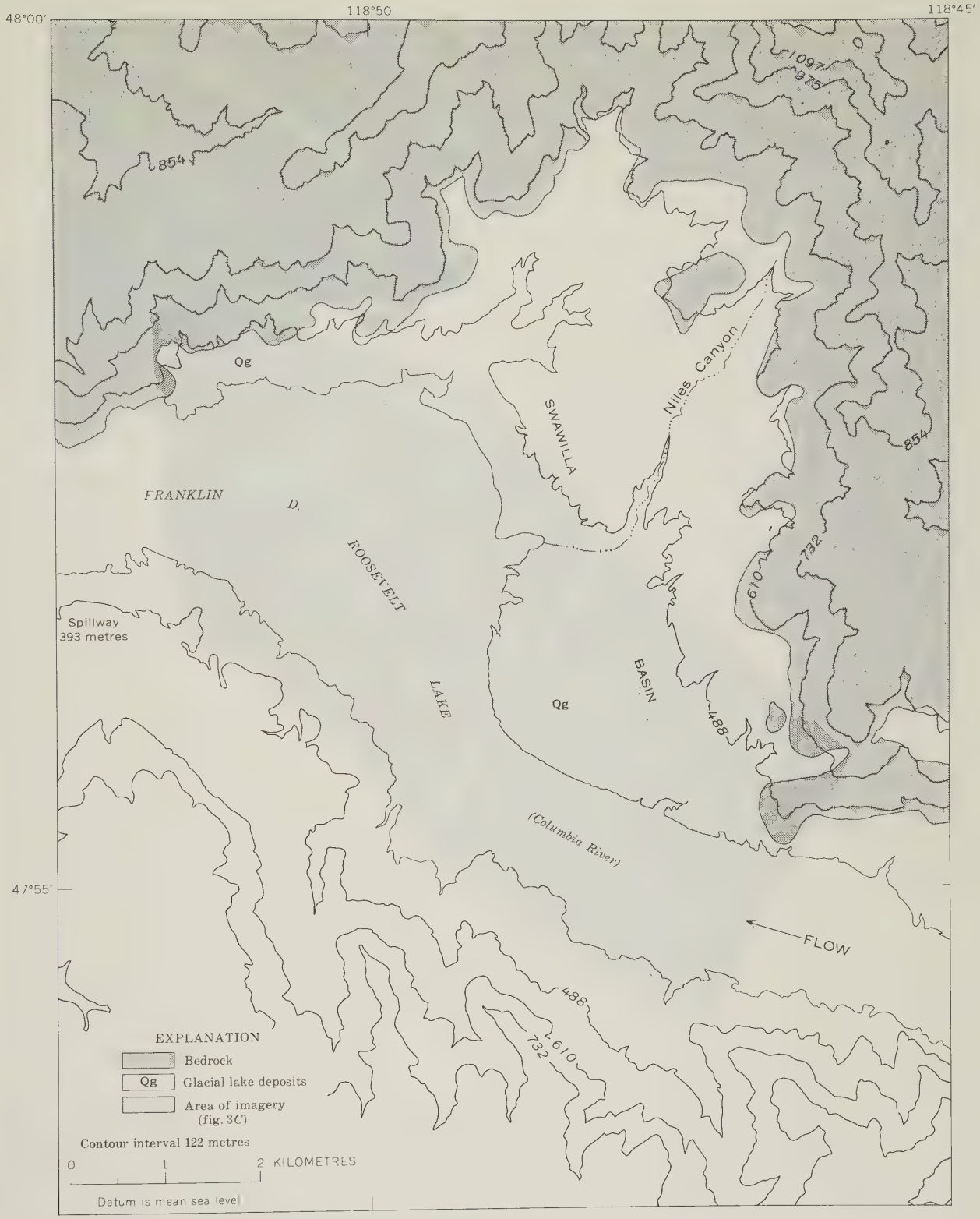

FIGURE 6.—Sketch showing glacial deposits and bedrock and approximate extent of imagery of the Swawilla Basin. No geologic data available for south side of lake. Geology for north side modified from Pardee (1918).

During this period, the temperature difference between surface water and ground water is at a maximum.

REFERENCES CITED

Anderson, H. W., Jr., 1969, Water supplies for Coulee Dam National Recreation Area, Washington: U.S. Geol. Survey open-file report, 104 p.

Becraft, G. E., 1966, Geologic map of the Wilmont Creek quadrangle, Ferry and Stevens Counties, Washington: U.S. Geol. Survey Geol. Quad. Map GQ–538.

Campbell, A. B., and Raup, O. B., 1964, Preliminary geologic map of the Hunters quadrangle, Stevens and Ferry Counties, Washington, U.S. Geol. Survey Mineral Inv. Map MF–276.

Fischer, W. A., Davis, D. A., and Sousa, T. M., 1966, Freshwater springs of Hawaii from infrared images: U.S. Geol. Survey Hydrol. Inv. Atlas HA–218.

Hunn, J. D., and Cherry, R. N., 1969, Remote sensing of offshore springs and spring discharge along the Gulf Coast of Central Florida *in* 2d Ann. Earth Resources Aircraft Program Status Rev.: Houston, Tex., NASA Manned Spacecraft Center, v. 3, p. 39–1 to 39–7.

Jones, F. O., Embody, D. R., and Peterson, W. L., 1961, Landslides along the Columbia River valley, northeastern Washington: U.S. Geol. Survey Prof. Paper 367, 98 p.

Lee, Keenan, 1969, Infrared exploration for shoreline springs at Mono Lake, California test site: Symposium on Remote Sensing of the Environment, 6th, Michigan Univ., Ann Arbor, Proc., p. 1075–1087.

Lohman, S. W., and others, 1972, Definitions of selected groundwater terms—revisions and conceptual refinements: U.S. Geol. Survey Water-Supply Paper 1988, 21 p.

Mills, J. W., 1969, High-calcium limestones of eastern Washington: Washington Div. of Mines and Geol. Bull. 48, 186 p.

Pardee, J. T., 1918, Geology and mineral deposits of the Colville Indian Reservation, Washington: U.S. Geol. Survey Bull. 677, 186 p.

Pluhowski, E. J., 1972, Hydrologic interpretations based on infrared imagery of Long Island, New York: U.S. Geol. Survey Water-Supply Paper 2009–B, 20 p.

Richmond, G. M., Fryxell, R., Neff, G. E., and Weis, P. L., 1965, The Cordilleran Ice Sheet of the northern Rocky Mountains and related Quaternary history of the Columbia Plateau *in* Wright, H. E., and Fry, D. G., eds., The Quaternary of the United States, a review volume for the 7th Cong. of the Internat. Assoc. for Quaternary Research: Princeton, N.J., Princeton Univ. Press, p. 231–242.

Simons, W. D., and Rorabaugh, M. I., 1971, Hydrology of Hungry Horse Reservoir, northwestern Montana: U.S. Geol. Survey Prof. Paper 682, 66 p.

Thompson, T. H., 1974, Computer model for determining bank storage at Hungry Horse Reservoir, northwestern Montana: U.S. Geol. Survey Prof. Paper 833, 16 p.

Weaver, C. E., 1920, The mineral resources of Stevens County: Washington Geol. Survey Bull. 20, 350 p.

Wood, C. R., 1972, Ground-water flow: Photogramm. Eng., v. 38, no. 4, p. 347–352.

Jour. Research U.S. Geol. Survey
Vol. 5, No. 1, Jan.–Feb. 1977, p. 11–16

TRANSVERSE MIXING IN THE MOBILE RIVER, ALABAMA

By WILLIAM MEYER, Indianapolis, Ind.

Abstract.—Transverse dispersion in the Mobile River was measured by (1) ground-based techniques using water samples and a fluorometer and (2) by aerial photography. Magnitude of the transverse mixing coefficient obtained by the two methods was 6.2 feet squared per second (0.58 metre squared per second) and 5.0 feet squared per second (0.46 metre squared per second), respectively. The value of the numerical coefficient k, which relates the transverse mixing coefficient E_z to shear velocity U^* and average depth of flow, d, by the relationship $k=E_z/U^*d$, was 7.2.

Transverse dispersion was measured in the Mobile River in southern Alabama by ground-based techniques described by Yotsukura, Fischer, and Sayre (1970) and by remote-sensing techniques described by Murray, Smith, and Sonu (1970). Although the techniques described by Murray, Smith, and Sonu (1970) had been used successfully in large bodies of water such as the Gulf of Mexico, they had not been used previously in a large stream. This study afforded the opportunity to do so and, in addition, allowed a comparison of the results obtained from the two techniques. This report summarizes the two approaches used and the results obtained from the investigation.

Acknowledgments.—This investigation was a joint effort of U.S. Geological Survey personnel from the Alabama District and from the Remote Sensing Research Project, Prescott, Ariz.

TRANSVERSE MIXING

Transverse mixing is described by the transverse mixing coefficient E_z, which defines rate of cross-channel mixing. The transverse mixing coefficient in open-channel flows is assumed to have the form

$$E_z = k\ U^*\ d, \qquad (1)$$

where U^* is shear velocity, d is depth of flow, and k is a numerical constant (Yotsukura and others, 1970). Little experimental data are available for values of k in large, slow-moving natural streams. Yotsukura, Fischer, and Sayre (1970) obtained a value of k that ranged from 0.6 to 0.7 for a 6.0-mile (9.6-kilometre) reach of the Missouri River near Blair, Nebr., and reported that Glover (1964) obtained a value of k equal to 0.72 for the Columbia River near Richland, Wash. Secondary flow increases the effective values of k at bends in a river. Sayre and Yeh (1973) reported that the average k for a 180° bend in the Missouri River was 3.4.

Description of the test reach

The part of the Mobile River tested for transverse mixing consisted of the first 3.0 mi (4.8 km) of the river immediately below the confluence of the Tombigbee and Alabama Rivers. This point is approximately 36 river miles (58 km) north of Mobile Bay. Topographic relief is extremely low through this section, and much of the area is swamp. In the 3.0 mi (4.8 km) tested, the Mobile River flows 1.0 mi (1.6 km) in an approximately southerly direction and then bends gently to flow almost straight in a southwesterly direction (fig. 1). Physical characteristics of the channel are represented by data obtained at five measuring sections during the study as shown in table 1.

Flow from the Alabama River enters the Tombigbee River at an angle of about 45° at their confluence. Discharges and velocities of the two streams were virtually identical at the time of the study. Vertical and transverse temperature readings along the lower reaches of both streams indicated that the temperature difference between the two streams was only 0.50°C (Celsius). The Tombigbee River, whose temperature was measured from top to bottom at quarter points across its width, had a uniform temperature of 20.5°C. The Alabama River, whose temperature also was measured from top to bottom, was sampled at quarter points across its width and had a uniform temperature of 20°C. On November 15, 1972, the same measured sections showed the water temperature in the Tombigbee River to be 20°C and the temperature in the Alabama River to be 19°C (J. R. Harkins, written commun., 1973).

Aerial color photographs of the Alabama and the Tombigbee Rivers obtained during the study exhibited

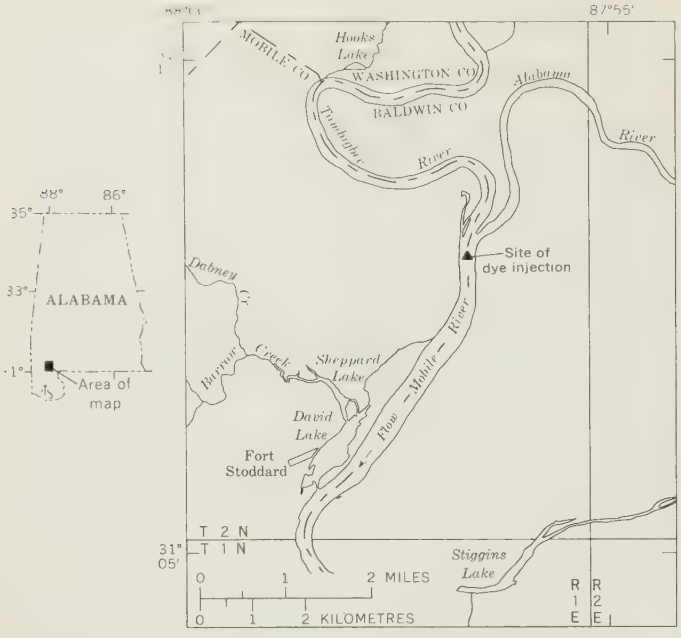

FIGURE 1.—Location of study reach. Base from U.S. Geological Survey Tenshaw topographic quadrangle, scale 1:62,500; 1943.

TABLE 1.—*Physical characteristics of measuring sections on the Mobile River, Ala.*

[x, downstream distance from continuous fixed-point dye release; U^*, shear velocity in feet per second]

Measuring section	x (ft)	Width (ft)	Area (ft²)	Average depth (ft)	U^* (ft/s)
1	1,750	1,230	25,200	20.0	0.064
2	6,745	1,512	22,200	15.0	.056
3	10,165	1,410	17,466	12.4	.051
4	13,135	1,548	24,300	16.0	.058
5	16,185	1,340	24,900	18.5	.062

tonal differences between the two rivers, and the common boundary between the rivers after forming the Mobile River was clearly observable. (See fig. 2, a black-and-white reproduction.) Turbulent eddies with areas of as much as 100,000 ft² (9,290 m²) were created along this boundary (fig. 2). These eddies were observed from a boat on the water surface, but their extent was not realized until after the color film had been developed. The tonal differences between the two rivers as exhibited by color photographs taken from the air were barely discernible to an observer on a boat.

In the study, dye was released very near the boundary between the two rivers. Dispersion of the dye, as demonstrated by aerial color photographs, seemed to be primarily controlled by the boundary zone and the turbulent eddies within it (fig. 2).

Test procedure

The basic procedure used to obtain field information on the transverse mixing coefficient required a continuous, fixed-point injection of Rhodamine-WT dye at a given rate into the stream. Cross-channel measurements of dye concentration at five downstream sections were then obtained.

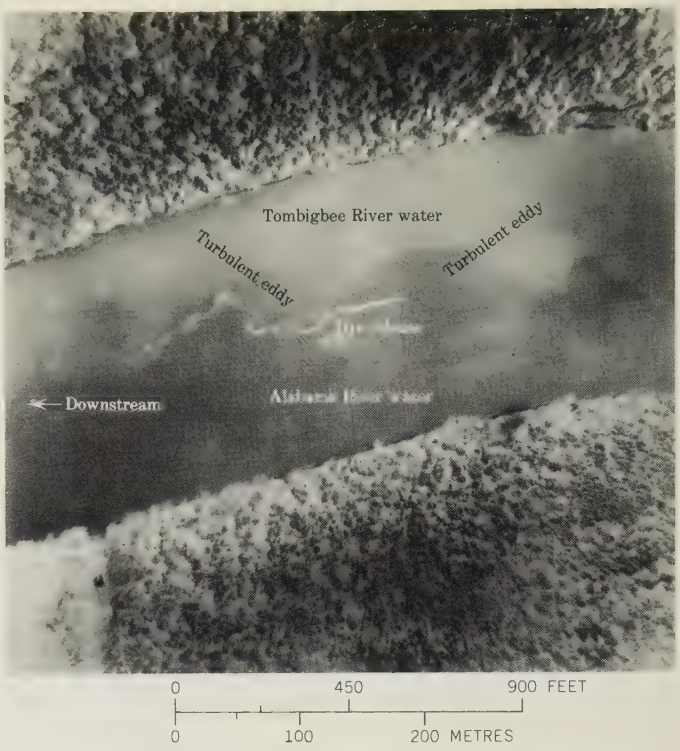

FIGURE 2.—Dye movement down the Mobile River.

The continuous fixed-point injection was made at approximately the center of the Mobile River, immediately downstream from the confluence of the Tombigbee and Alabama Rivers. A boat was anchored at this point. A constant-head tank was mounted on the boat with the hose from the tank extending over the boat and ending several feet above the water level. Injection of the dye was begun at 9:55 a.m., c.s.t., November 17, 1972, and an average flow rate of 0.136 gallon per minute (0.01 L/s) was maintained until 12:22 p.m. The injected dye consisted solely of Rhodamine-WT, 20-percent solution. Altogether, 20 gal (76 L) of the dye solution were injected during the test.

Water samples for determination of dye concentration were collected in chronological and downstream order at the five sampling cross sections. Sample collection began at section 1 at 10:58 a.m. and ended at section 5 at 2:52 p.m. (table 1). From 3 to 5 minutes were required to complete sample collection at each section. The measuring sections were established roughly an equal distance apart downstream from the injection point. Actual downstream distance of each section was later established from a photomosaic (scale

1:4,000) constructed of the entire test reach. Section 1 was 1,750 ft (533 m) downstream from the point of injection, whereas section 5 was 16,185 ft (4,933 m) downstream from the dye-injection point. Cross-channel width at each section was measured by stadia.

The approximate center of each measuring section was marked by an anchored float, and the channel edges were marked with flagging. A boat was moved slowly at a constant speed across the channel section, and dye samples were obtained by dipping a sample bottle below the water surface at equal time intervals as the boat moved across the section. Concurrent with each sampling run a sonar was operated to obtain depth of channel and to identify the location of each dye sample. Sonar readings were recorded on a chart that was run at a constant speed during the traverse; site of each sample collected at the surface was designated by a mark on the chart. This technique allowed the location of each surface sample to be established within an accuracy of about 5.0 ft (1.5 m). The number of samples collected in the five sections ranged from 12 to 15. The concentration of dye in each sample was then determined by means of a fluorometer and a calibration curve. Data for each section are presented in table 2.

TABLE 2.—*Distribution of dye concentration in transverse direction, transverse mixing test on the Mobile River, Ala., November 17, 1972*

Station	Distance from left bank (feet)	Dye concentration (micrograms per litre)
Cross section 1		
[1,750 feet=distance from injection point; 1,230 feet=width of measuring section]		
1	92	0.1
2	170	.2
3	262	.0
4	350	.0
5	478	.9
6	565	.4
7	688	3.0
8	808	8.1
9	955	1.7
10	1,072	.1
11	1,170	.1
12	1,200	.0
Cross section 2		
[6,745 feet=distance from injection point; 1,512 feet=width of measuring section]		
1	70	1.2
2	190	1.9
3	290	3.7
4	400	3.2
5	510	4.4
6	750	3.0
7	865	1.5
8	975	1.1
9	1,060	.6
10	1,150	.4
11	1,250	.7
12	1,355	.5
13	1,450	.0

TABLE 2.—*Distribution of dye concentration in transverse direction, transverse mixing test on the Mobile River, Ala., November 17, 1972*—Continued

Station	Distance from left bank (feet)	Dye concentration (micrograms per litre)
Cross section 3		
[10,165 feet=distance from injection point; 1,410 feet=width of measuring section]		
1	55	4.5
2	152	1.7
3	245	4.4
4	342	3.4
5	580	3.8
6	682	2.3
7	772	4.2
8	880	4.1
9	990	2.7
10	1,102	1.6
11	1,202	1.0
12	1,308	1.3
Cross section 4		
[13,135 feet=distance from injection point; 1,548 feet=width of measuring section]		
1	50	1.6
2	146	2.5
3	281	1.6
4	350	2.0
5	472	1.9
6	572	2.3
7	674	2.0
8	784	2.4
9	890	4.4
10	992	4.0
11	1,092	2.6
12	1,200	1.4
13	1,305	1.4
14	1,408	1.3
15	1,498	1.0
Cross section 5		
[16,185 feet=distance from injection point; 1,340 feet=width of measuring section]		
1	70	1.8
2	170	1.3
3	278	2.3
4	355	1.7
5	452	2.4
6	545	3.0
7	644	3.5
8	740	3.8
9	839	4.2
10	935	4.9
11	1,025	3.9
12	1,118	6.0
13	1,210	1.7
14	1,286	.8

Several temporary staff gages were installed at the edge of the Mobile River to determine the slope of the water surface during a time-of-travel study on November 14, 1972. The decrease in water surface was measured for the first 4.4 mi (7.1 km) of the river. Values computed for water-surface slope were used to compute an energy slope for the transverse mixing test; this value, 0.000006, was assumed to be constant throughout the test reach. Velocity was measured along a measuring section (fig. 1) of the Mobile River 20,800 ft (6,340 m) downstream from the point of the dye re-

lease. Measurements were begun at 10:50 a.m. on November 14, 1972, and were continued until 5:15 p.m. Average velocity for the section during the measuring period was 0.98 ft/s (0.3 m/s). This value was used for the transverse mixing study on November 17, 1972.

In addition to the ground-based information, low-level, large-scale (1 in=333 ft and 1 in=166 ft or 25.4 mm=102 m and 25.4 mm=51 m), aerial color photographs of the dye-colored water were obtained at short time intervals during the study.

CALCULATION OF THE TRANSVERSE MIXING COEFFICIENT

Method of moments

The relationship

$$E_z=\frac{\bar{U}}{2}\frac{\mathrm{d}\sigma_z^2}{\mathrm{d}x} \qquad (2)$$

may be used to provide a useful first approximation to the transverse mixing coefficient for dispersion of a tracer from a continuous point source. U is the mean flow velocity, σ_z^2 is the variance of the transverse distribution of the tracer, and x is the distance downstream from the point of injection of the tracer.

Assumptions involved in the derivation of equation 2 are that (1) flow is occurring in an infinitely wide, open channel with uniform depth and (2) flow velocity is uniform throughout the channel width. Because such conditions did not exist in the Mobile River, the equation can be used only to provide an approximation of E_z. A more valid method of analysis would require computer simulation of field data (Yotsukura and others, 1970).

Determination of variance of the transverse distribution of dye involved constructing a graph of concentration, C, versus cross-channel distance, z, for each section from the data in table 2 and calculating variance from the relationship

$$\sigma_z^2=\frac{\Sigma[C_i\times(z_i-\bar{z})^2]}{\Sigma C_i} \qquad (3)$$

for C_i equal to the concentration at the point z_i. Further, $z_{i+1}-z_i$ is chosen equal to a constant. The factor $\bar{z}$ is obtained from the relationship

$$\bar{z}=\frac{\Sigma C_i z_i}{\Sigma C_i}. \qquad (4)$$

Plottings of σ_z^2 versus distance are shown in figure 3. The first two points in figure 3 indicate a nearly linear increase in σ_z^2 with distance, and the slope of the line of best fit yields a value for the transverse mixing coefficient equal to 6.2 ft²/s (0.58 m²/s) for this reach. The value of k obtained from equation 1 and data in table 1 is 7.2. This value of k is one order of magnitude larger than that previously reported for large streams. Unfortunately, a substantial amount of dye had reached both sides of the river at cross sections 3, 4, and 5, so that reliable calculation of σ_z^2 was impossible for these sections.

Nobuhiro Yotsukura (written commun., 1973) has suggested several possibilities that either singly or in some combination could produce a large degree of mixing, including: (1) A jet effect produced by velocity difference of the two rivers, (2) a lateral density difference between the two rivers, (3) a small average velocity combined with some stratification, or (4) transverse convections due to the bend. Of these possibilities, item 4 seems most likely. In addition, as suggested by J. R. Harkins (written commun., 1973), the angle at which flow from the Alabama River entered the Tombigbee River would certainly cause a jet effect (item 1). Item 3 is also a possibility. All these possibilities would increase the mixing action in the bend immediately downstream in a southwesterly direction and should enhance the mixing of the water from the two streams. Because of the temperature difference of only 0.5°C between the two rivers, the large degree of mixing observed probably did not result from item 2.

Analysis of aerial photographs

Variance of the transverse distribution of dye can be approximated from an aerial photograph by two meth-

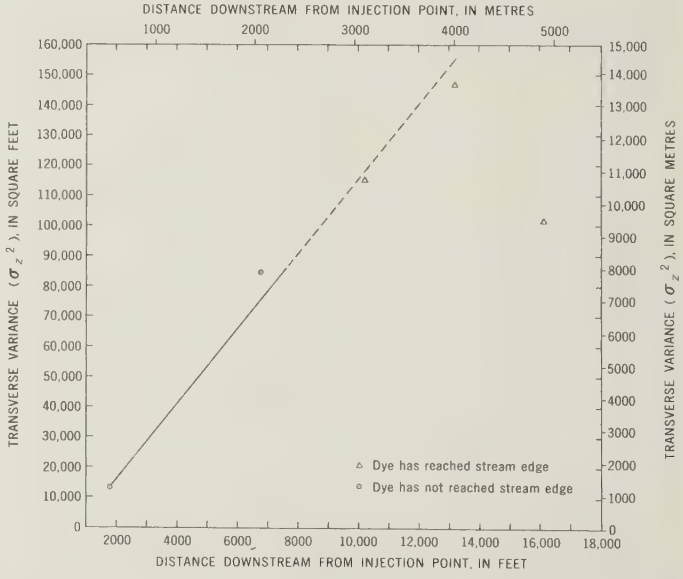

FIGURE 3.—Transverse variance of dye distribution versus downstream distance from the injection point. Transverse variance was determined from water sample taken from the water surface by boat.

ods. The first method consists of correlating levels of dye concentration, as recorded by surface sampling (Ichiye and Plutchak, 1966). This method requires that the film record a uniform density level for the host water or that differences in this level be accountable. The second method consists of setting the half width of the dye spread in the lateral direction equal to the standard deviation σ_z, as suggested by Murray, Smith, and Sonu (1970). For such purposes, the outer boundary of the dye, as determined visually from a photograph, is assumed to represent a line of equal dye concentration detectable to the eye. These methods have been used in determining mixing coefficients in estuaries and oceans.

The author attempted a densitometric analysis of the dye spread shown on colored aerial photographs. The photographs indicated that movement of the dye was confined primarily to the turbulent eddy zone created by the mixing of the Tombigbee and Alabama Rivers and that density level of the water alone in this zone changed rapidly in an unaccountable manner; thus, fluctuations in the density of the dye were masked by fluctuation in the density level of the host water. The dye spread probably could have been analyzed by color separation of the photographs followed by densitometric analysis, but this technique was considered to be beyond the means of the study.

Figure 4 shows the results of visually examining the aerial photographs obtained at different times over the dye plume. As suggested by Murray, Smith, and Sonu (1970), halfwidth of the dye spread was measured at various distances downstream from the point of release, and the squared values were plotted against their respective distances. Three different time periods were examined by photography: 10:40 a.m., or 45 minutes after beginning of injection; 11:36 a.m., or 1 hour and 41 minutes after injection; and finally, 12:15 p.m., or 2 hours and 20 minutes after injection. Figure 4 shows an increasing rate of dye dispersion in about the first 1,000 ft (305 m) of travel; beyond 1,000 ft (305 m) the dispersion rate tends to increase linearly. The slope of the line of best fit through the linear part of the data yields a transverse mixing coefficient of 5.0 ft²/s (0.46 m²/s) for this section of the study reach.

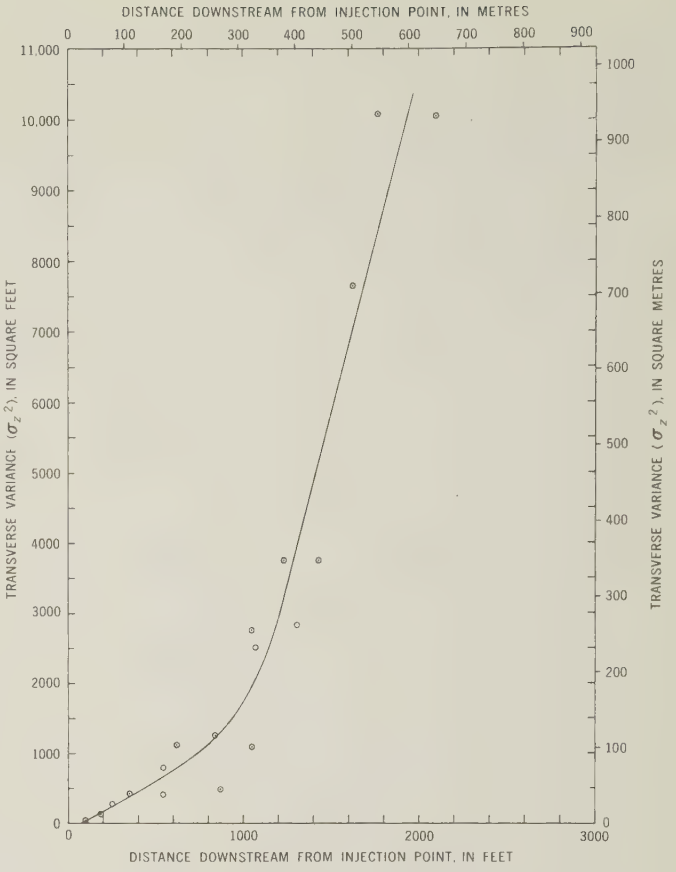

FIGURE 4.—Transverse variance of dye distribution versus downstream distance from the injection point. Transverse variance was determined visually from aerial photographs at 10:40 a.m., 11:36 a.m., and 12:15 p.m., c.s.t.

SUMMARY AND CONCLUSIONS

As approximated by the method of moments, a value of the transverse mixing coefficient equal to 6.2 ft²/s (0.58 m²/s) was obtained for a 1.0-mi (1.6-km) section of the Mobile River immediately downstream from the confluence of the Tombigbee and Alabama Rivers. Visual examination of the dye spread as recorded by colored aerial photographs yielded a transverse mixing coefficient of 5.0 ft²/s (0.46 m²/s) for the first 2,100 ft (640 m) of the study reach.

The numerical coefficient k described by the relationship $k=E_z/U^*d$ was 7.2 for the 3.0-mi (4.8-km) study reach. This value represents an increase of nearly one order of magnitude over that previously reported for large natural streams. Transverse convections due to the bend just below the confluence of the Alabama and the Tombigbee Rivers and the jetlike mixing of the two waters caused by the angle at which flow from the Alabama River entered the Tombigbee probably combined to increase the value of k.

This study is the first in which remote-sensing techniques were used in addition to standard ground-based techniques to obtain an approximation of the transverse mixing coefficient of a large stream. The numerical values for the coefficient obtained by the two methods were very close, although the standard technique allowed a much larger section of the river to be studied than that allowed by remote sensing.

REFERENCES CITED

Glover, R. E., 1964, Dispersion of dissolved or suspended materials in flowing streams: U.S. Geol. Survey Prof. Paper 433–B, 32 p.

Ichiye, Takashi, and Plutchak, N. B., 1966, Photodensitometric measurement of dye concentration in the ocean: Lamont Geol. Observatory, Contr. 923, p. 364–370.

Murray, S. P., Smith, W. G., and Sonu, C. V., 1970, Oceanographic observation and theoretical analysis of oil slicks during the Chevron spill, March 1970: U.S. Coast Guard rept. 714104/A/006–2, p. 101.

Sayre, W. W., and Yeh, Tso-Ping, 1973, Transverse mixing characteristics of the Missouri River downstream from the Cooper Nuclear Station: Iowa Univ., Iowa Inst., Hydraulic Research Rept. 145, 46 p.

Yotsukura, Nobuhiro, Fischer, H. B., and Sayre, W W.., 1970, Measurement of mixing characteristics of the Missouri River between Sioux City, Iowa, and Plattsmouth, Nebraska: U.S. Geol. Survey Water-Supply Paper 1899–G, 29 p.

Jour. Research U.S. Geol. Survey
Vol. 5, No. 1, Jan.–Feb. 1977, p. 17–32

DATING AND RECURRENCE FREQUENCY OF PREHISTORIC MUDFLOWS NEAR BIG SUR, MONTEREY COUNTY, CALIFORNIA

By LIONEL E. JACKSON, Jr., Menlo Park, Calif.

Abstract.—Botanical evidence based on the dendrochronology and root horizons of redwoods (*Sequoia sempervirens*) and radiocarbon dating were used to date prehistoric mudflows near Big Sur, Calif. At least three periods of mudflow activity were delineated for the approximate prehistoric period 1370–1800. Two historic periods of mudflow activity have occurred, 1908–10 and 1972–73. The documentation of mudflows as characteristic surficial processes in the Santa Lucia Range indicates a hazard to development on recent mudflow deposits in this region.

From mid-October 1972 through mid-February 1973, mudflows from the rugged Santa Lucia Range repeatedly invaded the community of Big Sur, Calif. (figs. 1, 2). The flows were generated by intense winter rains falling on the steep slopes of the Santa Lucias which had been denuded by the Molera fire in August 1972. Damage from mudflows and floodwater was predominantly confined to areas marginal to the lower courses of Pheneger, Juan Higuera, and Pfeiffer-Redwood Creeks (fig. 2). Within these areas California State Highway 1 was blocked by mud, boulders, and vegetational debris; structures were partly buried, heavily damaged, or leveled; automobiles were swept into the Big Sur River; and private and public recreational areas were littered with bouldery debris. One life was lost as a result of the mudflow activity.

A reconnaissance of the mudflow-afflicted areas of Big Sur following the first flows in October 1972 showed that the structures and roads damaged by mudflows and attendant floodwater were generally on alluvial fans deposited by Pheneger, Juan Higuera, and Pfeiffer-Redwood Creeks. Older mudflow deposits, almost identical to those freshly deposited, were well exposed along stream channels in these fans.

The alluvial fans of these three streams are dominantly covered with forests of redwood (*Sequoia sempervirens*). Subsequent investigation of the fans indicated that the root systems of the redwoods have, over the years, acted as bedding markers along the tops and bottoms of the older mudflow deposits. Thus, by dating root layers, a chronology and recurrence frequency of mudflow activity could be established. Such a recurrence frequency is useful in evaluating

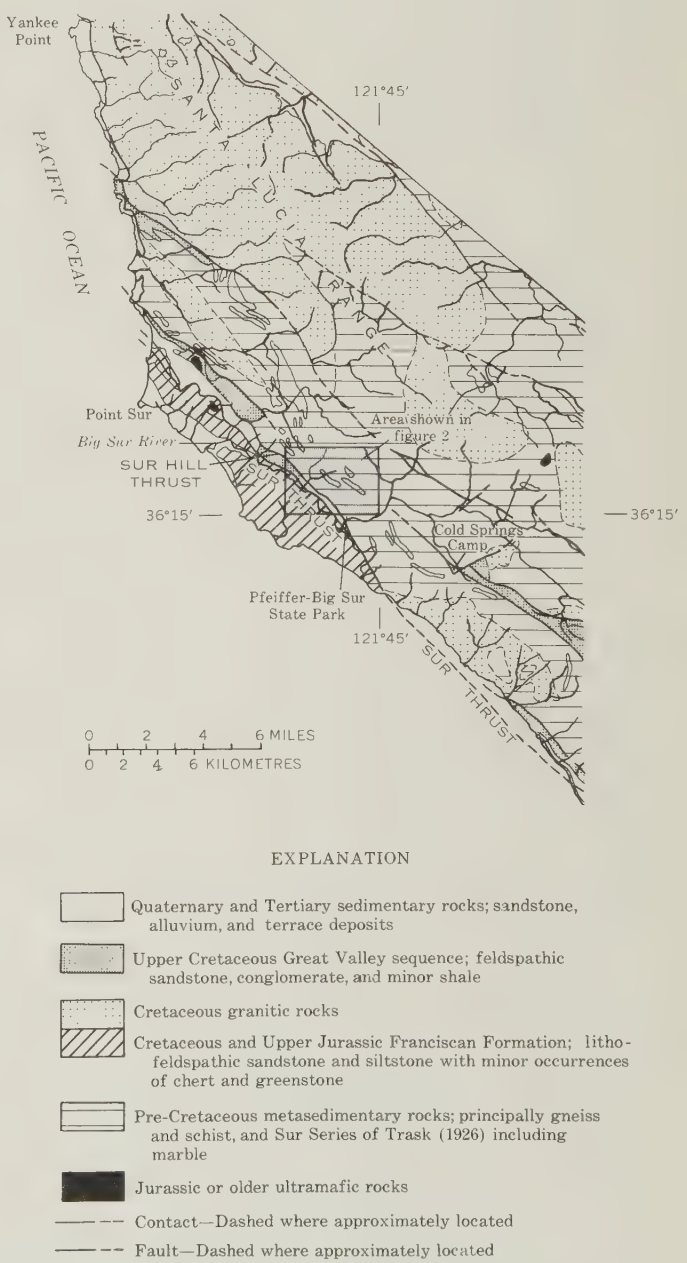
Yankee Point
121°45′
PACIFIC OCEAN
SANTA LUCIA RANGE
Point Sur
Big Sur River
Area shown in figure 2
SUR HILL THRUST
36°15′
Cold Springs Camp
Pfeiffer-Big Sur State Park
SUR THRUST
0 2 4 6 MILES
0 2 4 6 KILOMETRES
EXPLANATION
Quaternary and Tertiary sedimentary rocks; sandstone, alluvium, and terrace deposits
Upper Cretaceous Great Valley sequence; feldspathic sandstone, conglomerate, and minor shale
Cretaceous granitic rocks
Cretaceous and Upper Jurassic Franciscan Formation; lithofeldspathic sandstone and siltstone with minor occurrences of chert and greenstone
Pre-Cretaceous metasedimentary rocks; principally gneiss and schist, and Sur Series of Trask (1926) including marble
Jurassic or older ultramafic rocks
Contact—Dashed where approximately located
Fault—Dashed where approximately located

FIGURE 1.—Generalized geology of the Big Sur area, Calif. Base from U.S. Geological Survey Santa Cruz map, scale 1:250,000, 1965. Geology modified from Jennings and Strand (1958) and Gilbert (1971).

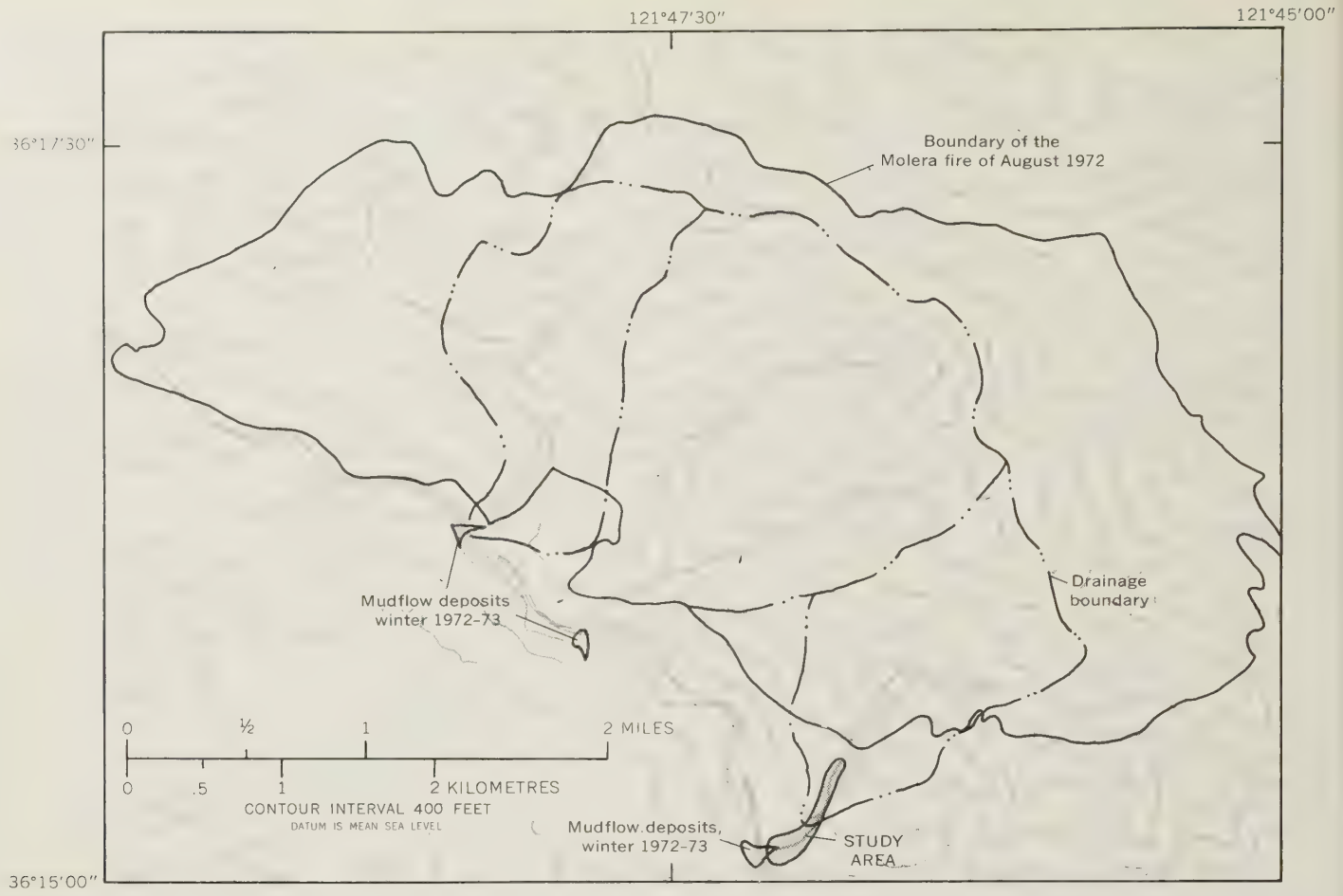

FIGURE 2.—Boundaries of the Molera fire of August 1972 and of the three major drainages that produced mudflows during the following autumn and winter. Base from U.S. Geological Survey Big Sur topographic quadrangle, scale 1:24,000, 1956.

mudflow hazards for land-use planning and in designing and routing roads and bridges in the mudflow-prone coastal margin of the Santa Lucia Range.

Acknowledgments.—The author is grateful for the cooperation he received from the staff of Pfeiffer–Big Sur State Park and the residents of Big Sur. Dr. W. J. Barry of the California Department of Parks and Recreation provided expertise in forest ecology and expedited this project. Carol N. Jackson assisted in the field. Richard H. Fuller, U.S. Geological Survey, helped in clay mineralogy determinations. E. J. Helley and R. H. Campbell, U.S. Geological Survey, assisted in the field and laboratory, and Helley provided his knowledge of dendrochronology.

SETTING

The community of Big Sur is situated along the Big Sur River (fig. 2) and straddles the northwest-trending Sur thrust—a major structural boundary of the Santa Lucia Range in this area. East of the thrust are Cretaceous granitic intrusive rocks and the pre-Cretaceous metamorphic rocks of the Sur Series of Trask (1926) which compose the core of the range. West of the thrust are the complex eugeosynclinal rocks of the Cretaceous and Upper Jurassic Franciscan Formation which form the basement west of the fault (Gilbert, 1971). The Sur thrust bifurcates into two parallel faults in the Big Sur area (fig. 1)—the Sur Hill thrust on the east and the Sur thrust on the west. Sandwiched between these two faults is a narrow wedge of Tertiary sandstone (Oakeshott, 1951). Pleistocene and Holocene deposits discontinuously mask the bedrock geology along the Big Sur River.

The topography and drainage of the area generally parallel the regional northwest-trending structure. Relief is rugged east of the Sur thrust. For example, the altitude ranges from 120 feet (37 metres) at the mouth of the Juan Higuera Creek to 3,550 ft (1,080 m) atop Cabezo Prieto less than 2 miles (3 kilometres) to the east (fig. 2). Slopes are commonly 45° or greater on the granitic and metamorphic terrain east of Big Sur, but they are generally less precipitous on the Franciscan terrain west of the Sur thrust.

The climate of the area is Mediterranean with al-

most all rainfall occurring between October and April. Mean annual precipitation at Pfeiffer–Big Sur State Park averages about 41 inches (1,000 millimetres) per year; however, extremes in mean annual precipitation as low as 21 in (530 mm) and as high as 80 in (2,000 mm) have been recorded. Summer advection fogs, which are common in the area, supplement mean annual precipitation through drip from forest trees. Mean annual precipitation increases with altitude in the Big Sur area. For example, 80 in (2,000 mm) of rain was recorded at Pfeiffer–Big Sur State Park during the winter 1940–41; Cold Springs Camp, 7 mi (12 km) south of the park, received 160 in (4,100 mm) of rain (Pearson and others, 1967, p. B–5). The altitude of Pfeiffer–Big Sur State Park averages 216 ft (65.8 m), and that of Cold Springs Camp, 1,350 ft (411 m).

The distribution of vegetation is controlled primarily by exposure and topography. Coastal chaparral dominates on very steep or south-facing slopes. North-facing slopes, deep narrow canyons, and valley bottoms are mantled by conifers and hardwoods. Redwood is the dominant tree in these forests.

The upper parts of the drainage basins of Pheneger, Juan Higuera, and Pfeiffer-Redwood Creeks and several adjacent unnamed basins were denuded of their vegetation by the Molera fire in August 1972 (fig. 2). The combination of the steep fire-denuded slopes and intense rains of the autumn and winter 1972–73 helped to generate the mudflows in the Big Sur area (Cleveland, 1973). The only other mudflows recorded in these basins since the area was settled in 1860 occurred during the winters 1908, 1909, and 1910. The flows followed a 1907 forest fire which burned the vegetation in the three basins (L. R. Helm, written commun., 1973).

The most extensive mudflow deposits in the Big Sur area are along the lower courses of Pheneger, Juan Higuera, and Pfeiffer-Redwood Creeks. In these areas, alluvial fans and valley fills have been deposited primairly from mudflow activity. The fans grade upstream into valley fills which are constricted by steep-sided canyon walls cut from river and older mudflow deposits and bedrock. The valley fills are generally bounded upstream by an abrupt increase in channel gradient which usually coincides with the change in lithology at the Sur Hill thrust. The downstream fans abruptly flare at the mouths of the canyons near their confluence with the Big Sur River. Gradients on the fans and upstream valley fills range from 6 to 10 percent. The mudflow deposits are typically not well sorted and are composed of particles that range in size from clay to boulders greater than 10 ft (3 m) in length. Minor lenses of fluvial deposits occur within the mudflow deposits. These deposits probably represent fluvial reworking following deposition of the mudflows.

PREVIOUS INVESTIGATIONS

Most geologic investigations in the Big Sur area have been concerned primarily with bedrock geology. Trask (1926) first mapped the Point Sur 15′ quadrangle. Oakeshott (1951) mapped the Pfeiffer–Big Sur State Park area and mentioned the Pleistocene and Holocene deposits along the Big Sur River. Gilbert (1971) mapped parts of the Big Sur area during his study of the Sur fault. Cleveland (1973) and Rodine (1975) investigated the generation of mudflows in the Big Sur area during October and November 1972.

INVESTIGATIVE METHODS

Detailed study of the mudflow stratigraphy was made of one of the three alluvial fan–valley fill complexes. The mudflow deposits along Pfeiffer-Redwood Creek in Pfeiffer–Big Sur State Park (fig. 2) were chosen because of the extensive degradation of the channel of Pfeiffer-Redwood Creek by mudflows and floodflows during the winter 1972–73. Vertical channel degradation of as much as 6.0 ft (1.8 m) was recorded in some places. As a result, much of the mudflow stratigraphy along the creek is well exposed. In some places the deposits are completely exposed down to bedrock.

A base map, scale 1:480, of Pfeiffer-Redwood Creek between the Big Sur River and a point 1,240 ft (378 m) upstream was available through the California Department of Parks and Recreation. The remaining reach of the creek between the mapped area and Pfeiffer Falls was sketch-mapped by tape and compass. These maps were combined and used in plotting geologic and botanical features (fig. 3).

Living trees and carbon-14 dating were the two sources of data used to date and correlate mudflow deposits.

Use of redwoods in dating mudflow deposits

Redwoods grow abundantly in the canyons and on north-facing hillsides of the Big Sur area. These trees are able to survive the periodic fires, mudflows, and floods which frequent the Big Sur area because of the following growth characteristics: The growth of adventitious roots, the growth of a ring of sprouts around a parent stump (fairy ring development), healing of fire or impact injuries to the trunk, and buttress ring growth following tilting of the trunk. These responses to injury or burial provide evidence for the dating of past catastrophic events.

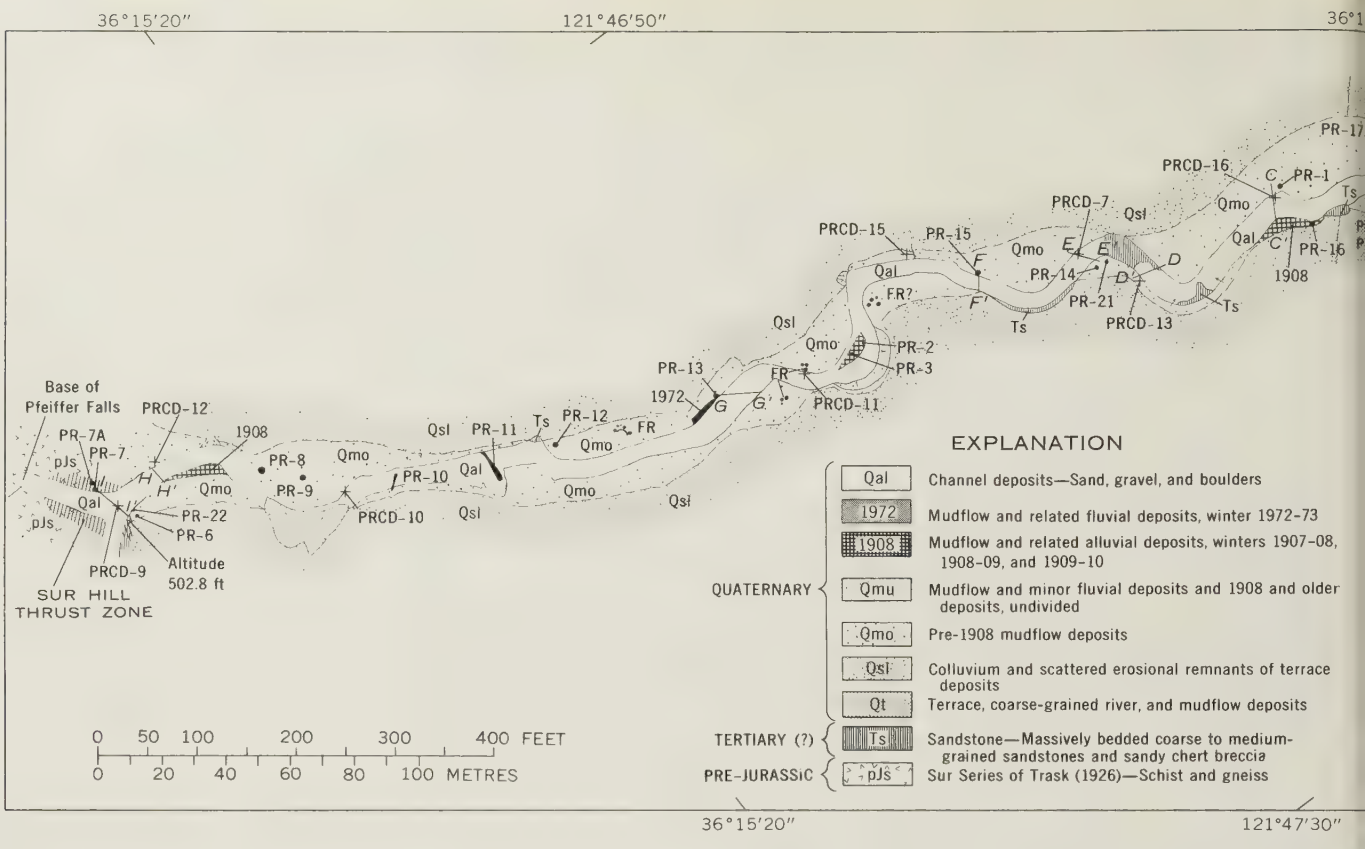

FIGURE 3.—Geology and selected botanical features along P

Fundamental to all uses of the redwood to date past catastrophic natural events is its long lifespan. Individual specimens in the 500- to 1,000-year-old range have been identified in the Big Sur area.

Root system.—Redwoods lack tap roots (Fritz, 1934). Instead they develop extensive, relatively thin root horizons that, in the study area, never exceeded 4 ft (1.2 m) in thickness. Redwoods are able to withstand periodic burial by mudflows or flood-deposited sediment because of their propensity for negative geotrophic root growth (roots growing toward the surface following burial) and subsequent development of a new and shallower root system (Stone and Vasey, 1968). Negative geotrophic root growth restores the flow of water and nutrients into the tree which would otherwise be inhibited by the newly deposited sediments (Stone and Vasey, 1968). The vertical roots are eventually supplanted by horizontal shallower root systems developed from adventitious buds on the buried stem (fig. 4). A schematic cross section of the root horizons of old redwoods that have experienced several mudflows during their lifetimes is shown in figure 5, trees 2 and 3. Each root horizon marks the top of the underlying mudflow and the bottom of the overlying deposit. Furthermore, the presence of a buried root horizon indicates a significant hiatus between successive mudflows. Without such an indicator it is impossible to determine whether two successive mudflows were deposited during the same winter or 100 years apart. Figure 6 shows examples of the appearance of some of these adventitious roots in the field.

The relations between root horizons and mudflow deposits used to date past mudflow events in this study are illustrated in figure 5. Tree 1 in figure 5 has only a single root system. Cores were taken from trees with a single root horizon. The annual rings in the cores were counted in the laboratory in an attempt to find the oldest trees. The ages of the oldest trees sampled are the minimum ages of the deposits underlying the trees. Ages of trees with several root systems (fig. 5; trees 2, 3) are the minimum ages of the deposits below the lowest and original root system. Counting the root horizons above the original root system determines the number of mudflows which buried the tree deeply enough to cause it to develop new root systems. If the number of root zones is divided into the age of the tree, then the result is the average recurrence interval (in years) for mudflows at that site and of a character capable of causing development of a new root zone. Thus, the division of the number of subsequent

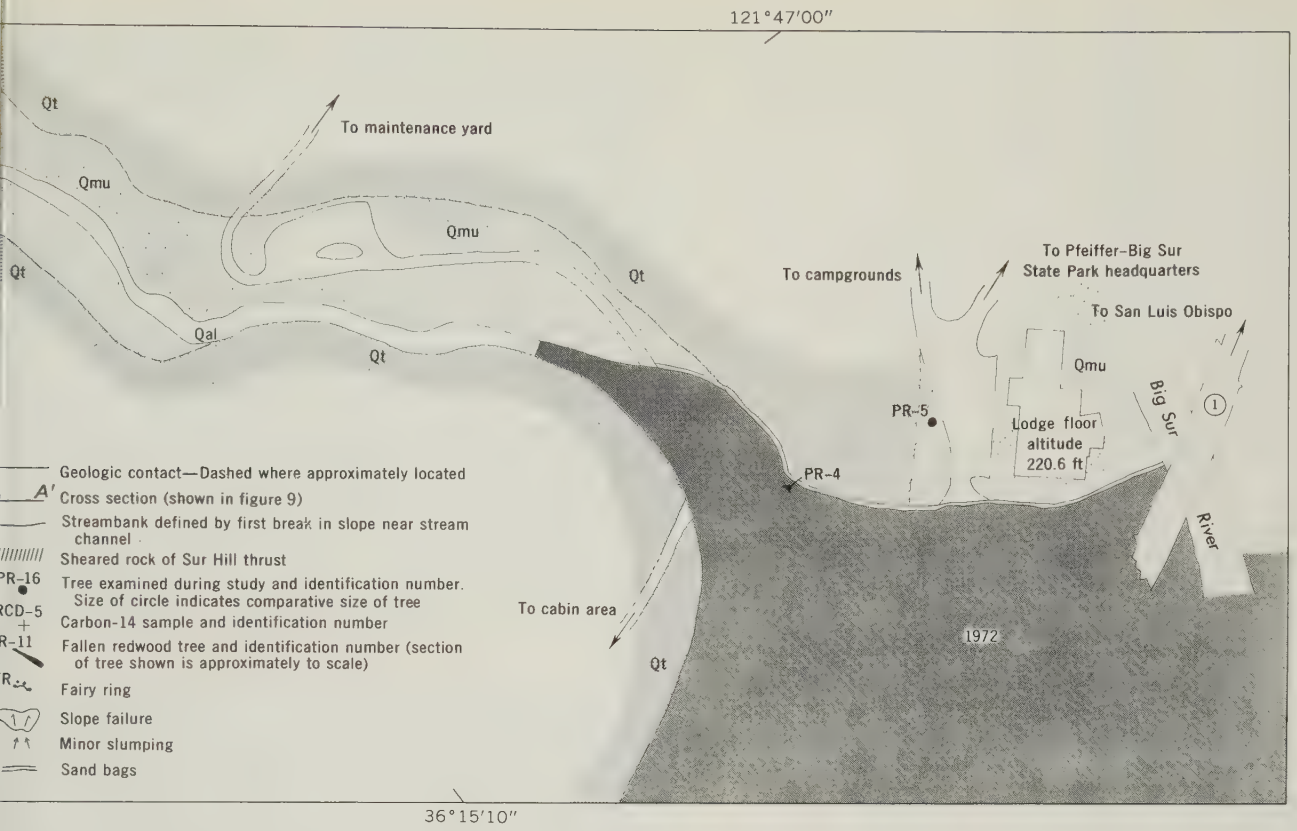

Creek between Pfeiffer Falls and the Big Sur River.

root horizons into the age of the tree produces the minimum average mudflow recurrence interval. Where trees with different numbers of multiple roots were located in close proximity, minimum and maximum ages were established for the mudflows. Table 1 describes tree cores examined during this study.

Mudflow recurrence frequencies determined by root-horizon studies must be regarded as minimum values owing to the complex history of streams such as Pfeiffer-Redwood Creek. Constant channel migration and attendant cutting and filling complicate the stratigraphy of deposits adjacent to the channel. For example, the mudflow deposits of 1972–73 are only sporadically deposited along the upper part of the Pfeiffer-Redwood Creek (fig. 3).

Trunks.—Redwood trunks may record mudflow events in several ways. The pounding of mudflows or floodwater-driven bedload against the upstream side of the trees strips away the bark and phloem and scars the underlying xylem. For example, scars from the mudflows of 1908–10 are still visible on some trees along both Pfeiffer-Redwood and Pheneger Creeks. If no subsequent flows attack these trees, the scars will eventually be healed by peripheral growth around the scar, which can be identified in annual-growth-ring studies (see section "Field and Laboratory Procedures"). When such a scar is identified, the year of the responsible flow may be estimated by dating the first complete annual growth ring on the outside of the scar (Sigafoos, 1964).

Forest fire scars are recorded in the redwood in a similar manner. Fire scars are significant because, on the basis of the past 113 years of recorded history, mudflow-producing winters (1907–10 and 1972–73) have been preceded by fire, suggesting a direct relation between the two phenomena. At any rate, fires seem to have been frequent events near Pfeiffer-Redwood, Juan Higuera, and Pheneger Creeks. Many of the redwoods along these streams are burned out inside or have multiple fire scars by the time they are 200 or 300 years old. This situation can be partly accounted for by the fact that the stands of usually fire-resistant redwoods, which grow in the bottoms and on the sides of narrow valleys, end abruptly, and the flammable chaparral vegetation on the surrounding slopes begins. When the chaparral burns, the intense fire overcomes the natural resistance of the redwoods and causes damage.

The only other trees growing with the redwoods in

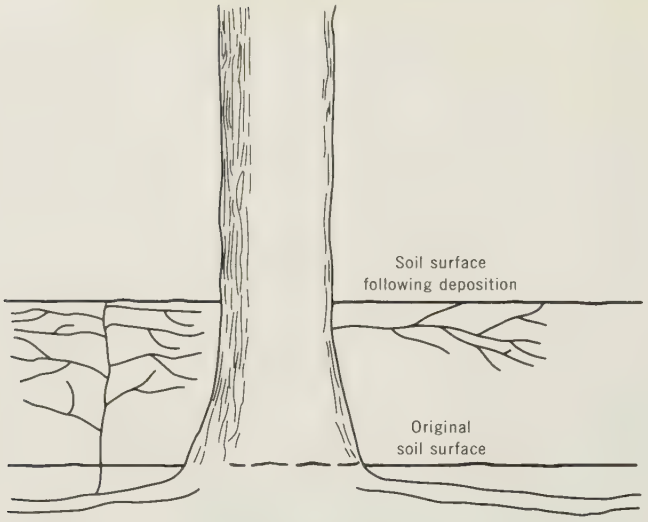

FIGURE 4.—Schematic representation of a new redwood root system developing after burial of old root system by flood or mudflow deposits. (Modified from Stone and Vasey, 1968.)

these valleys are hardwoods which can rapidly resprout after fires.

Any tilting of the ground surface resulting from marginal slumping, or any injury to the redwood which causes the tree to tilt, is recorded by the formation of a buttress. Buttresses are identified by unusually wide growth rings which develop in the direction of tilt. The buttress mechanically compensates for the tree's unbalanced weight distribution (Fritz, 1934). The initiation of buttress ring growth can precisely date the tilting of a tree. Buttress dating has already found application in dating tree tilting from past seismic events (Page, 1970; LaMarche and Wallace, 1972).

Fairy rings.—Fairy rings are circular stands of redwood trees that have a common origin as sprouts from a preexisting parent tree (fig. 7). The sprouting takes place as a response to an injury to the mother tree, usually by fire (Stone and Vasey, 1968). The presence of a fairy ring growing on mudflow deposits, especially where only one root horizon is present beneath the fairy ring, indicates relative antiquity for the underlying deposits. Coring of the fairy-ring trees will date the injury to the mother tree, however, and not the age of the underlying mudflow deposits.

Carbon-14 dating

Carbon-14 dating was used in this study for two purposes: To date deposits whose ages appeared to be greatly in excess of the trees growing on them and to date old root horizons which were not visibly connected to any living tree.

Radiocarbon ages in radiocarbon years were corrected to absolute ages in calendar years by using the bristlecone pine chronology of Seuss (1970). The rapid variations in atmospheric radiocarbon concentrations during the past several hundred years caused four of the radiocarbon samples to have two or three possible calendar ages. Table 2 is a compilation of these dates. The locations of the samples are shown in figure 3.

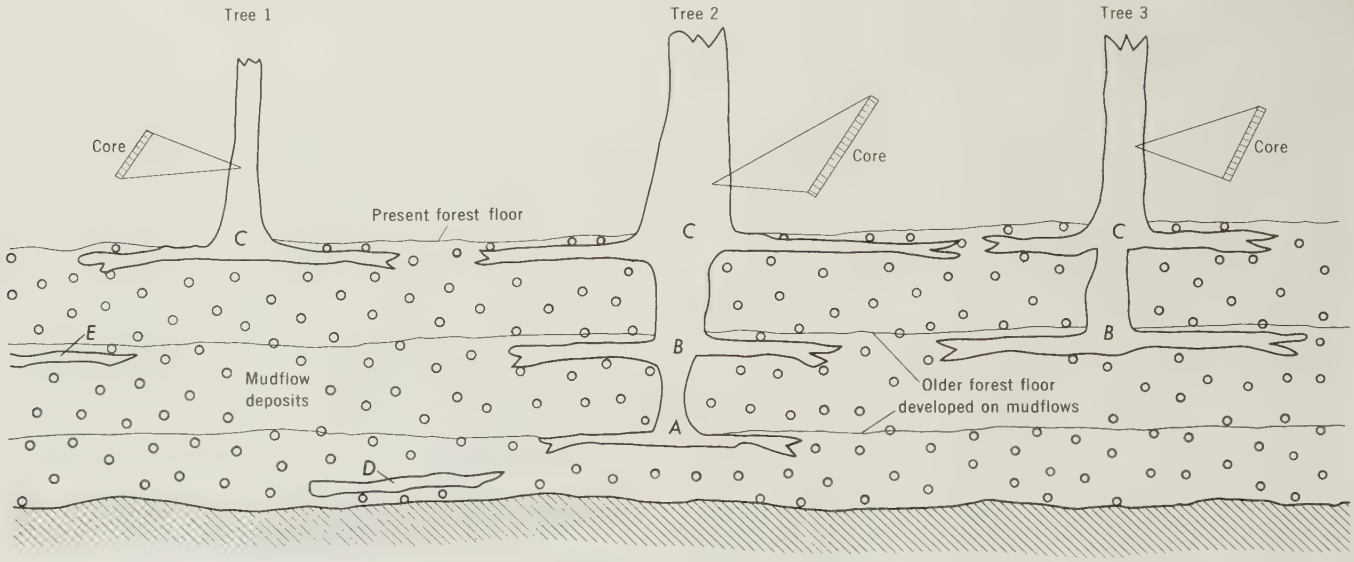

FIGURE 5.—Cores taken from trees 1, 2, and 3 and rings counted to determine minimum age of tree. For tree 1 (only one root horizon), this dated top mudflow. For trees 2 and 3, which had experienced several mudflows, ring counting dated minimum age of lowest and original root system. Division of number of root horizons (*A*, *B*, and *C*) into this minimum age gave a minimum recurrence interval of mudflows. Samples from old root horizons not apparently connected to any living tree (*D* and *E*) were dated by carbon-14 methods to determine ages of mudflow deposits.

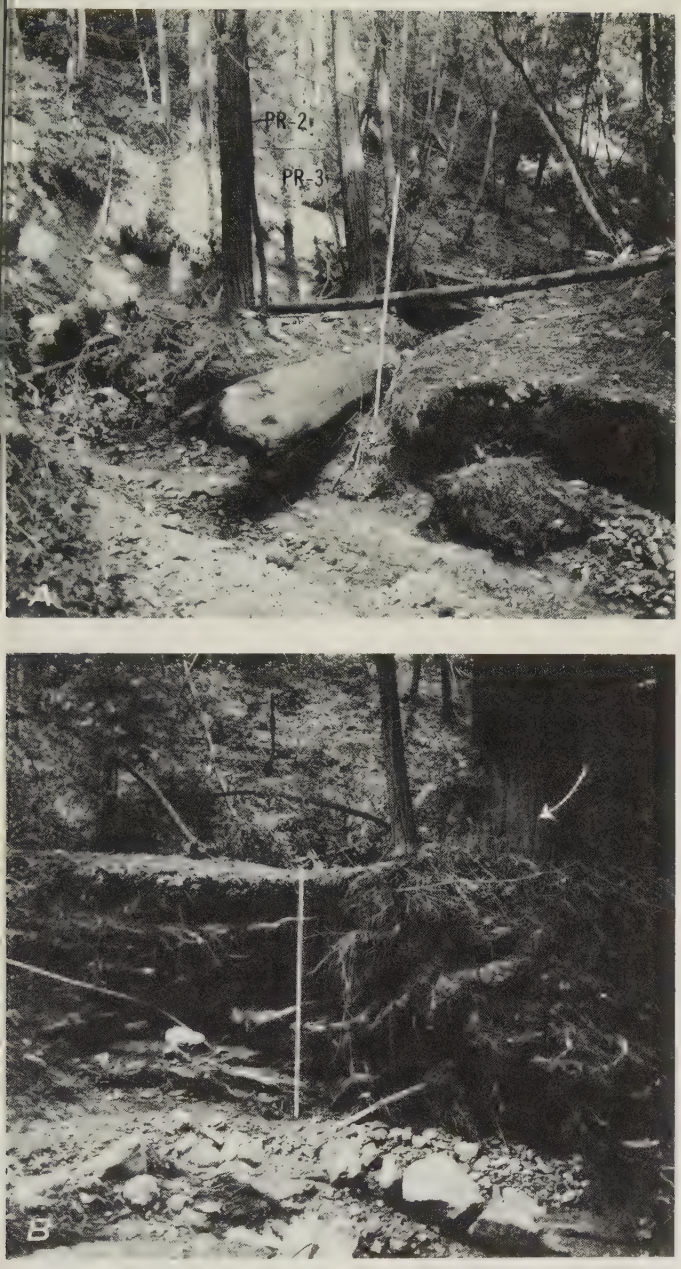

FIGURE 6.—Examples of redwood-root horizons along Pfeiffer-Redwood Creek. *A*, Two young redwoods, PR–2 in the foreground and PR–3 in the background, with single root horizons growing in the deposits of the mudflows of the winter 1907–08. Both trees, PR–2 and PR–3, dated the deposits within 1–5 years. The large underlying log is part of the underlying deposit. The stadia rod is 8 ft (2.2 m) in length. *B*, Root horizons below 472-year-old tree PR–1. Five root horizons including the present forest floor are present below this tree; however, only the upper two root horizons and the second root horizon from the bottom belong to this tree. The youngest deposits may predate the mudflows of 1908–10. The stadia rod is 11 ft (3.4 m) in length. Note the large size of some of the channel-sediment clasts and the height of the mud splatter marks on tree PR–1 (indicated by the arrow).

Because of the relative youthfulness of the ages determined for the carbon-14 samples collected along Pfeiffer-Redwood Creek, significant differences are possible between the age of a sample and the age of the mudflow from which it was collected. If a woody material entrained in a mudflow originated near the center of the trunk of a tree or if the period of time between the death of the tree and the incorporation of the material in the mudflow was a long one, then the age of the sample could be greatly in excess of that of the flow. Conversely, if the dated sample was a root, then it cannot be determined whether the root began growing in the deposit 1 year or 100 years after the flow. Furthermore, the carbon-14 age determined for a sample is a mean of the range of dates when each of the woody cells composing it died. Consequently, the carbon-14 dates obtained along Pfeiffer-Redwood Creek were regarded as minimum or maximum limits of the ages of the mudflows from which they were collected.

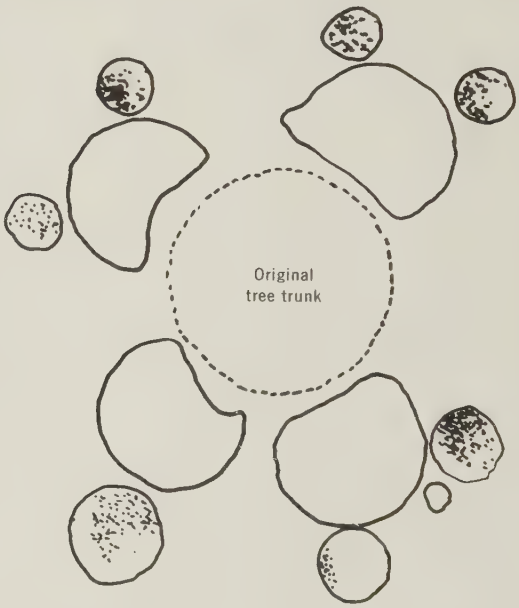

FIGURE 7.—Schematic representation of the development of a fairy ring. The fairy ring is shown as the shaded trunks. Repeated fires during several hundred years critically injured the original tree in the center. In response to this injury, sprouts began growing from its base. Of these sprouts only three or four survived. The others, along with the critically injured mother tree, were killed and consumed by successive fires. As this sequence is repeated, the fairy ring enlarges until it finally loses its identity among the surrounding trees. (Modified from Stone and Vasey, 1968.)

TABLE 1.—*Description of trees dated*[1]
[Locations shown in fig. 3]

Tree number	Circumference[2] (ft)	Root structure	State of preservation	Stratigraphic significance	Core length, excluding bark (in)	Core recovery	Number of annual rings counted	Number of missing annual rings[3]	Total age (years)	Remarks
PR-1	18	A minimum of 3 and a maximum of 5 root systems counting the present roots.	Completely intact.	The multiple root systems of this tree indicate that a minimum of three mudflows have occurred during its lifetime.	34.5	Good to poor. Core is fragmented in places. Core passed close to pith.	465	7	472	Ring 323 abuts against a possible impact scar. Core barely missed the pith.
PR-2	5.2	Single root layer.	do.	The tree overlies and accurately dates the mudflows at 1908.	18.7	Core completely penetrates tree. Recovery is good on upstream side of pith and poor on downstream side due to fragmentation.	64	—	64	Age may range from 57 years to 65 years due to missing rings, false rings, and core breakage. Five years were not added to the age because of the relative youth of the tree and low point on the trunk at which it was cored.
PR-3	5.8	do.	do.	The tree overlies and gives a minimum age for the mudflows at 1908.	21.4	Core completely penetrates tree. Recovery good to fair. Core is fragmented in places. Downstream end has the best record.	59	—	59	Age may range from 59 years to 65 years due to missing rings, false rings, and core breakage. Five years were not added to the age for the reasons stated above.
PR-4	15	Not known.	do.	Cored for climatic control.	21.2	Good, only 4 breaks within the core. Core stopped short of pith.	319	25	344	
PR-5	29	do.	Coring revealed the tree to be hollow.	do.	26.8	Good to fair. Numerous breaks near end of core.	338	No estimate attempted.	>338	Tree is burned out at center.
PR-6	17	Possibly two root horizons.	Completely intact.	The tree and its root systems assign a maximum age to the deposits within and below the older roots and a minimum age to deposits overlying the older roots.	24.6	Good. Core narrowly missed the pith.	418	86	504	
PR-7	12	Two root horizons.	Burned out at base.	The multiple root horizons indicate past burial by mud flows.		Not cored.				
PR-7A	10	do.	Tree is intact but is densely covered by many large burls, possibly indicating frequent injury.	The tree and its roots assign a minimum age to the deposits within and below its lowest roots and a maximum age to deposits overlying its lowest roots.	17.1	Good. Only one bad break in core. Core did not reach pith.	122	<80 ?	<200>122	Buttress growth pattern between rings 90 and 100. Regenerative growth was encountered after ring 122. This growth appears to mark a fire scar or other injury. Drill could not penetrate beyond this point.

		cealed. Only surficial roots are clearly exposed.	at base.	of the tree indicates that the underlying deposits predate the 1908 mudflows.						
PR-9	18	do.	do.	The apparent old age of the tree indicates that the underlying deposits predate the 1908 mudflows.		do.				
PR-10	5	Single root horizon.	Completely intact. Toppled due to undercutting by mud and floodflows.	The age of the tree assigns a minimum age to the underlying mudflow deposits.	18	Complete redwood slab. Three radii were counted.	151	20	171	Slab was cut 20 ft above the base of the tree. Twenty rings were added to the ring count to compensate for this assuming the loss of one annual ring per foot from the base.
PR-11	20	do.	Burned out at base. Toppled by undercutting by mud and floodflows.	The large size of the tree and its single root horizon indicate that the underlying sediments are at least several hundred years old.		Not cored.				
PR-12	13.1	Roots obscured, but surficial roots well developed.	Tree 75 percent consumed by fire.	Tree size and root system indicate that the underlying deposits predate 1970.		Not cored.				
PR-13	12.5	Two distinct root horizons.	Completely intact.	Tree age assigns minimum age to deposits within and below its lowest roots and minimum age to deposits overlying its lowest roots.	21.2	Good. Core passes close to pith.	182	>54	>236	Fire scar after ring 161. Core is broken at this point so no estimate of how many rings the fire burned can be made. Buttress-like growth present from 1812 to 1836.
PR-14	11	Two distinct and well-exposed root horizons.	do.	do.	12.5	Good. Core does not reach pith but is very close.	363	15	378	
PR-15	16.5	Two root horizons.	do.	do.	24.8	Fair to poor. Inner 3.9 in is highly fragmented.	545	5	550	
PR-16	12.6	Two root systems.	do.	Tree apparently buried by mudflows of 1908-1910.	16.1	Excellent. No breaks. Core missed pith by about 1 in.	91	9	100	
PR-17	16	Roots not exposed.	Intact.	May indicate considerable age for underlying deposits.		Not cored.				
PR-18	23	do.	Burned out at base.	do.		do.				

See footnotes at end of table.

TABLE 1.—*Description of trees dated*[1]—Continued

Tree number	Circumference[2] (ft)	Root structure	State of preservation	Stratigraphic significance	Core length, excluding bark (in)	Core recovery	Number of annual rings counted	Number of missing annual rings[3]	Total age (years)	Remarks
PR-19	17	Two well exposed root horizons.	Intact, but partially uprooted and leaning against several adjacent trees. Lower trunk bears scars of mudflows of 1908-1910 and 1972-1973.	The upper root horizon may date the 1908 mudflows or the last mudflows before these. Lower root horizon assigns a minimum age to the underlying deposits.	20	Very good. Only one break within the core. Core did not reach pith but stopped within a few rings.	214	12	226	
PR-20	16.4	Two root horizons.	Half of tree has been burned.	The tree and its roots appear to have the same stratigraphic relationships as PR-19.		Not cored.				
PR-21	12	do.	Completely intact.	The tree and its roots assign a minimum age to deposits within and below the lower roots and a minimum age to deposits overlying the older roots.	14.3	Excellent. No breaks. Core misses pith by less than 0.4 in.	372	13	285	
PR-22	15.7	do.	Completely intact but with sharp lean and bow to its trunk.	The tree appears to have sprouted following an injury to a pre-existing tree due to its exposed position across from Pfeiffer Falls. Its root-age relationship is not clear.	21.8	Good. Only two breaks. Core passes close to pith.	221	94	311	
PR-23	28	Three well exposed root horizons.	Intact. Three trunks.	Root system may predate trees. No cores taken. The two oldest root horizons were carbon dated.		Not cored.			520±80 (calendar years)	

[1]Fairy ring trees are not included in the table but are plotted separately in figure 3.
[2]Measured at chest height above the ground surface.
[3]If the core missed the pith, the number of missing rings was estimated by estimating the missing radius and dividing it by the unit width of the last 10 annual rings of the core. Five years were added to each tree age (Helley and LaMarche, 1973) to allow for growth to the height from which the core was extracted (unless otherwise noted).

eld and laboratory procedures

Significant geological and botanical features of the udy area were mapped (fig. 3). Cores were taken om 13 redwood trees by using a power tree borer veloped by the Geological Survey of Canada Parker, 1970) which cuts a 19.0-mm core and a vedish increment borer which cuts a 4.50-mm core. ne complete section of a fallen redwood was cut g. 8), and the annual rings of the samples were unted in the laboratory. Fire scars, impact injuries, riods of buttress growth, and the general condition d quality of the core were noted during counting d are listed in table 1.

Stream cross sections were plotted (figs. 3, 9) and notographs were taken (fig. 6) of the mudflow and dwood root horizons adjacent to locations along feiffer-Redwood Creek where trees were cored or car-on samples were collected. These photographs and oss sections were used to document the locations of rbon-14 samples and root horizons.

ources of error in annual ring studies

Some counting error must be assumed for highly agmented cores where rings may have been destroyed uring the coring operation or unknowingly counted vice. Error from this source is probably less than percent of the total age of even the most fragmented res examined. Discontinuous rings, which are com-on in redwoods (Fritz, 1940) and do not completely encircle the tree (fig. 8), are another source of error. Errors in tree ages owing to discontinuous rings cannot be estimated unless several cores are taken per tree. The ring count on tree PR–10, which was a complete redwood cross section (fig. 8*B*), ranged from a maximum of 151 rings to a minimum of 148 rings over the three radii that were counted, a maximum error of 2 percent. It is hoped that the age error owing to missing rings of the cores counted is as small, although larger errors are possible.

DATA AND FIELD OBSERVATION ANALYSES FOR DEVELOPING MUDFLOW CHRONOLOGY

Data for tree cores and carbon-14 samples taken near each cross section (fig. 9) were compared with field observations to determine which data were reliable and should be used to define periods of mudflow activity. Discussion of two cross sections (*C–C′* and *E–E′*) will show how partial or questionable data were evaluated and how the data and field observations were used to determine dates of mudflow activity.

Cross section C–C′.—The left bank of Pfeiffer-Redwood Creek at this site shows more root horizons than any other individual section exposed along the creek. Tree PR–1 (fig. 3), which yielded an age of 472 years, and the root stratigraphies underlying it are pictured in figure 6*B*. This section was exposed by the scouring and undermining of mudflows and torrential surges of floodwaters that almost caused the tree to topple. Only

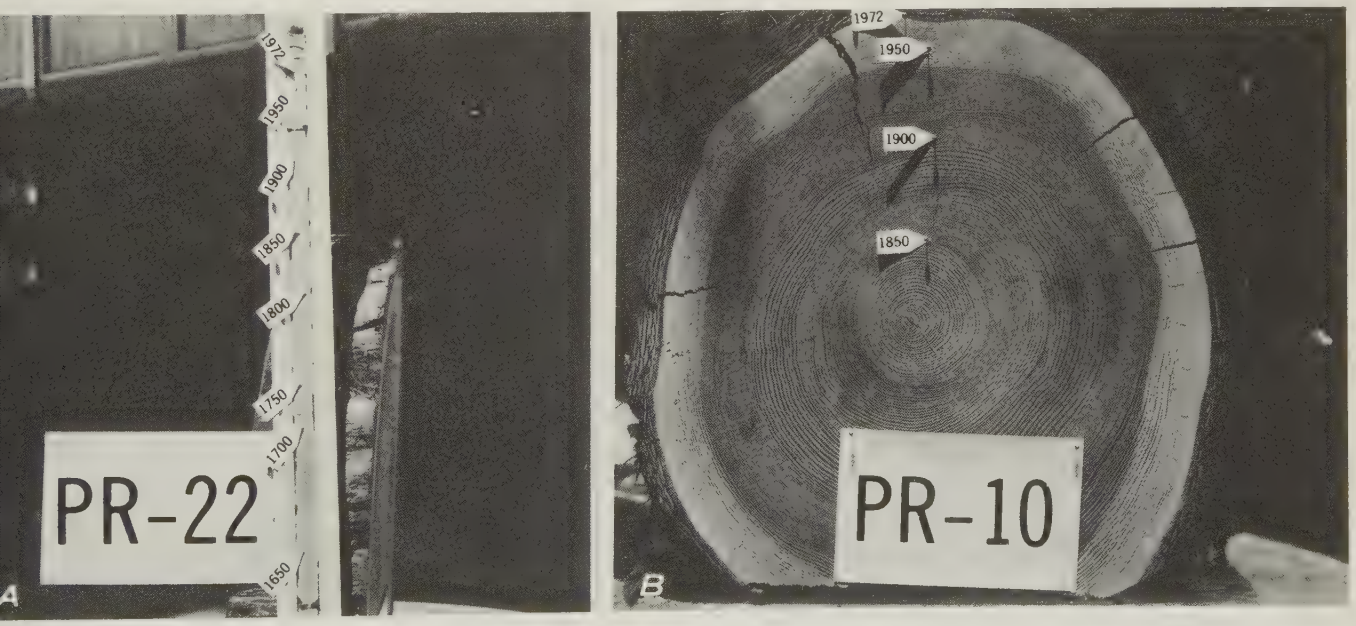

IGURE 8.—Examples of core and slab samples prepared for annual-growth-ring studies. *A*, A part of the core taken from tree PR–22. The core was oriented for ring counting, bonded to the pregrooved mounting board, and sanded flush with the mount. *B*, A slab from fallen redwood PR–10. Note that the ring widths vary and that some of the rings are discontinuous. The cards are 5 by 8 in (130 by 200 mm).

TABLE 2.—*Data for carbon-14 samples*[1]

[Location of sampling sites shown in figure 3. B.P., before present; 1950 is year 0]

Sample	Age,[2] including bristlecone pine correction		Bristlecone pine correction[3]	Description	Comments
	Years B.P.	Year			
PRCD–4	<180	----	-----	Sampled from the first old root layer below present root system of tree PR–23 (fig. 9, cross section *B–B′*).	Sample age indicates deposition of the overlying mudflow deposits between 1860, the date of settlement, and 1770, which is 180 years older than 1950. Sample assigns a minimum age to the underlying mudflow.
PRCD–5	520±80	1430	—150	Sample from the second and oldest root system below the present roots of tree PR–23 (fig. 9, cross section *B–B′*).	Sample assigns a maximum age limit for the overlying mudflow deposits and a minimum age for the underlying deposits.
PRCD–6	<180	----	-----	Sample from the lowest root horizon on the left side of the bank of Pfeiffer-Redwood Creek (fig. 9, cross section *E–E′*). This root horizon is not visibly connected to any living tree.	Older age of the overlying root horizon indicates that this sample is anomalously young and should be discounted.
PRCD–7	510±80	1440	—165	Sample from roots (possibly a younger root horizon) overlying PRCD–7 in the left bank (fig. 9, cross section *E–E′*).	Sample assigns a maximum age to overlying mudflow deposits and a minimum age to underlying deposits.
PRCD–9	400±80	1550	180	Sample taken from the lowest root horizon in the left bank (fig. 9, cross section *I–I′*).	Sample assigns a maximum age to overlying and a minimum age to underlying deposits.
	450±80	1550	230		
PRCD–10	1110±80	840	0	Sample is part of a trunk or large branch entrained in clay-rich mudflow deposits. Mudflow either rests on or is close to bedrock.	Sample assigns a maximum age to overlying deposits and a minimum age to underlying deposits, if present.
PRCD–11	310±80	1640	—120	Sample from an old and decomposing root layer 50 ft upstream from tree PR–3.	The youngest of the three possible dates assigns a minimum age to the underlying deposit, and the oldest of the three possible dates assigns a maximum age to the overlying deposits.
	410±80	1540	—190		
	450±80	1500	—230		
PRCD–12	350±80	1600	—70	Sample from the clay-rich mudflow deposit in the left bank (fig. 9, cross section *H–H′*). Deposit directly overlies bedrock.	Sample assigns a maximum age to overlying deposits.
	470±80	1480	—270		
PRCD–13	510±80	1440	—155	Sample is a log fragment entrained in a mudflow deposit near bedrock in the right bank (fig. 9, cross section *D–D′*). Sample is stratigraphically below the root horizons from which PRCD–6 and PRCD–7 were sampled.	Sample assigns a maximum age to overlying deposits.
PRCD–15	580±80	1370	0	Sample is from a log in a mudflow unit correlative to the lowest unit in figure 9, cross section *F–F′* about 65 ft upstream from tree PR–15 (fig. 3).	Sample assigns maximum age to overlying and a minimum age to underlying deposits.
PRCD–16	310±80	1640	—120	Stratigraphically lowest root layer below tree PR–1 (fig. 9, cross section *C–C′*).	Sample date should be discounted because of several possible calendar ages for carbon-14 age and the possibility that the lone root sample grew into the section after the overlying deposit or deposits were laid down.
	410±80	1540	—190		
	450±80	1500	—230		

[1] Samples analyzed by Teledyne Isotopes, Westwood, N. J., using the Libby half-life of 5,568 years. Samples were pretreated for the removal of humic acids and carbonates before analysis.

[2] Corrections for variations in atmospheric carbon-14 were made from the bristlecone pine chronology of Seuss (1970).

[3] Negative sign indicates that the correction increased the sample's age.

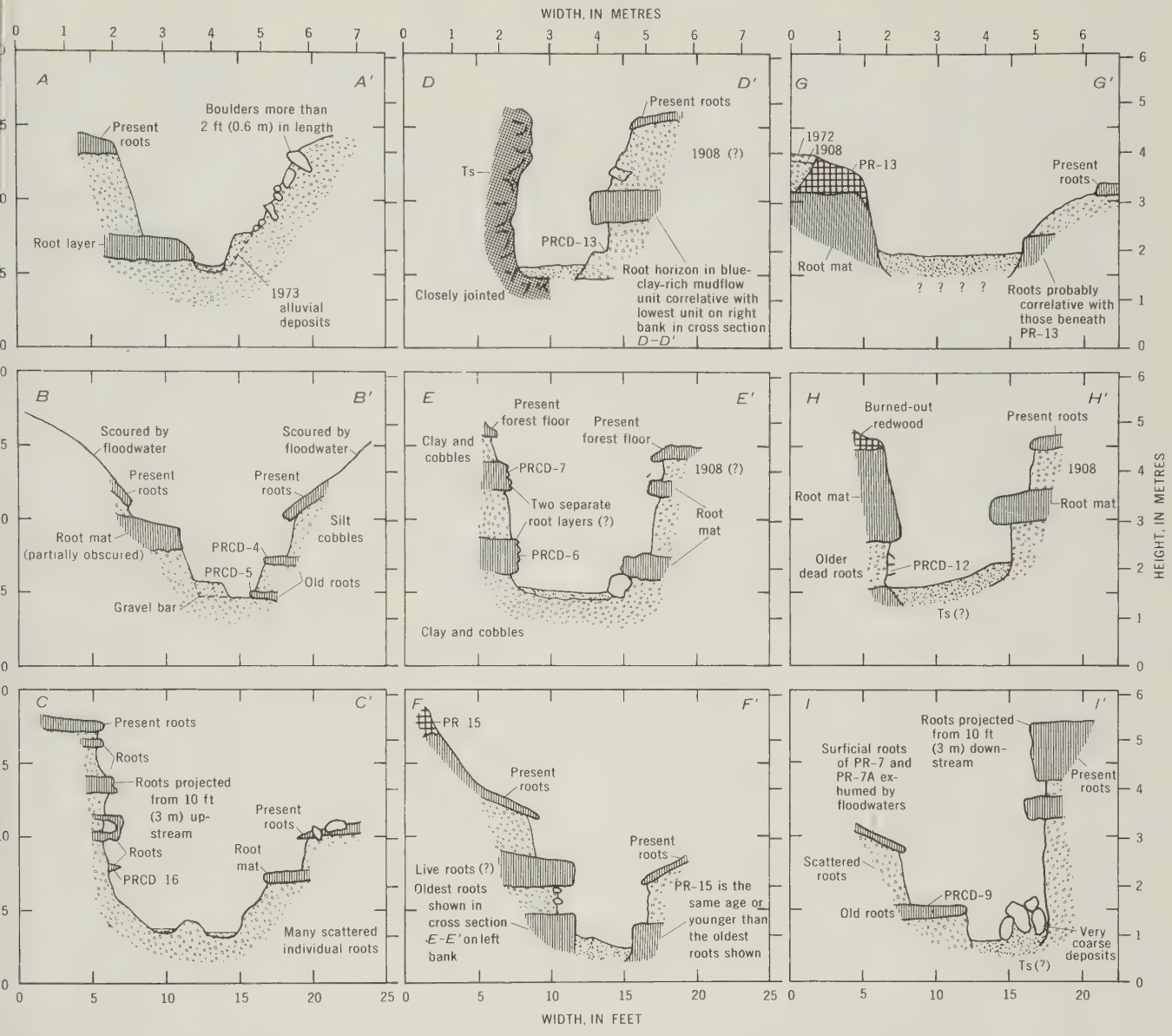

GURE 9.—Cross sections of mudflow deposits and redwood root horizons along Pfeiffer-Redwood Creek. The cross sections illustrate key stratigraphic relations which were useful in identifying individual mudflow events. All views are looking downstream.

e second lowest and the two upper root horizons e physically connected to tree PR–1. The third root rizon from the top of cross section *C–C'* is projected om a short distance upstream (fig. 6*B*). The main ot in this horizon tapers in the direction of tree PR– and the root does not appear to have been connected this tree in the past. Carbon-14 sample PRCD–16 s collected from the lowest root layer below tree R–1. This root layer was not visibly connected to R–1. Owing to past variations in atmospheric car- n, the uncorrected age, 190 radiocarbon years be- re present, could be corrected to three possible calendar ages by the bristlecone pine calibration curve—310, 410, and 450 years before present. All dates are younger than the PR–1 tree. This apparent reversal in stratigraphy probably results from contamination of the sample by fine younger rootlets which were growing pervasively through the sample. Although only visibly uncontaminated fragments of the sample were submitted for analysis, enough young carbon-14 was apparently present to render the sample useless.

Ring 323 (from the outside of the tree) of the core obtained from tree PR–1 terminates against a scar which appears to have been the result of an impact

injury or abrasion. This may be significant because it could date a mudflow event of about 320 years before present.

Two distinct root horizons, which are present on the opposite side of cross section *C–C′*, are connected to tree PR–16. PR–16 yielded an age of 100 years, indicating that the upper set of roots dates from the 1908 mudflows and that the lower set suggests the underlying deposits are older than 100 years. Correlation of these underlying deposits with those on the opposite side of the stream is not clear. The 1908 deposits are fresh in appearance and do not seem to correlate with the youngest deposits on the left side of the cross section *C–C′*.

Taken together, the two sides of this cross section indicate that as many as four or as few as two periods of mudflow activity have occurred between about 1500 and 1908. This count would depend upon whether three root horizons or one root horizon below tree PR–1 was assumed to mark mudflow events since the tree began growing. The lowest root horizon below PR–1, without further evidence, would have to be regarded as predating PR–1 and cannot be included in this total. The abrasion scar noted in the core of PR–1 dates one of these flows at about 320 years (1653).

Cross section E–E′.—Two carbon samples were collected from the root horizon on the left side of the channel. Carbon-14 sample PRCD–6 was from the lower part of a very thick root horizon, and PRCD–7 was from the upper part of this thick root horizon. PRCD–6 dated at less than 180 years, and PRCD–7 yielded a corrected age of 510 years before present (1440). The most apparent explanation for this reverse stratigraphy is that PRCD–6 was sampled from a much younger root which grew into the mat at a later date; PRCD–6 date should be discounted. The age 510 years before present for PRCD–11 is the same as that yielded by PRCD–13, indicating the two are very close in carbon-14 age and probably mark the same mudflow period. No age was determined for the mudflow deposit overlying this root horizon. The lowest root horizon on the right bank of *E–E′* is the same horizon that overlies PRCD–13 and is probably correlative to the root horizon across the channel from which PRCD–6 and PRCD–7 were sampled. The next shallowest root horizon on the right side of cross section *E–E′* contains the lowest roots of the multiple-rooted trees PR–14 and PR–21; these trees yielded tree-ring ages of 377 years and 385 years, respectively. The deposits overlying this root horizon may date from the 1908 mudflow event. In summary, this cross section provides evidence for two mudflow events prior to the beginning of the historical record in 1860. The older occurred about 1440, and the younger, between 1440 and 1588.

DISCUSSION AND CONCLUSIONS

Figure 10 is a diagrammatic compilation of all the usable data collected along Pfeiffer-Redwood Creek during this study. The ages are plotted in a downstream direction from left to right. Radiocarbon dates with more than one possible calendar date have not been incorporated in this figure. The data represented in this figure indicate that at least three mudflow events have occurred along Pfeiffer-Redwood Creek between about 1370 and the beginning of recorded history of the area in 1860. The shaded bands bounded by dashed lines in the figure indicate the apparent minimum and maximum age ranges of these mudflow events. The breadth of the timespan between these boundaries represents dating error due to core breakage, missing rings, minimum and maximum age relations of trees and radiocarbon dates to deposits, imprecision in carbon dating, imprecision in the conversion of radiocarbon years to calendar years, or the possibility of more than one mudflow period within a shaded band. The last mentioned is highly possible. For example, the mudflows of 1908–10 and 1972–73 left only scattered evidence of their occurrence along Pfeiffer-Redwood Creek. Because of the possibility of similar past events, the three prehistoric mudflow events delineated in figure 10 must be regarded as a minimum number.

If carbon-14 sample PRCD–10 (fig. 10) dates the mudflow deposit that entrains it, then the mudflow deposit is the oldest preserved along the lower course of Pfeiffer-Redwood Creek. Because PRCD–10 is the only absolute age control for this mudflow deposit, however, the relation of this mudflow deposit to others both upstream and downstream must remain uncertain.

If the age of this mudflow unit is about 1,100 years before present as indicated by PRCD–10, the 20 ft (6.0 m) of mudflow deposits above it indicate frequent and (or) massive mudflow activity during the past millenium. If the mudflow deposit dated by PRCD–10 is significantly younger than 1,100 years, then inferred past mudflow activity becomes even more certain.

The oldest mudflow deposits that can be dated with certainty were deposited between 1370 and 1440 (fig. 10). Part of the deposits of this flow are well marked by a buried root horizon that can be clearly traced from the vicinity of the collection point of sample PRCD–13 to the collection point of PRCD–15 (fig. 3). All usable carbon-14 dates determined for this

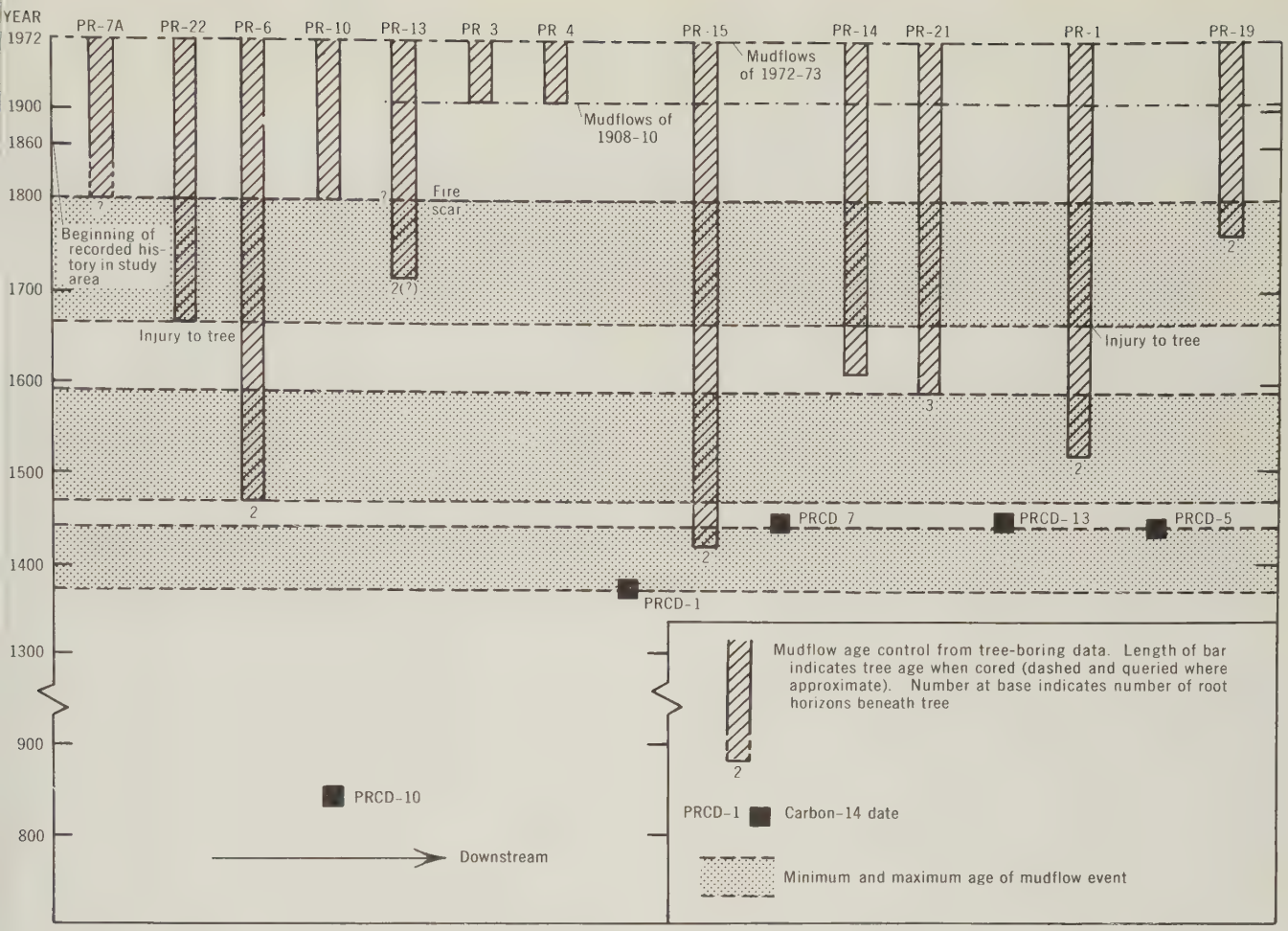

FIGURE 10.—Three prehistoric periods of mudflow activity along Pfeiffer-Redwood Creek as determined from geologic, botanic, and radiometric (carbon-14 dating) data. Prehistoric mudflow periods are shown as shaded bands bounded by broken lines. Three periods of mudflow activity during the past 600 years should be regarded as a minimum figure.

oot horizon range from 1370 to 1440. The minimum ge of the lowest roots of tree PR–6 is about 550 years 1423). This absolute age agrees well with the range f carbon-14 dates obtained from entrained material ithin the deposits.

Carbon-14 sample PRCD–5, which was sampled rom the lowest root horizon below tree PR–23, yielded corrected date of 1430. This date falls within the 370–1440 range; however, it could not be deter-ined if this root horizon marks the same mudflow vent.

Many of the deposits in the 1370–1440 age range are elatively clay rich compared to younger deposits. Un-ortunately, the clay mineralogy is the same within udflow deposits of all ages along Pfeiffer-Redwood reek and could not be used to distinguish between eriods of mudflow activity.

The second oldest event shown in figure 10 is defined rimarily by cross section *E–E′*. This event probably occurred sometime between the end of the 1400's and the end of the 1500's. Trees PR–14 and PR–21 assign a minimum age of about 385 years (1588) to the deposits underlying them. These deposits overlie the deposits of the 1370–1440 mudflow event. The oldest roots of tree PR–1 date within the 1500–1600 period, as does the root horizon from which sample PRCD–9 was taken. However, other than for the determined ages, direct or indirect relations between these two pieces of data and the mudflow event defined by trees PR–14 and PR–22 are not apparent.

The youngest prehistoric mudflow event or events probably occurred sometime between the mid-1600's and the late 1700's. Evidence for mudflow activity during this period is based on the minimum-maximum relation of tree PR–7A and carbon-14 sample PRCD–9, a fire scar in tree PR–13, apparent injuries to trees PR–1 and PR–22, and the minimum age relation of tree PR–10 to its underlying deposits. The tree in-

juries recorded by trees PR–1 and PR–22 in the middle 1600's and the fire recorded by tree PR–13 near the middle 1700's suggest the possibility of two separate mudflow events rather than one during this period.

Radiometric and dendrochronological evidence seems to indicate that no mudflow activity occurred between the early and middle 1600's and between about 1800 and 1860.

The dating and study of mudflow deposits along Pfeiffer-Redwood Creek indicate that mudflows have been periodic natural phenomena in the Big Sur area for at least the last 600 years and probably for as long as there have been heavy and intense rainfall and steep slopes mantled by chaparral vegetation in the Santa Lucia Range. Mudflow deposits in terraces along the lower course of Pfeiffer-Redwood Creek indicate that these conditions have prevailed for many thousands of years.

Redwood dendrochronology, redwood-root stratigraphies, and radiocarbon data indicate that a minimum of three periods of mudflow activity occurred under pristine conditions along the lower course of Pfeiffer-Redwood Creek between about 1370 and 1800. This yields an approximate recurrence frequency of about once every 140 years; however, this recurrence frequency should be considered a minimum figure because other mudflows may have passed through the lower course of Pfeiffer-Redwood Creek without leaving a detectable record.

Judging by the past 113 years of recorded history of the Big Sur area, fire plays an important role in the generation of mudflows. The two recorded periods of mudflow activity in the area of the community of Big Sur (the winters 1908–10 and 1972–73) followed fires that denuded the steep drainage basins to the east. Whatever the actual past recurrence frequency of mudflow events might have been in the Big Sur area and elsewhere in the Santa Lucia Range where similar conditions prevail, it has probably been modified by Man's activities in starting or suppressing fires.

The documentation of mudflows as a characteristic surficial process in the Santa Lucia Range indicates that a hazard exists to lives and property where mudflow-deposited fans are inhabited. Mudflow-deposited fans along the lower courses of steep, chaparral-covered drainage basins similar to Pfeiffer-Redwood Creek occur over much of the Santa Lucia Range. Development in these areas courts the possibility that a catastrophe like the Big Sur mudflows of the winter 1972–73 will occur again.

REFERENCES CITED

Cleveland, G. G., 1973, Fire + rain = mudflows, Big Sur, 1972: California Geology, v. 26, no. 6, p. 127–135.

Fritz, Emanuel, 1934, Story told by a fallen redwood: Save-The-Redwoods League, 6 p.

——— 1940, Problems in dating rings of California coast redwood: Tree Ring Bull., v. 6, p. 19–21.

Gilbert, W. G., 1971, Sur fault zone, Monterey County, California: Stanford, Calif., Stanford Univ., Ph. D. thesis, 75 p.

Helley, E. J., and LaMarche, V. C., Jr., 1973, Historic flood information for northern California streams from geological and botanical evidence: U.S. Geol. Survey Prof. Paper 485–E, 16 p.

Jennings, C. W., and Strand, R. G., 1958, Geologic map of California, *in* Jenkins, O. P., ed., Santa Cruz sheet: California Div. Mines and Geology, scale 1:250,000.

LaMarche, V. C., Jr., and Wallace, R. E., 1972, Evaluation of past movements on the San Andreas fault, Northern California: Geol. Soc. America Bull., v. 83, p. 2665–2676.

Oakeshott, G. B., 1951, Guide to the geology of Pfeiffer–Big Sur State Park, Monterey County, California: California Div. Mines and Geology Spec. Rept. 11, 16 p.

Page, Robert, 1970, Dating episodes of faulting from tree rings: Effects of the 1958 rupture of the Fair Weather Fault on tree growth: Geol. Soc. America Bull. v. 81, p. 3085–3094.

Parker, M. L., 1970, Dendrochronological techniques used by the Geological Survey of Canada, *in* Tree ring analysis with special reference to Northwest America: British Columbia Univ, Fac. of Forestry, Bull. No. 7, p. 55–73.

Pearson, R. C., Hayes, P. T., and Fillo, P. V., 1967, Mineral resources of the Ventana primitive area, Monterey County, California: U.S. Geol. Survey Bull. 1261–B, 42 p.

Rodine, J. D., 1975, Analysis of the mobilization of debris flows: Stanford, Calif., Stanford Univ., Ph. D. thesis, 226 p.

Seuss, H. E., 1970, Bristlecone-pine calibration of the radiocarbon time-scale 5200 B.C. to the present, *in* Nobel Symposium 12—radiocarbon variations and absolute chronology: p. 304–311.

Sigafoos, R. S., 1964, Botanical evidence of floods and flood-plain deposition: U.S. Geol. Survey Prof. Paper 485–A, 35 p.

Stone, E. C., and Vasey, R. B., 1968, Preservation of coast redwoods on alluvial flats: Science, v. 159, no. 3811, p. 157–161.

Trask, P. D., 1926, Geology of the Point Sur quadrangle: Berkeley, Calif., California Univ. Pub., Geology, v. 16, no. 6, p. 119–186.

Jour. Research U.S. Geol. Survey
Vol. 5, No. 1, Jan.–Feb. 1977, p. 33–48

APPLICATION OF A HYDROMETEOROLOGICAL MODEL TO THE SOUTH-CENTRAL SIERRA NEVADA OF CALIFORNIA

By WENDELL V. TANGBORN and LOWELL A. RASMUSSEN, Tacoma, Wash.

Abstract.—A hydrometeorological streamflow-prediction model (HM model) developed for the North Cascades of Washington has been tested in the south-central Sierra Nevada of California. Twenty-four drainages ranging in mean altitude from 770 to 3,160 metres, including several of the major ones such as those of the Kern, Kings, and Merced Rivers, were examined. Eight U.S. National Oceanic and Atmospheric Administration precipitation stations were evaluated. Of these, three proved to be of significant value for nearly all the drainages used. Results are given for predictions on February 1, March 1, and April 1 of monthly runoff of five major drainages for the April–September season. Also demonstrated is the April 1 prediction of a daily hydrograph for the April–September season for 2 diverse years. The altitude distribution of storage and runoff, both observed and predicted, is determined by using several drainages with different area-altitude profiles. Results of this calculation for two drainages show that, on the average, approximately 50 percent of the April–July runoff originates above 2,800 m. The influence of subsequent precipitation on prediction accuracy is determined by relating prediction error and actual precipitation occurring after the prediction day. Results for three basins show that about 75 percent of the error of a January–September prediction on January 1 is due to precipitation occurring during the prediction season. Comparisons of prediction accuracy are made for five major drainages: the Kern River near Kernville; the Kings River below North Fork, near Trimmer (inflow to Pine Flat Dam); the Kings River at Piedra; the Merced River at Pohono Bridge, near Yosemite; and the Merced River below Merced Falls Dam, near Snelling. The accuracy of the HM model appears to be about 24 percent higher than existing operational methods in predicting the April–July runoff on April 1.

The Sierra Nevada of central California produces what could be considered the most valuable water in the world. Streamflow from this high mountain region is utilized with great economic advantage for irrigating the extensive farmlands of the San Joaquin Valley, and for hydroelectric power, public water supplies, fisheries, and many of the other needs of this region. Fortunately, streamflow in the Sierra from which downstream water supplies are obtained does not immediately follow precipitation. Winter precipitation occurring as snow is temporarily stored for as much as 9 months at higher altitudes and then released to lower altitudes during the warm dry months when it is most needed. The second advantage of this is that snow storage can be measured by several means through the winter and spring seasons, thus allowing water managers to predict subsequent summer streamflow. Efficient management of this important resource hinges on whether the total volume and space distribution of water stored as snow are accurately known each spring.

A hydrometeorological streamflow-prediction model (HM model), which uses only standard streamflow and precipitation data and is based on a calculation of actual basin storage, was developed for the North Cascades region of Washington (Rasmussen and Tangborn, 1976; Tangborn and Rasmussen, 1976). The application of the HM model to the south-central Sierra Nevada of California is the subject of this report.

The approach given here differs slightly from that of the North Cascades study. However, the central theme of both reports is nearly identical and, to avoid repetition, this report does not contain a detailed description of the development of the various concepts used in the model.

The main features of this model are:

1. Appears to be more accurate than existing methods.
2. Does not require expensive or environmentally intrusive instrumentation; uses only existing streamflow and precipitation installations.
3. Is comparatively simple to implement.
4. Has a built-in system to test the amount of storage available for runoff; this considerably improves the accuracy.
5. Provides a method amenable for extension to an automated, real-time system.
6. Predicts the time distribution of summer runoff and the altitude distribution of storage and potential runoff.

Acknowledgments.—We wish to thank the following reviewers of this manuscript: A. J. Brown, Department of Water Resources, California; and R. J. C. Burnash, National Weather Service.

DESCRIPTION OF THE REGION

Compared with the North Cascades, nearly all aspects of the south-central Sierra Nevada present a striking contrast. The topography of the western side is a moderately inclined slope that was not as deeply dissected by Pleistocene glaciation as the North Cas-

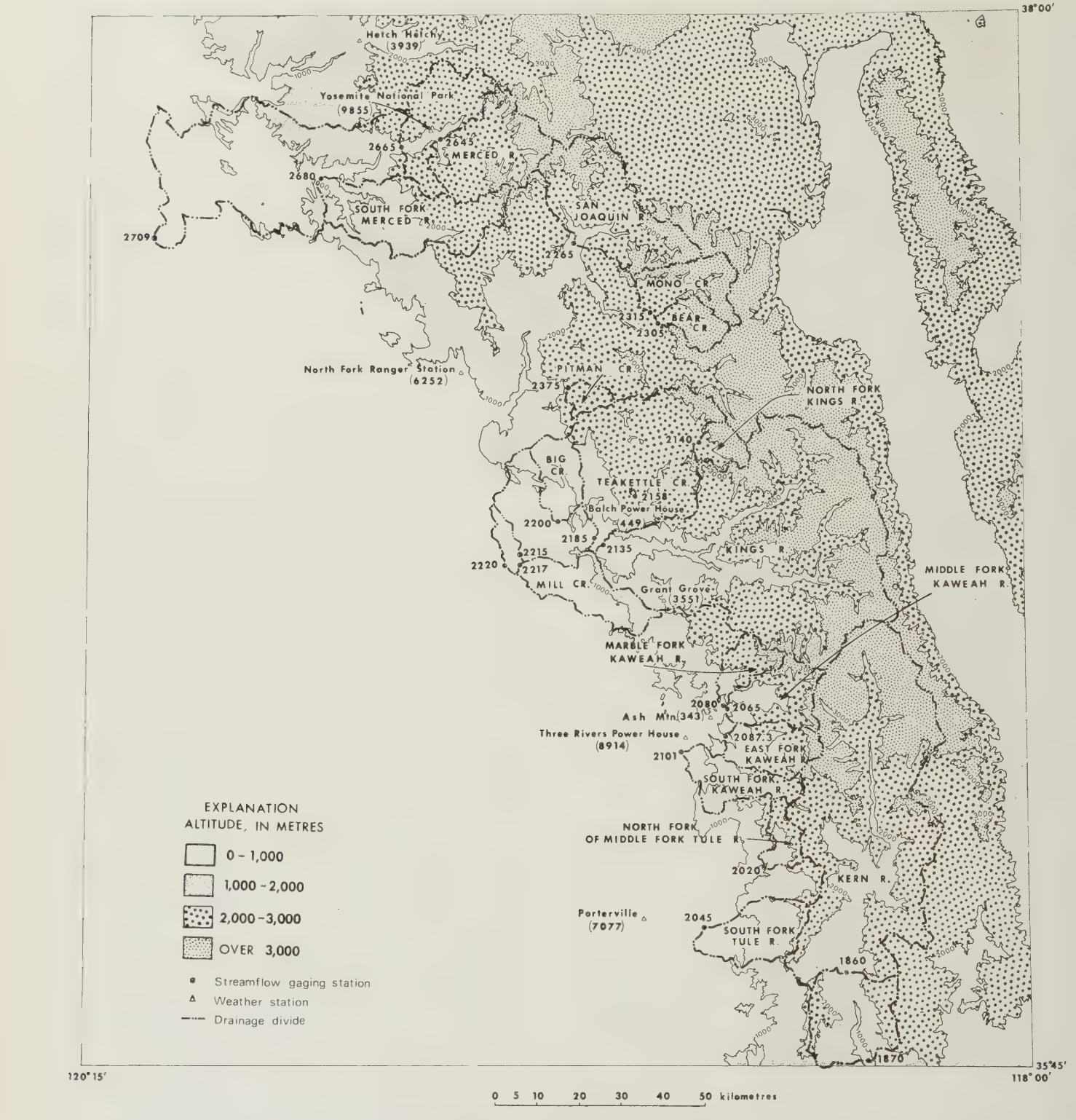

FIGURE 1.—The south-central Sierra Nevada of California. Shown are the 1,000-, 2,000-, and 3,000-m contours, drainage divides, and gaging stations of 24 drainage basins plus the location of 8 precipitation stations used in this study. Base from U.S. Geological Survey topographic 1:250,000 maps of San Jose, Mariposa, Fresno, and Bakersfield. Modified by authors.

ades (fig. 1). Conversely, the slope on the eastern side s very steep, the result of high-angle dip-slip fault- ng. Partly because it has not been so heavily glaciated, he Sierra is higher and more massive, resulting in a reater proportion of area at high altitudes. The mean ltitude of the study region is 2,130 metres.

The climate is also markedly different from that of he North Cascades. Annual precipitation is less than alf and occurs more as short, intense winter storms. Rain-shadow effects from the coastal ranges appear to e considerably more subdued; consequently precipita- ion patterns in the Sierra are much less complex. Un- ike the North Cascades, precipitation stations are lo- ated at higher altitudes and appear to more precisely epresent regional values. The evaporation-transpira- ion potential is undoubtedly much greater than in the North Cascades but actual losses are probably not re- lected by this difference because there is relatively ess vegetation in the Sierra. Also, the summer-pre- ipitation fraction is significantly smaller than in the North Cascades, suggesting that less evaporation oc- urs in the Sierra.

Hydrologically, two features stand out in this region f the Sierra. One is that because of the higher alti- udes, a much larger fraction of the total annual run- ff occurs during the summer season (0.45 at the mean ltitude of the North Cascades and 0.72 at the mean ltitude of the Sierra). Second, the coefficient of varia- ion is significantly higher than in most other parts of he country (U.S. Geological Survey, 1970, p. 120) oth on an annual and seasonal basis. The combina- ion of a large fraction and the high variability of ummer runoff, coupled with hot dry summers and the arge economic value of seasonal streamflow, produces n unusual need for an accurate determination of the pring storage of water in the higher altitudes.

DESCRIPTION OF THE DATA USED IN THIS STUDY

Twenty-four drainage basins of the south-central Sierra were selected for analysis (table 1). Although many more with streamflow records are available in his region, it was necessary to limit the number to keep the study at a manageable size. In the selection f these drainages, the attempt was to represent the ntire region with respect to the altitude, latitude, nd orientation of each basin. It was necessary to con- ne the region to a rather narrow latitude band, be- ween lat 35°45′ N. and lat 38°00′ N., in order to retain omogeneity of the hydrologic variables. Although the rimary interest is in the higher altitude basins which ave a high proportion of snowmelt runoff, a few low- ltitude basins were included for a more complete rep- resentation of the region. Only those basins that have at least 15 years of continuous record were used.

With two exceptions only published runoff data were included. Those basins with large reservoirs and diversions, resulting in regulated streamflow at the gaging site, were not used to avoid making adjust- ments to correct for impairment of the natural flow. The exceptions were the Kings River at Piedra (No. 2220) (R. E. Leake, unpub. data adjusted for reservoir storage, evaporation, and diversions, 1976) and, to demonstrate the results with at least one impaired drainage, Mono Creek (No. 2315) (the change in stor- age of Lake Thomas A. Edison was used to make the necessary corrections to the published, regulated flow).

In order that the dimensions for both variables are compatible, both runoff and precipitation are given in millimetres. Runoff is given as a unit length (milli- metres averaged over the drainage basin). A factor to convert millimetres to acre-feet is given for each drain- age basin in table 1. Precipitation values were con- verted to millimetres from published monthly values in inches (U.S. National Oceanic and Atmospheric Administration, 1930–1973). Runoff data were re- trieved from U.S. Geological Survey computer storage files (Hutchison, 1975) as daily values and converted directly into millimetres averaged over the published drainage area.

Except for two examples when daily discharge was averaged over the period of record, the time increment used for all data was 1 month. The winter season is defined as October–March; the summer season is April–September except for a few times when the April–July season was used.

The fraction of the area within each 300-m altitude interval for each basin was planimetered on topo- graphic maps and converted to a fraction of the total drainage area. These results are given in table 2.

SELECTION OF THE OPTIMUM PRECIPITATION STATIONS

Originally, all U.S. National Oceanic and Atmos- pheric Administration (1952–1973) precipitation sta- tions in this region with an unbroken record of at least 20 years were used in the HM model to calculate the standard error of estimate for a prediction on the April–July season against all 24 drainage basins used in the study. Only eight consistently showed a low standard error of estimate and were retained for more detailed examination (see table 3). Of these, Grant Grove (No. 3551) is the most valuable station. It was the best, or among the best, for 14 basins, Balch Power House (No. 449) and North Fork Ranger Station (No. 6252) for 6 basins each, and Porterville (No. 7077)

TABLE 1.—*Streamflow gaging stations used in the south-central Sierra Nevada, Calif.*

Station No.	Station Name	Period of record used	Basin area (km^2)	Conversion factor[1]	Mean altitude (m)	Mean runoff: Annual[2] (mm)	Mean runoff: Winter[3] (mm)	Mean runoff: Summer[4] (mm)	Mean runoff: Summer percent of annual	Coefficient of variation, in percent: Annual[2]	Coefficient of variation, in percent: Winter[3]	Coefficient of variation, in percent: Summer[4]
11-1860	Kern River near Kernville	1952-73	2191	1.78	2600	314	77	236	75	62	45	71
1870	Kern River at Kernville	1954-73	2613	2.12	2460	268	73	196	73	65	54	74
2020	North Fork of Middle Fork Tule River near Springville	1952-73	102	.0827	2120	507	202	306	60	66	80	68
2045	South Fork Tule River near Success	1957-73	282	.229	1290	126	67	59	47	107	108	112
2065	Middle Fork Kaweah River near Potwisha Camp	1952-73	264	.214	2280	558	147	411	74	64	60	67
2080	Marble Fork Kaweah River at Potwisha Camp	1952-73	133	.108	2310	664	147	517	78	60	71	64
2087.3	East Fork Kaweah River near Three Rivers	1953-73	222	.180	2280	478	110	368	77	63	71	64
2101	South Fork Kaweah River at Three Rivers	1959-73	225	.182	1570	267	88	179	67	83	98	76
2135	Kings River above North Fork, near Trimmer	1952-73	2476	2.01	2610	524	98	426	81	52	52	54
2140	North Fork Kings River below Meadow Brook	1957-73	97.6	.0791	3110	739	76	663	90	49	41	52
2158	Teakettle Creek at Site No. 3, near Patterson Mountain	1958-69	2.23	.00181	2340	572	162	410	72	71	56	86
2185	Kings River below North Fork, near Trimmer	1952-74	3476	1.98	2500	552	119	433	78	52	49	56
2200	Big Creek above Pine Flat Lake, near Trimmer	1954-73	181	.147	1200	248	157	91	37	80	94	101
2215	Kings River below Pine Flat Dam	1952-73	4002	3.25	2280	480	62	418	87	44	72	45
2217	Mill Creek near Piedra	1958-73	329	.267	770	110	78	32	29	131	147	140
2220	Kings River at Piedra	1952-73	4387	3.56	2120	473	109	364	77	57	60	58
2265	San Joaquin River at Miller Crossing	1952-73	658	.533	2790	828	128	700	85	37	40	41
2305	Bear Creek near Lake Thomas A. Edison	1952-73	136	.110	3160	612	66	546	89	42	30	45
2315	Mono Creek below Lake Thomas A. Edison	1952-73	240	.195	3070	590	102	488	83	42	94	48
2375	Pitman Creek below Tamarack Creek	1952-73	59.3	.0481	2460	627	80	547	87	58	97	62
2645	Merced River at Happy Isle Bridge, near Yosemite	1952-73	469	.380	2730	667	87	580	87	42	61	44
2665	Merced River at Pohono Bridge, near Yosemite	1952-73	831	.674	2630	663	107	556	84	44	61	46
2680	South Merced River near El Portal	1952-73	624	.506	1840	493	164	329	67	56	64	58
2709	Merced River below Merced Falls Dam, near Snelling	1952-73	2748	2.23	1620	416	134	282	68	54	66	53

[1]The conversion factor times the runoff in millimetres gives the runoff in thousands of acre-feet.

[2]Oct. 1 to Sept. 30.

[3]Oct. 1 to Mar. 31.

[4]Apr. 1 to Sept. 30.

and Yosemite Park Headquarters (No. 9855) for 1 basin each. Two pseudostations were formed from the first three: No. 1111 by averaging Grant Grove and Balch Power House, and No. 1112 by averaging those two along with North Fork Ranger Station. One or the other of the pseudostations was either better than or as good as any of the eight individual stations for all but six basins (see table 4).

SELECTION OF THE PERIOD OF RECORD TO USE IN A HYDROMETEOROLOGICAL MODEL

The length of record to use in examining any hydrologic phenomenon is a crucial part of modeling development (Hannaford, 1964) Changes with time of the climatic variables that produce precipitation, air temperature during precipitation (which will determine whether precipitation is snow or rain), evaporation, and ablation, are known to exist. However, the period and amplitude of these changes are not easily discerned. Subtle changes in the relationship between runoff and precipitation are extremely important in most hydrologic modeling techniques, yet little is known of the cause and magnitude of these changes.

Most streamflow prediction models use a specific time period as a base from which comparisons are made. Longer periods (over 30 years) often cause difficulties in modeling because of the tendency of hydrometeorologic relationships to change with time (the infringement of man cannot be disregarded here) and simply because of the low probability of having sev-

TABLE 2.—*Area-altitude distributions of drainage basins in the south-central Sierra Nevada, Calif.*

Station No.	Name	Altitude intervals, in metres													
		0 to 300	300 to 600	600 to 900	900 to 1200	1200 to 1500	1500 to 1800	1800 to 2100	2100 to 2400	2400 to 2700	2700 to 3000	3000 to 3300	3300 to 3600	3600 to 3900	3900 to 4200
1-1860	Kern River near Kernville				0.004	0.051	0.067	0.040	0.133	0.163	0.139	0.127	0.117	0.052	0.008
1870	Kern River at Kernville			0.005	.026	.073	.089	.140	.145	.147	.120	.107	.098	.044	.007
2020	North Fork of Middle Fork Tule River near Springville				.085	.067	.140	.164	.202	.166	.152	.024			
2045	South Fork Tule River near Success	0.013	0.103	.155	.186	.188	.165	.107	.060	.021	.002				
2065	Middle Fork Kaweah River near Potwisha Camp			.013	.052	.084	.124	.134	.139	.144	.126	.117	.058	.009	
2080	Marble Fork Kaweah River at Potwisha Camp			.011	.028	.029	.074	.225	.208	.158	.160	.091	.015		
2087.3	East Fork Kaweah River near Three Rivers			.010	.043	.096	.132	.129	.128	.132	.142	.145	.039	.003	
2101	South Fork Kaweah River at Three Rivers	.002	.088	.130	.159	.156	.114	.078	.053	.127	.080	.013			
2135	Kings River above North Fork, near Trimmer		.012	.026	.031	.043	.050	.097	.103	.117	.139	.156	.157	.061	.008
2140	North Fork Kings River below Meadow Brook									.076	.283	.365	.235	.041	
2158	Teakettle Creek at Site No. 3, near Patterson Mountain							.100	.500	.400					
2185	Kings River below North Fork, near Trimmer	.001	.012	.026	.034	.048	.056	.100	.124	.158	.151	.125	.114	.044	.006
2200	Big Creek above Pine Flat Lake, near Trimmer	.019	.070	.168	.249	.238	.169	.073	.013	.001					
2215	Kings River below Pine Flat Dam	.005	.037	.081	.058	.050	.055	.088	.107	.137	.131	.108	.100	.038	.005
2217	Mill Creek near Piedra	.065	.331	.272	.179	.110	.038	.005							
2220	Kings River at Piedra	.025	.094	.081	.053	.046	.050	.080	.098	.125	.120	.099	.091	.035	.005
2265	San Joaquin River at Miller Crossing					.005	.018	.048	.115	.217	.250	.218	.109	.021	.001
2305	Bear Creek near Lake Thomas A. Edison								.044	.066	.179	.304	.333	.072	.002
2315	Mono Creek below Lake Thomas A. Edison								.086	.142	.176	.255	.232	.095	.013
2375	Pitman Creek below Tamarack Creek								.493	.341	.147	.019			
2645	Merced River at Happy Isle Bridge, near Yosemite						.009	.066	.184	.192	.266	.193	.077	.013	.001
2665	Merced River at Pohono Bridge, near Yosemite				.009	.014	.013	.056	.203	.214	.312	.123	.043	.011	.001
2680	South Fork Merced River near El Portal		.014	.044	.130	.163	.151	.127	.133	.142	.065	.027	.004		
2709	Merced River below Merced Falls Dam, near Snelling	.036	.108	.136	.140	.080	.065	.067	.118	.110	.078	.042.	.017	.003	

TABLE 3.—*Precipitation stations used in the south-central Sierra Nevada, Calif., during the period 1952–73*

Station No.	Name	Altitude (m)	Mean precipitation				Coefficient of variation, in percent		
			Annual[1] (mm)	Winter[2] (mm)	Summer[3] (mm)	Summer percentage of annual	Annual[1] (mm)	Winter[2] (mm)	Summer[3] (mm)
3	Ash Mountain	518	652	531	121	19	42	45	66
9	Balch Power House	524	757	620	137	18	39	43	55
51	Grant Grove	2006	1090	902	188	17	41	45	62
39	Hetch Hetchy	1180	878	691	187	21	30	34	49
52	North Fork Ranger Station	802	835	686	149	18	36	39	60
77	Porterville	120	284	232	52	18	40	46	76
14	Three Rivers Edison PH 2	290	547	448	99	18	42	45	71
55	Yosemite Park Headquarters	1215	922	744	178	19	33	37	48
11	Average of 449, 3551	----	924	761	163	18	39	44	58
12	Average of 449, 3551, 6252	----	894	736	158	18	38	42	58

[1]Oct. 1 to Sept. 30. [2]Oct. 1 to Mar. 31. [3]Apr. 1 to Sept. 30.

eral data-collection stations in operation simultaneously for many consecutive years.

The pragmatic approach is analyzing trends in hydrometeorologic relationships is, simply, what period of record gives the best fit between two dependent variables; namely, runoff and precipitation? For example, how far back should records of these variables extend to give the most accurate predictive qualities to a currently applied model?

The example given here is for the prediction period 1958–73. The HM model predicted April–July runoff for this period by use of a record of precipitation and runoff which extended back for a varied number of years. Because of changes with time in runoff-precipitation relationships, each year's prediction was based only on the previous period of record and was then recalculated each year.

The results of this analysis are shown in figure 2 for three main drainage basins used in this report. An

TABLE 4.—*Relationship between runoff and precipitation for all basins and precipitation stations in the south-central Sierra Nevada, Calif.*

[Standard error of estimate is given in millimetres for the April–July runoff when the October–March precipitation and a 1-month spring test season are used; standard deviation of the April–July runoff is also given]

Station		Standard deviation	Precipitation station (see table 3 for names)									
No.	Name		343	449	3551	3939	6252	7077	8914	9855	1111	1112
11-1860	Kern River near Kernville	152	53	40	34	66	52	49	39	70	33	36
1870	Kern River at Kernville	132	50	33	33	60	46	42	37	61	31	34
2020	North Fork of Middle Fork Tule River near Springville	197	76	71	59	91	79	72	64	99	60	63
2045	South Fork Tule River near Success	64	20	15	15	18	15	20	20	19	15	14
2065	Middle Fork Kaweah River near Potwisha Camp	254	81	84	75	111	99	57	72	122	77	82
2080	Marble Fork Kaweah River at Potwisha Camp	309	117	92	76	142	109	112	94	144	74	79
2087.3	East Fork Kaweah River near Three Rivers	220	71	50	68	74	60	58	55	83	60	58
2101	South Fork Kaweah River at Three Rivers	133	35	22	25	31	23	32	29	36	22	21
2135	Kings River above North Fork, near Trimmer	209	73	52	52	83	63	69	58	84	48	49
2140	North Fork Kings River below Meadow Brook	328	151	93	86	130	108	176	116	115	85	86
2158	Teakettle Creek at Site No. 3, near Patterson Mountain	325	88	48	42	89	72	77	58	88	40	41
2185	Kings River below North Fork, near Trimmer	221	88	67	55	95	75	99	72	95	56	58
2200	Big Creek above Pine Flat Lake, near Trimmer	90	54	42	44	41	37	53	51	38	43	41
2215	Kings River below Pine Flat Dam	210	73	54	51	81	64	68	61	84	48	50
2217	Mill Creek near Piedra	45	33	27	25	24	23	34	34	22	26	25
2220	Kings River at Piedra	195	65	50	48	70	57	62	56	74	45	47
2265	San Joaquin River at Miller Crossing	260	110	80	75	92	74	139	86	101	71	69
2305	Bear Creek near Lake Thomas A. Edison	211	99	67	78	86	69	123	81	70	71	67
2315	Mono Creek below Lake Thomas A. Edison	216	107	71	90	73	63	141	81	73	79	70
2375	Pitman Creek below Tamarack Creek	332	129	91	86	142	98	150	111	122	79	79
2645	Merced River at Happy Isle Bridge, near Yosemite	236	91	69	66	82	65	115	75	77	63	61
2665	Merced River at Pohono Bridge, near Yosemite	243	93	72	62	83	66	114	77	72	73	60
2680	South Fork Merced River near El Portal	186	76	65	56	73	59	82	70	68	57	56
2709	Merced River below Merced Falls Dam, near Snelling	144	60	49	48	55	46	66	57	49	47	46

exception is that the upper Kings River (No. 2135) was used instead of Nos. 2185 and 2215 because its record extends back to 1932. An average of five long-term precipitation stations (Nos. 343, 3939, 6252, 8914, and 9855) was used to reduce the effect of possible record breaks caused by station moves or other unnatural changes. The same precipitation-station average was used so that the results for all basins would be comparable.

On the basis of these results, it appears rather strongly that for the most accurate prediction the optimum year to begin the period in this region is 1952. This date applies more to some basins than to others, but for all basins a period beginning in 1952 gives the lowest standard error of estimate. For this reason, it was decided to use the more hydrologically stable 1952–73 period as the base for all subsequent calculations in this report.

FOUNDATION FOR THE HM MODEL

The basis for this hydrometeorological approach is simply that summer runoff is highly dependent on spring snow storage and that accurate predictions of

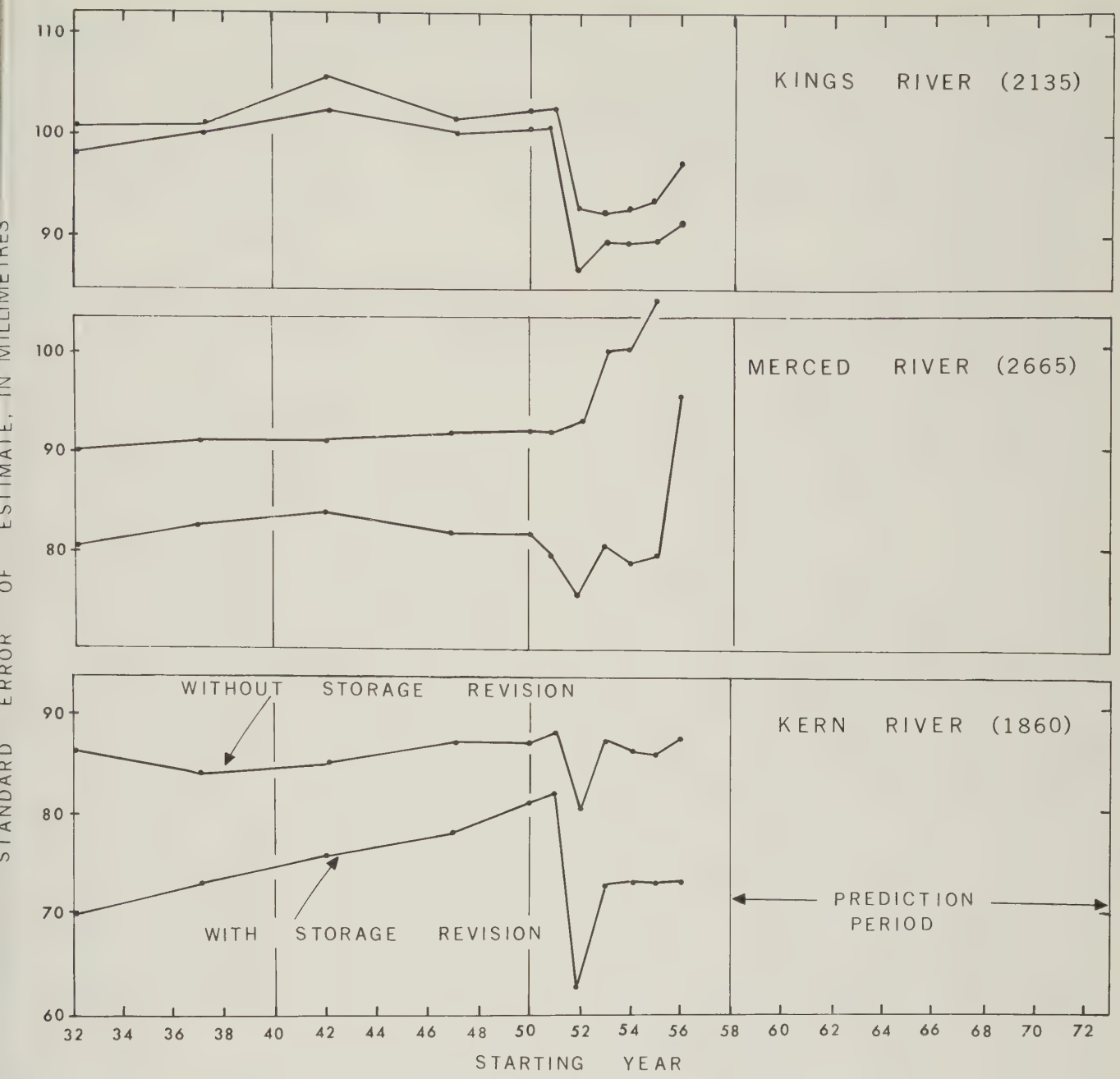

FIGURE 2.—The standard error of estimate for predicting April–July runoff on April 1 during the 1958–73 period as a function of the starting year of the runoff and precipitation variables used in the HM model. Each prediction is based only on antecedent data; for example, the 1965 prediction is computed from data from the starting year through 1964. The upper points for each drainage are for predictions without a storage revision; the lower are for those with a revised storage based on a 1-month spring test season. These results for three large basins in this region suggest that 1952 is the year to begin calculations for the highest accuracy of current predictions. Gaging-station numbers are indicated in parentheses after basin names.

both total runoff and timing are possible if the absolute storage is accurately known.

The absolute-storage approach, which is based on the principle of conservation of mass, has been introduced previously by several workers (Kohler, 1957; Hannaford, 1964). The main difference between the HM and earlier models is that this method uses only existing streamflow and precipitation records and has a built-in storage revision system (discussed in the next section).

The development given below deviates slightly from that given in Tangborn and Rasmussen (1976) in that storage is defined explicitly. This does not alter the final predictive equation; it does direct more emphasis to the role of storage in determining summer runoff. Storage, as defined here, includes the snowpack, ground water, and soil moisture; however, in most places the snowpack is the dominant factor in streamflow in this region.

For a defined drainage,

$$\text{spring storage} = \text{input} - \text{output},$$

which is approximately equal to winter precipitation less winter runoff:

$$S_w \approx P_w - R_w.$$

As basin precipitation, P_w, is unmeasured, it is assumed to be equal to some multiple, a, of gage precipitation

$$P_w = ap_w,$$

so that

$$S_w \approx ap_w - R_w,$$

where S_w = spring storage of water in a drainage basin,
P_w = winter precipitation (basin),
p_w = winter precipitation (gage), and
R_w = winter runoff (basin).

Summer runoff is approximately equal to spring storage plus summer precipitation less summer evaporation (which is defined here as the net effect of the sum of evaporation, transpiration, and condensation), or

$$R_s = S_w + P_s - L_s;$$

therefore

$$R_s = (ap_w - R_w) + P_s - L_s,$$

where R_s = summer runoff (basin),
P_s = summer precipitation (basin), and
L_s = summer evaporation (basin).

Basin storage at the end of the summer season is assumed to be small and is neglected in this development. The error this produces is not considered significant; however, there may be instances where this is not true.

Subsequent net summer precipitation and evaporation are assumed to be equal to the climate average and treated as a constant,

$$b = P_s - L_s.$$

When a and b are determined by a least-squares fit of R_s, R_w, and p_w, a predictive equation for summer runoff is formed as follows:

$$R_s^* = ap_w + b - R_w,$$

where R_s^* = predicted summer runoff, which is identical to that given in Tangborn and Rasmussen (1976).

Three conventional statistical measures are used in this report: the standard error of estimate (SE), the standard deviation (SD), and the coefficient of variation (δ).

$$\text{SE} = \left[\frac{1}{n}\Sigma(R^* - R)^2\right]^{\frac{1}{2}},$$

$$\text{SD} = \left[\frac{1}{n\text{-}1}\Sigma(R - \bar{R})^2\right]^{\frac{1}{2}}, \text{ and}$$

$$\delta = \text{SD}/\bar{R},$$

where $\bar{R} = \frac{1}{n}\Sigma R$ and n is the number of observations.

The coefficient of variation is also computed for precipitation.

STORAGE REVISION

Estimation of the total storage available for runoff each spring, whether it is in the snowpack or as ground water and soil moisture, is the most difficult element of a prediction model. Attempts to determine the total water storage of a drainage basin by snow surveys, precipitation measurements, and aerial snow-cover observations are fraught with problems because of the inherent difficulties of measuring snow depths and densities over rough, mountainous terrain. Also, changes in storage due to evaporation are as yet unmeasurable; consequently some method is necessary to monitor total storage continuously throughout the main ablation season.

A method to revise the initial spring storage estimate (as determined by winter precipitation less runoff) was devised for the North Cascades prediction model (Tangborn and Rasmussen, 1976). Basically, this procedure tests the total volume of storage by making short season runoff predictions in late winter and then revises the storage estimate and late season runoff prediction by an amount that is proportional to the error incurred in making the short season prediction.

The application of the storage revision method to runoff prediction in the Sierra appears even more successful in reducing errors than it was for the North Cascades. Some of the vast improvement in accuracy by this means in this region may be due to a greater dependence of summer runoff on the snowpack and less on summer precipitation and the much smaller carryover of storage from one year to the next. The length of the test season is a determining factor in accuracy improvement and was allowed to range from 0 to 4 months. In most applications the optimum test-season length was found to be somewhere between 0 and 1 month and a 10-day or 2-week length would appear to improve the prediction significantly. This is

demonstrated in figure 3 which shows the results for four basins. These curves, drawn between the 1-month points, have been approximately fitted, but represent the most logical shape based on the five given points. Apparently a more thorough analysis, using time increments of less than 1 month, is needed to realize the full value of this method.

On the basis of the HM-model principles, it would be possible to construct a real-time prediction model using daily or even shorter interval values of observed streamflow and precipitation. This method would instantaneously and automatically reevaluate basin storage by repeatedly making short-test predictions, revising storage each time to a new value depending on the resulting prediction error.

A continuous, up-to-date assessment of potential runoff for any subsequent season would be available by this interactive process. With this knowledge streamflow predictions could be updated whenever needed by water users. In some regions there is a definite need for this after major winter storms (Brown, 1974; Santeford, 1974). An added advantage in using only data from existing and relatively low-altitude streamflow and precipitation stations for such an automated system is that both data collection and telemetry to a central computer would be much less difficult than from harsher, high-altitude sites (Tarble, 1968).

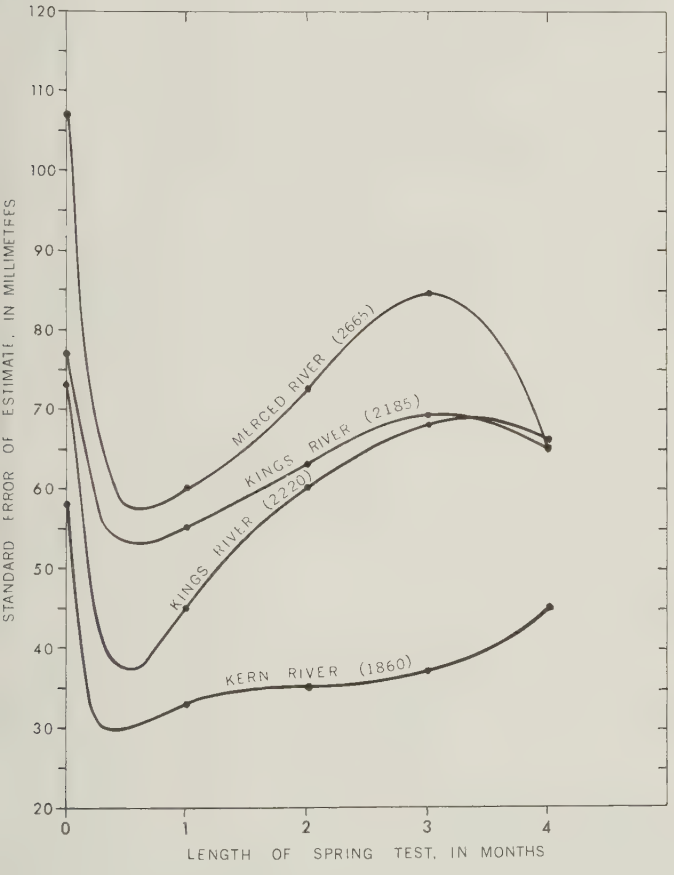

FIGURE 3.—Examples illustrating the optimum length of the spring test season for an April 1 prediction of April–July runoff. Results shown here for the four main basins in this study indicate that a test length of less than 1 month would significantly lower the standard error of these predictions. Gaging-station numbers are indicated in parentheses after basin names.

DISTRIBUTION OF RUNOFF WITH TIME

Beforehand knowledge of the amount of runoff expected to occur at any instant in time during the summer season is often of even greater economic importance than the total volume predicted for the full season (Tarble and Burnash, 1971). A predicted summer hydrograph is essential for maximum water-management efficiency as it allows water users sufficient time to plan for future supplies. The earlier this information is available each spring, the more valuable it is to those who need it.

Accuracy increases rapidly in proportion to the time interval of prediction. A 1-month interval can be predicted more accurately than can 1 day. The principal reasons for this are the unpredictability of meteorological factors that produce streamflow (mainly the energy which produces ablation) and, to a lesser degree in high-altitude basins with a large snowpack, precipitation occurring as rain. As the length of the prediction interval increases, the variability of these climatic elements about their long-term means decreases. In addition, the influence of these factors relative to storage as snow in determining the rate of runoff is less for longer seasons. However, it is possible to understand part of the inaccuracy of predicting the summer hydrograph by differentiation of the various processes that control runoff.

Six distinct factors determine the time distribution of runoff each summer:

1. Total volume of spring storage.
2. Spatial distribution of this storage with respect to altitude, orientation, and vegetation (chiefly forests).
3. Forms in which water are stored.
4. Energy available for ablation of the snowpack.
5. Evaporation.
6. Amount of precipitation and whether it occurs as rain or as snow.

The first three factors could possibly be determined on the prediction day; the last three cannot and the assumption must be made that climatic average conditions will prevail during the ablation season. Factor

4 is related to 2 in that spatial distributions of snow will, to some extent, determine ablation rates.

On the basis of present capabilities, the first factor, storage volume, is the only one of the six that can be used for predicting a summer hydrograph. Preliminary analysis of this region indicates that the altitude distribution of the snowpack also appears to be a significant factor in the time distribution of runoff. However, more detailed measurements of the space distribution of storage and how it is related to the timing of runoff are needed. The last three factors must await a significant breakthrough in long-term weather forecasting.

These monthly runoff determinations are based entirely on the total predicted storage. The distribution is computed by a linear fit between storage, approximated by observed runoff between the prediction day and through the prediction month, and the actual runoff occurring during that month (Tangborn and Rasmussen, 1976).

Results showing the time-distribution prediction made by the HM model on four basins (Kern River near Kernville; Kings River below North Fork, near Trimmer; Kings River at Piedra; and the Merced River at Pohono Bridge, near Yosemite) are shown in table 5. February 1, March 1, and April 1 predictions of the April–July monthly runoff were made in each case. As can be seen, the accuracy of the prediction of the summer hydrograph generally increases from February 1 to April 1. The distribution was made by determining the coefficients for a linear fit between the 1952–73 observed monthly runoff, R_m, and spring storage, S_0:

$$R_m = a_m S_0 + b_m.$$

Runoff data for the 1952–73 period was used to find the best fitting coefficients for each month. Storage, S_0, on the prediction day was approximated by runoff occurring subsequent to the prediction day and through the prediction month. For example, an April prediction made on February 1 would be

$$R^*_{(\text{April})} = aR^*_{(\text{February–April})} + b,$$

where a and b were predetermined by a fit of April runoff on February–April runoff. Interestingly, the approximation of S_0 by February–April runoff gave better results than a longer season, for example, February–July, which would seem to be a better estimate of total storage. This may be due to April runoff being more closely related to only part of total storage, that is, that of snow lying in exposed areas.

An approximate measure of the value of each month's prediction can be made by comparing the

TABLE 5.—*Accuracy of the predicted monthly distribution of runoff, in millimetres*

Station No.	Station Name	Prediction day	April Mean	April SD	April SE	May Mean	May SD	May SE	June Mean	June SD	June SE	July Mean	July SD	July SE	August Mean	August SD	August SE	September Mean	September SD	September SE
1860	Kern River	Feb. 1	35	22	14	68	51	28	70	52	28	38	34	18	16	12	6.0	8.7	5.3	3.3
	near Kernville	Mar. 1	--	--	10	--	--	24	--	--	22	--	--	18	--	--	6.3	--	--	3.3
		Apr. 1	--	--	11	--	--	15	--	--	15	--	--	10	--	--	4.3	--	--	1.9
2185	Kings River below	Feb. 1	63	27	21	133	75	39	131	79	47	66	57	36	27	18	12	4.2	11	9.6
	North Fork,	Mar. 1	--	--	15	--	--	35	--	--	43	--	--	37	--	--	12	--	--	9.8
	near Trimmer	Apr. 1	--	--	21	--	--	21	--	--	33	--	--	26	--	--	9.6	--	--	8.0
2220	Kings River at	Feb. 1	60	24	21	122	66	36	111	70	41	50	49	29	15	13	7.2	6.1	4.1	3.1
	Piedra	Mar. 1	--	--	15	--	--	30	--	--	38	--	--	32	--	--	8.2	--	--	3.5
		Apr. 1	--	--	20	--	--	31	--	--	27	--	--	17	--	--	5.3	--	--	2.4
2665	Merced River at	Feb. 1	92	32	33	211	99	54	172	97	59	61	56	36	15	13	8.5	5.7	4.4	4.3
	Pohono Bridge,	Mar. 1	--	--	27	--	--	46	--	--	60	--	--	41	--	--	9.6	--	--	4.3
	near Yosemite	Apr. 1	--	--	32	--	--	32	--	--	47	--	--	32	--	--	7.0	--	--	4.1

Note.--SD = standard deviation; SE = standard error of estimate.

standard error of estimate with that month's standard deviation. If the standard error is less than the standard deviation, the prediction method would be an improvement over using the mean flow as a prediction.

The prediction of daily discharge throughout the subsequent summer season is an important factor in water management (Barsch and Burnash, 1968; Hannaford and others, 1970). An illustration of how accurately the HM model is able to predict April–September daily values of discharge on April 1 is shown in figure 4. As only monthly values of predicted runoff are obtainable with the current system, a smooth curve that agreed with the observed discharge on April 1 and whose integral agreed with the predicted monthly values was constructed. Two years are shown as examples: 1969, a much above average runoff year, and 1972, a much below average year. Both years were about average with regard to prediction error. The accuracy and definition of this time distribution would likely be improved if a shorter time interval of data input were used.

The physical basis for relating runoff timing to storage is that for a given ablation potential, runoff rates are strongly dependent on the amount of storage occurring as snow. The areal distribution of the snowpack will, to some extent, also determine the runoff distribution as a widely dispersed snowpack will melt more rapidly than one with an identical volume concentrated in smaller areas. It can therefore be reasoned that some means of independently determining the areal coverage of the snowpack, that is, by satellite photography, would assist in predicting the time distribution of runoff.

PREDICTION OF THE ALTITUDE DISTRIBUTION OF STORAGE AND RUNOFF

The distribution with altitude of the source of mountain streamflow is often of practical interest because many water users are concerned with the effects of vegetation changes, cloud seeding, and other human activities which may alter the distribution of mountain water supplies. This information is of particular concern to land-use managers who must determine the best use of these mountain regions for all of society (Horn, 1973). In addition, the distribution of snow storage with altitude influences the timing of summer runoff. Knowledge of the spatial distribution would undoubtedly assist in determining the time distribution.

A plot of the mean summer (April–July) fraction of the mean October–July runoff as a function of basin mean altitude is shown in figure 5. This fraction, R_s/R_y, shows a much better fit with altitude than does either R_s or R_y individually. A fitted quadratic through these points gives the approximate distribution of R_s/R_y as a function of altitude for this region and can be used to determine the storage and potential

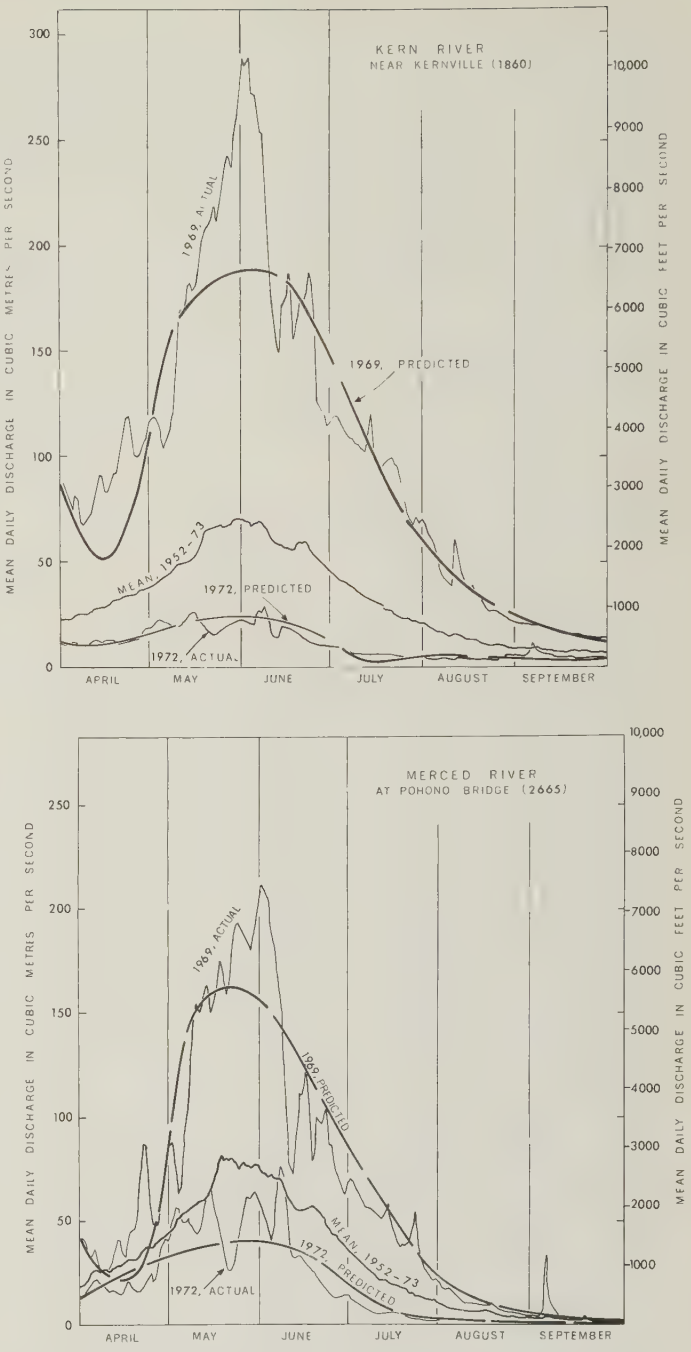

FIGURE 4.—The April 1 prediction of mean daily discharge throughout the summer (April–September) season. Shown are the actual and predicted dailies for 1969 and 1972, and the 1952–73 daily mean for the Kern River near Kernville (No. 1860) and the Merced River at Pohono Bridge, near Yosemite (No. 2665).

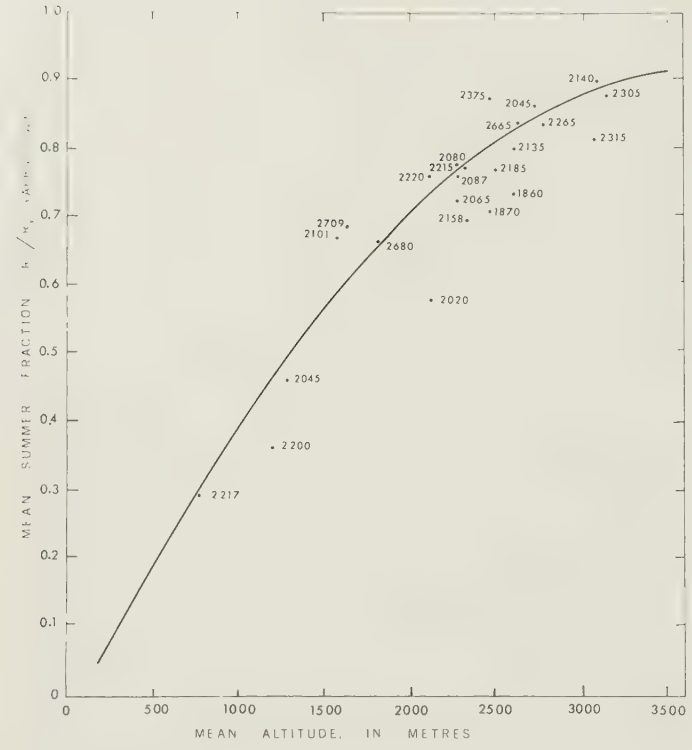

FIGURE 5.—The mean summer runoff fraction, $\overline{R}_S/\overline{R}_y$, versus mean basin altitude, $\overline{Z}$ for all basins used in this study. This fraction shows much less scatter than when either $\overline{R}_S$ or $\overline{R}_y$ are plotted against mean altitude. Many of the deviations from the best fitting quadratic of $\overline{R}_S/\overline{R}_y$ on Z can be explained by basin orientation. Basins 2101 and 2375 are strongly north oriented while 2200, 2020, 2158, 1860, and 1870 have a predominant south-facing orientation. Basin 2709 shows a large deviation from the fitted curve because the gaging station is located a distance downstream and the drainage area includes a large region which does not have a summer snowmelt component. The fitted curve does not appear to balance the scatter of points because of the dominance of storage at higher altitudes, and the area-altitude fractions instead of the mean are used in the fitting process. These results indicate that basin orientation significantly influences runoff timing. The relationship shown here is used to calculate the distribution of storage or summer runoff with altitude as demonstrated in figure 6.

runoff distribution. As most of these basins span a wide altitude range, the mean altitude is not the best variable to use. To account for the nonlinearity of the R_s/R_y versus Z function and the wide range in altitudes, the basin area-altitude fractions (table 2) are used in the fitting procedure (Rasmussen and Tangborn, 1976).

Most of the large deviations from the fitted quadratic can be explained by basin orientations. North-facing basins will tend to retain snow longer into the spring season and have a R_s/R_y fraction greater than than the regional average. Conversely, south-facing basins will lose snow more rapidly each spring and the fractions will be less than the average. Those basins that showed a large deviation from the mean function were not used in the final computation of the regional storage distribution. It is of interest to note that the North Cascades basins did not show this strong dependence on orientation of the summer runoff fraction. This may possibly be due to solar radiation being a less influential factor for snowmelt in the North Cascades than in the Sierra.

Knowing both the area and unit runoff for each altitude interval allows the determination of the total volume of storage (approximated by the observed or predicted April–July runoff) and potential summer runoff as a function of altitude. The approximate April 1 storage as a function of altitude is given by the following:

$$S_{ij}=X_j R_{yj} \sum_{k=i}^{n} A_{ij} f(Z_k),$$

where S_{ij} = Storage at and above the ith altitude interval (of n intervals) in basin j,
$f(Z_k)=R_s/R_y$ versus Z function for the region,
A_{ij} = Area-altitude fraction, ith interval, basin j,
X_j = Area of basin j, and
R_{yj} = Annual runoff of basin j.

Figure 6 shows the result of this calculation on the Kings River (No. 2185) and the Merced River (No. 2665). Although the Kern River is a main drainage, it was not included because it has a strong southerly orientation and does not fit well with this set of drainages. Using the predicted R_s^*/R_y^* for each basin, it is possible to make this determination of discharge versus altitudes before the main runoff season begins, thus giving water supply managers the benefit of knowing the potential runoff from each altitude zone.

EFFECT OF SUBSEQUENT PRECIPITATION ON PREDICTION ACCURACY

A scatter diagram of the prediction error each year for a January–September prediction season versus January–September precipitation demonstrates a high negative correlation, $r=-0.975$ (fig. 7). This occurs because greater than normal precipitation causes negative errors (predicted runoff is less than observed). Conversely, less than normal summer precipitation will cause positive errors.

Results for three basins, shown in figure 8, indicate that subsequent precipitation is a significant cause of prediction error throughout the late winter and early spring (to about April 1 for the Kern River, May 1 for the Kings River, and June 1 for the Merced River).

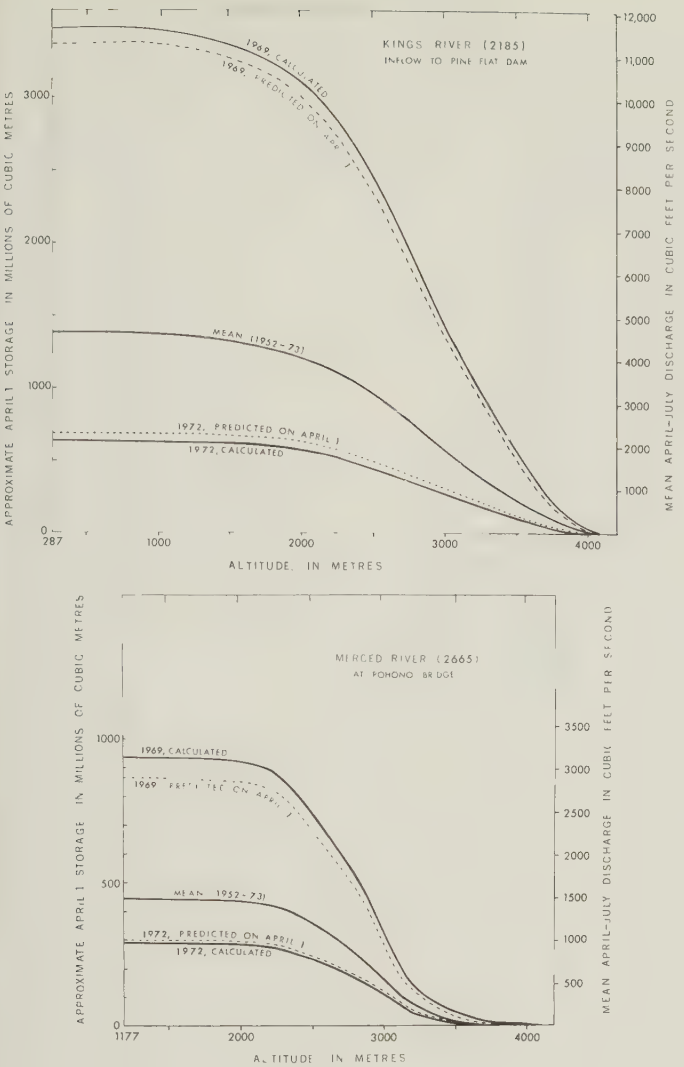
KINGS RIVER (2185)
INFLOW TO PINE FLAT DAM
1969, CALCULATED
1969, PREDICTED ON APRIL 1
MEAN (1952-73)
1972, PREDICTED ON APRIL 1
1972, CALCULATED
APPROXIMATE APRIL 1 STORAGE IN MILLIONS OF CUBIC METRES
MEAN APRIL-JULY DISCHARGE IN CUBIC FEET PER SECOND
ALTITUDE, IN METRES
MERCED RIVER (2665)
AT POHONO BRIDGE
1969, CALCULATED
MEAN 1952-73
1972, PREDICTED ON APRIL 1
1972, CALCULATED
APPROXIMATE APRIL 1 STORAGE IN MILLIONS OF CUBIC METRES
MEAN APRIL-JULY DISCHARGE IN CUBIC FEET PER SECOND
ALTITUDE IN METRES

FIGURE 6.—Inferred altitude distributions of storage for Kings River below North Fork, near Trimmer (No. 2185) and Merced River at Pohono Bridge, near Yosemite (No. 2665). The total storage is taken to be equal to the total April–July runoff. Five curves are shown for each basin, using the actual and predicted runoff for the wet year 1969, the actual and predicted runoff for the dry year 1972, and the mean actual runoff for the period 1952–73. These altitude curves are obtained by using the runoff values for several nearby basins with different area-altitude profiles.

After these dates unusual departures from normal precipitation appear to be inconsequential. These conclusions seem to disagree with those resulting from a study made earlier of the effects of summer precipitation in the high Sierra which indicates that a large part of the streamflow prediction error during the snowmelt period is due to summer precipitation (Hannaford and Williams, 1967). A study of high-altitude precipitation (above 2,750 m) in the upper Kings River basin indicates that considerably greater

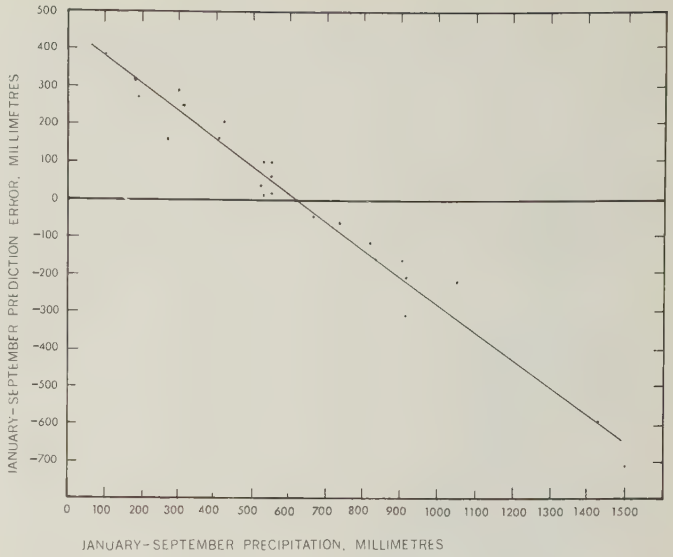

FIGURE 7.—Prediction error for a January 1 prediction of January–September runoff for the Kings River below North Fork, near Trimmer (2185) versus the actual precipitation occurring during the January–September season at station 1111. The correlation coefficient for this linear fit is —0.975, demonstrating the strong influence of subsequent precipitation on prediction error.

amounts of localized, convective precipitation may occur in these regions than occurs at established, lower altitude meteorological stations, particularly during the late summer season July–September (Henderson and others, 1974).

These results do suggest that increased efforts to forecast spring and summer precipitation would yield worthwhile improvements in early season streamflow predictions but that forecasting late summer precipitation would not be as useful for this purpose.

COMPARISONS WITH OTHER METHODS

Five drainage basins for which seasonal streamflow predictions have been made in the past were selected for accuracy comparison of the HM method with operational forecasts. These were chosen because of the major importance these drainages have in this region (California Department of Water Resources, 1959–1973). Only those basins with published records of natural flow were used, the one exception being the Kings River at Piedra (No. 2220); these records adjusted to natural flow were obtained from the Kings River Water Association (R. E. Leake, written commun., 1975). Comparisons are made for the April–July runoff season and the 1959–73 period in all cases. When available, comparisons of predictions made on February 1 and March 1 of the April–July flow are also given. The Kings River at Piedra (No. 2220) and

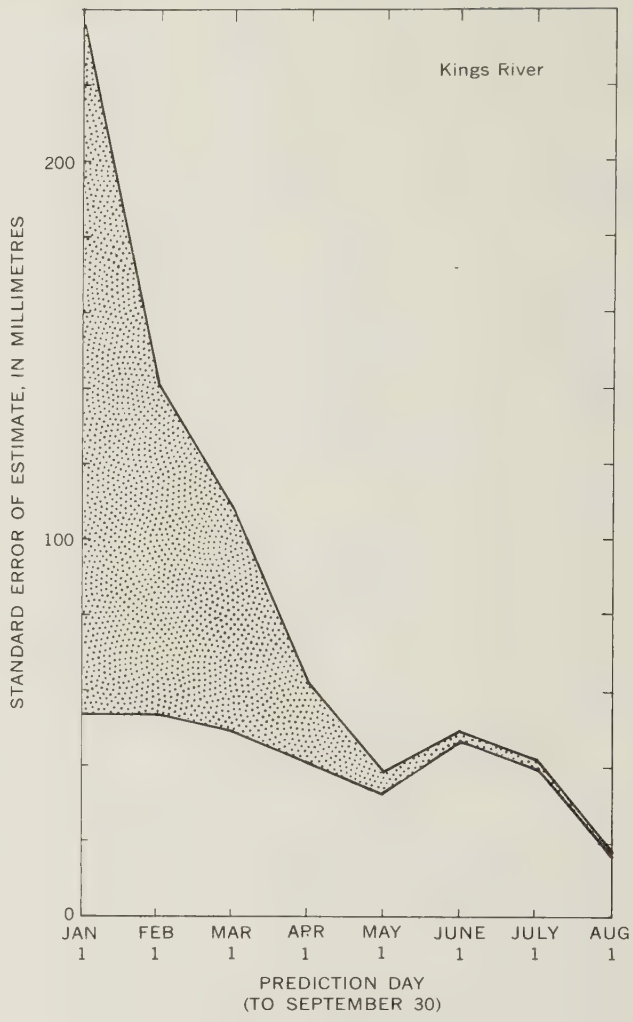

FIGURE 8.—The prediction error as a function of time of prediction for streamflow to the end of September (upper line) given for Kern River near Kernville (No. 1860), Kings River below North Fork, near Trimmer (No. 2185), and Merced River at Pohono Bridge, near Yosemite (No. 2665). The stippled area represents that part of the error due to the precipitation occurring in the basin subsequent to the prediction day. Relationships, such as the one shown in figure 7, are the basis for determining the relative influence of summer precipitation on prediction error given in these examples.

FIGURE 8.—Continued.

the Merced River at Pohono Bridge, near Yosemite (No. 2665) have predictions available for years extending back into the midthirties but comparisons could not be made for earlier years because of the previously discussed limitation of the HM model to post-1952 data (table 6).

These comparisons should be considered only as an approximate evaluation of the HM model and are not meant to reflect on the validity of the operational methods in use which, mostly, are extremely accurate. Certainly an established method which has had to evolve through the years cannot simply and equitably be compared year by year with a new method which benefits by the trials and experience of other workers in the field of hydrology. That is, the newly developed HM model has been compared here with an average of the operational models that have been used over the past 15 years. The current versions of the operational models presumably contain improvements in model design, in addition to their having access to the records of precipitation and runoff occurring in years after their predecessors were used. Had these current versions been used over the entire comparison period, as has the new HM model, then the operational models may well have enjoyed a far better record than is shown for them here.

Use of the HM model appears to give more accurate predictions than the present operational methods. If the improvement, I, is given as the percentage difference of the standard error of estimate,

$$I=\frac{(\mathrm{SE})_c-(\mathrm{SE})_{\mathrm{HM}}}{(\mathrm{SE})_c}\times 100.$$

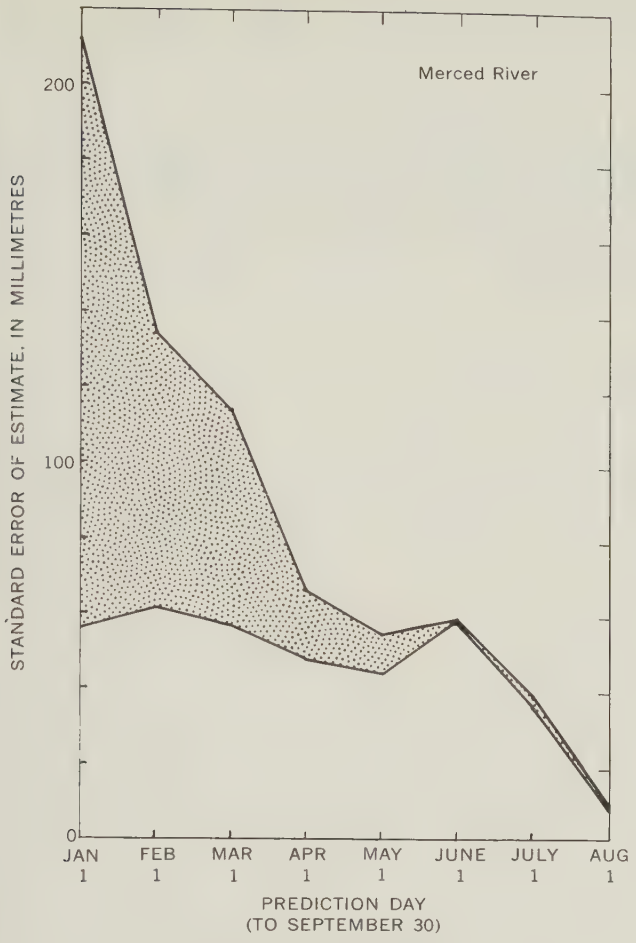

FIGURE 8.—Continued.

where $(SE)_c$ = standard error of the comparison method and

$(SE)_{HM}$ = standard error of the HM method.

the increase in accuracy varies from just less than 1 percent for the March 1 prediction on the Kings River inflow to the Pine Flat Reservoir (No. 2185) to 34 percent for April 1 prediction on the Merced River at Phono Bridge, near Yosemite (No. 2665). The average improvement in accuracy for all April 1 predictions is about 24 percent.

It should be emphasized that the HM model predictions were made each year on the basis only of data previous to that year. For this reason the mean error of these predictions, given in table 6, does not equal 0.

Comparisons of prediction accuracy of the summer hydrograph or monthly distributions were not possible because these data were not available for other methods.

PROPOSED IMPROVEMENTS IN THE HM MODEL

A number of improvements in the HM model can be visualized which would increase its accuracy and versatility for the Sierra and other mountain regions. Some of these involve a major change in current procedures (for example, the addition of an evaporation component); others could be implemented with minor changes. The most promising modification would be shortening the time interval for the input of precipitation and runoff. Both of these sets of data are now directly retrievable from computer linked storage files for most parts of the country with at least a daily frequency.

Improvements in predicting the summer hydrograph by a greater definition of the spatial distribution of the snowpack, particularly with altitude, is another proposed modification. There is little doubt that the ablation of snow varies with altitude; however, other factors such as changes in slope orientation and forest cover changes with altitude must be included in any model that takes altitude into account. Sublimation directly from the snowpack and other evaporation and transpiration losses are other elements in mountain hydrology which need to be included in a realistic physical model.

Perhaps the most promising approach would be a continuous-balance model that would account for the amounts of all forms of water as they enter, are temporarily stored, and then leave each of the nearly uniform hydrometeorological elements into which a drainage basin might be divided (Leavesley, 1973).

REFERENCES CITED

Barsch, R. E., and Burnash, R. J., 1968, Forecasting short-term discharge from snowmelt: Lake Tahoe, Nev., 36th. Ann. Western Snow Conf. Proc., p. 41–45.

Brown, A. J., 1974, Long-range goals and information needs of the coordinated snow survey program in California, *in* Santeford, H. S., and Smith, J. L., compilers, Interdisciplinary symposium on advanced concepts and techniques in the study of snow and ice resources, Monterey, Calif., 1973: Natl. Acad. Sci. Pub., p. 47–54.

California Department of Water Resources, 1959–1973, Water conditions in California: California Dept. Water Resources Bulls. 120–59 to 120–73.

Hannaford, J. F., 1964, Development of a digital river basin model: Nelson, British Columbia, 32d Ann. Western Snow Conf. Proc., p. 20–26.

Hannaford, J. F., Bush, R. H., and Barsch, R. E, 1970, The development and application of a hydrologic model as an operational tool: Victoria, British Columbia, 38th Ann. Western Snow Conf. Proc., p. 7–15.

Hannaford, J. F., and Williams, M. C., 1967, Summer hydrology of the High Sierra: Fresno, Calif., State Coll. Found. Atmospheric Water Resources Research, 26 p.

Henderson, T. J., Duckering, Dale, Henderson, Mike, Crouch, Lee, and Ankney, John, 1974, A High Sierra precipitation measurement program: Fresno, Calif., Atmospherics Inc., 52 p.

TABLE 6.—*Comparison of hydrometeorological (HM) and California Department of Water Resources (CDWR) predictions of the April–July runoff, in millimetres, for the 1959–73 period except that the February and March predictions for the Kern River near Kernville are for 1968–73.*

Station		Actual		Predictions											
				February 1				March 1				April 1			
				CDWR		HM		CDWR		HM		CDWR		HM	
No.	Name	Mean	SD[1]	Mean	SE[2]	Mean	SE[2]	Mean	SE[2]	Mean	SE[2]	Mean	SE[2]	Mean	SE[2]
1860	Kern River near Kernville	199	164	214	129	254	96	282	73	247	38	197	55	200	42
2215	Kings River below Pine Flat Dam	349	228	347	147	367	131	338	110	365	105	324	75	360	64
2220	Kings River at Piedra	323	212	316	138	337	124	308	108	335	102	296	76	330	60
2265	Merced River at Pohono Bridge, near Yosemite	503	248	---	---	---	---	---	---	---	---	462	109	533	72
2709	Merced River below Merced Falls Dam, near Snelling	258	150	244	106	269	86	242	101	272	92	232	77	267	56

[1]SD = Standard deviation.

[2]SE = Standard error of estimate.

Horn, W. L., 1973, Developing land use goals for California: Grand Junction, Colo., 41st Ann. Western Snow Conf. Proc., p. 22–29.

Hutchison, N. E., compiler, 1975, WATSTORE—National Water Data Storage and Retrieval System of the U.S. Geological Survey—User's guide: U.S. Geol. Survey Open-File Rept. 75–426, 791 p., 101 figs., 30 tables.

Kohler, Max, 1957, Water supply forecast development, 1951–56: Santa Barbara, Calif., 25th Ann. Western Snow Conf. Proc., p. 62–68.

Leavesley, G. H., 1973, A mountain watershed simulation model: Boulder, Univ. Colorado, Ph. D. dissertation, 174 p.

Rasmussen, L. A., and Tangborn, W. V., 1976, Hydrology of the North Cascades region, Washington—[Part] 1, Runoff, precipitation and storage characteristics: Water Resources Research, v. 12, no. 2, p. 187–202.

Santeford, H. S., 1974, A challenge in snow and ice, *in* Santeford, H. S., and Smith, J. L., compilers, Interdisciplinary symposium on advanced concepts and techniques in the study of snow and ice resources, Monterey, Calif., 1973: Natl. Acad. Sci. Pub., p. 3–8.

Tangborn, W. V., and Rasmussen, L. A., 1976, Hydrology of the North Cascades region, Washington—[Part] 2, A proposed hydrometeorological streamflow prediction method: Water Resources Research, v. 12, no. 2, p. 203–216.

Tarble, R. D., 1968, California federal-state snow sensor investigations, problems and records: Lake Tahoe, Nev., 36th Ann. Western Snow Conf. Proc., p. 106–109.

Tarble, R. D., and Burnash, J. C., 1971, Directions in water supply forecasting: Billings, Mont., 39th Ann. Western Snow Conf. Proc., p. 93–97.

U.S. Geological Survey, 1970, National atlas of the United States of America: U.S. Geol. Survey, 417 p.

U.S. National Oceanic and Atmospheric Administration, 1930–1973, Climatological data for California: U.S. Natl. Oceanic and Atmospheric Adm. Pub., v. 34 to v. 77.

Jour. Research U.S. Geol. Survey
Vol. 5, No. 1, Jan.–Feb. 1977, p. 49–52

PROCEDURE FOR ESTIMATING THE TEMPERATURE OF A HOT-WATER COMPONENT IN A MIXED WATER BY USING A PLOT OF DISSOLVED SILICA VERSUS ENTHALPY

By A. H. TRUESDELL and R. O. FOURNIER, Menlo Park, Calif.

Abstract.—A graphical method using a plot of dissolved silica versus enthalpy allows quick determination of the temperature of the hot-water component of a nonboiling thermal spring. The method is applicable to warm spring waters that either have not lost heat before mixing or have lost heat by separation of steam before mixing.

Fournier and Truesdell (1974) published graphical and analytical procedures for estimating the temperature and proportion of a hot-water component mixed with a cold water. These procedures, valid for warm springs of large flow rate, were based on heat and silica balances. This paper presents simplified graphical procedures for obtaining those results. The method makes use of the dissolved silica-versus temperature graph of Fournier and Rowe (1966, fig. 5), replotted in figure 1 as dissolved silica versus enthalpy of liquid water in equilibrium with steam. To simplify the procedure, we have chosen to plot enthalpy in International Table calories (cal_{IT}) per gram (above 0°C) rather than joules per gram because the enthalpy of liquid water is numerically approximately the same as the temperature.

In using figure 1, one may assume either that no steam or heat had been lost from the hot-water component before mixing or that steam had separated from the hot-water component at an intermediate temperature before mixing. In either event, it is necessary to assume that no loss of heat occurs after mixing, that the initial silica content of the deep hot water is controlled by the solubility of quartz, and that no further solution or deposition of silica occurs before or after mixing. These assumptions are discussed in greater detail in Fournier and Truesdell (1974).

PROCEDURE

Assuming no loss of steam or heat before mixing; then do the following:

1. Determine or estimate the temperature and silica content of nonthermal ground water in the region and plot as a point in figure 1, the silica-versus-enthalpy graph. Plot temperature in degrees Celsius as calories. This is shown as point A in figure 2.
2. Plot the temperature and silica content of the warm spring water as another point on the graph, point B in figure 2 (again plotting temperature as calories).
3. Draw a straight line through the two points and extend that line to intersect the quartz solubility curve, point C in figure 2. Point C is the enthalpy and silica content of the deep hot-water component.
4. Obtain the temperature of the hot-water component from its enthalpy by using steam tables (Keenan and others, 1969) or figure 3.
5. Determine the fraction of hot water in the warm spring by dividing the distance AB by AC.

It is possible that point B may plot at too high a silica value for the extension of line AB to intersect the quartz solubility curve. This may be due to the assumption of too low a value for the silica content of the nonthermal water, and this value may be increased if it seems reasonable. Alternately, the hot-water component may have lost heat, but not silica, before mixing. If heat was lost by separation of steam, it is possible to evaluate the situation.

Assuming steam loss from an adiabatically cooled liquid before mixing with cold water; then do the following:

1. Plot the temperature and silica contents of the warm and cold waters as in the above procedure (fig. 4, points A and D).
2. Draw a straight line between those points (A and D) and extend that line to the liquid-water enthalpy equivalent of the temperature at which

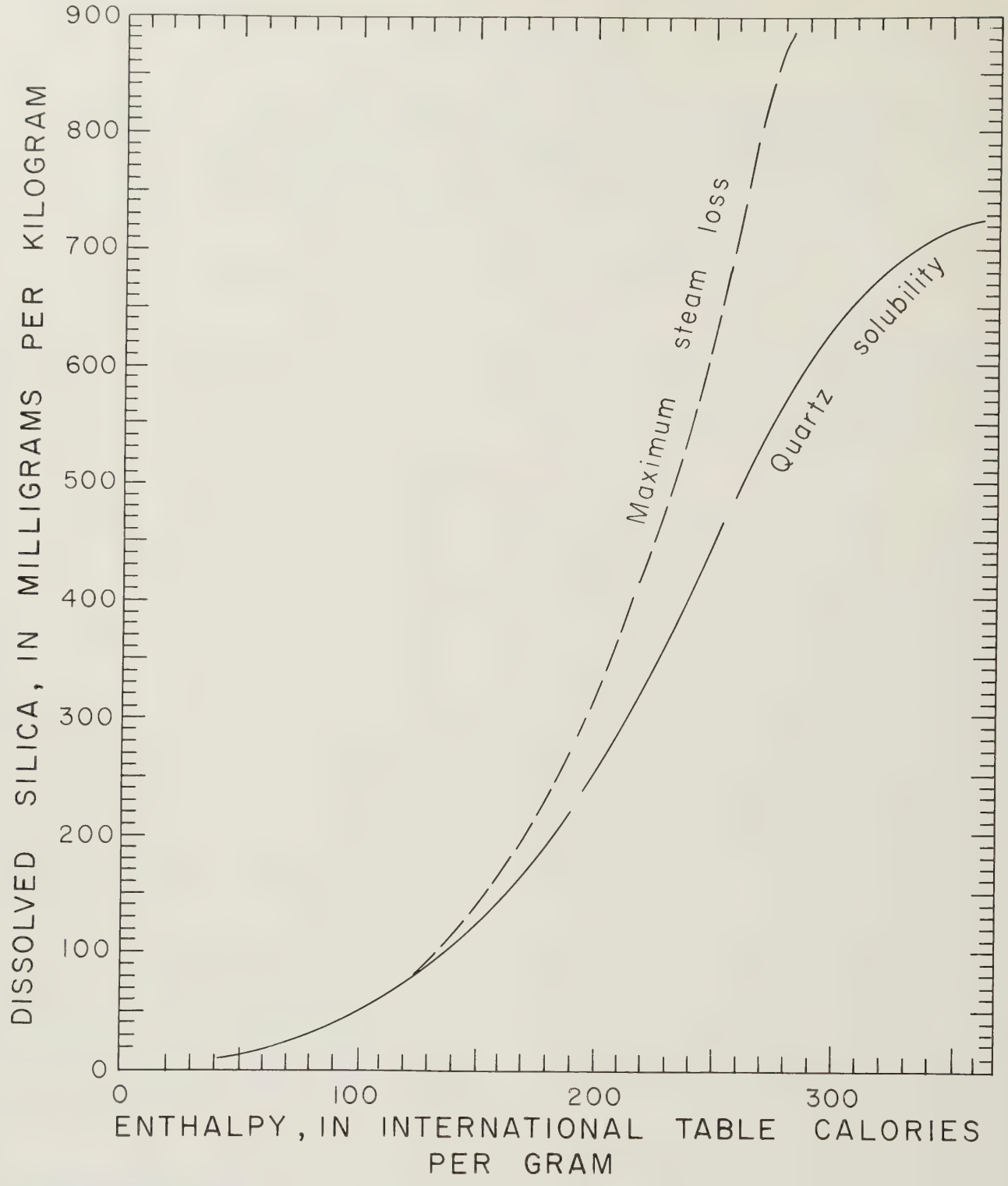

FIGURE 1.—Dissolved silica–enthalpy graph for determining temperature of a hot-water component mixed with cold water yielding warm spring water.

steam is assumed to have escaped before mixing (point E for 100°C in fig. 4).

3. Move horizontally across the diagram parallel to the abscissa until the maximum steam-loss curve is intersected (point F in fig. 4). Point F gives the enthalpy of the hot-water component before the onset of boiling, and point G gives the original silica content before loss of steam occurred.

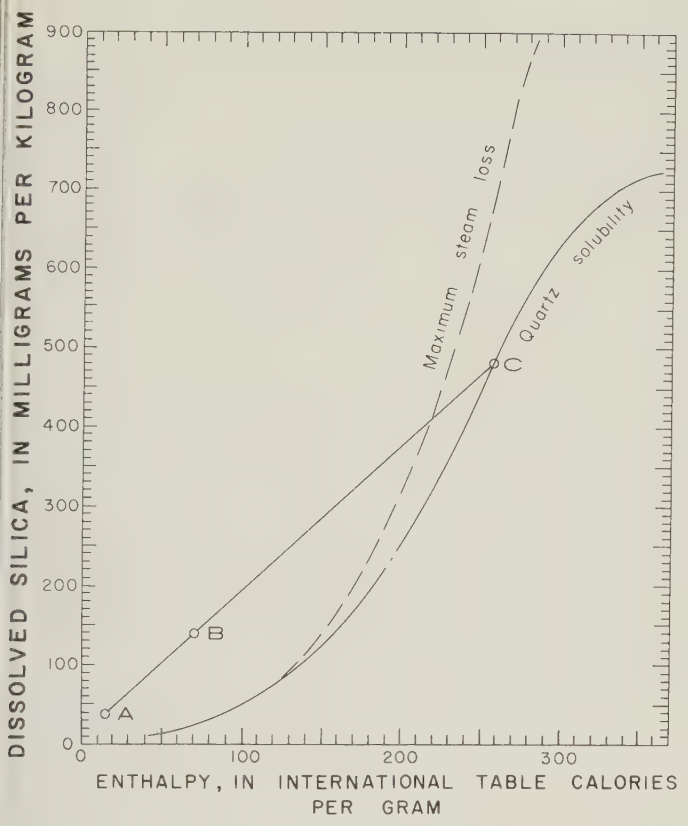

FIGURE 2.—Dissolved silica–enthalpy graph to be used when assumption is made that no steam or heat has been lost before mixing. See text for explanation.

4. Determine the fraction of hot water (after steam loss) in the warm spring by dividing the distance AD by AE. The weight fraction of original hot water lost as steam before mixing, x, is given by the formula

$$x = 1 - \frac{\text{silica value at point G}}{\text{silica value at point F}}.$$

If steam is lost at temperatures above 100°C, point F will lie on an intermediate steam loss (ISL) curve between the 100°C maximum steam loss (MSL) curve and the quartz solubility (QS) curve. The relative distance of the ISL curve from the QS and MSL curves is in the proportion $(H_{QS}-H_{ISL})/(H_{ISL}-H_{100})$ where H_{QS} is the enthalpy of liquid water at the quartz solubility curve at a given value of silica, H_{ISL} is the enthalpy of liquid water at the actual temperature of steam loss, and H_{100} is the enthalpy of liquid water at 100°C.

If steam separates at less than 1 atmospheric pressure, the enthalpy of the residual liquid water will be

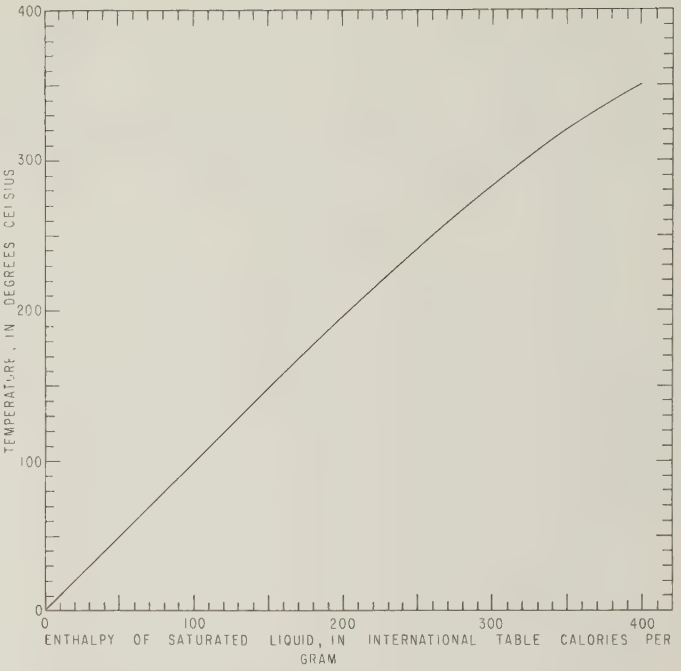

FIGURE 3.—Temperature-enthalpy relations for liquid water in equilibrium with steam.

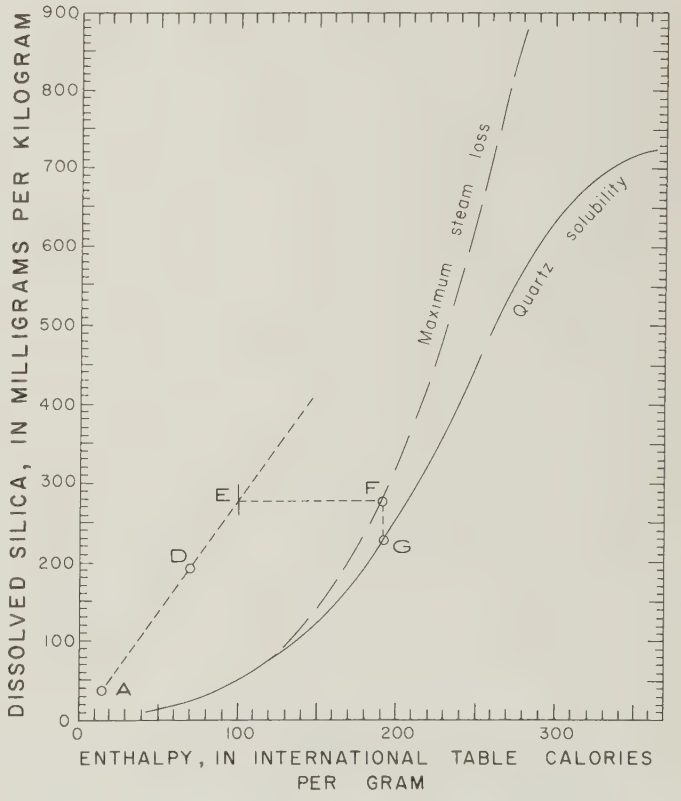

FIGURE 4.—Dissolved silica–enthalpy graph to be used when assumption is made that steam separated at 100°C from the hot-water component before mixing. See text for explanation.

less than 100 cal_{IT}/g. Point F will then be positioned on a different maximum steam-loss curve located slightly to the left of the maximum steam-loss line shown in figure 4. However, the change in position of the maximum steam loss curve as a function of the atmospheric pressure (altitude) is generally trivial.

DISCUSSION

The maximum enthalpy of the hot-water component that can be reliably determined is set by the point at which an extended line, such as AB (fig. 2), would be tangent to the quartz solubility curve. For most reasonable silica contents of nonthermal water, this will be at about 300 cal_{IT}/g (~285°C). Higher initial enthalpies of the hot-water component would cause an extended line to intersect the quartz solubility curve at two points, and the lower enthalpy point probably would be erroneously selected as the solution to the mixing problem. Although this presents a problem in interpretation, another problem inherent in dealing with very high enthalpy waters (above 275 to 300 cal_{IT}/g) is probably more serious. Quartz precipitates relatively quickly from such waters, and, therefore, temperatures derived from any relation assuming no silica precipitation are likely to be in error.

This method does allow easy evaluation of the effects of variations in assumed silica content and temperature of nonthermal water. The method also allows results obtained assuming no steam loss to be compared quickly with results obtained assuming steam loss at various intermediate temperatures. Similar graphical methods can be used to accommodate other silica phases such as chalcedony and cristobalite.

REFERENCES CITED

Fournier, R. O., and Rowe, J. J., 1966, Estimation of underground temperatures from the silica content of water from hot springs and wet-steam wells: Am. Jour. Sci., v. 264, p. 685–687.

Fournier, R. O., and Truesdell, A. H., 1974, Geochemical indicators of subsurface temperature—Part 2, Estimation of temperature of fraction of hot water mixed with cold water: U.S. Geol. Survey Jour. Research, v. 2, no. 3, p. 263–270.

Keenan, J. H., Keyes, F. G., and Moore, J. G., 1969, Steam tables. Thermodynamic properties of water, including vapour, liquid, and solid phases: New York, John Wiley & Sons, 162 p.

Jour. Research U.S. Geol. Survey
Vol. 5, No. 1, Jan.–Feb. 1977, p. 53–60

GEOCHEMISTRY OF AMPHIBOLITES FROM THE CENTRAL BEARTOOTH MOUNTAINS, MONTANA-WYOMING

By THEODORE J. ARMBRUSTMACHER and FRANK S. SIMONS, Denver, Colo.

Abstract.—Trends of variation of major- and minor-element contents in amphibolites from the central Beartooth Mountains strongly suggest that these rocks of andesitic composition are derived from a tholeiitic, mafic igneous parent and not from a sedimentary parent. Discriminant functions based on minor-element content also indicate igneous parentage, whereas functions based on major-element content indicate a sedimentary parent, suggesting that the general assumption that the regional metamorphism is isochemical may not be entirely valid. Furthermore, chemical data on the amphibolites do not fit the fractionation curves of average Beartooth metadolerites, the most likely precursor. If, however, it is assumed that regional metamorphism and formation of amphibolites were accompanied by potassium metasomatism, then the higher concentrations of SiO_2, Al_2O_3, K_2O, and potassium-related minor elements in the amphibolites relative to metadolerite can be explained.

As part of a program to evaluate the mineral resource potential of the Beartooth Primitive Area, Montana and Wyoming (Simons and others, 1973), numerous samples of amphibolite and other rock types were collected and analyzed spectrographically in order to establish background concentrations of various minor elements. The resulting large amount of information on the chemical composition of amphibolites also provided an opportunity to study the origin of these rocks. In order to further this study, 15 carefully selected samples (fig. 1) were analyzed for major and minor elements. Part of the data derived from the analyses indicates that the amphibolites formed from mafic igneous rocks rather than from sedimentary rocks; an igneous parentage for Beartooth amphibolites was suggested previously by van de Kamp (1969) and Simons and others (1973). However, some difficulty arises in defining the parent igneous rock if the metamorphism is considered to be isochemical, because the amphibolites are more nearly andesitic than basaltic in composition.

ROCK DESCRIPTIONS

The Precambrian terrane of the central Beartooth Mountains is mainly granitic gneiss. Migmatite, hornblende gneiss, biotite gneiss, and amphibolite are less abundant, whereas pegmatites, porphyry dikes, mafic dikes, orbicular rocks, agmatites, biotite schist, and metasedimentary rocks—quartzite, marble, iron-formation—constitute only a minor percentage of the terrane. Granitic rocks are locally abundant (Page and Nokleberg, 1972). Amphibolites occur throughout this terrane as irregular stocklike masses several kilometres across, as irregular blocks and angular fragments in agmatites, as partly disrupted or boudinaged tabular masses cutting host-rock foliation, and as layers and tabular bodies parallel to host-rock foliation. Contacts with enclosing rocks are typically sharp.

Most amphibolites are medium grained but some are either fine or coarse grained. Variable amounts of aplitic and granitic material commonly vein the amphibolites. Textures are typically homeoblastic but tend to be nematoblastic in the few amphibolites that show lineation. Modal plots of hornblende-rich rocks (fig. 2) show that most of these rocks contain nearly equal proportions of feldspar and mafic minerals, considerably more plagioclase than potassium feldspar or quartz, and more hornblende than biotite.

The following mineral assemblages have been identified in hornblende-bearing rocks; the number of samples of each type that were examined is given in parentheses:

Quartz-plagioclase-biotite-hornblende (87)
Quartz-plagioclase-microcline-biotite-hornblende (40)
Quartz-plagioclase-biotite-hornblende-clinopyroxene (12)
Quartz-plagioclase-hornblende-orthopyroxene (1)
Quartz-plagioclase-biotite-hornblende-orthopyroxene (1)
Quartz-hornblende-chlorite (1)
Plagioclase-hornblende-chlorite (2)
Plagioclase-biotite-hornblende-clinopyroxene-orthopyroxene (2)
Quartz-hornblende-garnet-epidote (1)

None of the mineral assemblages is restricted to a specific type of field occurrence.

Quartz is usually strained and quartz-quartz boundaries are sutured. Quartz grains that were originally

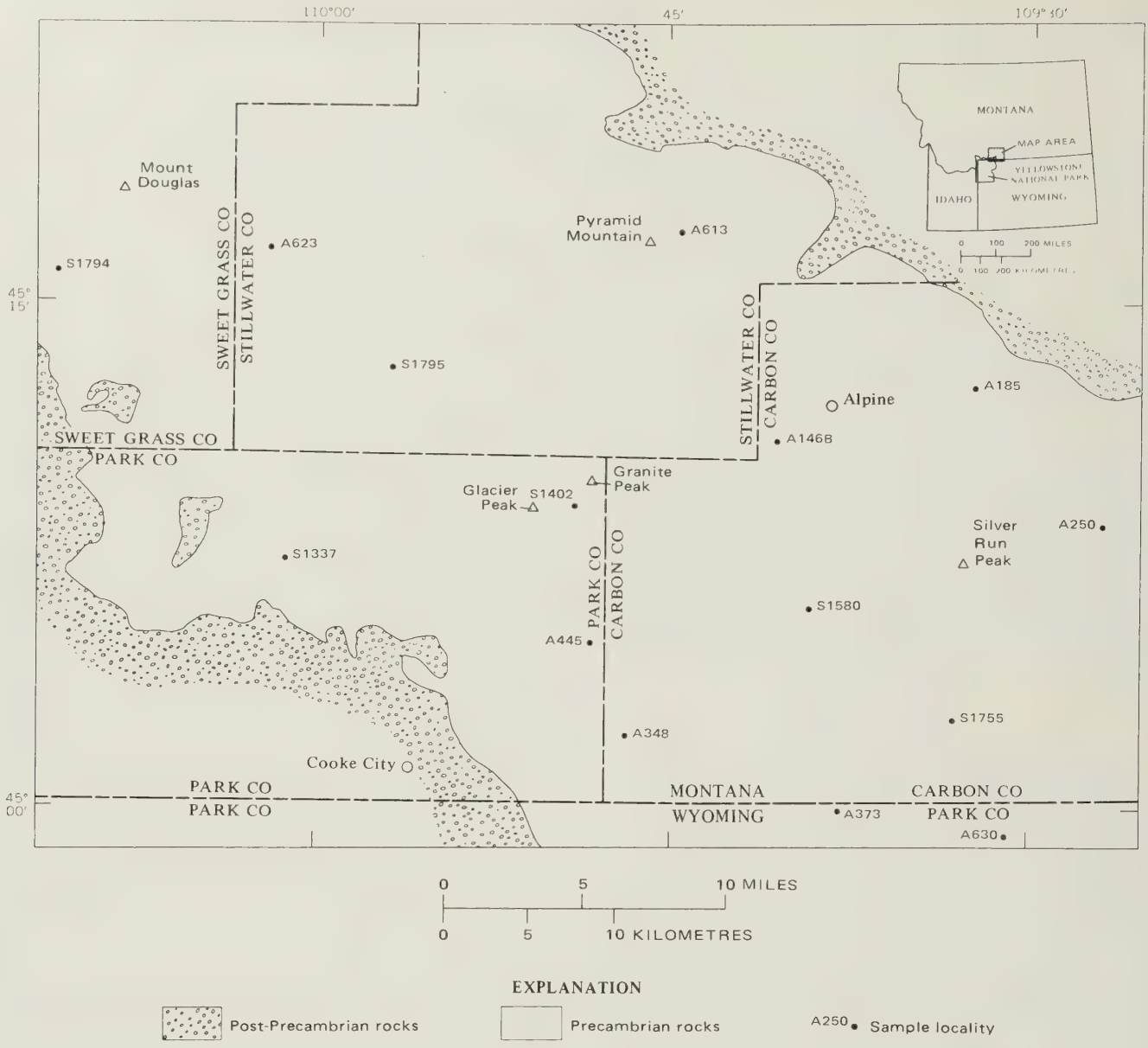

FIGURE 1.—Map of central Beartooth Mountains showing sample localities for chemically analyzed amphibolites.

larger seem to have recrystallized to finer grained quartz mosaics. The abundance of quartz varies widely.

Plagioclase, typically the most abundant mineral, has a composition near An_{35-40}; most plagioclase is partly sericitized and some is saussuritized. Twinning is weakly developed according to albite and Carlsbad twin laws or is absent. Glide twin lamellae are present in bent laths.

Microcline, if present, occurs in only minor amounts in most rocks ($\leq$3 volume percent), but may be abundant in some (11.4 volume percent in sample A348). Typically it is unaltered and appears to be paragenetically late.

Biotite is partly replaced locally by chlorite. Pleochroism is from neutral or pale reddish brown to dark chocolate brown or dark reddish brown. In most rocks biotite is less abundant than hornblende.

Hornblende is irregularly shaped to euhedral in habit and is typically unaltered. Occasional large euhedral crystals are poikiloblastic and contain numerous blebs of optically continuous quartz. Pleochroism is mainly from light yellowish green to dark olive green.

Accessory minerals are epidote, allanite, sphene, apatite, zircon, opaque oxides, pyroxene, and alteration products.

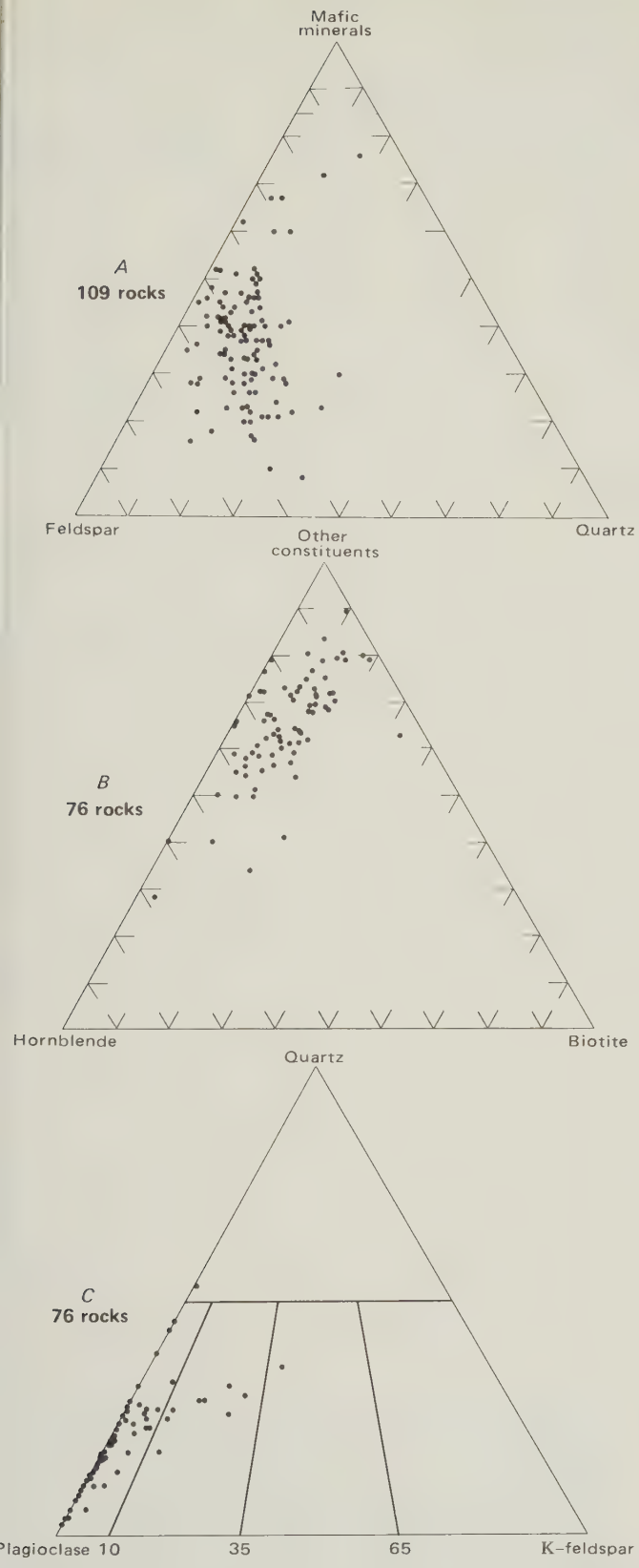

FIGURE 2.—Modal plots of hornblende-bearing rocks, Beartooth Mountains.

GEOCHEMISTRY

Major- and minor-element analyses of 15 lithologically diverse types of amphibolites from the central Beartooth Mountains (fig. 1) are presented in tables 1 and 2, together with Niggli values and ratios of key elements.

According to Leake (1964), comparison of the trends of variation of certain elements found in amphibolites with similar trends in igneous and sedimentary rocks is more useful in deducing the parent rocks of amphibolites than is comparison of average concentrations of these elements with similar averages in various rock series. He concluded (p. 239) that metasomatic changes are not important in the genesis of amphibolites. Plots of Niggli 100 *mg*, *c*, and *al*−*alk* values (fig. 3), *mg* versus *c* values (fig. 4), and *al*−*alk* versus *c* values (fig. 5), Niggli's *mg* against Cr and Ni (fig. 6), and weight percent Na_2O+K_2O against weight percent SiO_2 (fig. 7) show quite convincingly that the central Beartooth amphibolites follow a differentiation trend similar to that of Karroo continental tholeiites, that they fall within the fields of mafic igneous rocks instead of sedimentary rocks, and that they are predominantly tholeiitic in composition. Similar techniques and comparable results have been obtained by Herz and Banerjee (1973) for Brazilian amphibolites, by Van Alstine (1971) for amphibolites near Salida, Colo., by Preto (1970) for British Columbian amphibolites, by Nelson (1969) for amphibolites in western North Carolina, and by van de Kamp (1969) for amphibolites from the southeastern Beartooth Mountains. In each of these studies, isochemical metamorphism has been assumed or implied.

Application of discriminant functions (Shaw and Kudo, 1965) to the problem of origin of the central Beartooth amphibolites did not yield a unique solution (table 3). Functions X_1 and X_2 of Shaw and Kudo, calculated from minor-element contents, indicate an igneous origin for nearly all of the amphibolites, whereas function X_3, based on major element contents, indicates a decidedly sedimentary origin for the amphibolites. However, the evidence for an igneous origin provided by field relations, Niggli values, alkali/silica ratios, and minor-element content strongly indicates that a process other than metasomatism of sedimentary parent rocks is required to explain major element geochemistry of the amphibolites.

In order to determine whether metasomatic exchanges might have occurred, the average concentrations of major and minor elements and fractionation trends of central Beartooth amphibolites are compared with those of other pertinent rock series. The most

TABLE 1.—*Chemical analyses and Niggli values of amphibolites, central Beartooth Mountains*
[Chemical analyses by S. D. Botts]

Sample	1	2	3	4	5	6	7	8	9	10	11	12	13	14	15
Chemical analyses (weight percent)															
SiO_2	54.1	62.6	52.2	59.5	56.9	54.1	51.6	58.4	54.4	46.3	54.3	55.2	57.5	53.7	61.9
Al_2O_3	18.2	14.9	16.6	15.3	17.3	17.5	15.9	17.6	14.9	17.9	15.4	16.1	9.9	17.2	16.3
Fe_2O_3	2.5	2.5	3.6	1.7	2.9	2.2	2.5	2.5	5.2	3.0	1.5	3.6	1.8	3.9	2.3
FeO	4.8	4.1	6.0	5.0	4.0	4.8	4.8	3.3	6.4	9.6	5.9	5.0	4.2	5.0	2.7
MgO	5.3	2.7	5.2	3.4	4.5	6.1	7.6	3.4	3.5	8.4	10.1	5.0	12.6	4.6	2.6
CaO	8.9	4.8	8.1	5.9	7.0	8.5	6.4	5.4	6.9	6.8	6.8	6.6	9.3	7.7	4.6
Na_2O	3.3	3.6	3.2	3.4	3.8	4.0	4.2	4.1	3.3	2.6	2.6	3.3	1.9	3.6	4.2
K_2O	.88	3.0	1.7	2.1	1.4	.95	2.2	2.3	1.5	2.4	.93	2.3	.86	1.3	1.5
H_2O+	1.1	1.0	1.1	.88	1.1	1.1	2.0	1.5	.73	1.9	1.2	1.6	.90	1.3	1.7
H_2O-	.13	.10	.08	.08	.10	.08	.12	.17	.03	.20	.06	.10	.09	.07	.13
TiO_2	.46	.92	1.1	1.2	.54	.46	1.2	.62	1.5	.80	.36	1.1	.24	.86	.41
P_2O_5	.12	.42	.50	.55	.10	.08	.65	.12	.51	.07	.07	.35	.97	.05	.25
MnO	.08	.11	.10	.10	.10	.07	.07	.13	.37	.11	.11	.10	.12	.07	.18
CO_2	.08	.03	.01	.02	.07	.01	.02	.03	.06	.01	.08	.01	.01	.12	.04
Total	100	101	99	99	100	100	99	100	99	100	99	100	100	99	99
Niggli values															
al	28	30	25	29	29	27	24	33	25	24	23	28	14	29	36
fm	37	33	41	35	36	38	45	32	42	51	51	38	56	36	27
c	25	18	23	21	22	24	17	18	21	16	18	21	24	23	18
alk	10	19	11	15	13	11	14	17	12	9	8	13	6	12	19
si	143	217	137	195	165	140	132	186	155	103	135	161	139	152	232
k	.15	.36	.26	.29	.20	.14	.25	.27	.23	.38	.19	.31	.22	.19	.19
mg	.57	.43	.50	.48	.55	.61	.66	.52	.36	.55	.73	.58	.82	.55	.55

1. Amphibolite (S1337), mode in volume percent: quartz, 7.5; plagioclase, 63.7; biotite, 2.6; hornblende, 24.8; trace amounts calcite, allanite, epidote, opaque oxide.
2. Amphibolite (A348), mode in volume percent: quartz, 22.2; plagioclase, 34.9; microcline, 11.4; biotite, 12.7; hornblende, 15.7; trace amounts sphene, apatite, epidote, opaque oxide.
3. Amphibolite (A445), mode in volume percent: quartz, 6.4; plagioclase, 47.8; microcline, 2.0; biotite, 10.8; hornblende, 27.7; clinopyroxene, 1.5; trace amounts sphene, apatite, epidote, opaque oxide.
4. Amphibolite (A630), mode in volume percent: quartz, 16.3; plagioclase, 44.3; microcline, 2.9; biotite, 13.4; hornblende, 18.7; trace amounts sphene, epidote, zircon, apatite, opaque oxide.
5. Amphibolite (S1794), mode in volume percent: quartz, 10.3; plagioclase, 51.6; biotite, 8.9; hornblende, 20.8; epidote, 7.0; trace amounts muscovite, sphene, allanite, apatite, opaque oxide.
6. Amphibolite (A623), mode in volume percent: quartz, 2.0; plagioclase, 50.6; biotite, 5.6; hornblende, 39.7; epidote, 2.0; trace amount sphene.
7. Amphibolite (A613), strongly foliated; contains quartz, saussuritized plagioclase, chlorite, hornblende, sphene, and apatite; intensely altered.
8. Amphibolite (S1402); contains quartz, plagioclase, microcline(?), chlorite, hornblende, epidote; altered.
9. Amphibolite (S1580); contains quartz, plagioclase, microcline(?), biotite, hornblende, trace amount sphene.
10. Amphibolite (A146B); contains quartz, plagioclase, biotite, hornblende, clinopyroxene, trace amounts apatite, opaque oxide.
11. Amphibolite (A185), mode in volume percent: quartz, 4.3; plagioclase, 43.1; biotite, 4.7; hornblende, 45.1; chlorite. 1.5; trace amounts epidote, apatite, opaque oxide.
12. Amphibolite (A250), mode in volume percent: quartz, 11.7; plagioclase, 36.1; microcline, 2.9; biotite, 7.9; hornblende, 21.6; epidote, 16.6; pyroxene, 1.1; trace amounts sphene, chlorite, apatite, opaque oxide.
13. Amphibolite (S1755), mode in volume percent: quartz, 11.4; plagioclase, 16.4; biotite, 3.2; hornblende, 68.4; trace amounts epidote, opaque oxide.
14. Amphibolite (A373), mode in volume percent: quartz, 6.0; plagioclase, 46.1; microcline, 1.1; biotite, 8.3; hornblende, 33.3; epidote, 3.3; trace amounts muscovite, calcite, sphene, allanite, apatite, opaque oxide.
15. Amphibolite (S1795), contains quartz, saussuritized plagioclase, chloritized biotite, epidote, hornblende, trace amounts apatite, sphene.

logical parent for the amphibolites, if they are derived from mafic igneous rocks, would be one similar in composition to the mafic dikes and small intrusions of the area (Prinz, 1964; Mueller, 1971). The possibility that the amphibolites originated from the metamorphism of chemically similar graywackes (Rivalenti and Sighinolfi, 1969) is discounted because of the absence of evidence for the existence of such rocks in this terrane. Little, if any, similarity exists between the average major-element composition of central Beartooth amphibolite (table 4, col. 1) and undifferentiated Beartooth metadolerite (col. 7); the amphibolite contains larger amounts of SiO_2, Al_2O_3, Fe_2O_3, alkalis, and P_2O_5 and smaller amounts of FeO, MgO, MnO, TiO_2, and CaO. Most of the same dissimilarities exist in comparing average central Beartooth amphibolite (col. 1) and van de Kamp's (1969) average Beartooth amphibolite (col. 2). Furthermore, plots of both groups of

TABLE 2.—*Minor-element analyses and element ratios of amphibolites, central Beartooth Mountains*
[Quantitative spectrographic analyses by Chris Heropoulos, X-ray fluorescence analyses by B. P. Fabbi, fluorometric analyses by Roosevelt Moore and Joseph Budinsky]

Sample[1]	1	2	3	4	5	6	7	8	9	10	11	12	13	14	15
Quantitative spectrographic analyses (parts per million)															
Ba	230	740	880	1,060	360	210	2,700	520	700	550	250	790	135	420	280
Co	34	19	34	24	22	31	33	20	34	49	47	27	48	31	14
Cr	53	72	140	89	82	190	370	105	44	340	570	120	880	105	54
Cu	57	34	78	48	7	40	110	41	339	5	58	22	38	15	10
Ni	57	40	67	41	45	66	120	57	27	98	175	56	490	55	28
Sc	26	18	28	19	17	25	20	22	36	32	25	28	38	30	11
V	160	140	235	150	100	120	155	96	300	180	110	170	150	180	75
Zr	45	280	195	225	55	53	320	100	195	54	68	215	48	180	80
X-ray fluorescence analyses (parts per million)															
Rb	28	93	57	48	72	25	94	104	19	128	26	57	30	36	62
Sr	620	355	670	630	580	590	950	540	600	210	520	610	200	590	495
Spectrophotometric (Th) and fluorometric (U) analyses (parts per million)															
Th	2	8.2	3.7	8	4.8	2.1	2.4	0.3	3.4	0.8	3.9	8.4	3.1	8.4	6
U	.99	1.25	.95	.99	1.60	1.35	2.5	.55	.65	.31	.23	.31	.83	.59	.81
Ratios[2]															
Th/U	2.02	6.56	3.89	8.08	3	1.56	0.96	0.55	5.23	2.58	1.7	27.1	3.73	14.2	7.4
Rb/Sr	.05	.26	.09	.08	.12	.04	.1	.19	.03	.61	.05	.09	.15	.06	.13
K/Rb	261	268	247	362	161	316	195	184	658	155	296	335	237	300	202
K/Sr	12	70	21	28	20	13	19	35	21	95	15	31	36	18	25

[1] Sample descriptions given in table 1.
[2] Ratios for K/Rb and K/Sr recalculated from weight percent K_2O given in table 1.

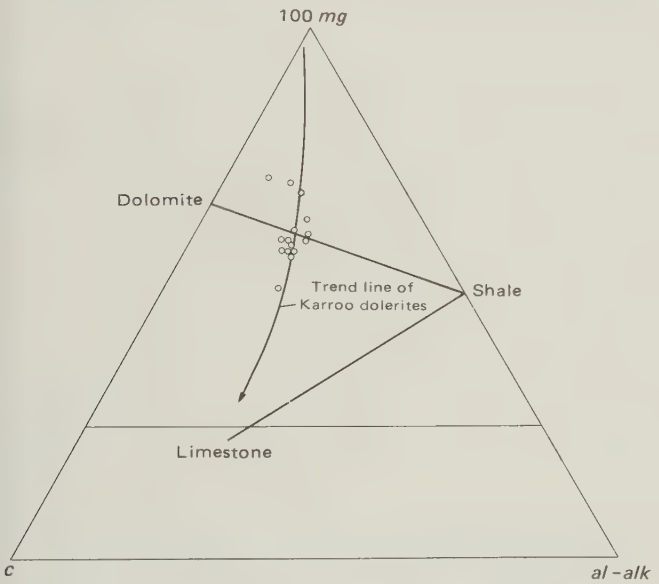

FIGURE 3.—Plot of Niggli 100 *mg*, *c*, and *al—alk* values for amphibolites from central Beartooth Mountains.

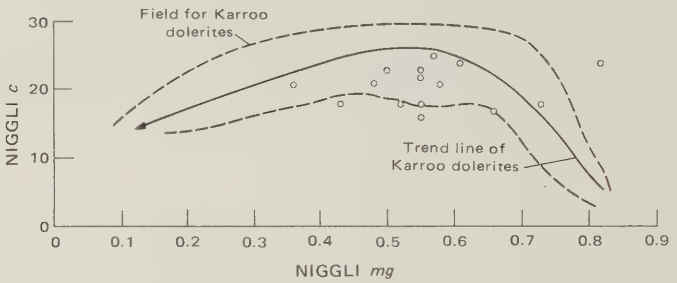

FIGURE 4.—Niggli *c* versus *mg* values for amphibolites from central Beartooth Mountains. Also shown are field and trend line for Karroo dolerites.

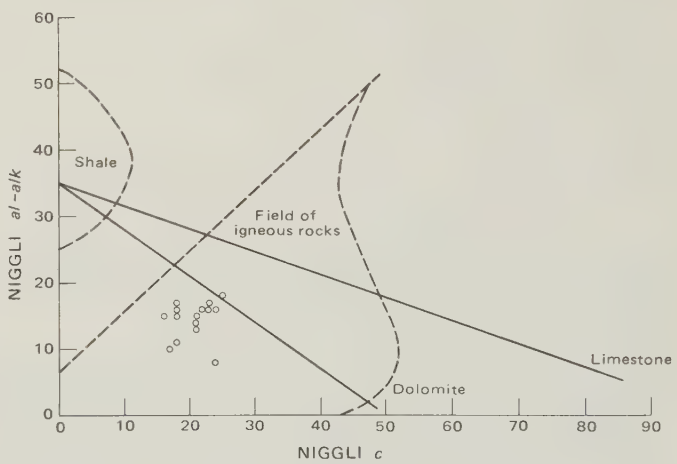

FIGURE 5.—Plot of Niggli *c* versus *al—alk* values for amphibolites from central Beartooth Mountains. The solid lines show trends of variation of shale-carbonate mixtures (van de Kamp, 1969, fig. 1*B*).

Beartooth amphibolites together with Prinz' (1964) fractionation trends for Beartooth metadolerites, on $(FeO+Fe_2O_3)$, (Na_2O+K_2O), and MgO and K_2O, Na_2O, and CaO diagrams (fig. 8), show that nearly three-fourths of van de Kamp's analyses closely follow the metadolerite trends, whereas amphibolites from the central Beartooth Mountains (this report) show no apparent relationship to these trends and appear to be deficient in total iron and to contain more K_2O relative to them. Comparison of modal plots of hornblende-

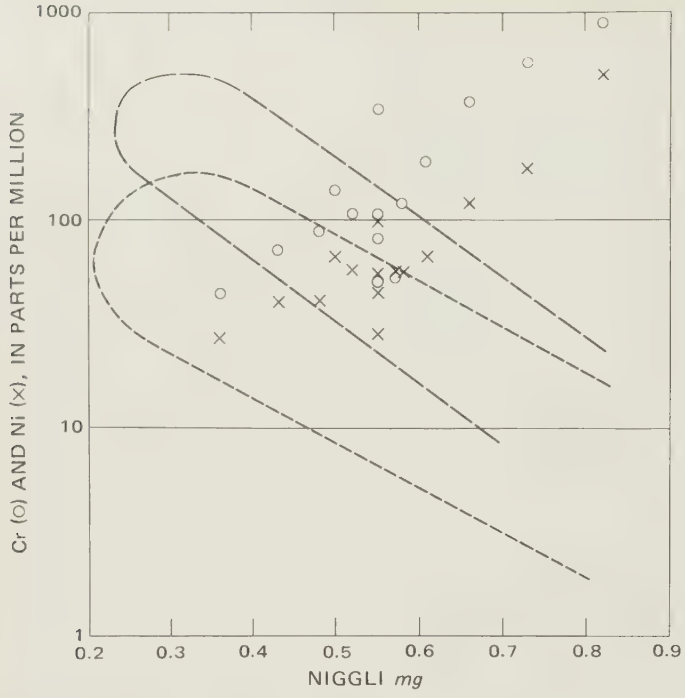

FIGURE 6.—Plot of Niggli *mg* versus Cr (○) and Ni (×) for amphibolites from central Beartooth Mountains. Long dashes outline shale-carbonate variation trend for Cr and *mg*; short dashes outline shale-carbonate variation trend for Ni and *mg* (van de Kamp, 1969, fig. 3*A*, 3*B*). Variations of Cr and Ni trend at nearly right angles to trends of sedimentary rocks.

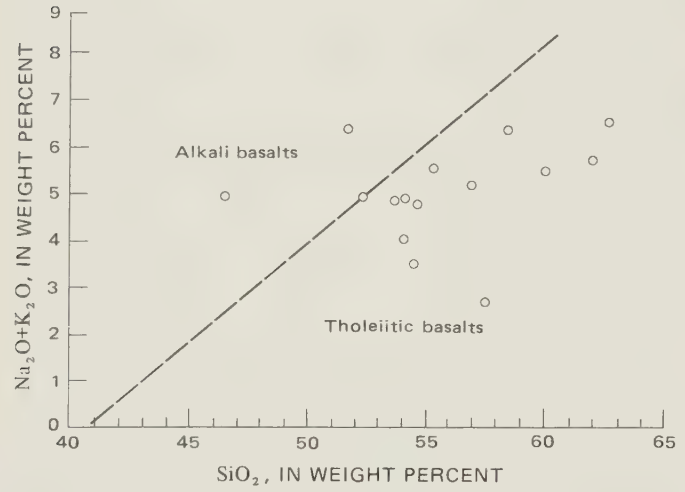

FIGURE 7.—Alkali-silica plot of amphibolites from central Beartooth Mountains; diagram modified from MacDonald and Katsura (1964).

rich rocks of this report (fig. 2) with those of similar rocks from the eastern and central Beartooth Mountains (Butler, 1969, p. 85, fig. 3) shows that rocks discussed in this report tend to be richer in total feldspar, suggesting either that they had a somewhat different, less mafic, igneous source or that potassium feldspar has been metasomatically introduced.

Average minor-element contents of central Beartooth amphibolites and various other rock groups are given in table 5. Central Beartooth amphibolites (col. 1) closely resemble amphibolites from throughout the Beartooth Precambrian terrane (col. 3), except possibly in terms of Zr content. On the other hand, more differences than similarities exist between central Beartooth amphibolites and southeastern Beartooth amphibolites (col. 2). Central Beartooth amphibolites

TABLE 3.—*Discriminant functions of amphibolites in which positive values denote igneous parentage and negative values denote sedimentary parentage*

[Discriminant functions derived by use of Shaw and Kudo (1965) formulas]

Sample [1]	[2]X_1	[3]X_2	[4]X_3
1	+8.90	+2.97	−6.72
2	−1.42	+1.35	−6.38
3	+3.21	+3.10	−1.61
4	+1.52	+1.84	−2.77
5	+2.93	+1.50	−8.35
6	+4.91	+2.75	−7.44
7	+.83	+2.47	−1.64
8	+1.94	+1.79	−13.25
9	+5.39	+3.54	−.57
10	+2.17	+3.95	−4.08
11	+4.35	+3.45	−5.44
12	+2.58	+2.71	−3.70
13	+2.06	+4.21	−1.68
14	+3.62	+3.07	−7.78
15	−.16	−.02	−10.64

[1] Sample numbers same as in table 1.
[2] $X_1 = -2.69 \log Cr - 3.18 \log V - 1.25 \log Ni + 10.57 \log Co + 7.73 \log Sc + 7.54 \log Sr - 1.95 \log Ba - 1.99 \log Zr - 19.58$.
[3] $X_2 = 3.89 \log Co + 3.99 \log Sc - 8.63$.
[4] $X_3 = 7.07 \log TiO_2 + 1.91 \log Al_2O_3 - 3.29 \log Fe_2O_3 + 8.48 \log FeO + 2.97 \log MnO + 4.81 \log MgO + 7.80 \log CaO + 3.92 \log P_2O_5 + 0.15 \log CO_2 - 15.08$.

TABLE 4.—*Average major-element compositions, in weight percent, of Beartooth amphibolites and various groups of igneous and sedimentary rocks*

	1	2	3	4	5	6	7
SiO_2	55.5	51.03	49.9	54.20	51.35	58.10	51.0
Al_2O_3	16.1	13.20	16.2	17.17	15.08	15.40	15.3
Fe_2O_3	2.8	3.20	3.0	3.48	2.55	4.02	2.2
FeO	5.0	7.46	7.8	5.49	8.33	2.45	8.9
MgO	5.7	10.13	6.3	4.36	7.57	2.44	8.6
CaO	6.9	8.58	9.8	7.92	9.39	3.11	9.7
Na_2O	3.4	2.65	2.8	3.67	2.25	1.30	2.4
K_2O	1.7	1.05	1.1	1.11	.87	3.24	.7
H_2O+	1.3	1.44	1.0	.86	1.21	5.00	----
H_2O-	.10	.01	----	-----	.10	----	----
TiO_2	.78	.69	1.6	1.31	.71	.65	.9
P_2O_5	.32	.10	.30	.28	.23	.17	.1
MnO	.12	.19	.17	.15	.21	----	.2
CO_2	.04	.15	----	-----	.01	2.63	----
Total	99.76	99.88	99.97	100	99.86	98.51	100
Oxidation ratio [1]	33.7	27.8	25.8	36.4	21.6	59.6	18.2

[1] $2Fe_2O_3 \times 100/2Fe_2O_3 + FeO$, values in mols (Preto, 1970, p. 780).

1. Average central Beartooth amphibolite, this report.
2. Average Beartooth amphibolite; calculated from data of van de Kamp (1969, table 2, p. 1130–1131).
3. Average continental tholeiite (Manson, 1967, table III, p. 222).
4. Average andesite (Nockolds, 1954, table 6, col. II, p. 1019).
5. Average amphibolite, eastern and central Beartooth Mountains, from Butler (1969, table 3, col. A, p. 89).
6. Average shale (Clarke and Washington, 1924, p. 32; total includes 0.64 percent SO_3, 0.05 percent BaO, and 0.80 percent C).
7. Parent magma, Archean metadolerites, Beartooth Mountains (Prinz, 1964, table 8, col. 1, p. 1243).

TABLE 5.—*Average minor-element compositions, in parts per million, and element ratios of Beartooth amphibolites and various groups of igneous and sedimentary rocks*

	1	2	3	4	5	6
Ba	655	411	500	250	700	285
Co	31	62	30	38	20	53
Cr	214	1,215	225	152	100	185
Cu	60	66	40	135	50	85
Ni	95	365	80	76	70	80
Sc	25	58	30	32	15	36
V	155	352	200	266	130	250
Zr	141	111	70	111	160	90
Th	4.4	12	---	2.7	[1] 10–13	---
U	.93	-------	---	.59	[2] 3.7	---
Rb	59	85	---	18	[1] 164	---
Sr	544	198	400	471	300	180
Th/U	5.90	-------	---	4.58	[1] 2–7	---
Rb/Sr	.14	.43	---	.04	.55	---
K/Sr	31	44	---	-----	-----	---

[1] Data from Rogers and Adams (1972a).
[2] Data from Rogers and Adams (1972b).

1. Average central Beartooth amphibolite; this report.
2. Average Beartooth amphibolite; calculated from data of van de Kamp (1969, table 2, p. 1130–1131).
3. Average of 97 semiquantitative spectrographic analyses of Beartooth amphibolites (Simons and others, 1973, table 4, col. 1, p. 47).
4. Average quartz-normative tholeiite (Prinz, 1967, table II, col. 1).
5. Average shale (Taylor, 1965, tables 6, 11, 15, 19, 21).
6. Geometric mean of 343 semiquantitative spectrographic analyses of mafic dikes, Beartooth area (Simons and others, 1973, table 5, p. 64).

are decidedly enriched (greater than 1.5 times) in potassium and related elements Ba, Rb, Th, and U as compared to average quartz-normative tholeiites (col. 4) and the very similar Beartooth mafic dikes (col. 6), whereas variations among other elements are not as systematic. The ferromagnesian-related minor-element content (Co, Cr, Ni) of central Beartooth amphibolites is consistently higher than that of average shale (col. 5), whereas that of the potassium-related elements Ba, Rb, Th, and U is consistently lower. The minor-element content of the central Beartooth amphibolites thus suggests that they most closely resemble quartz-normative tholeiites to which considerable amounts of potassium and related elements have been added, probably through potassium metasomatism.

Elliott (1973) showed that major changes in the composition of mafic rocks with increasing temperature of metamorphism include a decrease in Fe_2O_3, K_2O, P_2O_5, H_2O, and TiO_2 and an increase in FeO, CaO, and MgO, while Al_3O_3 and Na_2O remain essentially unchanged. Examples he chose were retrograde metamorphism of higher *P-T* gabbro to lower *P-T* amphibolite in south Norway and progressive metamorphism of amphibolites in the Adirondack Mountains of New York (Engel and Engel, 1962). Comparison of average central Beartooth amphibolite (table 4, col. 1) with Prinz' (1964) parent metadolerite (col. 7) shows that compositional changes similar to these, except perhaps the change in TiO_2, would have occurred if the amphibolite had been derived from the metadolerite.

Preto (1970) and Elliott and Cowan (1966) have calculated the oxidation ratios[1] of amphibolites and have compared the values with similar ratios calculated for various assemblages of associated intrusive and extrusive mafic rocks. The average oxidation ratio of several intrusive assemblages is 16.5 and of several extrusive assemblages is 26.8 (Elliott and Cowan, 1966, p. 323). If, as suggested by Chinner (1960), metamorphism does not appreciably affect the oxidation state of rocks, then the oxidation ratio of amphibolites must be inherited from their parent mafic rock (Preto, 1970, p. 780) and the parent rock can be determined.

Oxidation ratios of central Beartooth amphibolites range from 18.6 to 43.4 and average 33.7 (table 4, col. 1). These values tend to be considerably greater than the oxidation ratio of the Beartooth parent metadolerite, 18.2 (table 4, col. 7), which is typical of the values for intrusive mafic rocks. The average oxidation ratio of the amphibolites also seems to be considerably greater than that of extrusive rocks, but it is less than that of average shale (table 4, col. 6). It appears, therefore, that the metamorphic event which resulted in the formation of the amphibolites may not have occurred in a closed system relative to oxygen. Again, the concept of isochemical metamorphism does not seem to apply to the formation of amphibolites in the central Beartooth Mountains.

DISCUSSION

Variation diagrams using various combinations of Niggli values and major- and minor-element contents show that central Beartooth amphibolites follow compositional trends of mafic igneous rocks rather than those of sedimentary rocks and, therefore, have igneous parentage. However, the identity of the parent is problematical because metamorphism does not seem to have been isochemical. Chemically, the amphibolites most closely resemble average andesite (table 4, col. 4), but andesitic rocks are more commonly associated with calc-alkaline, or orogenic, suites and have not been reported from the Precambrian terrane of the Beartooth Mountains or from similar terranes elsewhere in the middle Rocky Mountains. In geologic terms, the most likely igneous parent is tholeiite, similar in composition to the metadolerite and quartz dolerite dikes present in the area, but amphibolites do not plot very close to fractionation curves for Beartooth metadolerite (fig. 8). If, however, potassium metasomatism accompanied the formation of the amphibolites, as suggested by the occurrence of paragenetically late microcline, a tholeiitic igneous parent can be envisioned. The enrichment of amphibolites in SiO_2, Al_2O_3, K_2O, and potassium-related minor elements, relative to metadolerite, strongly supports such a possibility.

[1] Mol $2Fe_2O_3 \times 100/(2Fe_2O_3 + FeO)$.

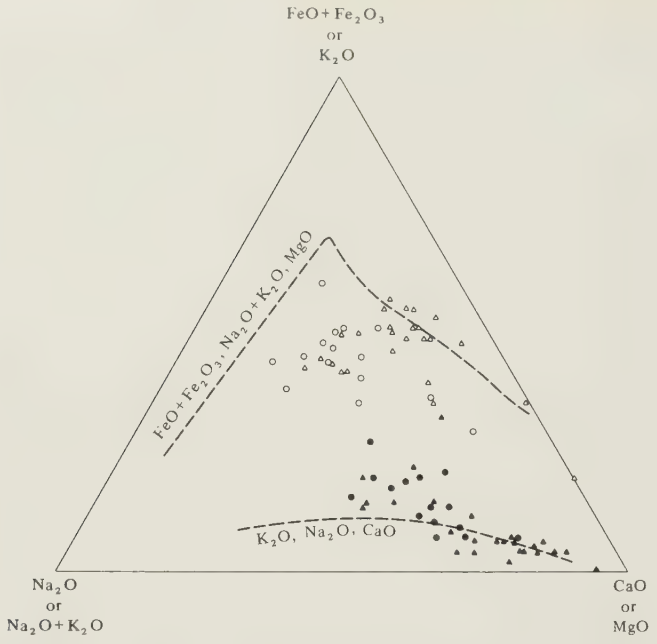

FIGURE 8.—Plots of central Beartooth amphibolites (circles) and southeastern Beartooth amphibolites of van de Kamp (1969) (triangles) on ($FeO+Fe_2O_3$), (Na_2O+K_2O), and MgO diagram (open symbols) and K_2O, Na_2O, and CaO diagram (closed symbols). The dashed lines represent fractionation trends of Beartooth metadolerites (Prinz, 1964).

REFERENCES CITED

Butler, J. R., 1969, Origin of Precambrian granitic gneiss in the Beartooth Mountains, Montana and Wyoming, *in* Igneous and metamorphic geology—A volume in honor of Arie Poldervaart: Geol. Soc. America Mem. 115, p. 73–101.

Chinner, G. A., 1960, Pelitic gneisses with varying ferrous/ferric ratios from Glen Cova, Angus, Scotland: Jour. Petrology, v. 1, p. 178–217.

Clarke, F. W., and Washington, H. S., 1924, The composition of the earth's crust: U.S. Geol. Survey Prof. Paper 127, 117 p.

Elliott, R. B., 1973, The chemistry of gabbro/amphibolite transitions in South Norway: Contr. Mineralogy and Petrology, v. 38, p. 71–79.

Elliott, R. B., and Cowan, D. R., 1966, The petrochemistry of the amphibolites of Holleindalen Greenstone Group, Jotunheimen, Norway: Norsk Geol. Tidsskr., v. 46, p. 309–326.

Engel, A. E. J., and Engel, C. G., 1962, Progressive metamorphism of amphibolite, northwest Adirondack Mountains, New York, *in* Engel, A. E. J., James, H. L., and Leonard, B. F., eds., Petrologic studies (Buddington Volume): Geol. Soc. America, p. 37–82.

Herz, Norman, and Banerjee, Subrata, 1973, Amphibolites of the Lafaiete, Minas Gerais, and the Serra do Navio manganese deposits, Brazil: Econ. Geology, v. 68, no. 8, p. 1289–1296.

Leake, B. E., 1964, The chemical distinction between ortho- and para-amphibolites: Jour. Petrology, v. 5, p. 238–254.

Manson, Vincent, 1967, Geochemistry of basaltic rocks—Major elements in basalts, p. 215–269, *in* Hess, H. H., and Poldervaart, Arie, eds., Basalts—The Poldervaart treatise on rocks of basaltic composition: New York, Interscience Pub., v. 1, 482 p.

MacDonald, G. A., and Katsura, T., 1964, Chemical composition of Hawaiian lavas: Jour. Petrology, v. 5, pt. 1, p. 82–133.

Mueller, P. A., 1971, Geochemistry and geochronology of the mafic rocks of the southern Beartooth Mountains, Montana and Wyoming: Houston, Tex., Rice Univ. Ph. D. thesis, 58 p.

Nelson, A. E., 1969, Origin of some amphibolites in western North Carolina, *in* Geological Survey research 1969: U.S. Geol. Survey Prof. Paper 650–B, p. B1–B7.

Nockolds, S. R., 1954, Average chemical compositions of some igneous rocks: Geol. Soc. America Bull., v. 65, p. 1007–1032.

Page, N. J, and Nokleberg, W. J., 1972, Genesis of mesozonal granitic rocks below the base of the Stillwater Complex in the Beartooth Mountains, Montana, *in* Geological Survey research 1972: U.S. Geol. Survey Prof. Paper 800–D, p. D127–D141.

Preto, V. A. G., 1970, Amphibolites from the Grand Forks quadrangle of British Columbia, Canada: Geol. Soc. America Bull., v. 81, no. 3, p. 763–782.

Prinz, Martin, 1964, Geologic evolution of the Beartooth Mountains, Montana and Wyoming—Pt. 5, Mafic dike swarms of the southern Beartooth Mountains: Geol. Soc. America Bull., v. 75, no. 12, p. 1217–1245.

——— 1967, Geochemistry of basaltic rocks—Minor elements in basalts, p. 271–323, *in* Hess, H. H., and Poldervaart, Arie, eds., Basalts—The Poldervaart treatise on rocks of basaltic composition: New York, Interscience Pub., v. 1, 482 p.

Rivalenti, Giorgio, and Sighinolfi, G. P., 1969, Geochemical study of graywackes as a possible starting material of para-amphibolites: Contr. Mineralogy and Petrology, v. 23, p. 173–188.

Rogers, J. J. W., and Adams, J. A. S., 1972a, Thorium, *in* Wedepohl, K. H., ed., Handbook of geochemistry: v. II–3, chap. 90.

——— 1972b, Uranium, *in* Wedepohl, K. H., ed., Handbook of Geochemistry: v. II–3, chap. 92.

Shaw, D. M., and Kudo, A. M., 1965, A test of the discriminant function in the amphibolite problem: Mineralog. Mag., v. 34, no. 268, p. 423–435.

Simons, F. S., Armbrustmacher, T. J., Van Noy, R. M., Zilka, N. T., Federspiel, F. E., and Ridenour, James, 1973, Mineral resources of the Beartooth Primitive Area and vicinity, Carbon, Park, Stillwater, and Sweet Grass Counties, Montana, and Park County, Wyoming, *with a section on* Interpretation of aeromagnetic data, by L. A. Anderson: U.S. Geol. Survey open-file rept., 207 p.

Taylor, S. R., 1965, The application of trace element data to problems in petrology, p. 133–213, *in* Ahrens, L. H., Press, Frank, Runcorn, S. K., and Urey, H. C., eds., Physics and chemistry of the earth: New York, McGraw-Hill, v. 6, 510 p.

Van Alstine, R. E., 1971, Amphibolites near Salida, Colorado, *in* Geological Survey research 1971: U.S. Geol. Survey Prof. Paper 750–B, p. B74–B81.

van de Kamp, P. C., 1969, Origin of amphibolites in the Beartooth Mountains, Wyoming and Montana—New data and interpretation: Geol. Soc. America Bull., v. 80, no. 6, p. 1127–1136.

Jour. Research U.S. Geol. Survey
Vol. 5, No. 1, Jan.–Feb. 1977, p. 61–81

GEOCHEMICAL AND PETROLOGICAL STUDIES OF A URANIFEROUS GRANITE FROM THE GRANITE MOUNTAINS, WYOMING

By J. S. STUCKLESS, C. M. BUNKER, C. A. BUSH,
W. P. DOERING, and J. H. SCOTT, Denver, Colo.

Abstract.—Granite rocks from the Granite Mountains, Wyo. have been proposed as the source of uranium deposits in the Crooks Gap, Gas Hills and Shirley Basin uranium districts, Wyoming. We have divided these granitic rocks into four units: (1) a biotitic phase which forms the dominant unit at the western end of the Granite Mountains, (2) a leucocratic phase which was found from 215 to 405 metres in drill hole GM–1, (3) silicified zones which crosscut the granitic rocks and form topographic highs, and (4) fractured zones, in drill hole GM–1, which seem to have been hydrothermally altered. The biotitic phase is hypidiomorphic-granular to xenomorphic-granular alkali granite with anomalously high contents of U (10 parts per million), Th (50 ppm), and Pb (50 ppm). Fission-track studies show that uranium is located in zircon, sphene, apatite, monzite, xenotime, biotite, chlorite, epidote, and magnetite; no intergranular uranium was found. The leucocratic phase is mineralogically similar to the biotitic phase, but contains less than half as much iron. It is xenomorphic granular and commonly contains rounded and retrograded garnets, which suggests that this phase is either metamorphic or contaminated with metamorphic materials. The leucocratic phase has anomalously high contents of U (8 ppm) and Pb (55 ppm), but has a low Th content (10 ppm). The silicified phase and fracture zones exhibit cataclastic and crystalloblastic textures and are highly variable in mineralogy. Potassium-bearing minerals are generally absent. Microcline is replaced by albite and (or) quartz, and biotite is replaced by clinozoisite. Uranium values may be anomalously high in the fracture zones. One sample contains 1100 ppm radium-equivalent uranium. In this and other uranium-rich samples from the fracture zones, the uranium is associated with iron oxides which commonly fill microfractures. According to our model and currently available data, an alkali granite is the best crystalline source rock for uranium, especially if it is unmetamorphosed and rapidly exposed to near-surface conditions for the first time when a favorable basin existed nearby.

Previous researchers (Rosholt and Bartel, 1969; Rosholt and others, 1973) have documented a Cenozoic uranium loss from the granite of the Granite Mountains, Wyo. Surface samples and core samples recovered from depths of 30–50 metres were shown to be approximately 80 percent deficient in uranium relative to the radiogenic daughter products ^{206}Pb and ^{207}Pb. Rosholt and Bartel (1969) calculated an average uranium loss from the granite of 20 grams per kilogram. They concluded that the granite had lost 1,000 times the uranium reserves plus production in Wyoming and therefore the granite was the most probable source rock for the uranium deposits in the surrounding districts.

In this current study we recovered core samples to a depth of 405 m in order to determine (1) the maximum depth of uranium leaching, (2) whether uranium has been reconcentrated at depth in Cenozoic time, (3) the geochemical and petrologic characteristics of the granite, and (4) the possible sites of and mechanisms for uranium loss. In this paper we concentrate on the geochemical and petrologic characteristics of this uraniferous granite.

Acknowledgments.—We are indebted to the U.S. Energy Research and Development Administration (formerly Atomic Energy Commission) for providing neutron-neutron, natural gamma, magnetic susceptibility, gamma-gamma, and electrical logs of drill-hole GM–1. Sample preparation was done by Gerry Cebula, Jack Groen, Norman Lewis, and Carol Gent. Sulfur and iron analyses were made by Leon Groves. We wish to thank Z. E. Peterman and R. A. Hildreth for use of their unpublished maps of the western end of the Granite Mountains.

GEOLOGIC BACKGROUND

The Cenozoic geology of the Granite Mountains has been compiled by Love (1970) and the Precambrian geochronology has been reported by Peterman, Hildreth, and Nkomo (1971), Nkomo and Rosholt (1972), and Rosholt, Zartman, and Nkomo (1973). The lower Precambrian rocks can be subdivided into three major groups: amphibolite-grade metamorphic rocks, granitic rocks, and diabase dikes. These rocks form the core of the Granite Mountains and are exposed as a west-

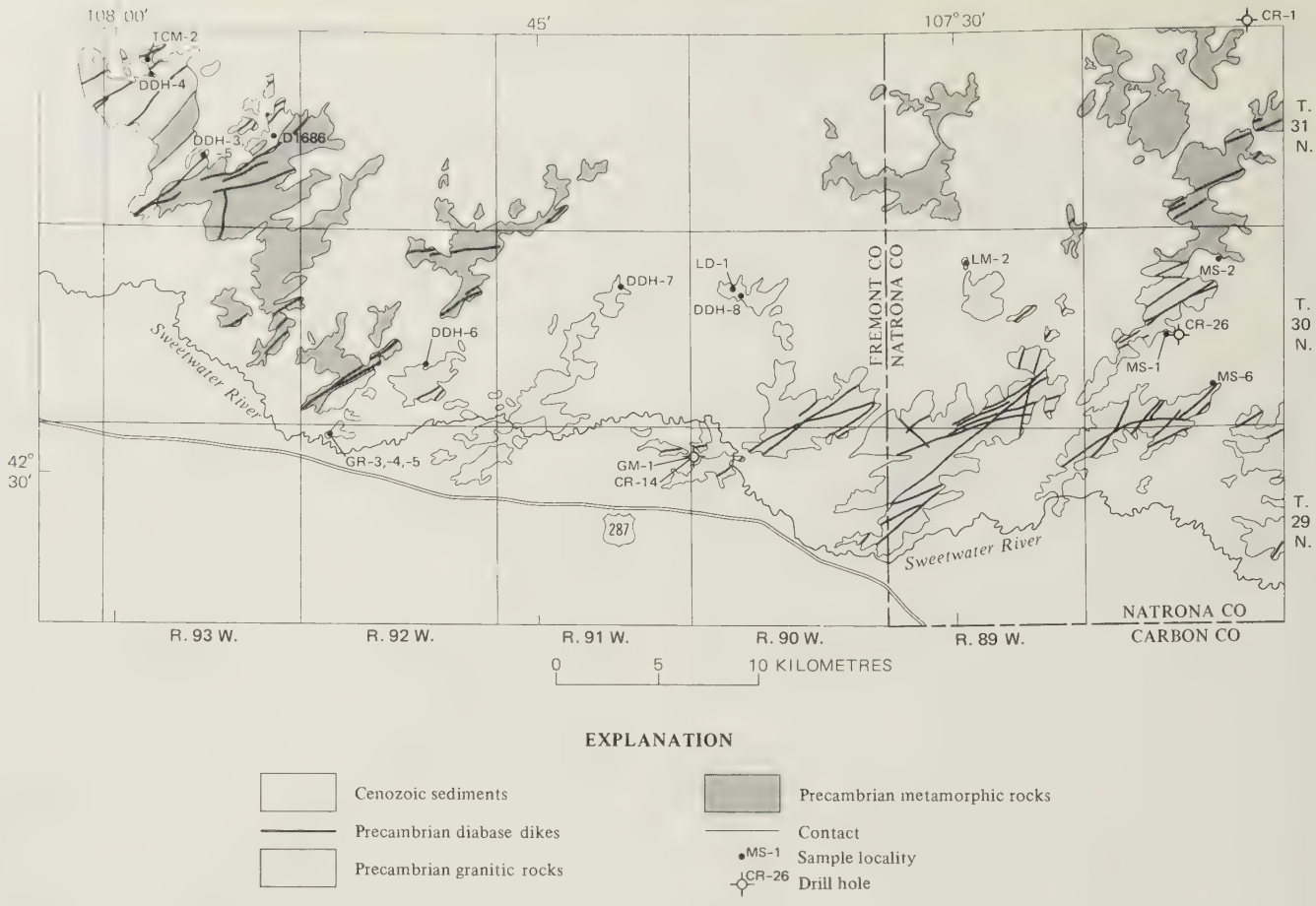

Figure 1.—Generalized Precambrian geology of the western end of the Granite Mountains and sample localities. Geology from Z. E. Peterman and R. A. Hildreth (unpub. data, 1974).

northwest-trending fault block which is approximately 105 kilometres long.

The metamorphic rocks crop out along the northwestern corner of the Granite Mountains and, in general, the foliation and outcrop patterns both strike to the northeast. The metamorphic rocks are bounded along a nearly east-west line to the north of the granite and strike east to northeast. These rocks are dominantly coarse- to fine-grained biotite-quartz-feldspar paragneisses and orthogneisses that contain both plagioclase and potassium feldspar; migmatites and augen gneisses are common, particularly near the contact with the granite. Small elongate bodies of amphibolite, nephritic jade and serpentinite constitute a minor proportion of the metamorphic assemblage, and are peneconcordant with the major structures and lithologic contacts in the metamorphic rocks. Peterman, Hildreth, and Nkomo (1971) reported a Rb-Sr whole-rock age of 2925±80 million years for the gneissic rocks and Nkomo and Rosholt (1972) reported a Pb-Pb isochron age of 2950±120 m.y. for a suite of similar rocks from the same area.

Granite rocks form the main mass of the Granite Mountains. We have divided the granite into leucocratic, biotitic phases, and silicified and fracture zones. Of these units, only the biotitic phase and silicified zones have been recognized in outcrop. The units penetrated by drill holes were the biotitic and leucocratic phases and the fracture zones. Most of the outcrops at the western end of the Granite Mountains are formed by a medium- to coarse-grained biotitic granite which is light gray and at a few localities exhibits a weak foliation. A reddish, coarse-grained biotite granite crops out along the northwestern and northern edges of the Granite Mountains (loc. TCM–1 and CR–1, fig. 1). Both localities are separated from the main granitic mass by outcrops of metamorphic rock, but outcrops at the second locality are too small to be shown on the scale of figure 1. Aplites are commonly associated with the reddish granite, but are rare in the main mass of granitic rocks.

In outcrop the granitic rocks are generally massive and exhibit large exfoliation surfaces such as at Lankin Dome. Locally the rock may be highly jointed or

contain small discontinuous iron-stained zones of decomposed rock. Small veinlets and isolated large crystals of microcline are ubiquitous throughout the main granite body.

Potassium-poor silicified zones form a volumetrically minor portion of the granitic rocks, but are conspicuous because of their resistance to erosion. These silicified zones are extremely leucocratic and form blocky outcrops. Potassium feldspar is strongly altered or absent. Biotite is partly to wholly replaced by opaque oxides, chlorite, clinozoisite, and (or) epidote. In outcrop the silicified zones occur as tabular bodies, concordant with horizontal jointing in the granite or as north to northeast trending dikelike zones that cut the granitic rocks. The tabular bodies act as cap rocks for many of the exfoliated granite knobs and may be as thick as 25 m. The dikelike zones often form ridges or ridge crests. These zones are generally a few tens of metres wide and less than a kilometre long, but one silicified zone is nearly a kilometre wide. Contacts between the granite and silicified zones may be either sharp or gradational.

The age of the main granitic mass has been determined as 2610±70 m.y. by a Rb-Sr whole-rock isochron (Peterman and others, 1971) and as 2790±80 m.y. by a Pb-Pb whole-rock isochron (Rosholt and others, 1973). A lead isotopic analysis of one sample from the reddish, coarse-grained biotite granite collected north of the main granitic mass (loc. CR–1; fig. 1) was concordant with the Pb-Pb whole-rock isochron for the metamorphic rocks suggesting that this phase may be older than the main granitic body (Nkomo and Rosholt, 1972).

Diabase dikes are common throughout the Granite Mountains, but constitute only a small fraction of the total rock exposed. The dikes generally strike northnortheast to east. Most are several tens of metres wide; exposures range in length from 1 to 5 km. A sample from one of the larger dikes yielded a K-Ar whole-rock age of about 2600 m.y. (Z. E. Peterman, oral commun., 1974).

No other Precambrian rocks are known to crop out in the Granite Mountains, but geochronologic evidence suggests that the area was affected by a minor thermal event that probably occurred between 1500 and 1700 m.y. (Nkomo and Rosholt, 1972; Rosholt and others, 1973; Z. E. Peterman, oral commun., 1974). Igneous and metamorphic rocks of this age have been reported in Precambrian terrains west and south of the Granite Mountains (Catanzaro, 1967; Hills and Armstrong, 1974).

During the Paleozoic and Mesozoic Eras the Precambrian rocks were buried beneath sediments, mainly of shallow marine and continental origin, as epicontinental seas transgressed and regressed over the region. Evidence of this period of sedimentation has been largely removed from the immediate area of the Granite Mountains, but at the extreme western edge of the mountains the metamorphic rocks are overlain by a Cambrian sandstone (Love, 1970).

From the close of the Cretaceous until the close of the Eocene the Granite Mountains were subjected to profound uplift with concomitant downwarping of the adjacent basins. Rapid erosion of the up-faulted block during early Eocene time produced a boulder conglomerate over 600 m thick to the south of the Granite Mountains (Love, 1960). During middle to late Oligocene, topography became more subdued and the granitic rocks were partly buried by rhyolitic volcanic ash and arkosic debris (Love, 1970). Burial of the mountains continued until after middle Pliocene time when the area was downwarped and downfaulted (Love, 1960). In the late Pliocene or early Pleistocene, epeirogenic uplift along reactivated Tertiary fault systems produced the partly exhumed, subdued topography of the present day Granite Mountains (Rosholt and others, 1973).

ANALYTICAL PROCEDURES

Sample selection

Samples analyzed during this study include outcrop samples considered to be representative of units not found in the deep drill hole (GM–1); they include shallow core samples obtained with a portable Wenke drill, intermediate-depth samples taken from three 60-m drill cores obtained from the Wyoming Geological Survey, and a series of samples from the 410-m hole (GM–1) drilled by the U.S. Geological Survey (Stuckless, 1975). The core from the deep drill hole was analyzed at approximately 3-m intervals by choosing 30- by 5-centimetre core samples that megascopically appeared to be representative of a 3-m interval.

Sample preparation

One-fourth of the core selected for analysis was cut with a diamond saw, and removed and saved as a permanent record. Surfaces of the remaining core were cleaned with emery paper and rinsed with distilled water before crushing. Surface samples were treated in a similar fashion, with the exception that weathered and altered surfaces were broken off and discarded before crushing.

Coarse crushing (−32 mesh) was accomplished using a mechanical steel-jaw crusher and disc pul-

verizer. Equipment was thoroughly cleaned between samples. Approximately 10 g of the coarse-crushed material was split off and ground to −100 mesh using a diamonite mortar and pestle. Fine crushing (−200 mesh) was done in an agate mortar and pestle. Mortars and pestles were cleaned with quartz sand between samples. The finely crushed material was used for X-ray fluorescence analyses and isotopic studies.

X-ray fluorescence

X-ray fluorescence was used for the Rb, Sr, Pb, Fe, and S analyses. The X-ray fluorescence units were operated at 75 kilovolts and 46 milliamperes to obtain the maximum line intensities for Rb, Sr, and Pb. Fe and S were analyzed at 50 kV and 37.5 mA. The targets and analyzing crystals used were W and LiF for $K\alpha$ of iron, Cr and PET for $K\alpha$ of sulfur, Mo and LiF for $K\alpha$ of rubidium and strontium, and Mo and LiF for $L\alpha$ of lead. The $L\alpha$ line was used for lead to minimize interference from other elements.

Iron and sulfur values were obtained by comparing the count-rate data to a calibration curve based on mixtures of reagent grade $FeSO_4 \cdot 4H_2O$ and $CaCO_3$. Precision for the iron analyses is ±8.0 percent (2σ), and precision for the sulfur analyses is estimated at ±15 percent (2σ) with detection limit of 5 parts per million.

Lead values were obtained by comparing X-ray count for the unknowns with X-ray count rates for 26 whole-rock samples from the Granite Mountains for which lead has been determined by isotope dilution. Standards were analyzed with each set of unknowns, and a total of 103 determinations were used to generate a calibration curve by a least-squares regression. The mean variance of the known samples about the calibration curve is 4.5 ppm. For most samples the resulting error is less than ±10 percent, but for a few low-lead samples the resulting error is as high as ±25 percent.

Rubidium and strontium were analyzed during a single run and the data were reduced by use of a computer program that corrects for absorption effects. This is accomplished by measuring the molybdenum Compton scattered peak which is inversely proportional to the mass absorption coefficients (Reynolds, 1967). Precision (±2σ) for the reported results is 8.2 percent for Sr, 9.2 percent for Rb, and 3.1 percent for the Rb/Sr ratio. The greater precision for the Rb/Sr ratio is obtained because the matrix effects on Rb and Sr X-radiation are essentially identical in any given sample (Doering, 1968).

Gamma-ray spectrometry

Radioelement (K, RaeU, and Th) contents of the samples were measured by gamma-ray spectrometry. Approximately 600 g of the −32 mesh material were sealed in 15-cm-diameter plastic containers. The containers were placed on a sodium iodide crystal, 12.5 cm in diameter and 10 cm thick. The gamma radiation penetrating the crystal was sorted according to energy by the associated electronic devices and the resulting spectra were stored in a 100-channel memory. The spectra were interpreted with the aid of a linear-least-squares computer method which matches the spectrum from a sample to a library of radioelement standards; the computer method for determining concentrations is a modification of a program written by Schonfeld (1966). Standards used to reduce the data include the USGS standard rocks, New Brunswick Laboratories standards, and several samples for which uranium and thorium concentrations had been determined by isotope dilution and mass or alpha spectrometry.

Uranium contents were measured indirectly by measuring the ^{226}Ra daughters (^{214}Bi and ^{214}Pb) to obtain radium-equivalent uranium (RaeU) values. Isotopic equilibrium between these daughters and ^{226}Ra was accomplished by allowing the sealed sample containers to sit for at least 21 days prior to the analyses. Radium-equivalent uranium is the amount of uranium required for secular isotopic equilibrium with the ^{226}Ra and its daughters measured in a sample. Thirty determinations of uranium by delayed neutron and isotope-dilution methods show that 73 percent of the samples may have recently (within the last 100,000 years) undergone a nearly uniform average daughter-product loss (or uranium gain) of 15 percent between masses 238 and 226, and 20 percent of the samples suggest variable amounts of daughter-product gain (or uranium loss). Unless otherwise stated, all uranium concentrations referred to in this paper are radium-equivalent values.

Although thorium is also measured from daughter products (^{212}Bi, ^{212}Pb, and ^{208}Tl), isotopic disequilibrium is improbable because of the short half-lives of the daughter products of ^{232}Th. Therefore, the daughter products measured are considered to be a direct measurement of thorium. Potassium is determined from the ^{40}K constituent which is radioactive and directly proportional to the total potassium.

All the radioelement data reported in this paper are based on replicate analyses. The coefficient of variation for the accuracy of these data, when compared to isotope-dilution and flame-photometry analyses, is about ±2 percent for RaeU and Th and about ±1

percent for K. These percentages are in addition to minimum standard deviations of about 0.05 ppm for RaeU and Th and 0.03 percent for K.

Petrographic techniques

Modal data reported in this paper are based on a minimum of 500 point counts on a 1-millimetre grid of standard 20-mm by 40-mm thin sections. The large standard deviations reported for average modes (table 1) of the various rock types reflect the inhomogeneities on a thin-section-sized scale and the coarse grain size of the rocks. Uranium distribution was determined by irradiating polished thin sections with a neutron dose of approximately 2×10^{16} n/cm^2. Induced fissions of ^{235}U were recorded in a low uranium muscovite detector which had a background fission-track density of 1,200 tracks/cm^2. The muscovite detector was pressed flat against the polished thin section during irradiation and subsequently etched for 15 s in 48 percent HF to develop the induced fission tracks. Black areas in the photographs of the detectors shown in figures 2–6, correspond to uranium concentrations greater than 30 ppm.

Geophysical logging

The neutron-neutron log was made within the drill hole by measuring backscattered neutrons from a ^{252}Cf source located 25 cm from the detector. Depth of penetration into the wall of the hole varies with the rock-moisture content; for low-porosity rocks such as those penetrated by GM–1, it is approximately 60 cm (Pirson, 1963). Because hydrogen has a large capture cross section for neutrons, the presence of water in pores and fractures or in the form of structural water, particularly that associated with alteration minerals (Nelson and Glenn, 1975) in the rock, reduces the number of backscattered neutrons, and thus this log is a good indicator of hydrous zones intersected by the drill hole.

The resistivity log was made with a short-normal electrode configuration having an electrode spacing of 40 cm between the current and potential electrodes. The depth of investigation is approximately twice this spacing or 80 cm. The resistivity log is a good indicator of porosity because electrical current flows through rock principally by ionic conduction in the saline water in pores and fractures. However, current flow may be augmented by the presence of metallic minerals.

Induced polarization (IP) measurements are made by applying electrical current to the rock adjacent to the borehole, then turning the current off and measuring the decay voltage for a short period of time. The response of the IP log in GM–1 is expressed as a percentage which is determined by dividing the integrated decay voltage (multiplied by 100) by the voltage measured while the current is turned on. During IP logging, current is applied to two electrodes, one on the borehole probe and the other grounded at the surface. Voltage is measured between two other electrodes, one on the probe and the other grounded at the surface. Depth of investigations is approximately twice the spacing between the current and voltage electrodes on the probe. In our measurements the probe-electrode spacing was 10 cm, and therefore the depth of investigation was about 20 cm.

Although IP anomalies are usually caused by concentrations of sulfide or oxide minerals (Zablocki, 1966), anomalies may be caused by high concentrations of saline water in fractures or large amounts of clay alteration minerals in igneous rocks. If sulfides are oxidized to sulfates, IP anomalies are greatly reduced or lost altogether.

The natural gamma-ray log detects gamma rays with energies from about 0.1 to 3 million electron volts. These energies are emitted principally by ^{226}Ra daughters in the uranium series, ^{228}Ra daughters in the ^{232}Th series, and ^{40}K. These daughter products may not be in equilibrium with their parent isotopes, particularly in zones of fractured rock where migration of radon may be important, and therefore gamma-ray anomalies do not necessarily represent high contents of uranium or thorium. The natural gamma-ray log has a background count rate of 2,000 c/s (counts per second) from an artificial isotope contained in the detector for gain stabilization of spectral response. The true count rate for the natural radiation in the granite can be determined by subtracting 2,000 c/s from the observed count rate.

Magnetic susceptibility of the core was measured in the laboratory at approximately 30 cm intervals. The magnetic susceptibility of a rock is a measure of the volumetric concentration of ferromagnetic minerals, chiefly magnetite, pyrrhotite, and ilmenite (Zablocki, 1966). The measured value has been empirically related to magnetite content by the formula $K=1940V^{0.47}$, where K is magnetic susceptibility in micro-cgs units and V is magnetite concentration in volume percent (Mooney and Bleifuss, 1953).

RESULTS

Petrography

Average modes for the biotitic and leucocratic phases of the granite encountered in drill hole GM–1 are given in table 1 together with ranges for modes of the fracture and silicified zones. Chemical analyses

for granite samples obtained from the three holes drilled for the U.S. Air Force (CR–1, CR–14, CR–26, fig. 1) are reported in table 2 together with Nockold's (1954) average alkali granite. Plagioclase is dominantly sodic oligoclase to albite, and therefore the calcic plagioclase to alkali feldspar ratio is much less than 0.3. Thus, on the basis of either chemical (Nockold, 1954) or modal data (Streckeisen, 1967), these rocks fall in the alkali granite class.

TABLE 1.—*Modal data for the major granitic rock units recognized in the Granite Mountains, Wyo.*

[Data are given in volume percent ±1σ, or as observed ranges for the highly variable units. Tr., trace; ---, not found]

	Biotitic phase [1]	Leucocratic phase [2]	Range of modes: Silicified zones [3]	Range of modes: Fracture zones [4]
Quartz	31.2±7.7	37.7± 8.5	18–61	17–38
Plagioclase	29.9±4.9	29.0± 6.7	8–58	49–77
Microcline	33.5±5.9	30.3±10.5	0–9	0–12
Biotite	4.9±5.3	1.2± 1.2	0–7.8	0–0.8
Epidote	.6±0.5	.1± 0.3	1.6–29	0.7–5.3
Opaques	.3±0.4	.2± 0.4	Tr.–0.9	0.2–2.3
Muscovite	.3±0.4	1.1± 0.2	Tr.–1.7	0–0.8
Accessories	.3±0.5	.1± 0.5	Tr.–2.0	Tr.–0.8
Garnet	---	.4± 0.4	---	---

[1] Biotitic phase based on 28 thin sections. Chloritized biotite is included with biotite.
[2] Leucocratic phase based on 19 thin sections. Chloritized biotite included with biotite.
[3] Range of modes for 6 samples from the silicified zones. Clinozoisite is included with epidote, and chloritized biotite is included with biotite.
[4] Range of modes for 6 samples from the fracture zones. Chlorite, probably originally biotite, varies from 3.4 to 0.7.

TABLE 2.—*Rapid-rock analyses for samples from the Granite Mountains, Wyo.*

[Data given in weight percent. Analyses of Wyoming samples by H. Smith using single solution procedure described in Shapiro (1967). Average alkali granite from Nockold (1954). ---, not reported]

	Hole No. and depth in metres: CR–1 41.00	CR–14 57.24	CR–26 60.66	Average alkali granite
Chemical analyses				
SiO_2	73.1	72.0	74.8	73.86
Al_2O_3	13.2	14.0	13.8	13.75
Fe_2O_3	1.4	.90	.50	.78
FeO	1.1	1.2	1.1	1.13
MgO	.80	.53	.24	.26
CaO	1.7	.48	1.1	.72
Na_2O	3.1	3.3	3.1	3.51
K_2O	4.4	5.6	5.2	5.13
H_2O+	.40	.46	.29	.47
H_2O-	.12	.08	.06	
TiO_2	.54	.15	.11	.20
P_2O_5	.08	.06	.04	.14
MnO	.03	.02	.02	.05
CO_2	.01	.01	.03	---
Total	100	99	100	100
CIPW normative minerals				
Q	33.7	29.6	33.6	32.2
C	.46	1.83	1.23	1.4
or	26.0	33.5	30.6	30.0
ab	26.3	28.3	26.1	29.3
an	7.86	1.95	4.99	2.8
en	2.00	1.34	.60	.6
fs	.03	1.23	1.46	1.1
mt	2.03	1.32	.72	1.2
il	1.03	.29	.21	.5
ap	.19	.14	.09	.3
cc	.02	.02	.07	.3
Salic total	94.31	95.16	96.77	95.16
Femic total	5.30	4.38	3.15	3.70

Modes for the major minerals in the biotitic and leucocratic phases are not significantly different although the leucocratic phase seems to be slightly richer in quartz. Modal amounts of mafic and trace minerals are generally lower in the leucocratic phase, but the muscovite content is greater. Fracture zone and the silicified zone samples are characterized by a marked decrease in abundances, relative to adjacent samples, or a total absence of biotite and potassium feldspar. These minerals appear to have been replaced by chlorite, clinozoisite (or epidote), magnetite, albite, and (or) quartz. In the fracture zones the plagioclase becomes more sodic, whereas in at least one silicified zone the plagioclase becomes more calcic.

The biotitic phase is a hypidiomorphic-granular to xenomorphic-granular, medium-grained, alkalic granite containing subequal amounts of quartz, plagioclase, and microcline. Biotite is the most abundant mafic mineral and is commonly partly altered to chlorite and (or) epidote (fig. 2*A*). Biotite is invariably poikilitic with fine-grained, nearly opaque, radioactive mineral grains which are surrounded by pleochroic halos. A semiquantitative electron-microprobe determination (P. W. Weiblen, oral commun., 1975) suggests that this mineral was originally sphene. Biotite, chlorite, and epidote are generally surrounded by a thin opaque rim, probably hematite. Other accessory minerals are zircon, apatite, monazite, and fine-grained muscovite and clays included within the plagioclase. These alteration minerals make the plagioclase appear cloudy in plane-polarized light (fig. 2*A*). Quartz exhibits an undulose extinction. Myrmekite was noted in a few thin sections.

The distribution of uranium in the biotitic phase is shown in figure 2*B*. The uranium distribution is similar to that reported by Bowie, Simpson, and Rice (1973) for the Aberdeenshire granites. The highest concentrations of uranium occur in the accessory minerals zircon, sphene, and monazite; according to published analyses of several mineral separates they generally contain several hundred to a few thousand ppm uranium (Doe, 1970). These show up as black dots in the detector, the largest of which is a zircon located near the center of the upper edge of figure 2*B*.

The second highest concentrates of uranium occur in epidotes, apatites, and the opaque alteration products of the biotites and chlorites. The higher concentrations of uranium around the biotites are particularly well displayed at the lower left-hand corner

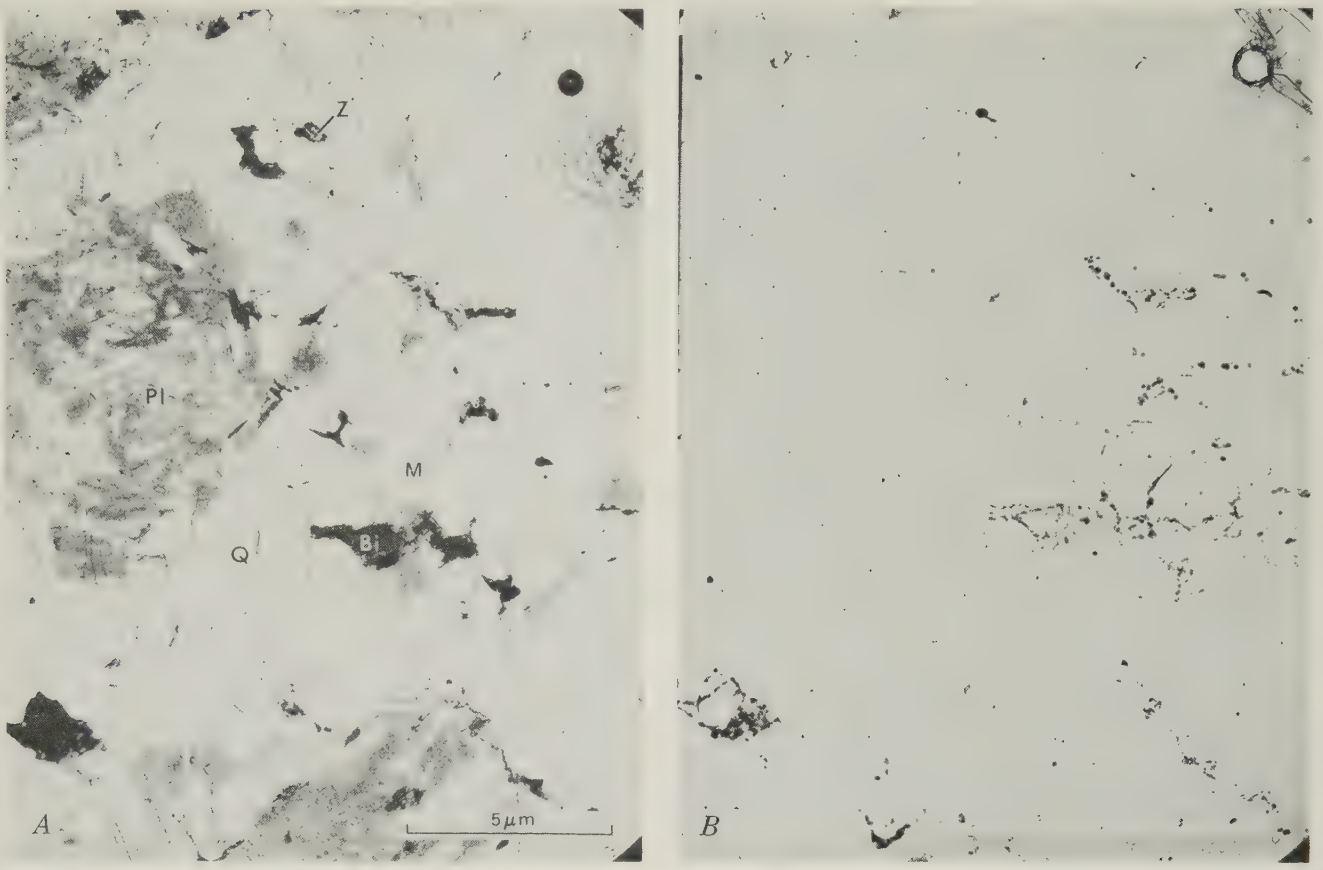

FIGURE 2.—Photomicrograph (plane-polarized light) of a biotitic-phase sample taken from 20.4-m depth (*A*) and uranium distribution in the sample (*B*). The dark circle in the upper right-hand corner of the photomicrograph and the clear circle in the detector are registration marks. RaeU content of the sample is 12.34 ppm. Q, quartz; Pl, plagioclase; Bi, biotite; M, microcline; Z, zircon.

and near the center of figure 2*B*. Although not clearly visible at the magnification used in figure 2*B*, biotite and chlorite contain 1–10 ppm U. When chlorite and biotite are intergrown, the chlorite generally contains more uranium. No evidence was found for measurable concentrations of uranium along intergranular boundaries or microfractures.

The leucocratic phase is typically medium grained and xenomorphic granular. Mutually sutured grain boundaries are common. Although quartz, plagioclase, and microcline are subequal in abundance for the average leucocratic phase, this phase is locally more inhomogeneous than the biotitic phase. These inhomogeneities (on the scale of 1 m or less) are reflected in the higher variability of potassium below the 220-m depth in GM–1 and the large 1σ for the modal data (table 1). Microcline commonly contains rounded crystals of quartz that are in optical continuity with one another. In many samples alteration of plagioclase to sericite and clays (fig. 3*A*) is more poorly developed than in the biotitic phase, but myrmekite is more common. Triple-grain boundaries of 120° and undulose extinction are common for quartz.

Biotite crystals are generally similar to those in the biotitic phase, but are less abundant (table 1) in most samples of the leucocratic phase. More of the biotite has been replaced by chlorite in the leucocratic phase; in a few samples, cleavage traces (001) in the chlorite occur at an angle to those in the biotite. Several intervals of core in the leucocratic phase are garnetiferous, with garnet attaining a maximum modal amount of 3.5 percent. In all samples, garnet is partly retrograded to chlorite and muscovite.

The distribution of uranium in the leucocratic phase is shown in figure 3*B*. Almost all the uranium is contained in the accessory minerals zircon and sphene, but small amounts are also contained within the biotite and chlorite. The apparent large size of the radioactive inclusions in the biotite (fig. 3*B*) are due to minor relief between the thin section and muscovite detector during irradiation. The general background content of uranium in the leucocratic phase (fig. 3*B*) is much

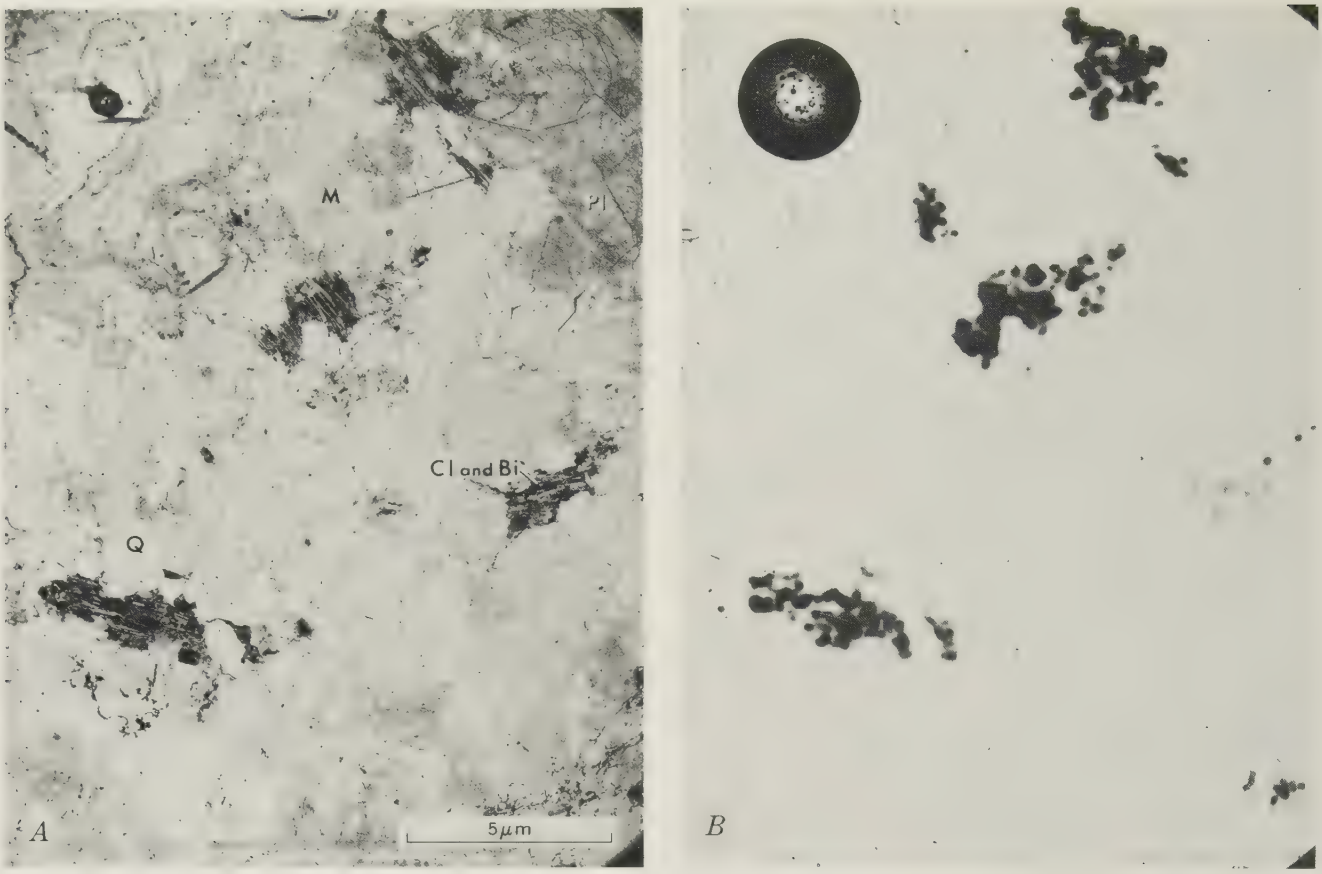

FIGURE 3.—Photomicrograph of a leucocratic-phase sample taken from 259.7-m depth (*A*) and uranium distribution in the sample (*B*). Registration marks are in the upper left-hand corner. RaeU content of the sample is 10.09 ppm. Q, quartz; Pl, plagioclase; Cl, chlorite; Bi, biotite; M, microcline.

lower than that in the biotitic phase (fig. 2*B*). This is true even when the leucocratic-phase contains nearly twice as much uranium as the biotitic-phase sample. As in the biotitic phase, there is no noticeable concentration of uranium along intergrain boundaries or microfractures.

Samples from the fracture zones which cut both the biotitic and leucocratic phases in drill hole GM–1 exhibit a well to poorly developed cataclastic to crystalloblastic texture with both subparallel and anastomosing cracks (fig. 4*A*). Several samples show a pseudomorphic replacement of microcline by albite which results in chessboard albite (Starkey, 1959; Gilluly, 1933). The large Carlsbad-twinned crystal that extends from the center of figure 4*A* to the left edge of the photograph is a microcline that has been partly replaced by albite. Most samples also have fine-grained intergrowths of albite and quartz. Biotite is generally replaced by stilpnomelane or chlorite, some of which is vermicular in form. Modal amounts of quartz, plagioclase, and microcline are highly variable as shown by the ranges given in table 1. Most samples exhibit a complete destruction of microcline. Some samples contain modal pyrite and (or) increased amounts of magnetite. The magnetite crystals are commonly surrounded by rutilated quartz.

Uranium distribution in the fracture zones differs sharply from either the biotitic or leucocratic phases. Uranium is strongly concentrated along fractures that have been filled with an opaque material, possibly hematite or a hydrous iron oxide. The same uranium-rich opaque material appears to have formed large (0.5 mm) anhedral grains in or near the anastomosing cracks (fig. 4*B*). A similar uranium enrichment was noted in the "shatter zone" of the Criffel granodiorite, Scotland (Bowie and others, 1973), where the uranium content was more than an order of magnitude greater than the normal background level for the granodiorite; the only uraniferous minerals found were hematite and its alteration products.

Two samples, collected just above zones of uranium enrichment in drill hole GM–1, contain large (0.5 cm) euhedral to subhedral crystals of magnetite that are mantled by thin rims or cut by veins of a uranium-

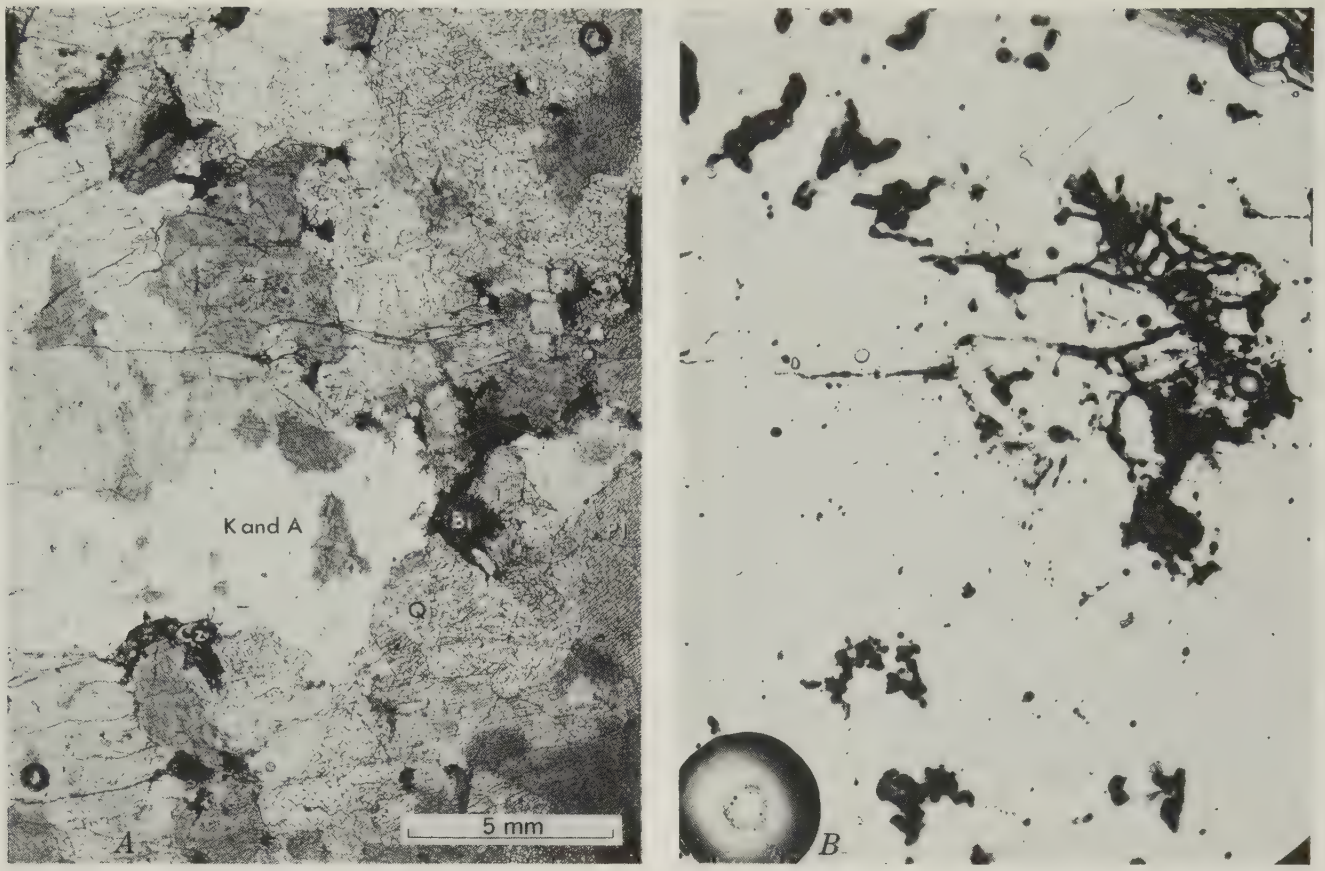

FIGURE 4.—Photomicrograph of a fracture-zone sample taken from 49.4-m depth (*A*) and uranium distribution in the sample (*B*). Registration marks are in the upper right-hand and lower left-hand corners. RaeU content of the sample is 52.91 ppm. Q, quartz; Pl, plagioclase, K and A, microcline and albite; Cz, clinozoisite; Bi, biotite.

rich mineral (fig. 5). This mineral appears to be an epidote. Within the magnetite crystal, slightly translucent red areas, probably hematite, exhibit minor enrichments of uranium (≈20 ppm). Both these two samples and the actual fracture zones contain the common uranium-bearing accessory minerals zircon, sphene, and epidote. The uranium content of chlorite in the fracture zones appears to be much higher than in either the biotitic or leucocratic phase. The general background level for uranium is also greater.

The silicified zones are generally crystalloblastic (fig. 6*A*) and highly variable in mineralogic composition. The range for modal data within the silicified phase is given in table 1. Quartz and (or) andesine have been introduced at the expense of microcline in all samples. In most samples, epidote, clinozoisite, or chlorite, together with an opaque phase, possibly hematite, have replaced biotite (fig. 6*A*). Much of the apparent variability in mineralogy of this phase is due to three samples collected perpendicular to the strike of the silicified zone (locs. Gr–3 through GR–5, fig. 1). Here, the contact with the biotitic phase is gradational and samples collected within 2 m of the biotitic phase contain appreciable amounts of microcline and (or) biotite. Some samples from the silicified zones contain several percent sphene and (or) apatite.

The distribution of uranium in the silicified zones (fig. 6*B*) is similar to that in the leucocratic phase. The background level of uranium is very low and most of the uranium is confined to altered biotites and accessory minerals. Epidote that has replaced biotite in the crystal just below the center at the left edge of figure 6*A* has preserved the poikilitic inclusions of radioactive accessories (dark points in the detector, fig. 6*B*); it also shows the high concentration of uranium in the opaque minerals, possibly hematite, around the epidote.

Chemical and logging data

Data for selected major and trace elements are given in table 3 and graphically presented as a function of depth in figures 7 and 8. Averages of these data for the four granitic rock units are presented in table 4. Chemical data for the surface samples and a few

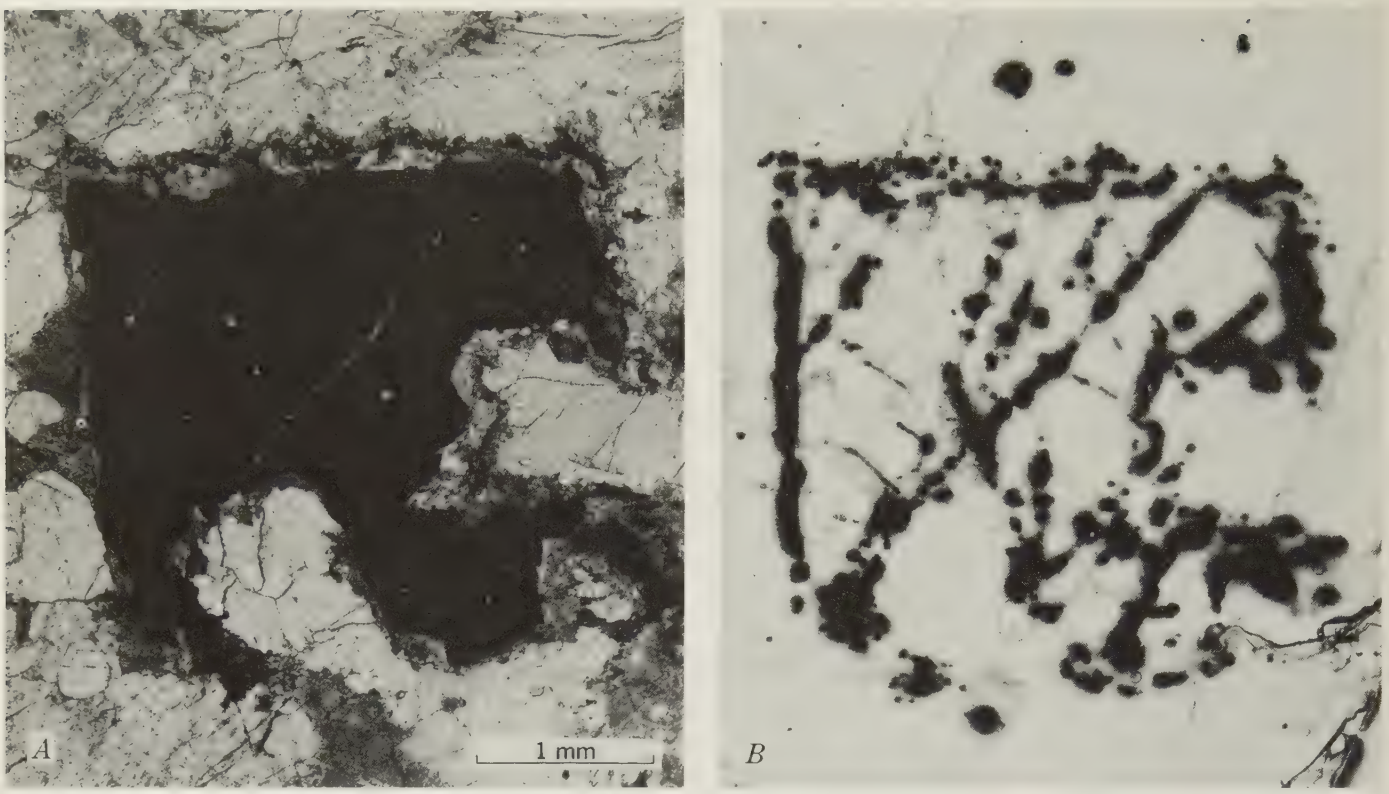

FIGURE 5.—Photomicrograph of a euhedral magnetite crystal (*A*) collected from a depth of 129.4 m. The fission-track distribution (*B*) shows that the magnetite is rimmed and cut by a uranium-rich phase, probably epidote. A few areas which show as gray in the detector appear to correspond to hematite replacement of the magnetite.

samples from the U.S. Air Force drill holes are presented in histogram form for comparison (fig. 9).

The lower trace-mineral and mafic-mineral contents in the leucocratic phase are readily apparent in fig. 7 near the 220-m depth. The average thorium content of the leucocratic phase is approximately a factor of 5 lower, and uranium, iron, and strontium are decreased by a factor of two, relative to the biotitic phase. The count rate for the neutron-neutron log is about 5 percent greater in the leucocratic phase than in the biotitic phase suggesting that this phase of the granite contains less water (both structural and nonstructural) and may partly reflect the lower mica content (table 1).

Fractures encountered in the drill hole are schematically shown in figure 7. Sections of core with fewer than one fracture per 60 cm are shown as unfractured. Sections of highly sheared rock (fracture zones) are shown by heavy lines. Sections with several breaks, but no alteration on the fracture surfaces are shown by short lines. Comparison of the fractures with the neutron-neutron log shows that most of the fractures contain water. Fracture zones (such as 47–52 m and 58–63 m) are usually limonitic, and plagioclase is chalky in appearance. A few of the fractured areas, such as 225–240 m and 265–270 m, exhibit only minor alteration and have only slightly lower neutron-neutron count rates. Both of these observations suggest less hydrous conditions than the fracture zones. The average porosity of the unfractured rock as estimated from the neutron-neutron log is less than 5 percent.

An alternate estimate of porosity can be obtained from the electrical resistivity log (fig. 7). The highest resistivities obtained in drill hole GM–1 approach 10,000 ohm-metres. Assuming water salinities similar to those of water in granites at the Nevada Test Site (Scott and others, 1967), the highest resistivities probably represent porosities as low as 0.1 percent. The large sections of high resistivity demonstrate the tightness of the granite in the vicinity of drill hole GM–1 and yet isotopic work in progress (Nkomo and Stuckless, 1975) suggests that even these sections of granite have lost uranium. Low resistivities that do not correspond to low neutron-neutron count rates probably reflect increased concentrations of sulfides, oxides, clays or the greater wall depths investigated by the resistivity tool.

Uranium (RaeU) concentrations exhibit the widest variations (1.6–1,100 ppm) among the tested parameters, and correspond closely to the natural gam-

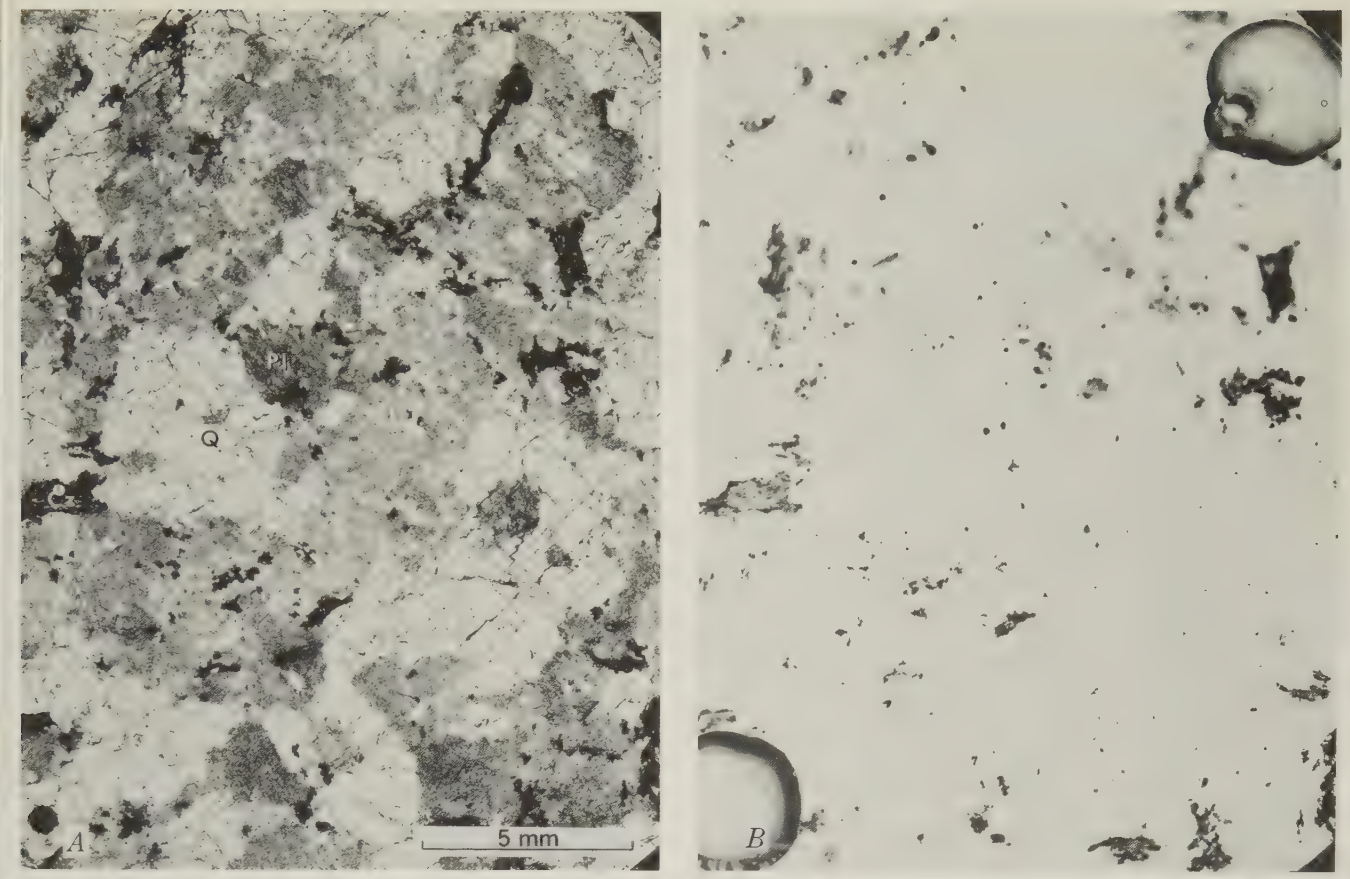

FIGURE 6.—Photomicrograph of silicified-zone sample MS–1 (*A*) and uranium distribution in the sample (*B*). Registration marks are in the lower left-hand and upper right-hand corners. Uranium content of the sample is 13.04 ppm. Q, quartz; Pl, plagioclase; Cz, clinozoisite.

ma log. A few narrow zones (for example, 130 m) intersected by the drill hole that had a high gamma count rate were seemingly not sampled for the laboratory measurements, and in other zones (for example, 350 m) only part of the high uranium rock was included with the laboratory sample. One sample high in uranium collected at 87.17 m was apparently not in secular equilibrium with the daughter products in the lower part of the decay chains.

Because uranium exhibits the greatest variability, correlation between uranium and other less mobile elements reported in this paper is unlikely. Even the Th/U ratio which typically ranges from 3 to 5 for most granitic rocks (Rogers and Adams, 1969) is highly variable (table 4). This ratio is generally between 5 and 10 in the biotitic phase and less than 3 for the leucocratic phase. Comparison of the natural gamma radioactivity and neutron-neutron logs shows that many of the fractures are greatly enriched in uranium and (or) gamma-emitting daughter products of the decay chain. This relationship is best displayed in the fracture zone from 47 to 52 m (figs. 7, 8).

The thorium content of the core samples is fairly constant for the upper 62 m, ranging from 53.9 to 73.4 ppm, but is more variable at depth (fig. 7) for the remainder of the biotitic phase and for surface samples of the biotitic phase (fig. 9). A few marked thorium lows in the core samples collected between 60 and 200 m correspond to minor increases in the neutron-neutron count rate. These sections of the core may represent mixtures of the biotitic and leucocratic phases. There is supporting evidence for this at 172 m where small, partly resorbed garnets are visible in hand specimen and the thorium content of the nearest sample is relatively low (table 3). Within the biotitic phase, thorium varies most consistently with iron (correlation coef, $R=0.86$). The general correlation between thorium and iron is apparently preserved even in the fracture zone 47–52 m in spite of the evident destruction of magnetite between 50 and 51 m. The correlation between iron and thorium is lower in the leucocratic phase ($R=0.50$) where the thorium content drops by an order of magnitude.

TABLE 3.—*Selected elemental data for samples from the Granite Mountains, Wyo.*

[N.D., not detected; ___, not found]

Sample	Depth (m)	RaeU (ppm)	Th (ppm)	Fe (%)	S (ppm)	Sr (ppm)	Rb (ppm)	K (%)	Pb (ppm)
GM-1	2.68	9.94	61.33	1.58	9.0	106	236	4.41	60.7
	5.58	10.58	62.40	1.53	9.0	106	232	4.64	51.4
	8.50	6.71	57.74	1.29	< 5	103	225	4.48	53.9
	11.46	4.95	54.49	1.34	5.4	105	231	4.78	54.0
	13.05	7.86	64.53	1.47	< 5	95.3	213	4.43	49.1
	17.43	6.83	59.11	1.60	< 5	97.8	232	4.41	49.2
	20.42	12.34	64.29	1.60	89.5	94.8	215	4.32	55.6
	23.32	8.66	64.88	1.47	12.7	88.4	227	4.38	51.4
	26.30	20.81	57.69	1.51	34.6	88.5	222	4.33	49.6
	29.20	10.89	59.32	1.53	9.0	88.7	223	4.44	53.5
	32.37	5.40	65.95	1.60	56.6	86.0	207	4.30	60.2
	35.33	4.94	61.12	1.51	14.5	88.6	2.9	4.53	50.6
	38.34	8.90	65.57	1.64	< 5	86.8	210	4.54	53.8
	41.33	7.70	69.10	1.64	< 5	85.9	207	4.55	54.8
	44.32	18.58	63.21	1.53	7.2	95.5	218	4.64	48.0
	46.91	9.04	57.52	1.12	12.7	113.1	145	3.15	45.2
	48.43	7.64	61.72	1.29	228	43.5	32.9	.42	28.6
	48.95	20.47	66.59	1.38	93.1	74.4	107	2.04	33.3
	49.44	52.91	56.78	.98	159	89.3	199	4.43	48.2
	50.11	1103.0	55.0	1.06	78.9	88.4	262	2.95	54.0
	50.75	106.9	56.05	1.15	< 5	38.4	18.7	.11	25.5
	51.79	62.14	62.03	1.32	12.7	93.9	2.8	4.31	46.4
	52.46	19.53	53.93	1.34	18.2	90.6	226	4.48	46.9
	55.60	7.55	55.15	.99	12.7	50.2	115	2.49	30.0
	58.49	7.59	37.60	.60	10.9	33.2	11.4	.21	28.0
	61.63	4.92	73.42	1.38	16.4	47.8	25.0	.54	18.5
	63.98	4.44	37.87	.80	27.3	71.0	176.7	3.65	37.7
	65.50	3.18	19.91	.56	20.0	87.6	221	4.48	43.1
	69.77	6.87	49.69	1.32	14.5	87.7	220	3.84	43.8
	72.63	6.00	43.29	.93	12.6	95.5	240	4.71	49.0
	75.62	19.70	66.26	1.42	49.3	99.2	276	5.13	64.2
	78.58	23.20	65.53	1.64	21.8	92.0	235	4.19	58.4
	81.62	16.01	46.88	1.06	49.4	89.9	246	5.25	57.2
	84.34	13.20	46.54	1.16	23.7	85.2	219	4.36	49.8
	87.17	45.51	45.11	0.93	14.9	92.9	246	4.56	50.5
	90.16	21.47	39.55	.91	14.5	97.3	267	5.25	50.8
	93.15	7.18	25.00	.56	5.4	89.7	202	4.39	46.6
	96.13	4.68	41.72	1.05	12.7	90.4	217	4.25	50.5
	99.24	5.71	37.49	1.04	9.0	99.1	216	4.09	46.8
	102.29	10.32	60.38	1.38	12.7	101	230	4.62	47.4
	105.34	11.10	49.71	1.21	5.4	100	181	3.64	42.8
	108.23	10.08	58.36	1.42	5.4	95.1	218	4.46	47.4
	111.22	7.41	40.06	.99	< 5	86.4	190	3.62	42.1
	114.24	10.97	68.91	1.64	38.3	98.3	239	4.39	45.7
	117.26	10.06	66.05	1.51	9.0	97.2	244	4.43	43.9
	120.24	7.64	61.39	1.42	16.4	93.5	218	4.27	47.1
	123.29	9.18	67.20	1.51	20.0	90.1	225	4.28	40.4
	126.31	7.36	65.55	1.51	18.2	83.2	190	4.33	43.7
	129.36	6.15	13.31	.86	12.7	82.3	179	4.16	36.2
	131.64	8.60	61.37	1.47	20.0	64.7	181	3.95	38.2
	134.78	6.85	69.45	1.68	78.5	32.4	88.6	1.17	61.1
	138.11	12.35	63.43	1.51	12.7	82.0	218	4.39	47.1
	141.12	8.19	64.68	1.55	16.4	78.2	202	4.18	42.8
	143.99	10.05	58.64	1.47	155	30.8	70.8	1.20	29.0
	147.04	7.98	62.09	1.42	166	23.1	48.6	.59	22.3
	150.08	7.30	68.23	1.21	< 5	80.3	182	5.05	45.6
	153.10	5.70	55.61	1.21	12.7	76.7	179	4.57	44.5
	155.66	10.16	68.23	1.53	9.0	63.0	108	2.45	36.6
	158.98	4.01	20.98	.60	10.9	66.5	166	4.43	42.7
	161.85	6.04	58.67	1.45	27.3	44.4	95.8	2.42	32.8
	164.71	15.60	31.29	1.01	41.9	63.8	122	3.09	33.3
	167.58	13.55	54.51	1.08	155	75.2	135	3.72	53.6
	171.27	7.49	16.76	.43	96.8	77.8	104	2.95	34.5
	174.10	6.51	59.38	1.32	85.8	85.8	144	3.25	44.2
	177.36	5.40	24.60	.43	69.3	82.0	136	3.91	57.9
	179.74	23.73	39.45	.86	23.7	75.5	134	3.63	45.2
	182.82	11.72	39.30	1.04	56.6	89.5	143	3.62	45.8
	185.99	9.57	47.34	.82	40.1	42.1	46.9	1.26	40.4
	188.95	10.84	56.33	1.42	5.4	77.8	150	4.02	51.2
	193.15	10.38	58.47	1.23	192	71.9	154	4.37	58.4
	198.64	10.84	55.58	1.51	12.7	75.6	159	4.04	58.6
	201.38	12.40	59.85	1.25	141	68.2	164	3.95	55.6
	204.13	12.09	42.77	1.25	217	51.2	146	3.41	53.1
	207.54	10.79	15.59	.86	27.3	38.1	90.8	2.84	54.0
	210.50	17.77	52.03	1.51	< 5	39.3	157	3.58	58.4
	213.51	8.51	31.46	1.08	9.0	44.9	163	3.85	51.3
	216.47	22.72	24.26	1.68	63.9	45.4	239	5.05	63.9
	219.73	5.56	11.94	.39	27.3	43.4	240	6.15	62.1
	225.40	4.78	14.36	.47	32.8	15.5	179	4.87	51.4
	228.20	5.83	4.06	.33	27.3	23.5	192	5.36	57.3
	230.95	20.27	7.35	.46	85.8	9.0	21.7	.46	21.0

TABLE 3.—*Selected elemental data for samples from the Granite Mountains, Wyo.*—Continued

Sample	Depth (m)	RaeU (ppm)	Th (ppm)	Fe (%)	S (ppm)	Sr (ppm)	Rb (ppm)	K (%)	Pb (ppm)
GM-1	232.87	4.15	3.42	.65	41.9	27.3	199	5.60	67.2
	235.25	7.91	3.26	.25	21.8	27.8	210	5.61	53.6
	239.70	9.77	10.66	.64	12.7	35.6	154	3.77	43.5
	240.56	5.92	11.13	1.12	23.7	39.2	183	3.49	47.7
	245.30	5.90	7.57	.20	16.4	31.4	171	3.88	42.0
	248.26	23.47	14.88	.54	133	39.8	183	3.50	46.3
	251.77	3.01	1.31	.35	34.6	20.9	183	4.67	49.8
	254.33	4.46	5.71	.48	71.4	20.3	145	4.11	33.9
	256.70	2.20	5.97	.33	34.6	41.7	205	6.25	71.1
	259.66	10.09	5.09	.55	111	35.1	167	5.04	58.9
	263.74	3.41	5.98	.18	16.3	35.9	140	4.73	58.8
	266.37	5.00	4.05	.52	< 5	19.9	58.8	2.03	44.7
	269.57	4.27	1.88	.23	5.4	32.1	120	4.02	42.6
	271.82	4.47	3.89	.65	12.7	25.0	134	4.60	47.0
	275.60	13.28	10.06	1.12	21.8	35.3	120	3.85	62.1
	278.43	3.29	8.98	.67	31.0	32.2	121	3.62	58.5
	281.24	39.64	4.97	.71	82.2	32.8	130	4.27	49.7
	284.62	8.88	10.90	.76	16.4	37.9	105	3.07	45.3
	287.70	4.90	5.63	.38	< 5	36.8	91.7	2.94	44.8
	290.72	20.93	9.69	1.55	9.0	34.8	77.8	1.56	78.1
	293.52	6.07	4.91	.46	23.7	32.5	65.0	2.22	45.3
	298.73	18.96	12.25	.69	20.0	31.5	88.5	3.16	57.7
	301.78	5.68	9.72	.33	12.7	36.7	125	4.15	50.8
	304.07	4.03	9.19	.53	< 5	34.5	125	4.67	60.2
	308.52	4.07	8.43	0.68	< 5	28.9	161	5.90	72.3
	311.57	8.40	11.76	.76	9.0	32.6	92.3	3.41	55.4
	314.89	3.05	5.17	.22	16.4	35.0	109	4.10	56.1
	319.49	6.51	11.78	.52	23.7	50.1	115	4.05	44.1
	322.54	5.75	14.51	.58	12.7	44.0	114	4.09	47.0
	326.11	5.71	13.68	1.25	16.4	31.3	95.0	3.42	68.5
	329.03	31.99	12.64	1.16	38.3	30.6	80.5	2.72	63.1
	332.08	4.35	12.18	1.16	5.4	22.9	18.8	.49	27.1
	335.07	3.56	10.03	.64	< 5	40.7	145	4.71	64.1
	338.79	18.88	6.49	.20	71.2	43.9	92.8	3.22	53.9
	342.08	12.31	10.89	.79	12.7	45.9	127	4.44	76.9
	345.10	20.03	13.63	.82	10.9	43.1	113	3.58	64.9
	350.12	40.96	11.81	.48	25.7	37.7	94.2	3.13	49.5
	352.53	4.54	14.99	.83	16.4	39.4	32.7	.59	41.9
	355.79	4.14	5.63	.15	5.4	30.3	83.9	2.83	45.3
	357.26	15.32	12.96	.37	214	29.9	98.9	3.39	54.2
	360.98	3.05	8.53	.33	< 5	28.1	105	3.98	55.4
	364.48	1.64	9.51	.39	< 5	37.3	120	4.26	60.4
	367.41	4.65	21.27	.77	5.4	38.7	103	3.56	58.1
	370.45	3.87	10.55	.49	< 5	41.9	104	4.00	56.9
	373.84	2.91	7.58	.71	9.0	45.9	113	4.07	54.8
	376.79	5.62	10.82	.58	16.4	42.3	87.3	3.26	58.7
	380.18	19.06	10.90	.65	12.7	45.1	119	4.47	60.8
	383.22	3.73	12.03	.19	20.0	44.6	134	5.03	58.2
	386.52	9.50	15.35	.61	7.2	43.2	117	3.96	57.3
	389.69	4.97	20.99	.81	5.4	44.3	117	3.95	51.5
	394.90	15.16	9.01	.38	82.2	39.6	90.7	3.50	41.9
	398.19	5.85	18.04	.54	12.7	39.3	106	3.82	58.6
	400.48	3.61	12.14	.31	23.6	43.6	131	4.76	59.2
	404.29	18.62	24.50	.61	12.7	49.1	131	4.37	54.6
	409.23	5.14	4.98	.47	12.7	41.2	133	4.30	58.2
MS-1	.0	13.04	43.93	.39	9.0	485	N.D.	.06	26.9
MS-6	.0	7.12	27.24	.25	16.4	329	26.1	.68	12.7
LD-1	.0	11.91	38.39	.30	9.0	463	N.D.	.06	22.3
LM-2	.0	9.60	7.57	1.08	20.0	636	2.9	.09	10.7
GR-3	3.	2.23	26.21	1.64	12.7	319	47.0	2.07	17.9
GR-4	3	7.91	17.44	1.06	16.3	425	25.7	0.78	9.1
GR-5	3	2.64	26.09	.19	5.4	709	31.6	.95	9.0
MS-2	0	.51	3.51	.27	< 5	107	149	5.31	27.6
TCM-2	0	2.97	19.67	2.42	12.7	520	107	2.78	53.6
D1686	0	2.14	27.72	---	---	83.8	166	3.73	40.22
CR-1	30.33	3.73	36.67	---	---	254	136	3.75	35.89
	41.00	20.0	40.6	1.90	9.0	298	134	3.9	22.2
	46.79	3.37	34.68	---	---	289	115	3.31	19.0
DDH-3	6.71	1.56	11.48	1.27	9.0	109	138	---	66.2
DDH-4	1.22	2.14	19.33	1.47	10.9	299	82.8	2.27	38.8
DDH-5	3.60	1.98	25.99	1.26	5.4	112	149	4.12	51.1
DDH-6a	1.07	2.05	21.65	.77	9.0	249	103	3.59	36.3
DDH-6b	1.16	2.07	23.88	1.91	12.7	195	100	3.96	42.0
DDH-7	.37	2.87	44.59	1.27	< 5	107	136	3.82	50.0
DDH-8	2.74	6.91	34.58	1.18	< 5	100	203	4.54	64.3
CR-26	30.24	4.94	42.49	---	---	117	169	4.50	58.6
	50.29	3.75	41.75	---	---	124	176	4.86	67.4
	60.66	4.72	50.2	1.25	5.4	126	155	4.15	45.8
CR-14	30.72	10.50	69.07	---	---	87.5	241	4.31	52.0
	47.95	10.50	64.48	---	---	95.6	223	4.62	51.2
	57.24	12.2	66.0	1.53	9.0	84.6	204	4.50	46.8

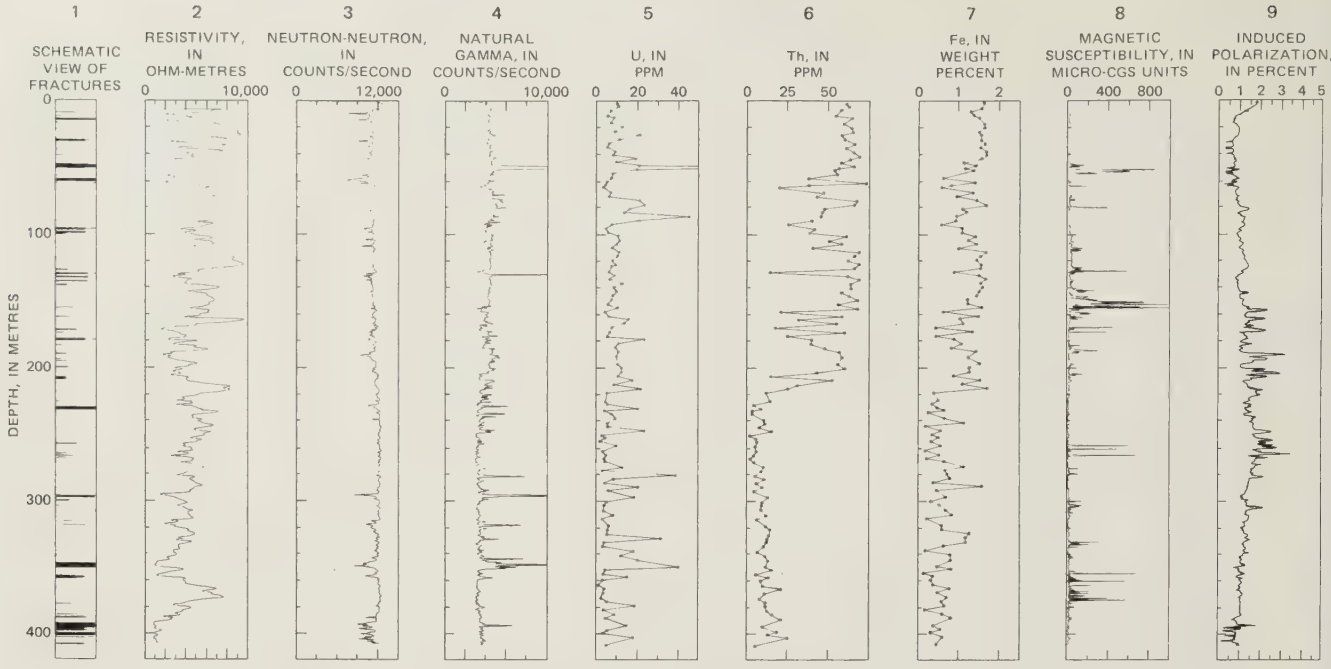

FIGURE 7.—Graphs of geophysical and geochemical data for drill hole GM–1.

TABLE 4.—*Averages for selected elemental data and ratios for samples from the Granite Mountains, Wyo.*

[Reported as average $\pm 1\sigma$]

Number of samples	Biotitic phase 83	Leucocratic phase 52	Fracture zones 20	Silicified zones 7
U (ppm)	9.8± 6.7	8.1± 7.1	76.7±243	7.8± 4.2
Th (ppm)	48.5± 16.2	9.7± 5.0	39.3± 25.8	26.7± 12.2
Fe (wt percent)	1.3± 0.4	.5± 0.3	1.1± 0.4	.7± .06
S (ppm)	28 ± 41	35 ± 26	62 ± 67	13 ± 5
Sr (ppm)	104 ± 69	37.5± 12.3	44.1± 23.5	481 ±147
Rb (ppm)	183 ± 50	132 ± 38	80.6± 70	19.4± 18.4
K (wt percent)	4.1± 0.8	4.2± 0.9	1.7± 1.4	.7± 0.7
Pb (ppm)	48.1± 9.1	54.6± 9.4	40.3± 16.0	15.5± 7.0
K/Pb	875 ±190	780 ±240	385 ±262	533 ±498
Th/U	6.5± 3.2	1.9± 1.4	3.7± 3.9	5.0± 4.1
$U/K \times 10^{-4}$	2.4± 1.6	2.1± 1.9	79.2±225	78.1± 96.2
K/Rb	230 ± 41	326 ± 48	209 ± 81	323 ± 68
Rb/Sr	2.1± 0.8	3.9± 2.0	1.8± 0.9	.05 ± 0.05
Th/K	12.1± 4.4	2.5± 1.4	69.3±116.4	223 ±318

Total iron content does not appear to correlate with the magnetic anomalies in the biotitic phase of the granite. This is reasonable because anomalies on the order of 1,000 micro-cgs units indicate a magnetic content of only 0.5 percent by weight (0.25 percent by volume) which constitutes only a small percentage of the total iron. Furthermore, thin sections from the more magnetic parts of the core generally have lower mafic-mineral contents suggesting that an increased proportion of the iron is contained in opaque minerals. With the exception of the three anomalies near 260 m, magnetic anomalies generally correlate with or occur near natural gamma radioactivity anomalies. Most of the magnetic anomalies are due to disseminated magnetite grains for which crystals attain a maximum diameter of 5 mm (fig. 5*A*); the three large anomalies near 260 m are due to large (2 to 3 cm) crystals of magnetite. Magnetic anomalies within the leucocratic phase appear to correlate with the iron content, particularly when iron increases without a concomitant increase in thorium. This may be due to the lower average iron content of the leucocratic phase such that magnetite constitutes a larger percentage of the total iron. The good correlation between thorium and iron appears to be reestablished in the last 30 m of the drill hole.

The relationship between iron and thorium can be explained if the poikilitic inclusions of radioactive minerals in the biotite form the dominant thorium sites and if the biotite is the dominant site for iron, that is, varying the amount of poikilitic biotite would produce a sympathetic variation of iron and thorium. Alternatively, the correspondence between iron and

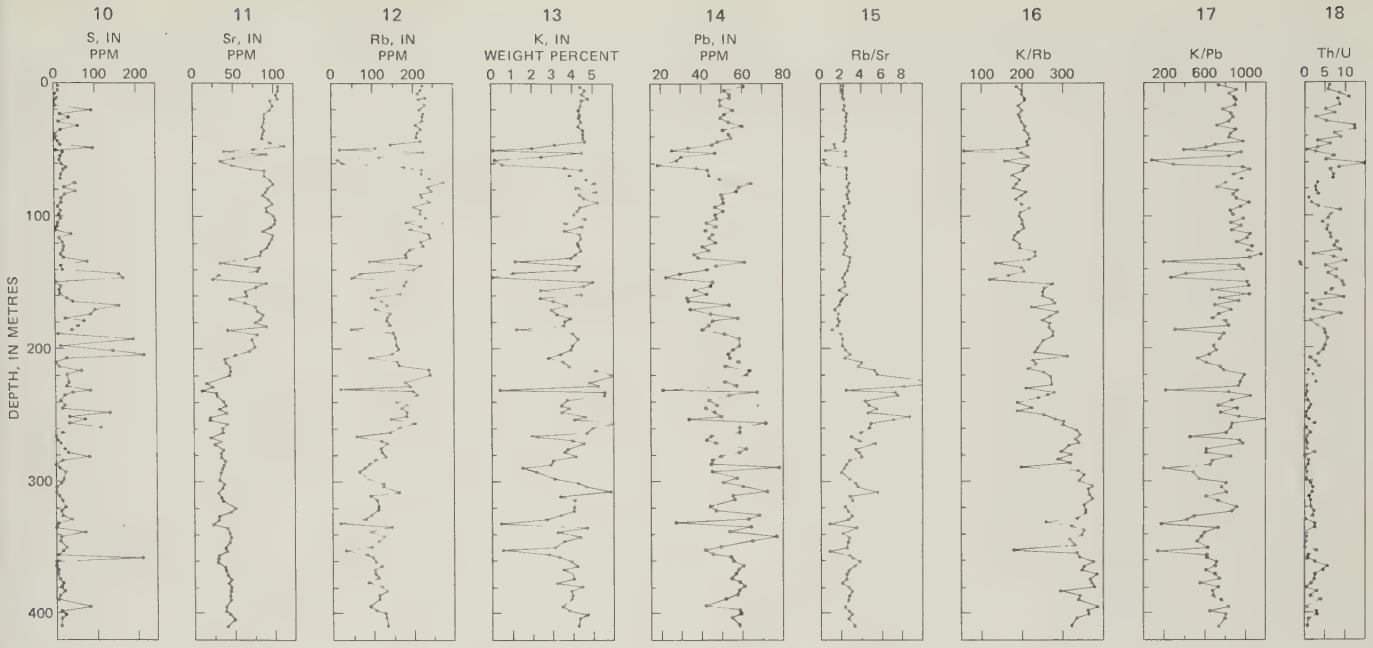

FIGURE 7.—Continued.

thorium may be normal for alkali granites; the large fluctuations in these two elements in the core samples from the biotitic phase may be caused by admixture with material derived from the leucocratic phase and resorbed into the melt. This latter explanation suggests that the leucocratic phase may have originated when the metamorphic roof rocks of the magma chamber broke loose and sank in the magma. Parts of this xenolith then spalled off and were assimilated to varying degrees by the surrounding magma. A suitable metamorphic parent rock was collected by Z. E. Peterman near loc. D1686 (fig. 1). This rock is xenomorphic granular, leucocratic, and contains euhedral garnets. The garnets in this rock do not exhibit retrograde alteration; thus if this rock does represent the parent of the leucocratic phase, retrograde alteration of garnets within the leucocratic phase must have been caused by reaction between the magma and the xenolith.

Sulfur contents of the GM–1 core samples are highly variable in both the biotitic and leucocratic phases of the granite. Sulfur concentrations in the upper 20 m of the bore hole vary from slightly above to below the limits of detection by X-ray fluorescence (5 ppm) and suggest sulfide oxidation and removal by leaching within the vadose zone. At the time of drilling, depth to water was approximately 30 m in the U.S. Air Force hole CR–14, 100 m to the east. Most of the higher sulfur concentrations, particularly between 50 and 300 m, correspond to induced polarization anomalies suggesting that sulfur is present as sulfide minerals. One such anomaly at 153 m corresponds to a small veinlet of pyrite and quartz that cuts the bore hole. A few of the induced polarization anomalies, such as the one at 310 m, appear to correspond to increased magnetite content rather than increased sulfides. The higher sulfur anomalies between 20 and 60 m and at 360 m do not correspond to induced polarization anomalies which suggests that the sulfides may have been oxidized to sulfate compounds. Sulfur contents greater than 100 ppm tend to correspond to large lows in alkaline-metal and alkaline-earth contents. This relationship is expressed in the detailed section shown between 45 and 55 m (fig. 8) where the alkaline-metal and alkaline-earth contents exhibit two strong lows. The first low occurs at 48.43 m and corresponds exactly to the first sulfur high. The second low occurs at 50.75 m which is 1.31 m deeper than the second sulfur high. However, the depth of the alkaline-metal and alkaline-earth low corresponds to the depth of total magnetite destruction (the low interval in the magnetic susceptibility log at 50-m depth) and the zone of most highly fractured rock (fig. 8). If a high sulfide anomaly existed at this depth, the pyrite could have been oxidized and the sulfur removed by leaching.

Strontium, rubidium, potassium, and lead contents of the core vary sympathetically as a function of depth (fig. 7). All four elements are strongly depleted in the fracture zones. Each element is slightly depleted

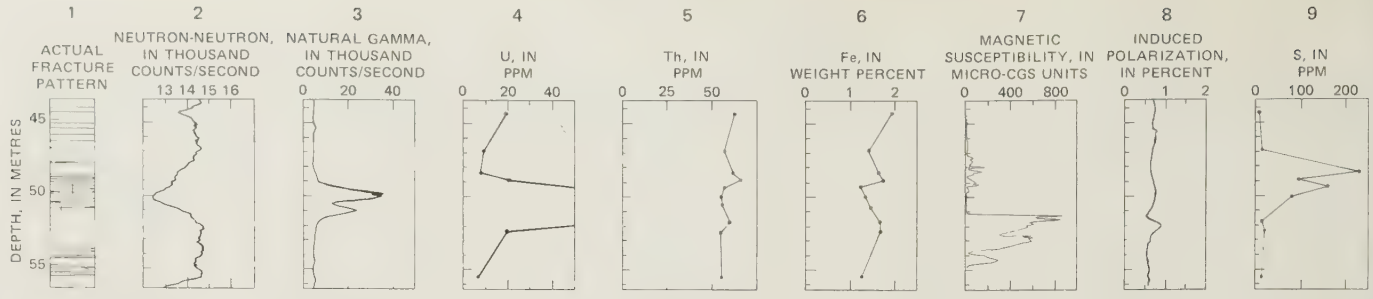

FIGURE 8.—Graphs of geophysical and geochemical data through the fracture zone between 44- and 56-m depths in drill hole GM–1.

in zones that contain less than average amounts of potassium feldspar, such as at 266 m, and slightly enriched in zones that contain more than average amounts of potassium feldspar, such as at 257 m. The similarities in behavior are not maintained within the silicified zones, where strontium is greatly enriched and rubidium, potassium, and lead are strongly depleted (table 4, fig. 9). This is due to the high modal abundance of clinozoisite and sodic feldspar, which have strong affinities for strontium (Iiyama, 1968), and the concomitant disappearance of potassium feldspar and biotite, which contain most of the alkali metals in the other phases of the granite.

The correlation between rubidium and strontium is very high in drill core samples of the biotitic phase ($R=0.85$) and is graphically evident from the remarkably constant Rb/Sr ratio (fig. 7). However the Rb/Sr ratio is much more variable for surface samples from the biotitic phase (fig. 9). Alteration within the fracture zones has removed both rubidium and strontium but has preferentially removed more rubidium (indicated by the smaller Rb/Sr ratio). This is caused by the disappearance of phases that have high Rb/Sr ratios such as potassium feldspar and biotite, but without a marked decrease in major strontium-bearing phases. The correlation between rubidium and strontium in the leucocratic phase ($R=0.14$) is much lower than in the biotitic phase. This is particularly evident in the upper 60 m of the leucocratic phase in the drill core. The poorer correlation is not related to any obvious mineralogic control and probably reflects original geochemical differences between the biotitic and leucocratic phase.

Potassium and rubidium exhibit a close geochemical correspondence in both the biotitic ($R=0.91$) and leucocratic ($R=0.85$) phases, but the K/Rb ratio is larger in the leucocratic phase (fig. 7. table 4). This may in part be due to the lower biotite content in the leucocratic phase, but is probably largely due to an original geochemical difference between the two phases. The low K/Rb ratios in the fracture zones (fig. 8) is because of the preferential removal of potassium. There is a slight tendency for the K/Rb ratios to increase in the deeper samples of the biotitic phase; mixing between the two phases could account for this trend.

Potassium and lead correlate fairly well in both the biotitic ($R=0.60$) and leucocratic ($R=0.68$) phases. The larger variability of the K/Pb ratios relative to the K/Rb ratios may indicate in part the poor analytical precision for the lead data which would make the the lead variations larger than those for rubidium. However, isotopic data (Rosholt and others, 1973) indicate that 30–60 percent of the lead is radiogenic and thus the variable K/Pb ratio is probably due to varying amounts of radiogenic lead, which accumulated after the granite had formed.

DISCUSSION AND CONCLUSION

Published data document the fact that the uranium concentration in igneous rocks increases with increasing silica (Rogers and Adams, 1969; Tilling and others, 1970) and that at any given silica content uranium increases with the degree of alkalinity (Tilling and Gottfried, 1969). The granitic rocks of the Granite Mountains are alkalic and high in silica and therefore a high uranium content is not surprising. The range of uranium concentrations for most granitic rocks ($SiO_2>70$ percent) has been reported as 2 to 15 ppm with an average of 4 ppm (Rogers and Adams, 1969). The biotitic phase reported in this paper is anomalous when compared with those concentrations. The uranium concentrations range from 3 to 45 ppm (table 3) and average 9.8 ppm (table 4). In addition Rosholt and others (1973) have reported an average uranium loss of 20 $\mu g/g$, which suggests that the average biotitic phase samples once contained about 30 ppm uranium. Even the leucocratic phase which has an average uranium content of 8.1 ppm (table 4) is anomalous relative to most granitic rocks. Furthermore, most samples from this phase also seem to have suffered recent uranium depletion (Nkomo and

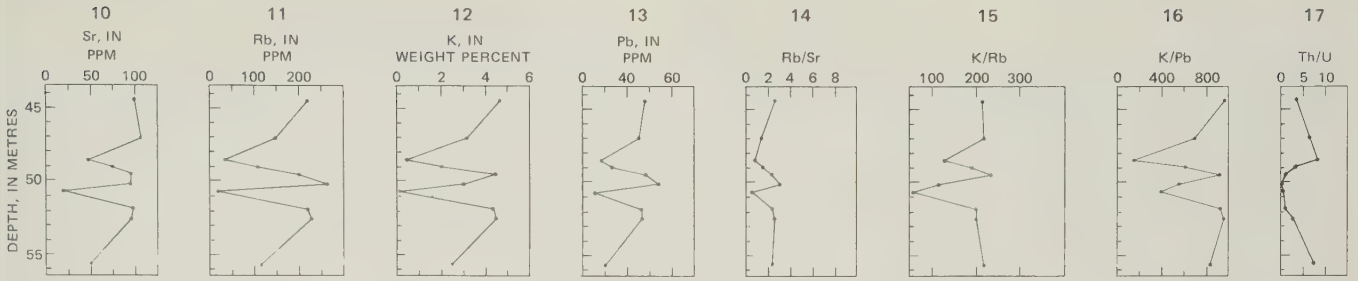

FIGURE 8.—Continued.

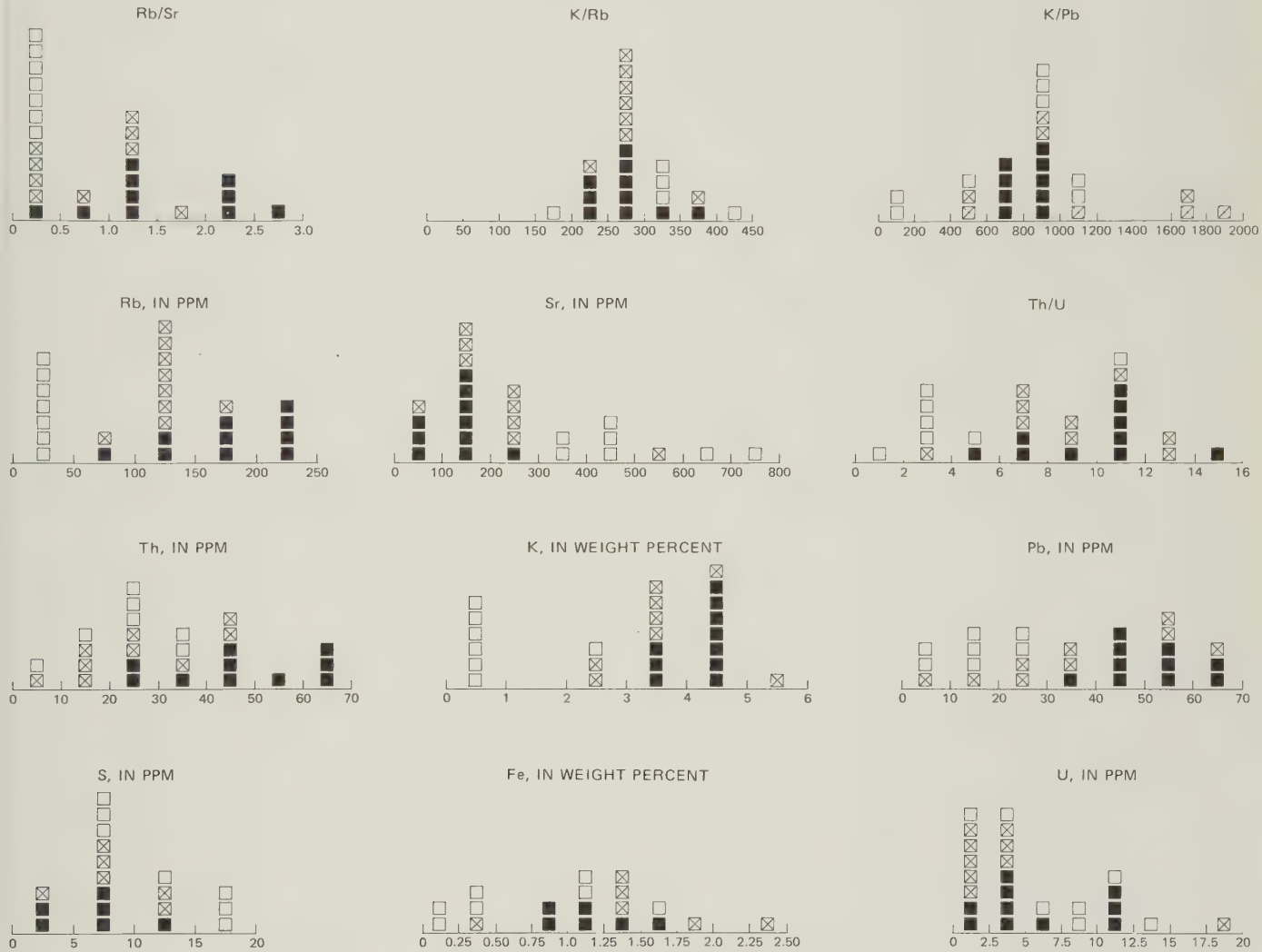

FIGURE 9.—Elemental distribution of surface and near-surface samples. Open squares, silicified-zone samples; solid squares, biotitic-phase samples; squares with X, leucocratic-phase samples, including one sample, TCM–2, and three samples from drill hole CR–1 collected north of the main mass of granitic rocks.

Stuckless, 1975) which suggests that the original uranium content was even more anomalous.

Thorium generally exhibits a close geochemical correspondence to uranium in igneous rocks. In granites (SiO_2>70 percent) Th/U ratios generally range from 3 to 5, and the average thorium concentration is 18 ppm (Rogers and Adams, 1969). In this respect, both the biotitic phase (avg Th=48.5 ppm) and the leucocratic phase (avg Th=9.7 ppm) are anomalous, but in opposite directions. The present Th/U ratio in

the biotitic phase (6.5) is not particularly anomalous, if the apparent uranium loss is considered, both the biotitic and leucocratic phase must have been more enriched in uranium relative to thorium than the average granitic rocks reported by Rogers and Adams (1969). The present Th/U ratio for the leucocratic phase (1.9) is anomalously low even if the uranium loss is not taken into account.

The apparent anomalies cited above may be due, in part, to the relative geochemical mobility of uranium in some crystalline rocks. Uranium-lead-isotope systematics have been used to demonstrate uranium loss from several Precambrian crystalline units. Granite samples from the Granite Mountains, Wyo., have lost as much as 80 percent of their original uranium (Rosholt and Bartel, 1969; Rosholt and others, 1973; Nkomo and Stuckless, 1975). Samples from the Ruin Granite and granite at Lollar Peak, Ariz., have lost approximately 50 percent of their original uranium (Ludwig, 1974). Samples of granitic metamorphic rocks from the Minnesota River valley have lost 50 percent of their original uranium (Goldich and others, 1975), and similar samples from the Granite Mountains exhibit a 65 percent uranium loss (Nkomo and Rosholt, 1972).

Isotopic evidence has also been used to document uranium loss from intermediate and mafic rocks. Published results of isotopic studies show uranium loss in intermediate rocks from the Granite Mountains (Nkomo and Rosholt, 1972) and from Australia (Gray and Oversby, 1972). Even mafic lavas from the Onverwacht Series from South Africa seem to have incurred a recent (Cenozoic) uranium loss (Sinha, 1972). Isotopic evidence suggests that uranium loss from most crystalline rocks is approximately 50 percent of the amount originally present. Nevertheless, the actual amount of uranium lost, in terms of micrograms per gram, from all rocks except the granites is small; this is because granite was originally richer in uranium.

Comparison of surface and drill-core samples has been used to demonstrate near-surface uranium loss from granites. The Conway Granite of New Hampshire contains approximately 30 percent less uranium above 200-m depth than at deeper levels (Rogers and others, 1965). Barbier (1968) reports that surface samples from a two-mica granite from the Massif Central in France are 50 percent deficient in uranium relative to samples taken at depth and that dominantly immobile uranium was not encountered until depths greater than 320 m.

Few unequivocal data have been published to document a lack of uranium mobility. Igneous examples are dominantly calc-alkaline to calcic in composition. Rosholt, Peterman, and Bartel (1970) report isotopic evidence for equilibrium between uranium and radiogenic lead in a granite cored in Saskatchewan at 2,225 m depth (24.4 m below the top of the Precambrian). Comparison of uranium contents in surface samples and deep (1–2 km) drill-hole samples from the Sierra Nevada batholith (Wollenberg and Smith, 1968; Tilling and others, 1970) does not suggest any noticeable increase in uranium at depth. A similar conclusion was reached by Tilling and Gottfried (1969) for rocks from the Boulder batholith, Montana. These two patterns of equal uranium contents in surface and drill-core samples are similar to the pattern observed in the Granite Mountains (fig. 7); however isotopic evidence (Nkomo and Stuckless, 1975) suggests that even deep samples in the Granite Mountains have lost uranium.

Several sites of and mechanisms for uranium loss can be proposed for the samples analyzed in this study. The seemingly lower original uranium content of the leucocratic phase could be attributed to an early uranium loss during metamorphism. Uranium loss during granulite-facies metamorphism has been documented by Gray and Oversby (1972), and textures within the leucocratic phase, together with such mineralogic phases as garnet, suggest high-grade metamorphism. Alternatively, the leucocratic phase could have lost uranium during a partial melting event if this phase represents a partially assimilated xenolithic block of country rock.

More recent uranium loss from all rock-type samples in this study and in Rosholt and others (1973) could be attributed to weathering. Similar explanations have been advanced by Richardson (1964) and Rogers and others (1965). However, the present low topographic relief between the Granite Mountains and surrounding basins, together with the great depth of uranium loss, make a simple weathering explanation seem unreasonable. Furthermore, the only evidence of weathering is a general sulfur depletion which appears to be confined to surface samples and the upper 20 m of the drill core (figs. 7, 9). If uranium loss is due to simple weathering, it most probably occurred during the time of high topographic relief proposed by Love (1960) for the Eocene Epoch.

An alternate mechanism for relatively recent deep uranium loss may be similar to a mechanism for lead from zircons, dilatancy as proposed by Goldich and Mudrey (1972). During uplift and erosion of a granite, release of overburden pressure causes near-surface rocks to dilate. During dilation, water may be lost, taking with it certain mobile elements such as uranium. The maximum depth of this effect is unknown,

but depths of several hundred metres have been postulated (Goldich and Mudrey, 1972).

Although several possibilities exist, possible sites for mobile uranium in crystalline rocks are poorly documented. Our preliminary studies suggest that in the biotitic-phase samples, uranium is confined to zircon, sphene, apatite, monazite, biotite, chlorite, and epidote. The first four of these minerals have been used for various uranium-lead geochronologic studies, and examples of reverse discordance (preferential loss of uranium over lead) have been reported for apatite, monazite, and rarely sphene. (See Doe, 1970, for summary.) Studies are currently underway to check for reverse discordance in all the uranium-bearing phases in the rocks from the Granite Mountains.

In addition to the known uranium-bearing phases it is possible that uranium was lost from currently unrecognizable uranium sites such as grain-grain boundaries and soluble-mineral phases. Our uranium distribution study of a single sample with equilibrium amounts of uranium and radiogenic lead (259.7 m, fig. 3) revealed neither type of site. However, it is possible that this sample lost no uranium because there were no mobile-uranium sites.

Several samples from drill hole GM–1 exhibit evidence of uranium gain. Uranium gain is chiefly localized in fractured rock and is probably best attributed to one of two fluid-related mechanisms: hydrothermal alteration or reprecipitation from meteoric waters. Much of the additional uranium may have been released by weathering and subsequently precipitated in fractures as reported by Rogers, Adams, and Gatlin (1965), Barbier and Ranchin (1969), and Barbier (1974). However, some uraniferous zones show signs usually attributed to hydrothermal alteration. These zones now exist as fractured and altered rock in which sulfur, fluorine, and chlorine are slightly enriched relative to the biotitic and leucocratic phases. The abundances of pyrite and magnetite increase, and abundances of potassium-bearing phases (such as biotite and microcline) decrease (fig. 8) in these zones.

The replacement of microcline by chessboard albite in several granites has been attributed to hydrothermal alteration (see Gilluly, 1933) from possible late-stage magmatic activity. The most uranium-rich samples in the fracture zone from 45 to 55 m in GM–1 contain too little lead (even if all the lead were radiogenic) to have existed in a closed system for the last 2.6 billion years. Even if this and other fracture zones were altered originally by late-stage magmatic fluids related to the granite emplacement, they must have gained uranium or lost lead in recent times. We have no evidence for more recent hydrothermal activity in the Granite Mountains and, therefore, conclude that a purely hydrothermal origin for the uranium enrichment is unlikely.

Barbier and Ranchin (1969) have reported the reprecipitation of uranium as autunite on fractures within a uraniferous granite from St. Sylvester, France. Barbier (1968) suggested that a two-mica granite from Monts de Blond, France, was oxidized to a depth of 320 m and reduced at greater depths; the oxidation affected both uranium and iron oxide distributions. If uranium was in motion within the granite from the Granite Mountains, changes in Eh or pH, which could precipitate some of the uranium, might be most common within the hydrothermally altered rock. Reaction of pyrite, oxygen, water, and uranium-bearing phases may hold uranium in solution with iron sulfate. If the solution pH rises appreciably within the fractures zones, uranium and iron oxides may precipitate together along small cracks thereby creating the type of uranium distribution shown in figure 4. It is also possible that the large crystals of magnetite as shown in figure 5 might have a localized effect on Eh or pH which could cause a precipitation of uranium. At present we are unable to draw any firm conclusions about the mechanism for concentrating uranium in crystalline rocks or about the characteristics of crystalline rocks as potential hosts.

A preliminary and tentative characterization of potential crystalline uranium-source rocks for sedimentary uranium deposits can be proposed on the basis of available data. First, an alkaline granite or possibly a syenite should be the most favorable rock type because the uranium content increases with the increase in silica content and degree of alkalinity. Second, the most favorable source rock should be an unmetamorphosed one because uranium can be lost during granulite facies metamorphism. Third, in order to form economic deposits the potential source rock should have had a rapid exposure to near-surface conditions for the first time when a favorable site for uranium deposition existed nearby. Because current studies indicate that the depth of uranium loss is greater than the depth of weathering, recently uplifted crystalline blocks with patches of sediments on top of them could have lost their mobile uranium while in a near-surface environment during or prior to the deposition of the overlying sediment. Granitic rocks of the Granite Mountains that might have lost uranium during a late Precambrian exposure would have been stripped away by the profound erosion of early Cenozoic time. Finally, if mobile uranium loss occurs before mechanical breakdown of the rock, sediments derived from crystalline rocks are unlikely to form a

source of uranium because the mobile uranium should have been lost prior to erosion.

REFERENCES CITED

Barbier, Jean, 1968, Altération chemique et remaniement de l'uranium dans le granite à deux micas des Monts de Blond (Limousin, France): Sci. Terra, v. 13, no. 4, p. 359–378.

Barbier, J., and Ranchin, G., 1969, Influence de l'altération météorique sur l'uranium à l'état de traces dans le granite à deux micas de St-Sylvestre: Geochim. et Cosmochim. Acta, v. 33, no. 1, p. 39–47.

Barbier, M. J., 1974, Continental weathering as a possible origin of vein-type uranium deposits: Mineralium Deposita, v. 9, p. 271–288.

Bowie, S. H. U., Simpson, P. R., and Rice, C. M., 1973, Application of fission-track and neutron activation methods to geochemical exploration, *in* Geochemical exploration 1972, International Geochim. Explor. Symposium Proc., no. 4, p. 359–372.

Catanzaro, E. J., 1967, Correlation of some Precambrian rocks and metamorphic events in parts of Wyoming and Montana: Mtn. Geologist, v. 4, no. 1, p. 9–21.

Doe, B. R., 1970, Lead isotopes: New York, Springer-Verlag, 137 p.

Doering, W. P., 1968, A rapid method for measuring the Rb/Sr ratio in silicate rocks, *in* Geological Survey research 1968: U.S. Geol. Survey Prof. Paper 600–C, p. C164–C168.

Guilluly, James, 1933, Replacement origin of the albite granite near Sparta, Oreg.: U.S. Geol. Survey Prof. Paper 175–C, p. 65–81.

Goldrich, S. S., and Mudrey, M. G., 1972, Dilatancy model for explaining discordant uranium-lead zircon ages, *in* Ocherki sovremennoy geokhimii i analiticheskoy khimii: Moscow, Izd-vo Nauka, p. 415–418.

Goldich, S. S., Doe, B. R., and Delevaux, M. H., 1975, Possible further evidence for 3.8 b.y.-old rocks in the Minnesota River valley of southwestern Minnesota: U.S. Geol. Survey Open-File Report 75–65, 11 p.

Gray, C. M., and Oversby, V. M., 1972, The behavior of lead isotopes during granulite facies metamorphism: Geochim. et Cosmochim. Acta, v. 36, no. 9, p. 939–952.

Hills, F. A., and Armstrong, R. L., 1974, Geochronology of Precambrian rocks in the Laramie Range and implications for tectonic framework of Precambrian southern Wyoming: Precambrian Research, v. 1, p. 213–225.

Iiyama, J. T., 1968, Experimental study of the distribution of trace elements between two feldspars; 1. distribution of Rb, Cs, Sr, and Ba at 600°C: Geochim. Internat., v. 15, p. 433–442.

Love, J. D., 1960, Cenozoic sedimentation and crustal movement in Wyoming: Am. Jour. Sci., v. 258–A, (Bradley volume), p. 204–214.

——— 1970, Cenozoic geology of the Granite Mountains area, central Wyoming: U.S. Geol. Survey Prof. Paper 495–C, 154 p.

Ludwig, K. R., 1974, Precambrian geology of the central Mazatzal Mountains, Arizona, Part 2, Lead isotope heterogeneity in Precambrian igneous feldspars: California Inst. Technology, Ph. D. dissert., 363 p.

Mooney, H. M., and Bleifuss, R. L., 1953, Magnetic susceptibility measurements in Minnesota, Part 2, Analysis of field results: Geophysics, v. 18, no. 2, p. 383–393.

Nelson, P. H., and Glenn, W. E., 1975, Influence of bound water on the neutron log in mineralized igneous rock, *in* SPWLA Logging Symposium, Soc. Prof. Well Log Analysts, 16th Ann., Salt Lake City, Utah, 1975: p. 1–9.

Nkomo, I. T., and Rosholt, J. N., 1972, A lead-isotope age and U-Pb discordance of Precambrian gneiss from Granite Mountains, Wyoming, *in* Geological Survey research 1972: U.S. Geol. Survey Prof. Paper 800–C, C169–C177.

Nkomo, I. T., and Stuckless, J. S., 1975, Uranium-lead systematics and uranium leaching in core samples from Granite Mountains, Wyoming [abs.]: Am. Assoc. Petroleum Geologist Bull., v. 59, no. 5, p. 918.

Nockold, S. R., 1954, Average chemical compositions of some igneous rocks: Geol. Soc. America Bull., v. 65, no. 10, p. 1007–1032.

Peterman, Z. E., Hildreth, R. A., and Nkomo, I. T., 1971, Precambrian geology and geochronology of the Granite Mountains, central Wyoming: Geol. Soc. America Abs. with Programs, v. 3, no. 6, p. 403–404.

Pirson, S. J., 1963, Handbook of well log analysis for oil and gas formation evaluation: Englewood Cliffs, N. J., Prentice-Hall, 326 p.

Reynolds, R. C., Jr., 1967, Estimation of mass absorption coefficients by Compton scattering; improvements and extensions of the method: Am. Mineralogist, v. 52, nos. 9 and 10, p. 1493–1502.

Richardson, K. A., 1964, Thorium, uranium, and potassium in the Conway granite, New Hampshire, U.S.A., *in* Adams, J. A. S. and Lowder, W. M., eds., The natural radiation environment: Chicago, Ill., Univ. Chicago Press, p. 39–50.

Rogers, J. J. W., and Adams, J. A. S., 1969, Uranium, *in* Wedepohl, K. H., ed., Handbook of geochemistry, Volume 2, Number 4: Berlin, Springer-Verlag, p. 92–B to 92–0.

Rogers, J. J. W., Adams, J. A. S., and Gatlin, B., 1965, Distribution of thorium, uranium, and potassium concentrations in three cores from the Conway Granite, New Hampshire, U.S.A.: Am. Jour. Sci., v. 263, no. 9, p. 817–822.

Rosholt, J. N., and Bartel, J A, 1969, Uranium, thorium and lead systematics in Granite Mountains, Wyoming: Earth and Planetary Sci Letters, v. 7, no. 2, p. 141–147.

Rosholt, J. N., Peterman, Z. E., and Bartel, A. J., 1970, U-Th-Pb and Rb-Sr ages in granite reference sample from southwestern Saskatchewan: Canadian Jour. Earth Sci., v. 7, no. 1, p. 184–187.

Rosholt, J. N., Zartman, R. E., and Nkomo, I. T., 1973, Lead isotope systematics and uranium depletion in the Granite Mountains, Wyoming: Geol. Soc. America Bull., v. 84, no. 3, p. 989–1002.

Schonfeld, Ernest, 1966, Alpha M—An improved computer program for determining radioisotopes by least-squares resolution of the gamma-ray spectra: U.S. Atomic Energy Comm., U.S. Natl. Lab., Oak Ridge, Tenn., ORNL–3975, 43 p.

Scott, J. H., Carroll, R. D., and Cunningham, D. R., 1967, Dielectric constant and electrical conductivity measurements of moist rocks; a new laboratory method: Jour. Geophys. Research, v. 72, no. 20, p. 5101–5115.

Shapiro, Leonard, 1967, Rapid analysis of rocks and minerals by a single-solution method, *in* Geological Survey research 1967: U.S. Geol. Survey Prof. Paper 575–B, p. B187–B191.

Sinha, A. K., 1972, U-Th-Pb systematics and the age of the Onverwacht Series, South Africa: Earth and Planetary Sci. Letters, v. 16, no. 2, p. 219–227.

Starkey, J., 1959, Chess-board albite from New Brunswick, Canada: Geol. Mag., v. 96, no. 2, p. 141–145.

Streckeisen, A. L., 1967, Classification and nomenclature of igneous rocks: Neues Jahrb. Mineralogie, Abh., v. 107, p. 144–240.

Stuckless, J. S., 1975, Preliminary results for bore hole GM–1, Granite Mountains, Wyoming: U.S. Geol. Survey Open-File Report 75–40, 8 p.

Tilling, R. I., and Gottfried, David, 1969, Distribution of thorium, uranium, and potassium in igneous rocks of the Boulder batholith region, Montana, and its bearing on radiogenic heat production and heat flow: U.S. Geol. Survey Prof. Paper 614–E, 29 p.

Tilling, R. I., Gottfried, David, and Dodge, F. C. W., 1970, Radiogenic heat production of contrasting magma series; bearing on interpretation of heat flow: Geol. Soc. America Bull., v. 81, no. 5, p. 1447–1462.

Wollenberg, H. A., and Smith, A. R., 1968, Radiogeologic studies in the central part of the Sierra Nevada batholith, California: Jour. Geophys. Research, v. 73, no. 4, p. 1481–1495.

Zablocki, C. J., 1966, Some applications of geophysical logging methods in mineral exploration drill holes, *in* SPWLA Logging Symposium, 7th Ann., Tulsa, Okla., 1966, Trans.: Soc. Prof. Well Log Analysts, p. U1–U13.

Jour. Research U.S. Geol. Survey
Vol. 5, No. 1, Jan.–Feb. 1977, p. 83–91

A COMPARISON OF SOME ANALYTICAL TECHNIQUES FOR DETERMINING URANIUM, THORIUM, AND POTASSIUM IN GRANITIC ROCKS

By JOHN S. STUCKLESS, HUGH T. MILLARD, Jr., CARL M. BUNKER, IGNATIUS T. NKOMO, JOHN N. ROSHOLT, CHARLES A. BUSH, CLAUDE HUFFMAN, Jr., and RONALD L. KEIL,[1]
Denver, Colo.; Golden, Colo.

Abstract.—Geochemical exploration for uranium requires accurate and precise determinations of low-level concentrations. We have used seven different techniques and four different treatments of the fluorometric method to analyze for uranium in granitic rocks. In addition we have used four analytical techniques for thorium and three analytical techniques for potassium, two elements that are commonly present in anomalous amounts within uranium provinces. Our results show that commonly used techniques for thorium and potassium determinations are both adequately precise and accurate, but that many techniques used for uranium determinations lack the necessary precision or accuracy for complete geochemical prospecting. We suggest that a combination of delayed-neutron determinations for uranium and γ-ray spectrometric analyses for radium equivalent uranium, thorium, and potassium provides the best data base for geochemical exploration for uranium. If more detailed interpretations are desired, the combination of γ-ray spectrometry and α-spectrometry may be best. Carefully done fluorometric analyses should be adequate for water, ore, mineralized rock, and other applications where high precision and accuracy are not required.

Interest in low-level uranium and thorium concentrations as a guide to exploration and the ever-decreasing radioelement contents needed for minable ore bodies have placed new constraints upon analytical chemists and exploration geologists. High levels of accuracy and precision are now needed for determinations in the parts-per-million range, and often geologists must choose the most cost effective and reliable method for analyzing samples. In this report, we compare results of several techniques to those obtained by isotope dilution using mass spectrometry. The isotope-dilution technique can yield accurate results for uranium and thorium to better than ± 1 percent (3σ) of the amount present throughout the range of 0.5 to 1,000 ppm (Garner and others, 1971).

[1] Natural Resources Laboratory, Inc., Geolabs Division, 1100 Simms St., Golden, Colo. 80401.

Acknowledgments.—We thank G. T. Cebula, J. W. Groen, and N. F. Lewis, Jr., for their careful preparation of the samples used in this study. N. F. Lewis also assisted with the γ-ray spectrometric analyses. Prof. S. S. Goldich of Northern Illinois University reviewed the manuscript and made several helpful suggestions.

ANALYTICAL PROCEDURES

All the analytical techniques used in this study have been described elsewhere, and the reader interested in the details is referred to the references cited. The following section gives only brief descriptions and modifications of the techniques used by us.

Sample preparation.—Sample preparation and the types of samples used are described in the accompanying article by Stuckless and others (1977). For each sample, 1–2 kg of rock were processed so that representative samples of outcrop or drill core could be obtained.

Mass spectrometry.—Uranium and thorium contents were obtained using standard isotope-dilution techniques as described by Tatsumoto (1966) and Rosholt, Zartman, and Nkomo (1973). Approximately 1 g of -200 mesh material was used for each analysis. Results are accurate and precise within ± 2 percent (2σ).

Delayed neutron.—Details of the procedure for determining uranium and thorium contents by the delayed-neutron technique are given by Millard (1976). Approximately 10 g of -32 mesh material were used for each analysis. Results are generally precise and accurate within ± 5 percent (2σ) except where Th/U ratios are greater than 8 or less than 2. The delayed-neutron values that are used in figures 1, 2, and 3 show the 2σ errors which were based on counting statistics for individual samples.

Alpha spectrometry.—The procedures used with the α-spectrometric technique are described by Rosholt, Doe, and Tatsumoto (1966), and modifications to the technique are described by Stuckless and Ferreira (1976). Approximately 1 g of −200 mesh sample was used for each analysis. Results are precise and accurate to within ±2 percent (2σ).

Gamma-ray spectrometry.—Radium-equivalent uranium (RaeU), thorium, and potassium values were obtained by sealed-can γ-ray spectrometry as described by Bunker and Bush (1966, 1967) and Stuckless and others (1977). About 600 g of −32 mesh material were used for each analysis. Results are accurate and precise to within ± (2 percent +0.10 ppm) for RaeU and Th to about ± (2 percent +600 ppm) for K (2σ).

Total beta-gamma counting.—Equivalent-uranium (eU) values were calculated by measuring the total β and γ radiation coming from the sample with an end-window counter and by assigning all the radioactivity to uranium-series products. Count rates were then compared to those for known uranium standards for which daughter products were in equilibrium with their parent isotopes. About 10 g of −32 mesh sample were used for each measurement and counting times were adjusted such that the counting statistics would be better than ±3 percent (1σ).

Fission track.—The determination of uranium contents by the fission-track technique using spark counting has been described by Cross and Tommasino (1970) and Becken (1972). In our adaptation of this method, approximately 0.1 g of finely ground sample was pressed into the surface of a cellulose pellet, covered with a 10-μm-thick Lexan detector, and irradiated. The Lexan was then etched with NaOH to develop fission-track holes which were counted by spark counting. The comparison of the number of fission tracks in the sample detectors to the number in detectors placed on standard pellets yielded the uranium contents of the samples. Under optimum conditions this technique has a precision of ±10 percent (2σ).

Fluorometry.—The general principles of fluorometric uranium methods have been described in many papers (see, for example, Grimaldi and others, 1954). The fluorometric measurement is precise within ±5 percent (2σ), if the samples are free from interference by absorbing elements, which quench fluorescence, or by enhancing elements, which increase fluorescence. The accuracy of this technique is dependent upon a quantitative recovery of uranium and the absence of interfering elements during the final measurement.

We have used four different methods of sample attack: (1) dissolution in HF, $HClO_4$, and HNO_3, (2) fusion with NaOH, (3) fusion with $LiBO_2$, and (4) leaching with boiling $HClO_4$ and HNO_3 followed by controlled refluxing to concentrated $HClO_4$. The first two methods of dissolution utilized 1 g of material, and each was followed by uranium extraction with ethyl acetate and formation of a fluorescent bead by fusion with NaF.

In separate experiments, the first method of attack was followed by a leach of the residual salts with concentrated $HClO_4$. The resulting solution was diluted to 10-percent $HClO_4$, and two aliquots were taken. A known amount of uranium (referred to as a spike) was added to one aliquot from each sample so that the existence of quenching of fluorescence by adsorbing elements (for example, Fe, Ti, Mn, Pt) could be examined. A fluorescent bead was made for each aliquot. If the difference between the uranium contents for two beads from one sample was not equal to the amount of spike added, the sample was rerun after either a separation of uranium or dilution to a point where quenching was not measurable.

The fusion with $LiBO_2$ was followed by dissolution of the molten fusion bead in 5-percent HF. This solution was then aliquoted, spiked, and measured as above. The solution obtained by leaching with $HClO_4$ and HNO_3 and refluxed to concentrated $HClO_4$ was diluted to 10-percent $HClO_4$, aliquoted, spiked, and measured as above. For ore or water samples any combination of the techniques used by us can yield an accuracy of ±5 percent.

Atomic absorption and flame photometry.—Approximately 0.5-g samples of −200 mesh material were digested in HF, $HClO_4$, and HNO_3 and analyzed for potassium by either the methods of Suhr and Ingamells (1966) for flame photometry or of Shapiro and Brannock (1962) for atomic absorption. Both methods have precision and accuracy of about ±1 percent (2σ).

RESULTS AND DISCUSSION

Sample preparation and splitting.—In any geochemical study that compares analytical techniques, problems in sample preparation and splitting are as important as those involved with the actual measurements. We have taken particular care to avoid contamination during each stage of crushing and pulverizing. Differences in elemental concentrations between subsamples ground to different finenesses are estimated to be less than 0.1 percent.

It is possible for subsampling errors to cause variations as large as 100 percent in certain types of geologic samples (Ingamells and others, 1972). We have adjusted subsample weights and grain sizes to mini-

mize this problem. Model calculations, which assigned all the uranium to small percentages of high-uranium zircon, suggest that splitting errors should be less than 0.4 percent for each of the techniques except fission track. The minor effect of splitting errors on the reported results is indirectly confirmed by the close agreement between uranium values obtained by delayed neutron and isotope dilution in combination with mass spectrometry (fig. 1). If splitting errors were significant, the results should exhibit a scatter that would be larger than that predicted by analytical precision.

Alpha spectrometry.—Fourteen samples were analyzed for uranium and thorium by α-spectrometry and mass spectrometry both in combination with isotope dilution. The results in table 1 show that all but one of

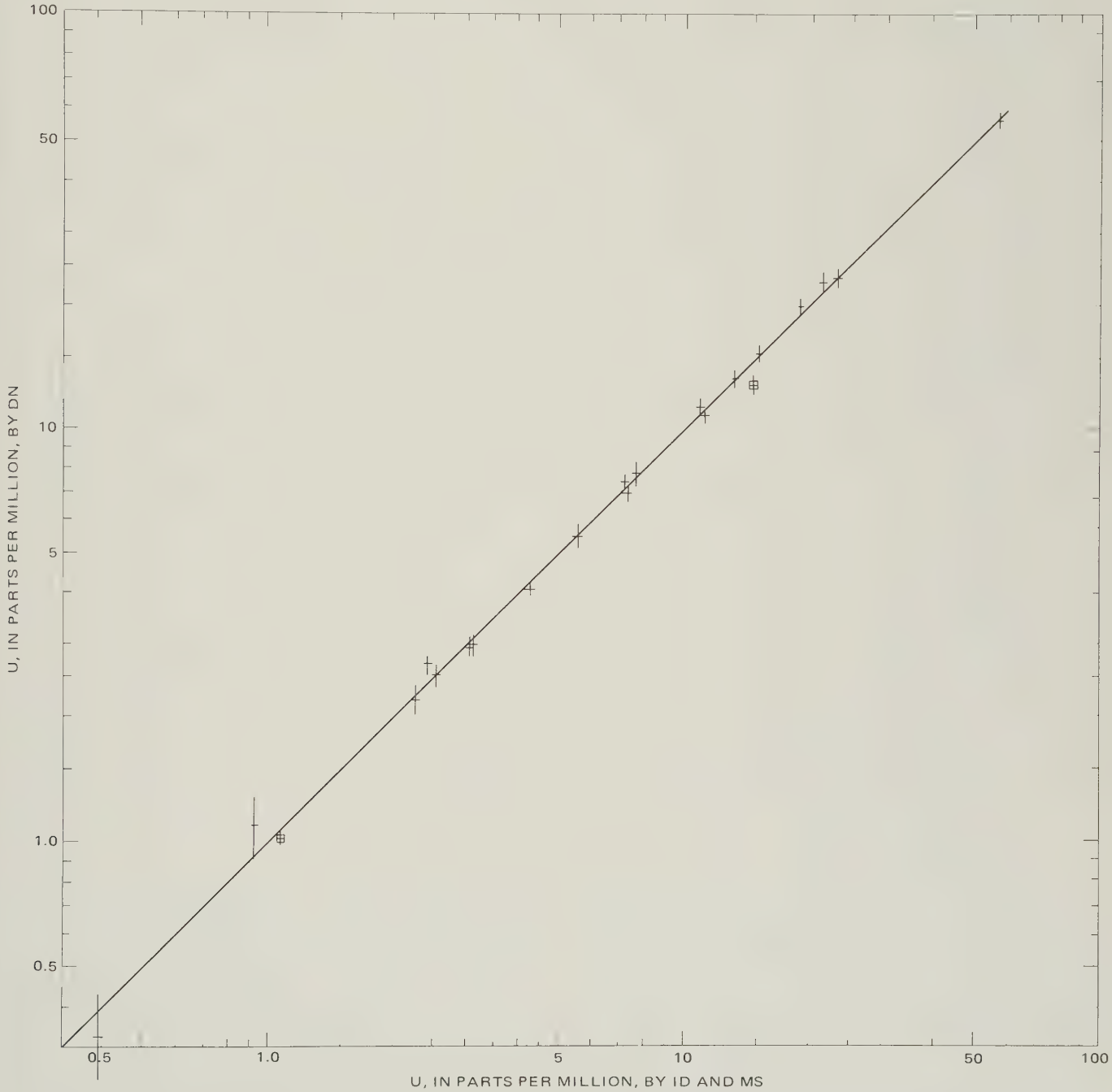

FIGURE 1.—Log-log plot of uranium contents obtained by the delayed-neutron (DN) technique versus those obtained by isotope dilution (ID) in combination with mass spectrometry (MS). A 1:1 line is shown for reference. Symbol sizes are equal to a 2σ error. The values for two samples were divided by 100; these are indicated by boxes with error bars.

TABLE 1.—*Uranium and thorium determinations, in parts per million, for granitic samples from the Granite Mountains, Wyo.*

[-, not determined; *, analytical precision unknown due to interference from other elements]

Sample No.	Uranium										Thorium			
	Isotope dilution		Delayed neutron	Fluorimetry				γ-ray spec RaeU	Fission track	Total β + γ eu	Isotope dilution		Delayed neutron	γ-ray spec
	Mass spec [1]	α-spec [2]	[3]	Digest.+ extract. [4]	Digest.+ spike [5]	Fusion + spike [6]	Leach spike [7]	[8]	[9]	[10]	Mass spec [1]	α-spec [2]	[3]	[8]
IR-12	0.39	-	0.34	-	-	-	-	0.42	0.61	-	4.51	-	5.20	5.89
SDNE-3	-	-	.81	-	-	-	-	.55	-	-	-	-	25.7	29.5
IR-21	-	-	.89	-	-	-	-		-	-	-	-	5.20	4.62
IR-11	-	-	1.04	-	-	-	-	.83	-	-	-	-	46.5	43.6
IR-8	.92	-	1.11	-	-	-	-	.96	1.31	-	37.71	-	35.0	38.6
SD-17	-	-	1.61	-	-	-	-	1.59	-	-	-	-	14.5	14.4
SDNE-12	-	-	1.65	-	-	-	-	1.59	-	-	-	-	12.4	11.9
SDNE-9	-	-	1.76	-	-	-	-	1.90	-	-	-	-	13.7	14.8
256.70	-	-	1.90	-	-	-	-	2.20	-	-	-	-	5.57	5.97
SD-11	-	-	2.07	-	-	-	-	1.77	-	-	-	-	27.5	29.2
DDH-6b	2.13	-	-	-	-	-	-	2.07	-	-	22.69	-	-	23.9
DDH-4	2.23	-	2.20	-	-	-	-	2.14	3.0	-	16.65	-	17.8	19.3
SD-4	-	-	2.24	-	-	-	-	1.73	-	-	-	-	24.7	24.5
SDNE-4	-	-	2.30	-	-	-	-	2.27	-	-	-	-	42.3	45.4
GR-3	2.40	-	2.71	-	-	-	-	2.23	-	-	26.65	-	21.9	26.2
GR-5	2.52	-	2.57	-	-	-	-	2.64	-	-	27.88	-	24.7	26.1
DDH-5	2.66	-	-	-	-	-	-	1.98	-	-	25.10	-	-	26.0
SD-6	-	-	2.86	-	-	-	-	2.28	-	-	-	-	14.2	15.1
BRG-5	-	-	2.91	-	-	-	-	2.72	-	-	-	-	40.1	38.2
251.77	3.04	-	2.96	-	-	-	-	3.01	-	-	1.37	-	.8*	1.33
SD-16	-	-	3.08	-	-	-	-	3.18	-	-	-	-	33.1	26.9
DDH-3	3.09	-	3.02	-	-	-	-	-	-	-	19.92	-	21.6	-
SD-1	-	-	3.36	-	-	-	-	2.63	-	-	-	-	35.4	30.2
DDH-7	3.69	3.60	-	-	-	-	-	2.87	-	-	46.03	40.00	-	44.6
TCM-2	3.74	3.81	-	-	-	-	-	2.97	-	-	19.18	16.86	-	19.7
SD-8	-	-	3.97	-	-	-	-	3.90	-	-	-	-	38.9	35.6
389.69	4.22	4.54	-	-	-	-	-	4.97	-	-	19.72	20.82	-	21.0
352.53	4.23	-	4.12	-	-	-	-	4.54	-	-	15.55	-	13.3	15.0
177.36	-	-	5.28	-	8	7	5	5.40	-	-	-	-	25.9	24.6
225.40	5.52	-	5.51	4.5	2	7	7	4.74	7.3	-	13.54	-	13.9	14.3
308.52	-	-	6.00	-	-	-	-	4.07	-	-	-	-	6.93	8.43
MS-6	-	-	6.82	-	-	-	-	7.12	-	-	-	-	29.8	27.2
GR-4	7.15	-	7.52	-	-	-	-	7.91	7.4	-	17.93	-	15.6	17.4
61.63	7.32	7.28	7.04	4.5	2	8	6	4.85	-	-	72.29	73.24	71.3	72.2
48.43	7.62	-	7.91	5.0	3	11	8	7.64	-	-	60.53	-	60.4	61.7
311.57	7.77	-	-	-	6	12	10	8.40	-	-	11.27	-	-	11.7
DDH-8	8.00	-	-	-	-	-	-	6.91	-	-	32.23	-	-	34.6
58.49	7.90	-	-	-	3	11	8	7.59	-	-	39.93	-	-	37.6
38.34	-	-	9.93	-	-	-	-	8.90	-	-	-	-	60.3	65.6
114.24	10.76	-	11.4	-	-	-	-	10.9	-	56	68.58	-	67.0	68.1
230.95	11.13	11.17	10.9	9.8	3	13	11	20.3	-	20	6.77	6.96	6.08	7.35
2.68	-	-	11.4	-	-	-	-	9.94	-	56	-	-	61.3	61.3
259.66	12.83	13.68	-	13	-	-	-	10.1	-	41	6.33	6.95	-	5.09
20.42	13.08	12.91	13.3	8.2	6	12	14	12.1	-	53	62.79	60.14	61.5	63.1
BRG-1	-	-	13.5	-	-	15	15	13.7	-	25	-	-	49.2	49.8
MS-1	15.15	15.37	15.4	13	13	17	16	13.0	-	26	44.49	43.73	42.4	43.9
290.72	18.92	-	20.0	15	5	18	18	20.9	-	34	8.85	-	5.5*	9.7*
404.29	21.52	22.67	22.9	21	13	24	20	18.6	16.1	48	23.98	25.10	23.8	24.5
26.30	23.00	-	-	19	11	17	20	20.4	-	66	59.24	-	-	56.8
248.26	23.27	23.43	24.4	22	8	24	22	23.5	20.0	47	15.06	15.06	8.1*	14.9
78.58	27.32	26.30	-	-	-	-	-	22.6	-	60	63.84	65.22	-	63.8
87.17	56.21	56.43	56.5	48	44	49	53	44.5	61	91	43.86	46.32	42.9	44.2
50.75	106.0	107.5	101.9	89	25	-	105	106.9	101	120	59.46	55.11	48.6	56.1
50.11	1459	1378	1290	1430	1200	1240	1300	1103	1170	1240		45.83	-57*	55*

[1] Isotope dilution and mass spectrometry. Analyst: I. T. Nkomo.
[2] Isotope dilution and α-spectrometry. Analysts: C. P. Ferreira and J. N. Rosholt.
[3] Analysts: H. T. Millard and D. A. Bickford.
[4] Fluorimetry following complete sample digestion and U extraction. Analysts: E. J. Fennelly and J. G. Crock.
[5] Fluorimetry following complete digestion of the sample and no separation of U but with a spike used to determine the amount of quenching of fluorescence. Analysts: R. Kiel and K. Edwards.
[6] Fluorimetry following fusion with $LiBO_2$ and no separation of U but a spike used to determine the amount of quenching of fluorescence. Analysts: R. Kiel and K. Edwards.
[7] Fluorimetry following leaching of sample with boiling $HClO_4$ and HNO_3 and no separation of U but a spike used to determine the amount of quenching of fluorescence. Analysts: R. Kiel and K. Edwards.
[8] γ-ray spectrometry. Analyst: C. A. Bush.
[9] Analyst, A. Bartel.
[10] Analyst: J. S. Stuckless.

the pairs of uranium values agree within the limits of precision of the 2σ level, and that nine of the pairs of thorium values agree within the limits of precision at the 2σ level. Although the α-spectrometry technique is adequately accurate for most geologic problems, it is a relatively expensive and time-consuming technique and therefore is not well suited for routine geochemical exploration. However, because the technique can measure the amounts of uranium and the long-lived daughter isotopes in the uranium decay chain (^{238}U, ^{234}U, ^{230}Th), it is useful for some specific problems that require measurements of radioelement disequilibria. (See, for example, Stuckless and Ferreira, 1976.)

Delayed neutron.—Twenty-two samples were analyzed for uranium and thorium by delayed neutron and by isotope dilution using mass spectrometry (table 1, figs. 1 and 2). All but two of the pairs of uranium values agree within the limits of precision at the 2σ level (fig. 1). The precision of the two techniques is similar except for two samples with low uranium contents and high (>15) Th/U ratios. For these samples the correction for the thorium interference adds a

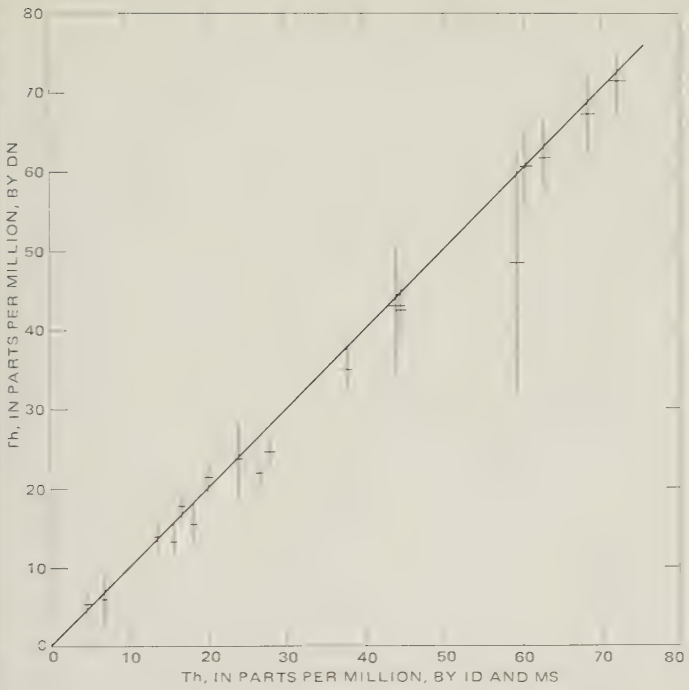

FIGURE 2.—Arithmetic plot of thorium contents obtained by the delayed-neutron (DN) technique versus those obtained by isotope dilution (ID) in combination with mass spectrometry (MS). A 1:1 line is shown for reference. Symbol sizes are equal to a 2σ error. Four samples for which the uranium interference with the thorium value (obtained by the delayed-neutron technique) was excessive have been omitted.

large uncertainty to the measured uranium content (fig. 1). The delayed-neutron technique is rapid, and commercially available services are relatively inexpensive. These features, combined with the precision and accuracy of the technique, make it a highly desirable tool for analyzing granitic samples.

Thorium contents obtained by the delayed-neutron technique are not as precise or accurate as the uranium determinations, but the results are still adequate for most geochemical exploration purposes. Of the 22 analyzed pairs, 4 contained too much uranium to allow an accurate measurement of the thorium content by the delayed-neutron technique. Of the remaining 18 pairs only 2 pairs of thorium values exhibited a statistically significant difference (fig. 2).

It should be noted that the precision and accuracy of the delayed-neutron technique shown here is due in part to the type of reactor used and the composition of geologic standards used for calibration. For example, samples that contain large amounts of neutron-moderating light elements, such as carbon and hydrogen, can yield erroneous values for uranium and thorium because of in situ thermalization of neutrons, but for granites this is not a problem.

Gamma-ray spectrometry.—Thirty-two samples were analyzed for RaeU and thorium by γ-ray spectrometry and for uranium and thorium by isotope dilution in combination with mass spectrometry (table 1). An additional 20 samples were analyzed for RaeU and uranium by γ-ray spectrometry and the delayed-neutron technique respectively. The results of all 52 pairs of analyses are shown in figure 3. Sealed-can γ-ray spectrometry is a very precise technique, but actually gives a measurement of ^{226}Ra. It yields a uranium value only if there is secular equilibrium within the upper part of the ^{238}U decay chain. RaeU is significantly different (greater than 2σ) from uranium in 34 of our 52 granitic samples and this difference would lead to errors ranging from +100 to −34 percent in the calculated uranium values. Most of the RaeU values are lower than actual uranium values by 15–20 percent.

Although RaeU may not yield an accurate measurement of the uranium content, the results obtained by sealed-can γ-ray spectrometry may prove useful in geochemical exploration programs. Significant differences between uranium and RaeU may indicate the presence of labile uranium which in turn may identify a particular granite as a likely source rock for nearby sedimentary uranium deposits or as a favorable rock for in situ leaching of uranium (Stuckless and Ferreira, 1976).

A second benefit of γ-ray spectrometry as an exploration tool is that one measurement yields thorium and potassium contents as well as RaeU values. Granitic rocks with high uranium contents also tend to have high thorium and potassium contents. These two elements are not as easily leached from surface outcrops as is uranium and therefore may be useful in the identification of high-uranium granite where extensive surface leaching has removed much of the original uranium.

Although one-third of the 29 pairs of thorium values obtained by γ-ray spectrometry and isotope dilution in combination with mass spectrometry do not agree within the limits of precision at the 2σ level (fig. 4), the true error is not very large. Consequently the results are sufficiently accurate for most geochemical purposes.

Total beta-gamma count.—Fifteen samples that contained more than 10 ppm U were analyzed for eU by total β-γ counting. For those samples that contained less than 100 ppm U, the eU values were 61 to 420 percent higher than the uranium values (table 1). This is largely due to the β-γ activity contributed by the thorium decay series and ^{40}K. However, one sample (No.

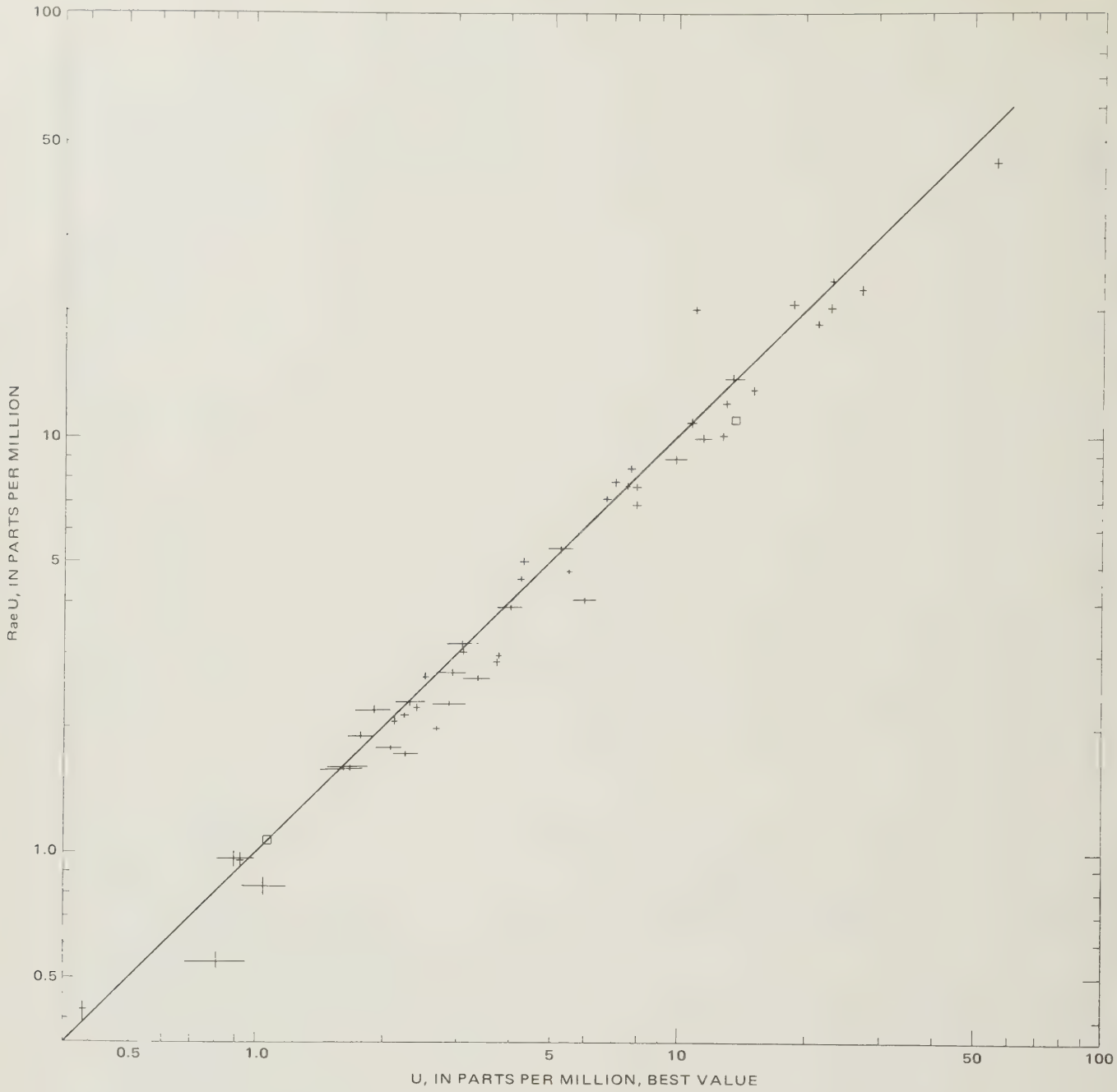

FIGURE 3.—Log-log plot of radium equivalent uranium (RaeU) obtained by sealed-can γ-ray spectrometry versus uranium. Thirty-two of the uranium values were obtained by isotope dilution in combination with mass spectrometry. The remaining 20 values were obtained by the delayed-neutron technique. The latter values can generally be identified by the larger error bars. All error bars represent a 2σ error. A 1:1 line is shown for reference. The values for two samples have been divided by 100; these are indicated by boxes.

230.95) contained only small amounts of thorium and potassium (tables 1 and 2), and the high eU value is attributed to excess ^{226}Ra. Although total β-γ counting is a rapid and simple technique for which counting statistics can be adjusted to yield good precision, the accuracy of the technique as an estimate of uranium content in granitic rocks is very poor. We therefore conclude that total β-γ counting has only limited usefulness in uranium exploration programs in granitic terrains.

Fission track.—Ten samples that represented the entire range of uranium concentrations were chosen for fission-track analysis. Only 3 of the 10 samples yielded uranium concentrations that agree with those obtained

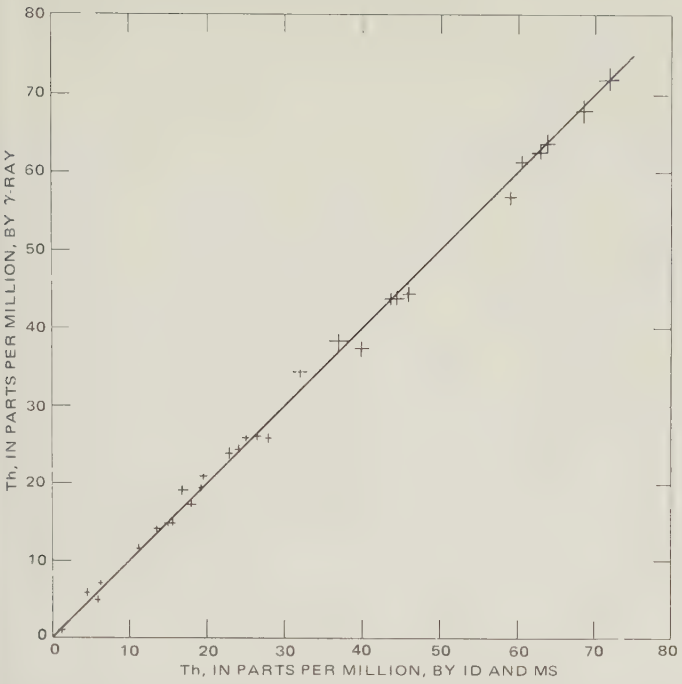

FIGURE 4.—Arithmetic plot of thorium contents obtained by sealed-can γ-ray spectrometry versus thorium contents obtained by isotope dilution (ID) in combination with mass spectrometry (MS). A 1:1 line is shown for reference. Symbol sizes are equal to 2σ errors. Three samples for which uranium interference with the thorium values (obtained by γ-ray spectrometry) was excessive have been omitted.

by isotope dilution in combination with mass spectrometry within the expected limits of error (table 1). This poor agreement is partly due to the problem of adjusting irradiation parameters to fit samples whose uranium concentrations varied more than 4 orders of magnitude. Furthermore, such a small amount of sample is actually measured (<0.1 g) that splitting errors are no longer insignificant. Finally, a single high-uranium grain may create many fission tracks that cannot be resolved and are thus counted as a single track. The latter two problems are particularly serious for coarse-grained rocks and to a lesser extent for disseminated-type ore deposits. Thus, the usefulness of the fission track using spark-counting technique is limited to certain volcanic rocks, water, and other geologic samples that lack point-source concentrations of uranium and gross inhomogeneities.

Fluorometry.—Uranium values obtained by the fluorometric method are strongly dependent on the procedures used for chemical preparation of the sample. Many granite samples will not release all their uranium unless the granite is completely dissolved. Thus, partial attacks, such as with 4 N HNO_3 or fusion with NaOH, may yield low values for uranium. Several elements that are common in granites can interfere with fluorescence measurements if they are present in the final bead in large enough amounts. Therefore, either a chemical separation or a determination of the amount of interference is necessary if an accurate determination of concentration is to be made. Four different sets of fluorometric determinations are reported in table 1 and results are summarized in figure 5. A fifth set of determinations in which the samples were fused with NaOH and uranium was extracted with ethyl acetate is not reported. These results were lower than or equal to those obtained by dissolution and uranium extraction and will not be discussed further.

The two sets of fluorometric data that were obtained following the HF digestions exhibit a strong bias toward values that are too low (fig. 5*A* and *B*). We therefore conclude that this method does not allow the quantitative recovery of uranium from the sample. Possible explanations include: (1) loss of uranium

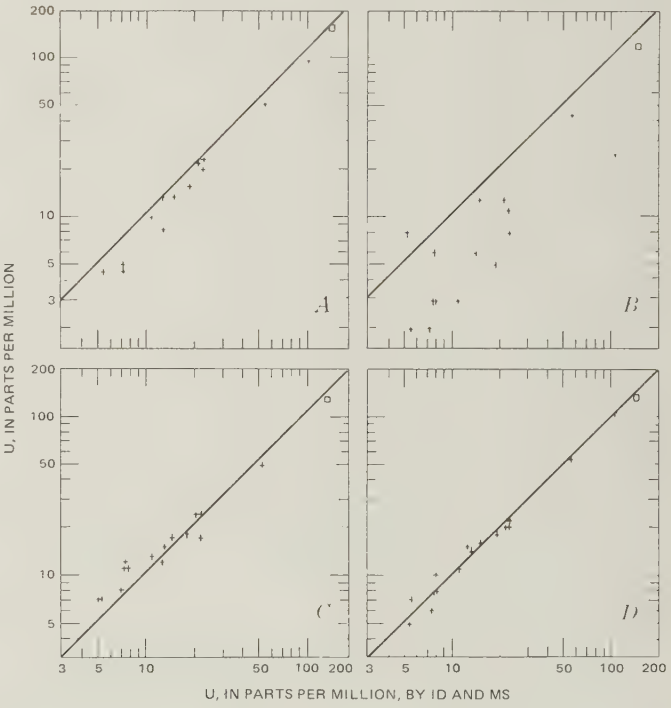

FIGURE 5.—Log-log plots of uranium contents obtained by the fluorometric method versus those obtained by isotope dilution (ID) and mass spectrometry (MS). *A*, digestion of the sample in HF, $HClO_4$, and HNO_3 and extraction of uranium; *B*, digestion of the sample in HF, $HClO_4$, and HNO_3 and spiking an aliquot so that interference of fluorescence could be examined; *C*, fusion with $LiBO_2$ and spiking an aliquot, and *D*, leaching with hot $HClO_4$, and HNO_3 and spiking of an aliquot. All plots show 5-percent error bars for the fluorometric values and a 1:1 reference line. In each plot the value of one sample has been divided by 10; this sample is shown by a square.

from the sample as UF_6 at the time the sample is dried, (2) loss of uranium with the dissolution residue as an insoluble phase, and (3) loss of uranium from the final solution by coprecipitation with $Zr(OH)_4$. Until the problems associated with the total digestion mode of sample attack are resolved, we believe that fluorometry is best used with other types of sample attack.

Fluorometric uranium values that were obtained following either fusion with $LiBO_2$ or leaching with oxidizing acids agreed better with those obtained by isotope dilution using mass spectrometry (fig. 5*C* and *D*). Only 2 of the 16 uranium values obtained following the $LiBO_2$ fusion agree with the expected value within the expected limits of precision, but 7 values agree within ±10 percent. Most of the samples that show a larger disagreement contain less than 10 ppm U. Some of the apparent disagreement can therefore be ascribed to the difference in the number of significant figures. Thus, the accuracy of the technique for granitic samples that contain more than 10 ppm U appears to be ±10 percent.

Of the 17 fluorometric uranium values that were obtained following the hot oxidizing acid leach of the sample, 14 agree with the expected value within ±10 percent. With one exception, the larger disagreement is for samples that contain less than 10 ppm U. The good accuracy obtained by the hot oxidizing acid leach method is somewhat surprising because the leach was not expected to affect some of the uranium-bearing minerals such as zircon.

The results of our study suggest that the fluorometric technique is sufficient for most routine analyses. Its usefulness is limited by somewhat poorer precision and accuracy relative to delayed-neutron or isotope-dilution analyses. This is especially true for samples that contain less than 20 ppm U. Our results also suggest that the inclusion of control samples that are mineralogically similar to the unknown samples is advisable to check the accuracy of the fluorometric technique as applied to a specific problem.

Potassium analyses.—A thorough comparison of potassium analyses by the atomic absorption and flame-photometric techniques is given by Dalrymple and Lanphere (1969). Both of these techniques have a reported precision and accuracy of approximately ±1 percent. Our results for flame photometry and atomic absorption (table 2) do not agree within this limit of precision, especially for potassium contents of less than 1 percent. However, the absolute differences are small, and therefore we feel that the accuracy is adequate for application to problems associated with geochemical prospecting for uranium in crystalline rock.

TABLE 2.—*Potassium determinations, in weight percent, for samples from the Granite Mountains, Wyo.*

[*, poor precision due to interference of U and Th; -, no data]

Sample No.	F.P.[1]	γ-Ray[2]	A.A.[3]	A.A.[4]
MS-1	0.058	0.06	0.071	0.07
SD-8	.053	.01*	.066	-
50.75	.20	.11*	.23	.25
61.63	.43	.54	.49	.44
230.95	-	.46	-	.46
352.53	.59	.59	.63	.66
GR-4	-	.78	-	.83
GR-5	.97	.95	.98	1.00
GR-3	-	2.07	-	1.91
DDH-4	2.18	2.27	2.25	2.16
SD-11	3.04	3.09	2.98	3.16
CR-1-41.0	-	3.71	-	3.65
SD-17	4.06	4.03	4.07	4.07
50.11	-	2.95*	-	4.15
PD-5	4.37	4.50	4.14	-
CR-26-60.6	-	4.21	-	4.32
404.29	-	4.37	-	4.48
251.77	-	4.67	-	4.57
87.17	-	4.56	-	4.57
CR-14-57.2	-	4.47	-	4.65
225.40	4.67	4.87	4.65	4.65
81.62	4.86	5.25	-	-
383.22	4.87	5.03	-	-
SDNE-12	5.20	5.22	5.2	4.82
232.87	5.42	5.60	-	-
308.52	5.77	5.90	5.75	5.81
256.70	5.90	6.25	5.84	5.89
219.73	5.92	6.15	-	-

[1]F.P. = flame photometry; analyst: Wayne Mountjoy.
[2]γ-ray = γ-ray spectrometry; analyst: C. A. Bush.
[3]A.A.[1] = atomic absorption; analyst: Wayne Mountjoy.
[4]A.A.[2] = atomic absorption as part of rapid rock analysis; analysts: H. Smith and S. Botts.

Figure 6 compares the potassium values obtained by γ-ray spectrometry with those obtained by chemical methods. Where more than one chemical value was available, we have chosen to use that obtained by flame photometry. The figure shows that the γ-ray spectrometric values are in good agreement with the chemical values although a slight positive bias may exist for high (>4.5 percent) potassium contents.

CONCLUSIONS

Uranium is typically associated with thorium and potassium in igneous rocks, and therefore large-scale geochemical exploration programs for uranium can benefit from the identification of thorium and potassium anomalies. Our results show that γ-ray spectrometry is more than adequate for this purpose. In addition, γ-ray spectrometry yields RaeU values which can be used as an estimate of uranium content.

Disequilibrium within the upper part of the ^{238}U decay chain may indicate the presence of labile uranium (Stuckless and Ferreira, 1976). Labile uranium may indicate a favorable source of uranium for sedimentary traps or a potential target for commercial in situ leaching. Our results show that disequilibrium to the extent of 10 percent or more between ^{238}U and ^{226}Ra can be identified by comparing RaeU values with uranium obtained by the delayed-neutron technique, and that as few as 50 samples from a particular igne-

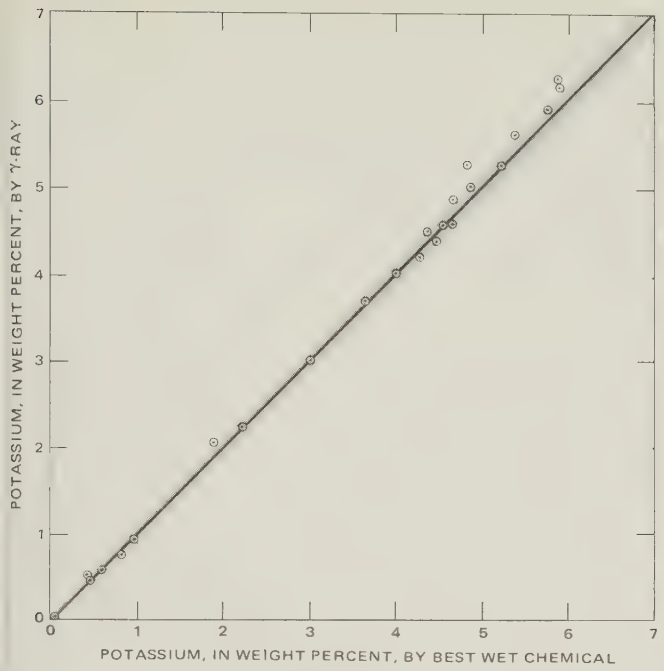

FIGURE 6.—Arithmetic plot of potassium contents by γ-ray spectrometry versus those obtained by chemical techniques. Values obtained by flame photometry have been plotted in preference to those obtained by atomic absorption when more than one chemical value for potassium was available. A 1:1 reference line is shown together with a 2σ field of error for the γ-ray spectrometric value. Stippled area represents error of $\pm$(2 percent +600 ppm).

ous unit may be needed to test for disequilibrium. We therefore suggest that the combination of delayed neutron for uranium and γ-ray spectrometry for RaeU, thorium, and potassium should provide an excellent data base for geochemical exploration for uranium in crystalline rocks.

The best technique for identifying disequilibrium in the upper portions of the uranium decay chain is α-spectrometry because this technique in combination with isotope dilution yields quantitative and precise measurements of the amounts of ^{238}U, ^{234}U, and ^{230}Th. These measurements can identify disequilibria that are greater than 4 percent. However, this technique is time consuming and expensive and is best reserved for very detailed studies.

Our evaluation of the fluorometric method shows that it is still an excellent technique for determining uranium. It cannot be used in conjunction with γ-ray spectrometry to identify ^{238}U–^{226}Ra disequilibria that are less than 15 percent, particularly if uranium contents are less than 10 ppm. However, if the proper care is taken to obtain a quantitative recovery of uranium from the sample, results should be adequately accurate for a wide variety of applications, such as assays in conjunction with mining operations or analyses of samples from identified target areas. In addition the fluorometric method has been proved to be an effective exploration tool in hydrogeochemical programs.

REFERENCES CITED

Becken, K., 1972, Dosimetry applications of track etching: Topics in Radiation Dosimetry, Supp. 1, p. 79–142.

Bunker, C. M., and Bush, C. A., 1966, Uranium, thorium, and radium analyses by gamma-ray spectrometry (0.184–0.352 million electron volts), *in* Geological Survey research 1966: U.S. Geol. Survey Prof. Paper 550–B, p. B176–B181.

——— 1967, A comparison of potassium analyses by gamma-ray spectrometry and other techniques, *in* Geological Survey research 1967: U.S. Geol. Survey Prof. Paper 575–B, B164–B169.

Cross, W. G., and Tommasino, L., 1970, A rapid reading technique for nuclear particle damage tracks in thin foils: Radiation Effects, v. 5, p. 85–89.

Dalrymple, G. B., and Lanphere, M. A., 1969, Potassium-argon dating—principles, techniques and applications: San Francisco, W. H. Freeman and Company, 258 p.

Garner, E. L., Machlan, L. A., and Shields, W. R., 1971, Standard reference materials—uranium isotopic standard reference materials: U.S. Natl. Bur. Standards Spec. Pub. 260–27, 162 p.

Grimaldi, F. S., May, Irving, Fletcher, M. H., and Titcomb, Jane, compilers, 1954, Collected papers on methods of analysis for uranium and thorium: U.S. Geol. Survey Bull. 1006, 184 p.

Ingamells, C. O., Engels, J. C., and Switzer, P., 1972, Effect of laboratory sampling error in geochemistry and geochronology, *in* Geochemistry, Sec. 10: Internat. Geol. Cong., 24th, Proc., Program 24, p. 405–415.

Millard, H. T., Jr., 1976, Determinations of uranium and thorium in USGS standard rocks by the delayed neutron technique, *in* Flanagan, F. J., ed., Description and analyses of eight new USGS rock standards: U.S. Geol. Survey Prof. Paper 840, p. 61–65.

Rosholt, J. N., Doe, B. R., and Tatsumoto, Mitsunobu, 1966, Evolution of the isotopic composition of uranium and thorium in soil profiles: Geol. Soc. America Bull., v. 77, no. 9, p. 987–1004.

Rosholt, J. N., Zartman, R. E., and Nkomo, I. T., 1973, Lead isotope systematics and uranium depletion in the Granite Mountains, Wyoming: Geol. Soc. America Bull., v. 84, no. 3, p. 989–1002.

Shapiro, Leonard, and Brannock, W. W., 1962, Rapid analysis of silicate, carbonate, and phosphate rocks: U.S. Geol. Survey Bull. 1144–A, 56 p.

Stuckless, J. S., Bunker, C. M., Bush, C. A., Doering, W. P., and Scott, J. H., 1977, Geochemical and petrologic studies of a uraniferous granite from the Granite Mountains, Wyoming: U.S. Geol. Survey Jour. Research, v. 5, no. 1, p. 61–81.

Stuckless, J. S., and Ferreira, C. P., 1976, Labile uranium in granitic rocks, *in* International symposium on exploration of uranium ore deposits, Proc. Symposium. (In press.)

Suhr, N. H., and Ingamells, C. O., 1966, Solution technique for analysis of silicates: Anal. Chemistry, v. 38, no. 6, p. 730–734.

Tatsumoto, Mitsunobu, 1966, Isotopic composition of lead in volcanic rocks from Hawaii, Iwo-Jima, and Japan: Jour. Geophys. Research, v. 71, no. 6, p. 1721–1733.

Jour. Research U.S. Geol. Survey
Vol. 5, No. 1, Jan.–Feb. 1977, p. 93–101

SOME CHARACTERISTICS OF PELE'S HAIR

By WENDELL A. DUFFIELD, EVERETT K. GIBSON, Jr.,[1] and
GRANT H. HEIKEN,[2] Menlo Park, Calif., Houston, Tex., Los Alamos, New Mex.

Abstract.—Pele's hair is a filamentous variety of brown sideromelane glass that forms during eruption of basaltic lava. Strands of Pele's hair form from droplets of lava that are spun or stretched into filaments during quenching, and others may form as chilled streamers of lava. Common elongate vesicles, sometimes twisted, indicate extreme stretching and twisting during hair formation. Hair diameter ranges from about 1 to 300 micrometres. Refractive index of hairs decreases with hair diameter and is most probably a function of the process of formation rather than chemical composition. Masses of Pele's hair form natural spun-glass filters that trap small particles and serve as sites for sublimate deposition. Such deposition may begin even while hair is falling to the ground through an eruption fume cloud. Sublimates include carbonates, sulfates, sulfur, and less commonly hydrocarbons, thus complicating the interpretation of volatiles in Pele's hair in terms of original magmatic constituents. Vesicles, which provide the most nearly pure samples of magmatic volatiles, contain mostly H_2O and CO_2.

During vigorous gas-driven eruption of basaltic lava, a variety of pyroclastic materials may form, inincluding fine strands of brown sideromelane glass known as Pele's hair. Relatively little Pele's hair forms compared with the bulkier pyroclastic products, and much of this hair is quickly dispersed downwind during eruption. Masses of hair may collect around active vents, but these commonly are quickly covered by subsequent flows that may remelt the glass strands. Thus, there is little chance for the preservation of sizeable deposits of Pele's hair; such samples must be collected at the time of hair formation or shortly thereafter.

We collected several samples of Pele's hair that formed during eruptions of Kilauea Volcano in 1969–72. Most samples were only a few hours to several days old when collected; some were gathered while strands of Pele's hair, together with clots of spatter and scoria, fell on and around us downwind from lava fountains. Subsequent studies of hair morphology, refractive index, chemical composition, and sublimate coatings indicate that caution must be used in comparisons with bulkier though contemporaneous or closely allied eruption products.

[1] National Aeronautics and Space Administration.
[2] Los Alamos Scientific Laboratory.

HAIR FORMATION AND MORPHOLOGY

Near-surface acceleration due to expansion of gases (Shaw and Swanson, 1970) drives jets of basaltic lava that partly solidify in air to form droplets, irregularly shaped clots, and glass threads (Pele's hair). According to previous workers (Wentworth, 1938; Williams and McBirney, 1969; Heiken, 1972, 1974), Pele's hair forms from droplets that are stretched into threads. Hairs with attached droplets (fig. 1), known as Pele's tears, indicate that some strands form in this manner. Most strands are free of such droplets but have broken ends and thus may have formed from droplets or from chilled streamers of melt. Isard (1971) calculated that such streamers should break up into droplets only

FIGURE 1.—Photomicrograph of hair attached to clot of spatter. Note roughly circular outline of exposed vesicles on clot and elongate outlines of those on hair, indicative of stretching during hair formation.

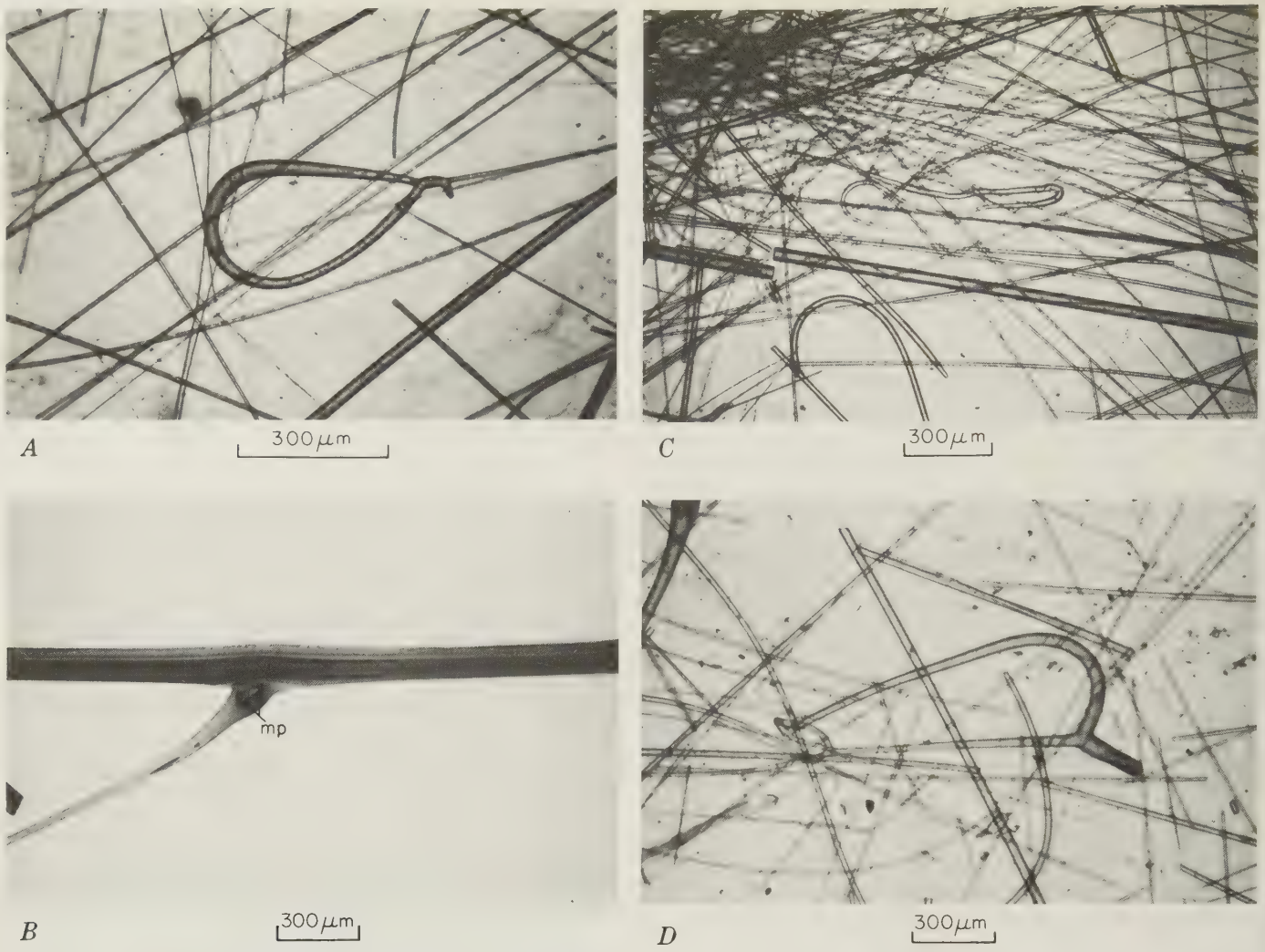

FIGURE 2.—Photomicrographs of Pele's hair showing common shapes. *A*, Closed loop. *B*. Branching. Note microphenocrysts (mp) where branch is attached to main hair, and small, nearly invisible branch between the two larger filaments. *C*, Mass of rods including S- and hook-shaped hairs. *D*, Tuning fork.

if the viscosity of the material is less than 10^3 poises, and the work of Shaw, Peck, Wright, and Okamura (1968) suggests that much of the lava at Kilauea has a viscosity of 10^3 poises or less during eruption. Observation of Kilauea lava fountains, however, typically indicates simultaneous formation of Pele's hair and droplets. The formation of all such particles probably is a complex process involving rapidly changing temperature (and therefore viscosity) in a turbulent, expanding eruption fountain that is not readily amenable to quantitative analysis.

We have also observed the formation of Pele's hair at a few-metres-high cascade in a lava river and at a lava falls plunging as much as 120 m through violent updrafts into a pit crater. Almost certainly, some Pele's hair forms wherever clots of low-viscosity lava are introduced into strong air currents, and because these conditions occur most frequently at erupting vents, most Pele's hair is formed there.

Pele's hair has been described by several earlier workers (for example, Krukenberg, 1877; Dana, 1891; Wentworth and Macdonald, 1953). Typically, Pele's hair is roughly circular in cross section with a diameter between about 1 and 300 micrometres. In detail, the basic cylindrical form exhibits numerous modifications, including bent, bifurcated, and pretzellike shapes, and changes in diameter as much as an order of magnitude either abruptly over lumps caused by microphenocrysts and vesicles or gradually from one end of a strand to another (fig. 2). The interiors of hairs are also varied. Solid glass cylinders occur, but spherical to elongate vesicles are common. Elongate vesicles form capillary-like tubes parallel to hair axes

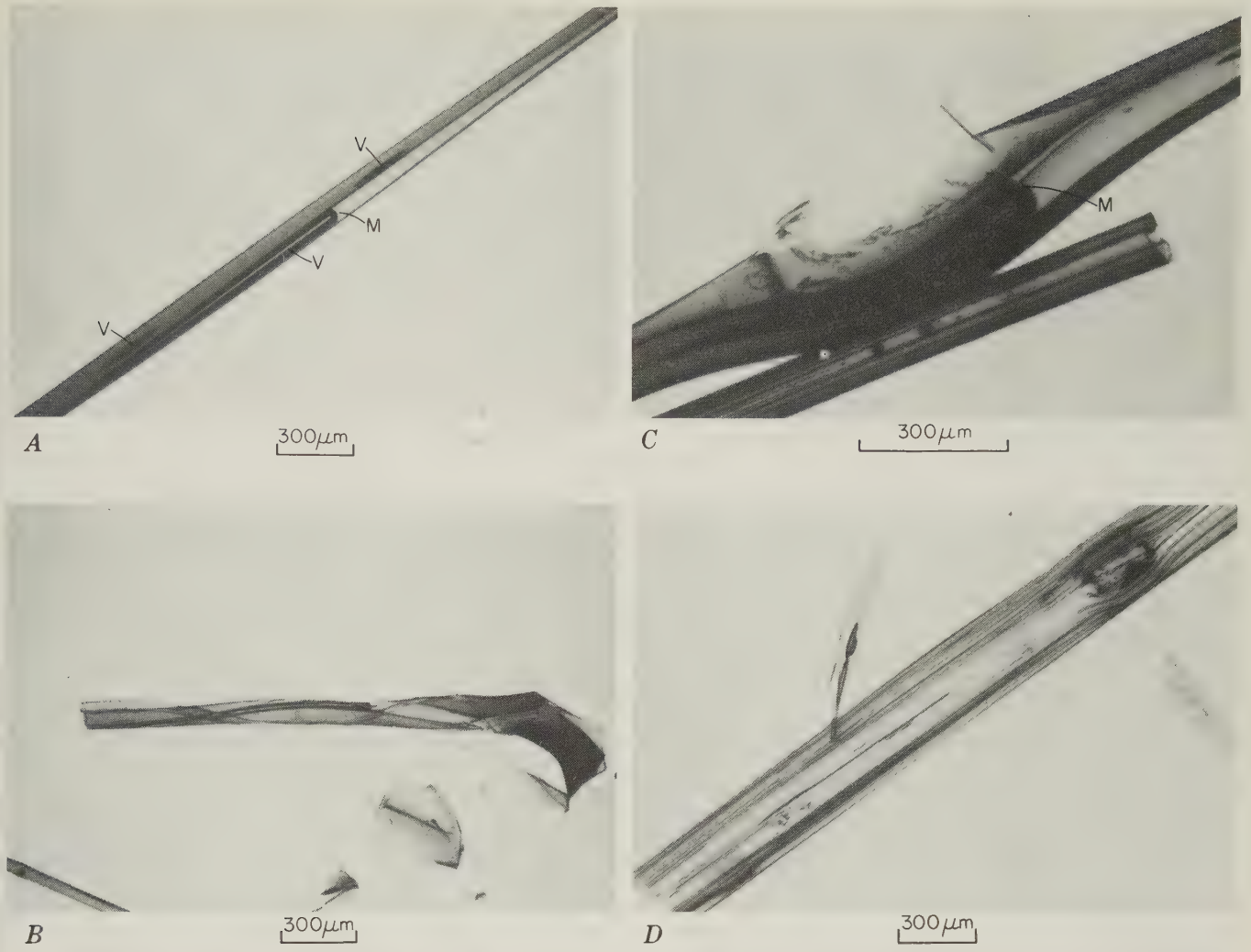

FIGURE 3.—Photomicrographs of Pele's hair with vesicles. *A*, Elongate vesicles (V) parallel to strand of hair. The longest vesicle was broken during sample preparation and partly filled with resin which formed a meniscus (M). *B*, Helical vesicle, indicative of twisting during hair formation. *C*, Thin-walled ovoid vesicle broken during mounting and longer vesicle with meniscus (M) in upper hair. End of lower hair shows pipelike shape caused by large near-axial vesicle. *D*, Highly ribbed surface caused by multiple, near-surface elongate vesicles. Vehicles curve around microphenocryst (mp) alined with long axis of hair.

and occur both singly and multiply, commonly producing a thin-walled tube or bundle of tubes (fig. 3).

At room temperature and pressure, vesicles contain a partial vacuum, but at higher temperatures vesicles burst and release mostly H_2O and CO_2. Abundant vesicles probably indicate initial high volatile content of the magma.

Some strands contain single crystals or clots of crystals as phenocrysts or microphenocrysts that commonly cause lumps in hair of otherwise rather uniform diameter. The longest dimension of a crystal generally is alined with the hair axis (fig. 3*D*). Both elongate vesicles and alined crystals attest to extreme stretching during the process of hair formation. The capillary vesicles suggest axial strain of several orders of magnitude relative to a presumably spherical gas bubble present in the lava before the stretching and solidification associated with hair formation. Helical vesicles also indicate some twisting (fig. 3*B*).

REFRACTIVE INDEX AND CHEMICAL COMPOSITION

The refractive indices of the glassy parts of about 90 samples of Pele's hair, spatter, pumice, and lava flows that formed during the 1969–71 Mauna Ulu eruption (Swanson and others, 1971) are summarized in figure 4. The range in refractive index shown by all types of materials is 0.031, although most values fall between 1.599 and 1.606, a range of only 0.007. Almost without exception, the refractive index of fine

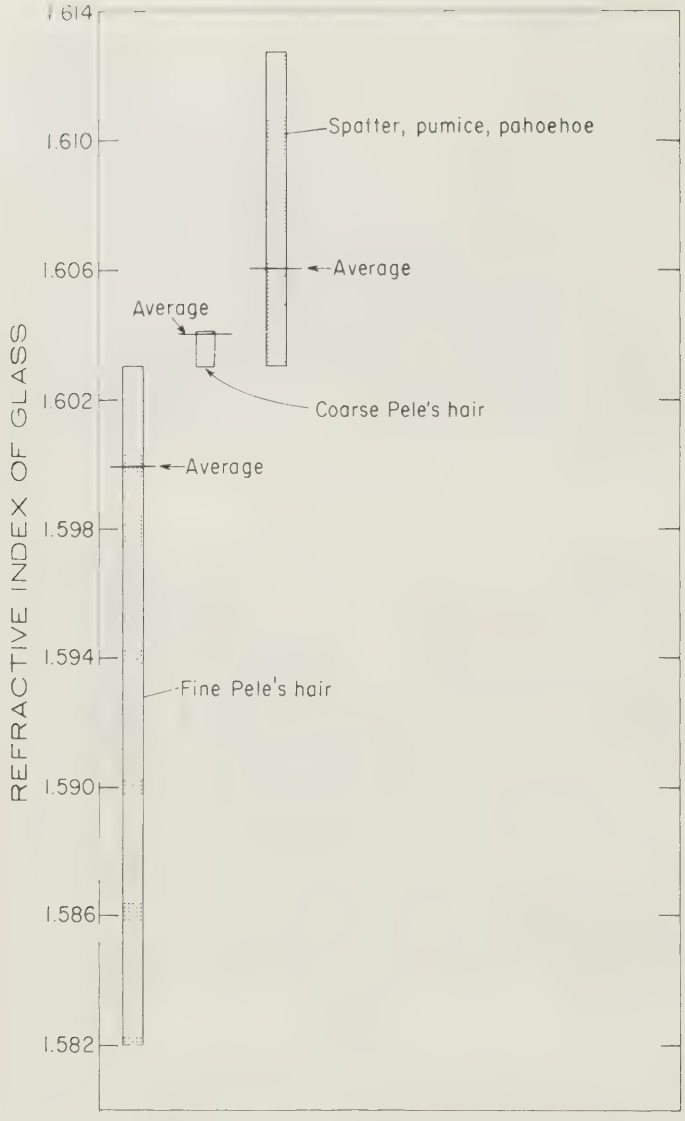

FIGURE 4.—Refractive indices of glassy parts of eruption products formed during 1969–71 eruption of Mauna Ulu, Kilauea Volcano, Hawaii. Indices were determined with sodium light in immersion oils that were checked periodically with an Abbey refractometer and corrected for temperature. Error of determination is estimated to be ±0.002. Samples were washed in distilled water to remove sublimate coating and then hand crushed. Only broken interior surfaces were used for refractive-index determinations.

hair (arbitrarily defined as less than about 75 μm in diameter) is less than that of coarse hair which in turn is less than that of most of the bulkier materials. These relations are further illustrated by examination of contemporaneous eruption products.

Thirteen sets of contemporaneous eruption products were obtained by hand sorting field-collected masses of Pele's hair into fine hair, coarse hair, and droplets that were attached to some strands of hair or clots of spatter caught in the mass of hair. Without exception, for each set of contemporaneous products, the finest material has the lowest refractive index (fig. 5). Furthermore, the hair of smallest diameter (sample PH–9) has the lowest refractive index of all studied material. In general, unambiguous intersample comparisons between refractive index and minimum dimension of particles are precluded by the estimated standard error (±0.002) in refractive-index determination and overlap in hair size caused by normal variation in diameter, even along individual hairs. Nonetheless, the consistency of the data (fig. 5) indicates that a direct relation between refractive index and the original minimum dimension of particles exists for all studied samples.

The refractive index of glass from fused or naturally glassy volcanic rock is commonly used to determine the silica content of the glass (George, 1924); silica increases as refractive index decreases. The refractive indices of a sample of Pele's hair (1.598) and droplets (1.604) broken from the ends of this hair suggest that the droplets are relatively poor in silica. However, chemical analyses (table 1) show that, within analytical precision, silica content is nearly the same for these two contemporaneous materials. Many electron microprobe analyses for silicon, iron, and magnesium were made along individual strands of Pele's hair that showed great axial variation of diameter. No measureable changes in these elements were found along these strands (B. A. Morgan, oral commun., 1973), thus suggesting variation in refractive index is caused by something other than major-element chemistry.

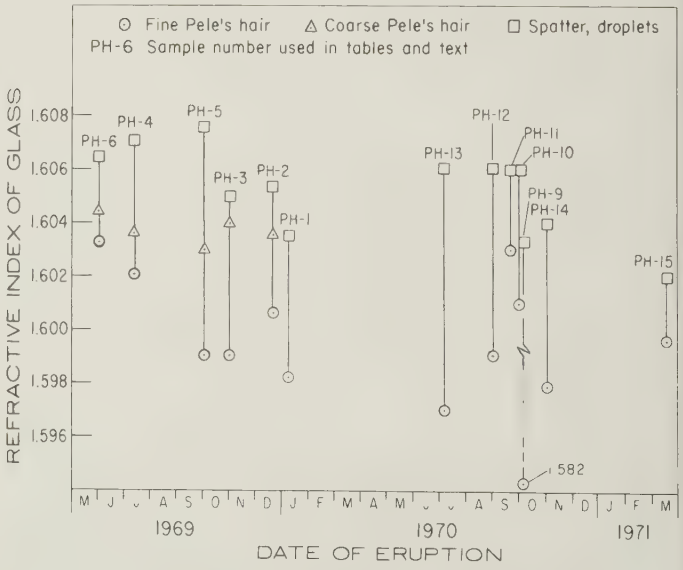

FIGURE 5.—Refractive indices of contemporaneous glassy eruption products of differing original dimension.

TABLE 1.—*Chemical analyses of Pele's hair (PH–1) and droplets (PH–1S) broken from this hair*

[Analytical methods are described in Shapiro and Brannock (1962), supplemented by atomic absorption tests; analyst, P. L. D. Elmore]

	PH-1	PH-1S
SiO_2	50.6	50.7
Al_2O_3	13.7	13.0
Fe_2O_3	.60	.90
FeO	10.0	10.0
MgO	7.6	9.5
CaO	11.3	10.0
Na_2O	2.2	1.9
K_2O	.51	.41
H_2O^+	.27	.37
H_2O^-	.06	.00
TiO_2	2.3	2.1
P_2O_5	.30	.28
MnO	.18	.19
CO_2	.02	.01
	99.60	99.40

Ross and Smith (1955, 1961) have shown that the refractive index of volcanic glass is a function of water content and state of oxidation of iron, as well as silica content. The presence of hydrated minerals, as firmly attached sublimate coatings, and vesicles that contain water vapor precluded a test of possible control of refractive index by differences in water content of the glass itself. Change in refractive index related to oxidation state of iron is also untested, but it seems unlikely that oxidation state of iron in Pele's hair and attached droplets would differ much if at all. Well-known properties of manmade glass fibers suggest that the refractive index of Pele's hair is primarily a function of the manner in which the hair formed.

Manmade glass fibers have many properties that differ from bulk glass of the same composition (Weyl and Marboe, 1964). For example, tensile strength is higher, and the density and refractive index are lower (Slayter, 1952). These differences are attributed to marked contrasts in the cooling histories of fiber versus bulk glass, with solidification under stress (Weyl and Marboe, 1964) and relatively high rates of cooling (Slayter, 1952) as important factors in determining the properties of the fibers. The shapes of Pele's hair and its contained vesicles attest to extreme stretching, bending, and twisting during formation of the hair. Furthermore, the most finely attenuated strands have the lowest refractive index, which is consistent with the idea that rate of cooling as well as state of stress during cooling controls refractive index of the resulting glass. Thus we suggest that our observations of refractive index of Pele's hair are best explained by the manner in which hairs form, with only possible minor effects related to chemical composition.

SUBLIMATES ON HAIR SURFACES AND VOLATILES IN VESICLES

Masses of Pele's hair that line the throats of fumaroles or rest on warm fuming lava flows become encrusted with sublimates. Generally, hair collected only minutes after its formation shows some surficial crusts, presumably deposited from the fume cloud through which the hair drifted to the surface. After a few hours in percolating fume, hairs may become completely coated (fig. 6*A*, 6*B*). Such sublimates may cement masses of hair together and may also cement tiny basaltic spheres to strands of hair (fig. 6*C*). We studied the volatile constituents in these sublimate coatings using the methods of Gibson (1973; 1974). Briefly, we heated samples to about 1,400°C at a rate of 6°C per minute in a vacuum of 2×10^{-6} torr and routed all evolved volatiles into a mass spectrometer for identification during heating. Near the melting temperature, vesicles burst, releasing additional volatiles that also were analyzed by the spectrometer. The weight of all samples was recorded continuously during heating. Most of the weight lost below 800°C represents the release of volatiles from sublimate minerals, whereas that lost above 800°C represents mostly degassing of the basaltic glass. Typical gas release profiles are shown in figure 7. These profiles differ depending principally upon the amount and variety of sublimate material present.

Microscopic examination of sample PH–10 shows that almost no sublimate material coats these hairs. During heating, only traces of volatiles were evolved below the melting point (fig. 7*A*). About 300 parts per million of adsorbed water was released around 100°C (see H_2O spike of fig. 7*A* and percentage weight lost in table 2), and a continuous diffusional loss of water occurred between 150° and 500°C. The release of CO_2 (30–60 ppm CO_2) between 400° and 600°C suggests traces of carbonates on hair surfaces. At the melting point of the glass (1130°±10°C), CO_2 and traces of CO were released suddenly, indicating the rupture of one or more gas-filled vesicles. Total weight loss was 2.31 percent after heating to 1400°C (table 2), with only 0.57 percent lost during heating to 800°C.

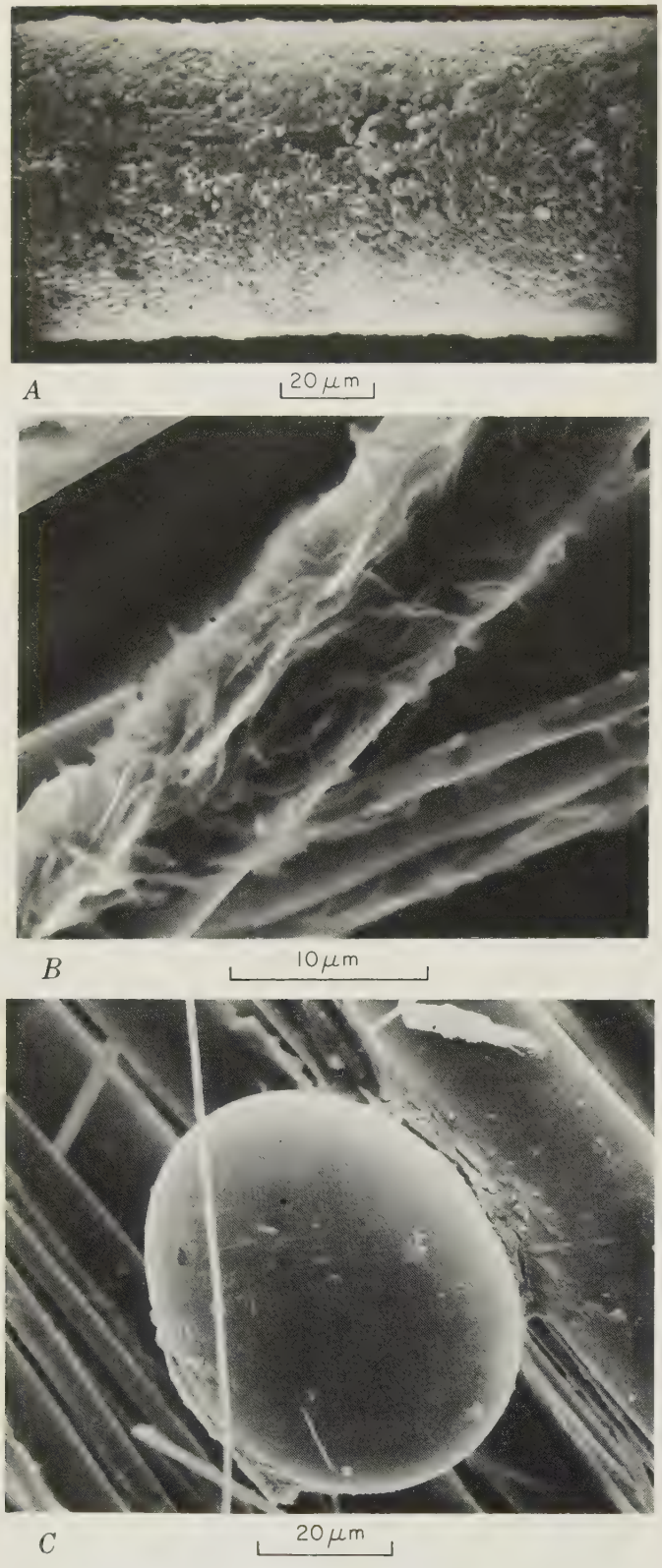

FIGURE 6.—Scanning electron micrographs of Pele's hair. *A*, Strand of hair almost completely coated with sublimate crust. *B*, Hair with feathery sublimate deposit (sulfur?) *C*, Small basaltic sphere cemented to Pele's hair by sublimate. Photomicrographs *B* and *C* by R. B. Finkelman.

Pele's hair in sample PH–14 is moderately crusted with sublimates. About 0.35 percent by weight of adsorbed water was released below 200°C (fig. 7*B*). The release of CO_2 between 400° and 550°C indicates a carbonate phase(s) in the sublimate crust. Similarly, the presence of a sulfate phase(s) is indicated by the release of SO_2 between 400° and 550°C (gypsum?). Elemental sulfur was released between 650° and 900°C. Total weight loss was 3.44 percent upon heating to 1400°C, and melting occurred at 1130° ± 10°C (table 2).

Pele's hair in sample PH–9 is completely coated with sublimates (fig. 6*A*). Below 300°C nearly 0.65 percent water was released (table 2 and fig. 7*C*). Methane and other hydrocarbons were released between 150° and 250°C. As with PH–14, the release of CO_2 and SO_2 between 400° and 550°C indicates the presence of carbonate and sulfate phases in the sublimate crust. A second release of CO_2 between 600° and 700°C suggests the presence of another carbonate phase, and additional CO_2 at about the melting temperature suggests gas release from vesicles. Microscopic sulfur crystals were melted and released as S_2 gas between 750° and 1000°C. Total weight loss was 7.03 percent after heating to 1400°C, with melting at 1120° ± 10°C.

DISCUSSION

Descriptions of the gas-release profiles for all studied samples are listed in table 3. The most extensively crusted samples give complex gas-release profiles that indicate the presence of sulfur, carbonates, sulfates, and in two samples, hydrocarbons in this crust, whereas hair with virtually no sublimates releases mostly H_2O and CO_2.

Gases released from such fresh uncrusted hair should represent a reasonably pure sample of the gases escaping from the lava at the time of eruption. Muenow (1973), reporting on gas-release studies of Pele's tears from eruptions of Kilauea in 1970–71, noted that the typical gas released from Pele's tears contained about 95 percent H_2O, 3.5 percent CO_2, 1 percent SO_2 (mole percent compositions), and traces of organic constituents. The gas release profiles for Pele's hair with sublimate coating are most similar to the profiles reported by Muenow (1973), suggesting that his samples included sublimates. In particular, samples of fresh Pele's hair did not evolve CO_2 as did Muenow's samples for the temperature interval 700°–800°C, and methane and other hydrocarbons were present only in Pele's hair that was heavily crusted with sublimates. Apparently the surfaces of small particles of volcanic glass are sites for the condensation and deposition of a wide variety of low-temperature minerals, even as

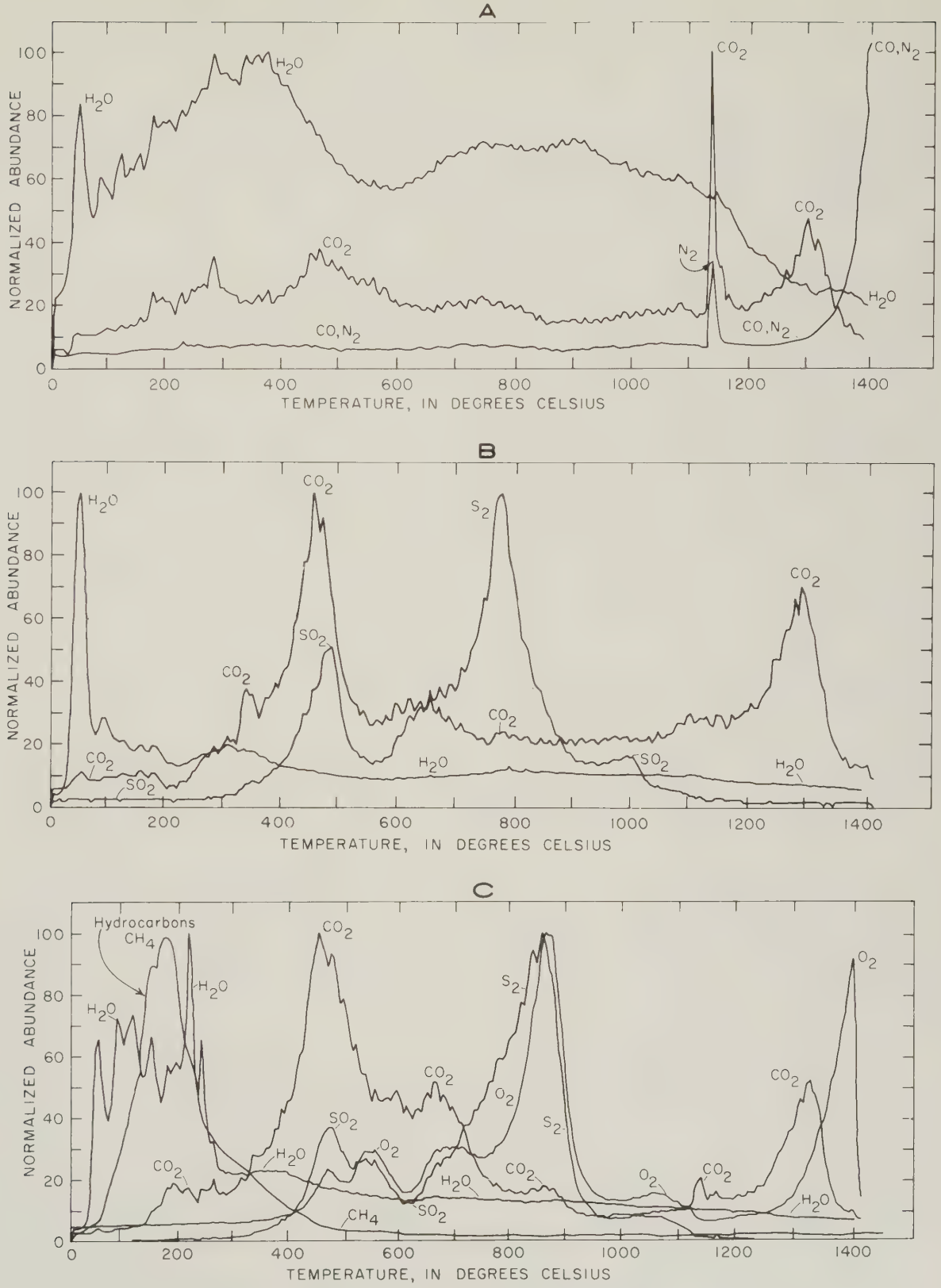

FIGURE 7.—Gas-release profiles of Pele's hair. See table 3 for further discussion. *A*, PH–10, virtually no sublimates. *B* PH–14, moderately coated with sublimates. *C*, PH–9, extensively coated with sublimates.

TABLE 2.—*Percentage weight lost from Pele's hair during heating at 6°C per minute under a vacuum of about* 2×10^{-4} *torr*

Sample No.	PH-5	PH-6	PH-9	PH-10	PH-14	PH-15	PH-23	PH-87	PH-87
Initial weight (milligrams)	112.43	124.38	105.02	121.68	111.76	86.28	153.76	157.69	159.07
Sublimate coating	Heavy	Virtually none	Heavy	Virtually none	Moderate	Moderate	Moderate	Heavy	Moderate
100°C	0.044		0.200	0.0329	0.231	0.336	0.026	0.044	0.006
200°C	0.133	0.008	0.646	0.107	0.351	0.406	0.052	0.082	0.013
300°C	0.276	0.016	0.932	0.230	0.411	0.533	0.098	0.127	0.019
400°C	0.480	0.040	1.179	0.296	0.642	0.684	0.124	0.165	0.019
500°C	0.720	0.048	2.053	0.403	0.899	1.159	0.150	0.203	0.031
600°C	0.872	0.064	2.595	0.452	0.976	1.298	0.156	0.228	0.044
700°C	0.960	0.096	3.013	0.510	1.122	1.425	0.228	0.247	0.063
800°C	1.085	0.129	3.412	0.567	1.259	1.553	0.280	0.292	0.088
900°C	1.218	0.169	4.230	0.608	1.404	1.669	0.306	0.336	0.126
1000°C	1.352	0.209	4.620	0.641	1.482	1,820	0.325	0.387	0.157
1100°C	1.565	0.346	4.857	0.740	1.610	2.121	0.442	0.476	0.258
1200°C	1.717	0.474	5.066	0.896	1.756	2.295	0.559	0.615	0.427
1300°C	2.144	0.981	5.504	1.282	2.175	2.747	0.891	0.964	0.780
1400°C	3.184	2.484	7.034	2.309	3.442	4.080	1.840	1.915	1.854
Melting point, ±10°C	1130°C	1120°C	1120°C	1130°C	1130°C	1120°C	1120°C	1120°C	1120°C

those particles are cooling and solidifying during eruption. Thus, interpretation of the origin of gases released on later examination is difficult.

CONCLUSIONS

Pele's hair forms by extreme stretching and twisting of lava as it cools and solidifies. This process of formation affects the refractive index of the resulting glassy strands in such a way that the refractive index decreases with diameter of the hair.

Masses of Pele's hair have a high ratio of surface area to weight and serve as natural spun-glass filters that trap small particles and provide sites for deposition of sublimate materials. Such deposition begins during initial descent of hair through its eruption fume cloud and may eventually account for as much as several percent of the total weight of a hair sample. The volatile constituents released on heating indicate that carbonates, sulfates and elemental sulfur are the most common sublimates. Water vapor and carbon dioxide are the most common volatiles released from hair with little or no sublimate coating.

Katsura (1967) believed that Pele's hair is the only material that represents a quenched sample of Hawaiian basaltic magma. It is true that Pele's hair is probably the most rapidly quenched subaerial eruption product, but the property that allows such rapid quenching (extremely small particle size) promotes similarly rapid contamination of the material; within days or hours weathering and contamination may advance to the stage at which it is virtually impossible to expose fresh interior. Bulkier glassy eruption products, such a lapilli-sized spatter, provide far better material for sampling quenched magma.

REFERENCES CITED

Dana, J. D., 1891, Characteristics of volcanoes: Dodd, Mead, and Co., New York, 399 p.

George, W. O., 1924, The relation of the physical properties of natural glasses to their chemical composition: Jour. Geology, v. 32, p. 353–372.

Gibson, E. K., Jr., 1973, Thermal analysis–mass spectrometer computer system and its application to the evolved gas analysis of Green River shale and lunar soil samples: Thermochim. Acta, v. 5, no. 3, p. 243–255.

——— 1974, Gas release study of selected volcanic ashes, *in* Heiken, G. H., An atlas of volcanic ash: Smithsonian Contr. Earth Sci., no. 12, p. 15–35.

Heiken, G. H., 1972, Morphology and petrology of volcanic ashes: Geol. Soc. America Bull., v. 83, p. 1961–1988.

——— 1974. An atlas of volcanic ash: Smithsonian Contr. Earth Sci., no. 12, 101 p.

TABLE 3.—*Descriptions of Pele's hair studied in heating experiments*

Sample Number	Site of formation	Type of activity	Date of collection	Maximum time between formation and collection	Volatiles released during heating
PH-5	Mauna Ulu	degassing lake	Sept. 29, 1969	21 hours	Water was the major gaseous phase released below 200°C and amounted to 1100-1300 ppm. Between 250 and 400°C sample lost 0.35% by weight, mostly CO_2 with traces of CO, O_2, and H_2O. Between 350° and 600°C, CO_2 from a carbonate and SO_2 from decomposition of a sulfate were released and amounted to 0.39% weight loss. After loss of low-temperature condensates sample was essentially depleted of volatiles other than reaction products formed at high temperatures. Large amounts of hydrocarbons with fragments of mass 41 were released between 250° and 400°C.
PH-6	do.	active fountain	May 27, 1969	Several hours	Sample contained a trace (less than 10-20 ppm) of H_2O adsorbed on surface, but had no surface condensates as indicated by lack of volatiles released below 800°C. Only 0.13 weight percent was lost upon heating to 800°C and only 2.48% after heating to 1400°C (with 1.5% being lost between 1300 and 1400°C).
PH-9	1/2 km S.E. of Mauna Ulu	cascading stream	Oct. 1, 1970	24 hours	Below 300°C, H_2O was the major gas phase released (around 0.65 weight percent). Between 150° and 250°C, methane was released. Release of CO_2 and SO_2 between 400° and 550°C indicates decomposition of carbonate and sulfate. A second release of CO_2 occurred between 600° and 700°C. Between 750° and 1000°C S_2 was evolved whereas SO_2 evolved at lower temperatures. The sulfur results from melting of sulfur crystals observed on surfaces of hair.
PH-10	Mauna Ulu	active fountain	Oct. 1, 1970	24 hours	Trace quantities of water (less than 20 ppm H_2O) were evolved around 100°C. A diffusion controlled loss of H_2O occurred between 150° and 500°C. Traces of sublimate carbonate are indicated by release of small amounts of CO_2 between 400° and 600°C. At melting point of glass (1130°C) CO_2 and a trace of CO were released suddenly, suggesting rupture of gas-filled vesicles.
PH-14	do.	do.	Oct. 29, 1970	24 hours	Unusually large amounts of water (0.35 weight percent) were released below 200°C. CO_2 from decomposition of carbonate was evolved between 400° and 550°C. Sulfate minerals decomposed between 440°c and 550°C and between 650° and 900°C. Both SO_2 and S_2 were evolved at higher temperatures.
PH-15	do.	degassing lake	June 16, 1971	3 months	Gas release profile is almost identical to that of PH-14. Below 200°C sample lost 0.41% water. Decomposition of sublimate carbonate and sulfate occurred between 400° and 750°C. Loss of S_2 and traces of SO_2 occurred between 850° and 1100°C. Near melting, sudden release of CO_2 and traces of CO indicated vesicle rupture.
PH-23	Kilauea Caldera	active fountain	Aug. 14, 1971	None-immediate collection	Trace of adsorbed water was released below 150°C. Sudden release of H_2O at 200°C suggests rupture of vesicles. Between 200° and 300°C vesicles containing H_2O and CO_2 ruptured causing "spikes" on gas release profiles. Evolution of SO_2 between 500° and 800°C suggests traces of sublimate sulfates, and traces of CS_2, probably a reaction product, were evolved between 700° and 1000°C. At melting point of glass (near 1120°C), CO_2 with traces of CO was released suddenly, indicating vesicle rupture.
PH-87	Rim of Makaopuhi Crater	120-m lava falls into crater	June 11, 1972	1 day	Traces of adsorbed H_2O, CO_2, CO and/or N_2 were evolved at low temperatures, and about 130 ppm H_2O was released by diffusion between 240° and 450°C. Traces of SO were evolved between 400° and 900°C and traces of CS_2 between 700° and 900°C. Additional SO_2 was evolved between 1000° and 1120°C and probably was a product of reaction between sulfur-bearing phases and silicates of the glass.

Isard, J. O., 1971, The formation of spherical glass particles on the lunar surface: Second Lunar Sci. Conf. Proc., Geochim et Cosmochim. Acta Suppl., 3, v. 3, p. 2003–2008.

Katsura, Takashi, 1967, Pele's hair as a liquid of Hawaiian tholeiitic basalts: Geochem. Jour., v. 1, p. 157–168.

Krukenberg, C. F. W., 1877, Mikographie der Glasbasalte von Hawaii [Micrography of basaltic glass from Hawaii]: Tubingen, 38 p.

Muenow D. W., 1973, High temperature mass spectrometric gas-release studies of Hawaiian volcanic glass: Pele's tears: Geochim. et Cosmochim. Acta, v. 37, no. 6, p. 1551–1561.

Ross, C. S., and Smith, R. L., 1955, Water and other volatiles in volcanic glasses: Am. Mineralogist, v. 40, p. 1071–1089.

——— 1961, Ash-flow tuffs: Their origin, geologic relations, and identification: U.S. Geol. Survey Prof. Paper 366, 81 p.

Shapiro, Leonard ,and Brannock, W. W., 1962. Rapid analysis of silicate, carbonate, and phosphate rocks: U.S. Geol. Survey Bull. 1144–A, p. A1–A56.

Shaw, H. R., Peck, D. L., Wright, T. L,. and Okamura, R., 1968, The viscosity of basaltic magma: An analysis of field measurements in Makaopuhi lava lake, Hawaii: Am. Jour. Sci., v. 266, p. 225–264.

Shaw, H. R., and Swanson, D. A., 1970, Eruption and flow rates of flood basalts: Second Columbia River Basalt Symp. Proc., Eastern Washington State College, Cheney, Wash., Mar. 21–23, 1969, Eastern Washington State College Press, p. 271–299.

Slayter, Games, 1952, Strength of glass: Am. Ceramic Soc. Bull., v. 31, no. 8, p. 276–278.

Swanson, D. A., Jackson, D. B., Duffield, W. A., and Peterson, D. W., 1971, Mauna Ulu eruption, Kilauea Volcano: Geotimes, v. 16, no. 5, p. 12–16.

Wentworth, C. K., 1938, Ash formations of the Island of Hawaii: Hawaiian Volcano Observatory, 3rd Spec. Rept., 183 p.

Wentworth, C. K., and Macdonald, G. A., 1953, Structures and forms of basaltic rocks in Hawaii: U.S. Geol. Survey Bull. 994, 98 p.

Weyl, W. A., and Marboe, E. C., 1964, The constitution of glasses: A dynamic interpretation: Vol. 2, Part 1 *of* Constitution and properties of some representative glasses: John Wiley and Sons, New York, p. 429–892.

Williams, Howel, and McBirney, A. R., 1969, An investigation of volcanic depressions, Pt. I, Airfall and intrusve pyroclastic deposits, and Pt. II, Subaerial pyroclastic flows and their deposits: U.S. Natl. Aeronautics and Space Adm. Research Grant NGR–38–003–012, prog. rept., 100 p.

Jour. Research U.S. Geol. Survey
Vol. 5, No. 1, Jan.–Feb. 1977, p. 103–116

CHEMICAL VARIABILITY IN THE LAKEVIEW MOUNTAINS PLUTON, SOUTHERN CALIFORNIA BATHOLITH–A COMPARISON OF THE METHODS OF CORRESPONDENCE ANALYSIS AND EXTENDED *Q*-MODE FACTOR ANALYSIS

By A. T. MIESCH and D. M. MORTON,
Denver, Colo., Menlo Park, Calif.

Abstract.—An extended method of *Q*-mode factor analysis that has been described previously offers a number of important advantages over conventional *Q*-mode factor analysis and correspondence analysis when applied to compositional data. Among these are the ability to compute the compositions, in the original units of the data, represented by the reference axes. The only special requirement of the data is that the values for each observation sum to a constant. Mathematically derived reference axes, such as the principal-components and varimax axes, commonly represent compositions that are partly negative. Even where no negative values are present, these compositions are comparatively difficult to interpret in petrologic terms and impossible or inappropriate to include in petrogenetic models. A model has been developed for the Lakeview Mountains pluton which employs vectors representing the compositions of melanocratic schlieren, leucocratic schlieren, and inclusions as the reference axes. When the effect of the inclusions is removed, the compositional zoning in the pluton is like that found in otherwise similar plutons in the Sierra Nevada batholith. The genetic implication of the model is that the inclusions were separated from the magma at least in its marginal parts. In the central part of the pluton, the inclusions were either separated to a lesser extent than in the marginal parts, or were reincorporated into the magma.

The structure and petrology of the Lakeview Mountains pluton in the southern California batholith were described by Morton (1969), and the chemical variations within it were described by Morton, Baird, and Baird (1969). The pluton is steep walled, tear shaped in plan, and is exposed in an area of 100 to 130 square kilometres; it is composed almost entirely of coarse-grained hornblende-biotite quartz diorite. A notable characteristic of the pluton is the ubiquitous occurrence of schlieren, resulting in extreme compositional variability of the rock on very small scales. Also common throughout the pluton are inclusions of diorite and quartz diorite that range in length from several centimetres to a metre; most of them are more fine grained, darker in color, and considerably more mafic than the enclosing rock. Like those in granitic rocks of the Sierra Nevada batholith (Bateman and others, 1963, p. D14), the inclusions in the Lakeview Mountains pluton are composed of the same minerals as the enclosing rock, although in different proportions.

An extensive sampling program was designed and executed in order to estimate the composition of the pluton and to assess the nature of the compositional

FIGURE 1.—Index map of the Sierra Nevada batholith and the Lakeview Mountains pluton in the southern California batholith.

variability within it (Morton and others, 1969). The program followed a preliminary investigation by Baird, McIntyre, Welday, and Morton (1967) and was based on a 610-m grid that extended over the entire pluton; at each grid intersection, nine samples were collected on a 15-m grid and composited into a single sample for analysis. The purpose of sampling on the 15-m grid at each sampling site was to minimize the effects of the local variation in composition caused by the schlieren because these effects could obscure any regional variation patterns that might be present.

A detailed trend analysis of the resultant data showed clearly that the central part of the pluton tended to be more mafic than the marginal parts, in contrast to other plutons, including those of the Sierra Nevada batholith. Moreover, the central part of the pluton contains abundant pegmatite dikes, giving evidence that the more mafic part of the pluton was the last part to crystallize. Assimilation of a hypersthene gabbro was suggested as a possible mechanism for the occurrence of the more mafic central part, but difficulties with this hypothesis were also pointed out (Morton and others, 1969, p. 1562).

David and Dagbert (1975) subjected most of the same compositional data to correspondence analysis and showed that the presence of the more mafic core of the pluton could also be shown by a map of loadings on their first principal-components axis. They also gave maps of loadings on two other principal-components axes and discussed the possible petrologic significance of four of the axes. It is one contention of this paper that although the principal-components reference axes can have some petrologic significance, they are purely mathematically derived and are difficult to interpret in terms of petrogenesis. Correspondence analysis used in this form, and for the type of problem at hand, is less satisfactory than an extended form of Q-mode factor analysis as described by Miesch (1976a, b) and Klovan and Miesch (1976).

The extended form of Q-mode factor analysis has been used to describe the compositional variation within the pluton in terms of end-member compositions that closely approximate those of rock types actually associated with the pluton. The resultant model has led to a new hypothesis that the unusual zoning in the pluton is related to the formation and redistribution of the diorite and quartz diorite inclusions.

Acknowledgment.—We are indebted to A. K. Baird of Pomona College for critical review of the manuscript and for helpful suggestions.

COMPARISON OF CORRESPONDENCE ANALYSIS AND CONVENTIONAL Q-MODE FACTOR ANALYSIS

Most geologic applications of both Q-mode factor analysis and correspondence analysis can be described in terms of the following model:

$$\widehat{W} = AF, \tag{1}$$

where A is a matrix of factor loadings, F is a matrix of factor scores, and $\widehat{W}$ is a matrix of estimates of some form of the original data. The matrix $\widehat{W}$ is N by M in size, where N is the number of rows representing observations or samples and M is the number of columns or variables. The matrix A is N by m in size, where m is the number of factors, and the matrix F is m by M. Prior to the very important paper of Klovan and Imbrie (1971), factor scores generally were not derived for the Q-mode model, and interpretations of the factor-analysis results were based solely on the loadings matrix, A. Since the work of Klovan and Imbrie, both A and F can be derived, and the product gives the matrix $\widehat{W}$ which can be compared directly with the original data, W, expressed in the same form.

The matrices A and F can be derived by factoring the minor and major products of W. (Actually, in practice, the formation of the major product is avoided, using the method of Klovan and Imbrie, 1971; see also David and others, 1974a). The minor product is here denoted by Z, where

$$Z = W'W, \tag{2}$$

and the major product by Z^*, where

$$Z^* = \mathrm{WW}'. \tag{3}$$

Matrix Z is M by M in size, and Z^* is N by N. The primary difference between correspondence analysis and Q-mode factor analysis, and between various forms of factor analysis for that matter, is in the formation of the matrix W.

For correspondence analysis, the original data matrix, X, is first divided through by the sum of the entire matrix, giving for each element

$$v_{ij} = \frac{x_{ij}}{\sum_{i,j} x_{ij}}, \tag{4}$$

where i designates a matrix row and j a matrix column. N row-sums are then formed by

$$\mathrm{sum}_i = \sum_j v_{ij}, \tag{5}$$

and M column-sums are formed by

$$\mathrm{sum}_j = \sum_i v_{ij}. \tag{6}$$

Finally, the elements of W are given by

$$w_{ij}=\frac{v_{ij}-(\text{sum}_i\,\text{sum}_j)}{(\text{sum}_i\,\text{sum}_j)^{1/2}}. \quad (7)$$

These transformations yield a data matrix that sums, across all rows and columns, to zero, and has a maximum rank of $M-1$ (assuming $M\leq N$). A primary effect of the transformations is to equalize the effects of the variables in determination of the matrix A.

Klovan and Imbrie (1971) provided two different initial transformations in their computer program for Q-mode factor analysis (CABFAC). Their purpose also, was to equalize the effects of the variables. Whether one or neither of these transformations is used, a final transformation consists of row-normalizing the entire data matrix. The more effective initial transformation is the scaling of each column (variable) to range from zero to one. In notation, parallel to that used for describing correspondence analysis, each element in X is transformed by

$$v_{ij}=\frac{x_{ij}-\min_j}{(\max_j-\min_j)}, \quad (8)$$

where $\max_j$ and $\min_j$ are, respectively, the maximum and minimum values in the jth column of X. If an initial transformation is not used, then $v_{ij}=x_{ij}$. The matrix of v_{ij}'s is row-normalized to give the elements of W by

$$w_{ij}=\frac{v_{ij}}{\left(\sum_j v_{ij}^2\right)^{1/2}}. \quad (9)$$

The maximum rank of the matrix W is M (assuming $M\leq N$).

Regardless of how the data are transformed, whether for Q-mode factor analysis or correspondence analysis, the matrix A can be derived as the eigenvectors of Z^* scaled by the square roots of the eigenvalues. These are the principal-components loadings. Klovan and Imbrie (1971) showed that the matrix F, containing the principal-components scores, is equal to the eigenvectors of Z. In the correspondence analysis, for purpose of plotting, each row of the N-by-m matrix A is scaled by the square root of the inverse of the corresponding sum_i (equation 5).

Whether the transformations have followed the route of correspondence analysis or one of the conventional routes of Q-mode factor analysis, the product of the matrices of A and F will equal the matrix W exactly if the number of factors, m, was set equal to the rank of W. If the number of factors is less than the rank of W, the product of A and F will be an approximation of W, referred to previously as $\widehat{W}$.

One exceedingly important difference between the methods of transformation for Q-mode factor analysis and correspondence analysis is in the row-normalization (equation 9), a procedure not used in correspondence analysis. The effect of row-normalization is to scale all sample vectors to unit length, and this scaling permits use of a fundamentally important measure—the communality. When the vectors are projected into a subspace with a number of dimensions fewer than the rank of W, by either ignoring one or more of the principal-components axes or by rotating two or more of these axes, the vector lengths generally are less than unity. The square of a vector length is its communality, h^2, and is an inverse measure of the degree to which the vector deviated from the space into which it was projected. The communality also provides an indication of the difference between the corresponding row in the original matrix W and the same row in the estimated matrix $\widehat{W}$. The measure of communality is widely used in almost all facets and applications of factor analysis, but one use that is especially pertinent to a comparison of factor and correspondence analysis is in the interpretation of vector diagrams. Where the diagrams are based on projected unit vectors (for example, Miesch, 1976b, figs. 4, 6, and 14), the proximity of only the short vectors can be an artifact of projection. Where the diagrams are based on vectors of variable length (for example, David and Dagbert, 1975, fig. 7), the nature of the projection for any vector cannot be ascertained from the length of the vector on the diagram, and the proximity of any two vectors could be an artifact of projection. This difficulty was recognized by David, Campiglio, and Darling (1974a, p. 136) and was pointed out again by May (1974, p. 1495).

One purported advantage of correspondence analysis is the facility for representing the variables in the same vector space as the samples. However, it has been shown (Klovan and Imbrie, 1971; Miesch, 1976a, b) that in Q-mode factor analysis, any composition (including, say, 100 percent SiO_2) can be represented as a vector in the sample-vector space. The degree to which the vector occupies the same space as the sample vectors is indicated by the vector communality, and, therefore, by the length of the vector on the vector diagram.

Diagrams showing projected vectors representing both the observations and the variables are basic to correspondence analysis, but the difficulty in interpreting these diagrams, caused by the failure to row-normalize the matrix W prior to computation of Z (and Z^* if computed), renders the diagrams difficult to interpret. Use of the absolute and relative contribu-

tions of the observations and variables (David and others, 1974a) for this purpose might be possible, but would be awkward at best and could be avoided by row-normalization.

EXTENDED *Q*-MODE FACTOR ANALYSIS

The factor model given in equation 1, used in both conventional *Q*-mode factor analysis and correspondence analysis, has some serious shortcomings for use in petrology. The first problem with the model of equation 1 is that the factor loadings in the A matrix have arbitrary signs, do not sum to unity for each sample, and, therefore, cannot be correctly interpreted as mixing proportions. A second problem is that the factor scores in the F matrix are dimensionless numbers and in no way resemble the compositions of end members that might have been mixed to form the individual samples. These two problems either prohibit attempts to interpret the factor model in petrologic terms, or at least make it unnecessarily difficult. A third problem is that the product of the A and F matrices (that is, the end-member "compositions" mixed in the "proportions" indicated by the loadings) yields not the original data in units of weight percent but the transformed data (matrix W), which have little meaning to the petrologist.

Another general problem with both conventional factor analysis and correspondence analysis is that the reference vectors, and consequently the factor scores, are purely mathematically derived, and it is only by coincidence that the scores can represent the compositions of geologic materials that were added to or subtracted from a system to cause compositional variation within it. Even if the scores did represent the compositions of geologic materials, the fact would not be easily recognizable because of the dimensionless numbers in which the scores are expressed.

These difficulties can be overcome by use of an extended form of *Q*-mode factor analysis described in references already cited. The only requirement of the method is that each row of the data matrix, X, sums to a value that is constant across all rows. This is generally no obstacle in petrologic investigations where the data consist of major compositional constituents, such as major oxides or major elements that can legitimately be expressed as oxides. The techniques of extended *Q*-mode factor analysis rely on the presence of the constant sum which provides a basis for scaling the A and F matrices so that the rows of A will sum to unity, the rows of F will be in the metric of the original data (usually weight percent) and will sum to the same constant, and the product of A and F will be an unbiased approximation of the original data matrix, X, usually as weight percent. The extended *Q*-mode factor model is:

$$\widehat{X} = AF \tag{10}$$

where, in this case, A is a matrix of composition loadings (or mixing proportions), F is a matrix of composition scores (or end-member compositions), and $\widehat{X}$ is an estimate of the original data. As with conventional factor analysis and correspondence analysis (equation 1), the term on the left side of the equation is exact, rather than an estimation, if the number of factors, m, is equal to the rank of W.

Unlike the factor loadings and scores in the A and F matrices of equation 1, the signs of the composition loadings and scores are fixed rather than arbitrary. Negative signs on a set of composition scores, therefore, can serve to show that the corresponding reference vector is entirely unrealistic in attempts to derive a petrogenetic model. This normally happens when the reference vector is far removed from the sample vectors, and is almost always the situation for all but the first of the principal-components reference axes and at least some varimax axes.

The ability to reproduce the data in its original forms, as weight percent, is not only reassuring to the petrologist, but also allows direct comparison of the data reproduced from the model with the original data so that a factor-variance diagram can be constructed. The diagram shows the proportion of the total variance in each variable that can be explained by models containing any number of factors and has considerable advantages over eigenvalues commonly used to select m. The cumulative sum of the eigenvalues, in factor analysis, merely gives the average row-sum-of-squares in $\widehat{W}$, or the average communality of the sample vectors. In neither factor analysis nor correspondence analysis do the eigenvalues give any information about either the individual variables or the degree to which the data matrix, in the original metric, can be accounted for by any factor model having m less than the rank of W.

A final advantage of the extended *Q*-mode factor method is that reference vectors might be found having composition scores that either approximate or equal the compositions of geologic materials (minerals, rocks, or magmas) that, on the basis of geologic and petrographic evidence, are thought to have been involved in the petrologic-mixing process. Thus, the petrologist might describe the compositional variation in terms of the compositions of real materials, rather than in terms of reference axes that represent either

unlikely compositions or compositions that are impossible as indicated by negative compositional values.

CHEMICAL DATA ON THE LAKEVIEW MOUNTAINS PLUTON

Execution of the sampling plan of Morton, Baird, and Baird (1969), referred to previously, led to 162 composite samples from a sampling grid that covered the entire exposed part of the pluton. The samples were analyzed by X-ray fluorescence spectrography for seven elements—silicon, alumnium, iron, magnesium, calcium, sodium, and potassium—and the specific gravity of each sample was measured. The entire data set is available as a photocopy of "Appendix B" of Morton, Baird, and Baird (1969). (See Morton and others, 1969, p. 1557, for ordering instructions.) The entire data set contains analyses of 22 samples of inclusions, 4 samples of melanocratic schlieren, and 4 samples of leucocratic schlieren, as well as those of the 162 samples of quartz diorite.

David and Dagbert (1975, p. 170) eliminated 15 of the 162 analyses from their correspondence analysis because they believed them to contain "aberrant" values. They used the original spectrographic data expressed as percentages of elements and the measures of specific gravity.

In the extended Q-mode factor analysis described here, the data on all 162 quartz diorite samples were used, and the elemental values were converted to oxides (SiO_2, Al_2O_3, FeO, MgO, CaO, Na_2O, and K_2O) and adjusted so that the oxides for each sample summed to 100 percent. The specific-gravity data were not used.

CORRESPONDENCE-ANALYSIS RESULTS OF DAVID AND DAGBERT (1975)

Starting with the original data matrix of size 147 by 8, as described in the preceding section, David and Dagbert (1975) applied the transformations as given in equations 4 through 7 of this paper and performed a principal-components analysis of the resultant matrix W. Only four of the principal-components axes were inferred to have possible petrologic significance, but the significances of the third and fourth axes were acknowledged to be questionable (David and Dagbert, 1975, p. 178). Their interpretations of only the first three principal-components axes will be discussed here:

1. The loadings of the variables on factor 1 indicate that this factor shows the antipathetic relationship of calcium, magnesium, and iron to silicon and potassium. A map of the sample loadings on factor 1 clearly shows a zoning of the pluton from the core outward to the margins, and the factor loadings for the variables (David and Dagbert, 1975, table II) indicate that the core is more mafic than the marginal parts, in accord with the findings of Morton, Baird, and Baird (1969). The suggestion was made that this factor "distinguishes biotite- and quartz-rich areas from the hornblende-rich areas," but there is no evidence from field investigations or in the modal data (Morton, 1969, p. 1543) that biotite and hornblende are distributed antipathetically. It was also suggested that the factor reflects a process of magmatic differentiation, but the nature of the process was not specified. The composition represented by factor 1, as well as the other factors, is unknown. One can only get an inkling of its general nature by inspection of the loadings of the variables on it.
2. Factor 2 was reported to separate aluminum-rich samples from those rich in iron, magnesium, and potassium, and it was suggested that the factor might represent the internal variation in the composition of biotite. The uncertainty in the interpretation of what factor 2 represents is understandable inasmuch as the composition represented by factor 2 is unknown. Factor 2 might just as well represent the occurrence of biotite, hornblende, or some other constituent. A map of the loadings of the sample vectors on factor 2 shows no strong regional trend.
3. The interpretation of factor 3, although admittedly questionable, was that it separates iron- and aluminum-rich samples from those rich in magnesium and calcium and that it might represent variations in hornblende composition. However, there is no evidence that the composition of hornblende varies within the pluton. A map of the sample vector loadings on factor 3 shows local variations in the marginal parts of the pluton. Again, the composition represented by this third reference axis is unknown, and so interpretation of its possible petrologic significance is difficult.

The basic problem with David and Dagbert's correspondence-analysis model is that the reference axes were selected on the basis of mathematical criteria alone, without attempt to use reference axes that represent compositions of geologic materials that actually may have been involved in the genesis of the pluton. Moreover, the precise compositions represented by the selected reference axes are not even known. In fact, it is not even known that the compositions represented by these axes are nonnegative.

Mathematically selected reference axes, even those that represent partly negative compositions, can be satisfactory where the only purpose of the exercise is to summarize the compositional variation in terms of a few components, and may even be useful as a basis for speculation on rock genesis. However, it is far more satisfactory to select reference axes on the basis of both mathematical and geologic criteria, thereby arriving at end members for the model that represent rock or mineral phases actually associated with the pluton.

EXTENDED *Q*-MODE FACTOR-ANALYSIS RESULTS

Principal components and varimax reference axes

Starting with the original data matrix of size 162 by 7, as described previously, the transformations given in equations 8 and 9 were applied, and the principal-components loadings and scores were derived using the CABFAC program of Klovan and Imbrie (1971). The loadings and scores were then scaled to composition loadings and scores using the method described by Miesch (1976a, b) and Klovan and Miesch (1976) to give six principal-components models, containing two to seven factors, that could be used to produce six estimates, $\widehat{X}$, of the original data matrix, X, using equation 10. The six estimated data matrices were compared with the original data matrix by means of coefficients of determination, r^2_j, leading to the factor-variance diagram, figure 2. The diagram indicates that models having three factors (end members) can explain 78 to 93 percent of the variance in each original oxide variable. [1] The addition of a fourth factor would serve to improve this situation by about 18 percent for Na_2O and Al_2O_3 (and by only 0.3 to 4 percent for the other oxides), but these gains do not seem to justify the increased complexity in the model. Consequently, a three-factor (or three-end-member) model seems appropriate. The absolute variances that can and cannot be accounted for by three-factor models are given in table 1, along with the estimated mean and total variance for each oxide.

The composition scores represented by the seven principal-components axes are given in part A of table 2. These are the compositions represented by the principal-components axes. The first of these axes is in the midst of the sample vectors and the composition it represents is close to the mean composition for all samples (table 1). It will be seen, however, that the compositions of all other principal-components axes contain

[1] The eigenvalues of the Z matrix were found to be 147.90, 9.59, 2.46, 1.16, 0.41, 0.35, and 0.12, indicating that a three-factor solution would account for 98.7 percent of the total sum of squares in W—not the variance in X.

FIGURE 2.—Factor-variance diagram for the Lakeview Mountains pluton, southern California batholith.

TABLE 1.—*Mean composition, in weight percent, and absolute variances accounted for and not accounted for by three-end-member model for the Lakeview Mountains pluton*

Constituent	Mean	Variance		
		Accounted for	Not accounted for	Total
SiO_2	60.12	2.4590	0.2064	2.6654
Al_2O_3	18.37	.4409	.1177	.5586
FeO	6.69	.3457	.0762	.4219
MgO	3.60	.1604	.0272	.1876
CaO	7.06	.3975	.0292	.4267
Na_2O	2.67	.0111	.0032	.0143
K_2O	1.49	.1295	.0117	.1412

TABLE 2.—*Composition scores, in weight percent, for the principal-components and varimax reference axes*

Constituent	A. Principal-components axes							B. Varimax axes		
	I	II	III	IV	V	VI	VII	I	II	III
SiO_2	60.21	82.85	23.37	96.11	90.21	68.07	70.14	53.25	64.84	41.53
Al_2O_3	18.35	10.20	−18.80	−15.57	7.34	16.97	19.71	21.42	16.90	.41
FeO	6.66	1.36	48.54	10.86	−31.10	8.97	2.68	7.92	5.43	27.31
MgO	3.58	−.21	31.70	.45	9.24	−1.06	11.02	4.50	2.71	17.45
CaO	7.03	−2.43	16.74	2.92	25.80	5.99	−3.63	10.00	5.12	12.05
Na_2O	2.66	1.26	−2.19	7.61	.98	1.99	2.33	3.18	2.41	.33
K_2O	1.51	6.97	.62	−2.37	−2.48	−.92	−2.26	−.26	2.59	.92

negative values. The reason for this is that the principal-components axes are far removed from the sample vectors, and progressive changes across the sample vectors, representing the compositional series, move into the negative regime as these axes are approached.

Because of the differences in methods used to form the W matrix, it is not expected that the principal-components axes from David and Dagbert's (1975) correspondence analysis represent precisely any of the corresponding compositions given in part A, table 2. However, a map of the composition loadings on the second principal-components axis (fig. 3) is very similar to David and Dagbert's map of loadings on their factor 1. (Recall that the maximum rank of a data matrix transformed for correspondence analysis is one less than that of a matrix transformed for Q-mode factor analysis.) The pattern of the map on figure 2 is antipathetic to David and Dagbert's map, but still shows that the core of the pluton is more mafic than its marginal parts. (Compare the pattern of composition loadings from figure 3 with the composition scores for principal-components axis II on table 2.) Also, a map of composition loadings on the third principal-components axis (fig. 4) is similar to David and Dagbert's map of loadings on their factor 2.

These map similarities apparently are not unusual. David, Campiglio, and Darling (1974b) observed that the similarities are commonly seen when comparing results from conventional principal-components and correspondence analysis.

A map of the composition loadings on the fourth principal-components axis (fig. 5) is totally different from David and Dagbert's map of loadings on their factor 3. This dissimilarity suggests that we have reached the point where the nature of the transformation used to arrive at the matrix W makes a difference in determining the positions of the principal-components axes. It also seems to be a good place to cease attempts to interpret the petrologic significance of the axes.

The first three principal-components axes were rotated into the varimax positions and the composition scores—the compositions represented by the axes in their new positions—were determined. These are given in part B of table 2. Except for the score value for K_2O on varimax axis I, the scores are entirely positive, but the axes were selected on mathematical criteria alone and there is no good reason to believe that they correspond to the compositions of any geologic materials within or associated with the Lakeview Mountains pluton.

The configuration of the three-dimensional varimax vector system is shown in figure 6 as a stereogram. Each of the vectors was restored to unit length after varimax projection so that they could be represented as points on an upper hemisphere. The points were then projected onto the stereogram in a vertical direction. Real or hypothetical vectors that plot within the area enclosed by the dotted line represent compositions that are entirely nonnegative. The entire vector system, including the principal-components and varimax axes, has been rotated 45° to the left about varimax axis III for the purposes of display on the diagram.

Oblique reference axes representing rock types in the pluton

A search for possible realistic end members was made by representing compositions of quartz, feldspars, biotite, hornblende, and other common igneous minerals as vectors in the seven-dimensional factor space and projecting them (Miesch, 1976a) into the vector system of figure 6. Vectors representing these compositions, however, occurred some distance from the three-dimensional varimax system and had low communalities after projection into it. The highest communalities after projection were for vectors representing the compositions of inclusions in the pluton and of melanocratic and leucocratic schlieren (Morton and others, 1969, app. B). Communalities for vectors representing 22 inclusions ranged from 0.8223 to 0.9870; those for four vectors representing melanocratic schlieren ranged from 0.8107 to 0.9462, and those for four vectors representing leucocratic schlieren ranged from 0.7098 to 0.9943. The highest communality for the inclusions was for sample RG2 (Morton and others, 1969, app. B). The highest communality for the melanocratic

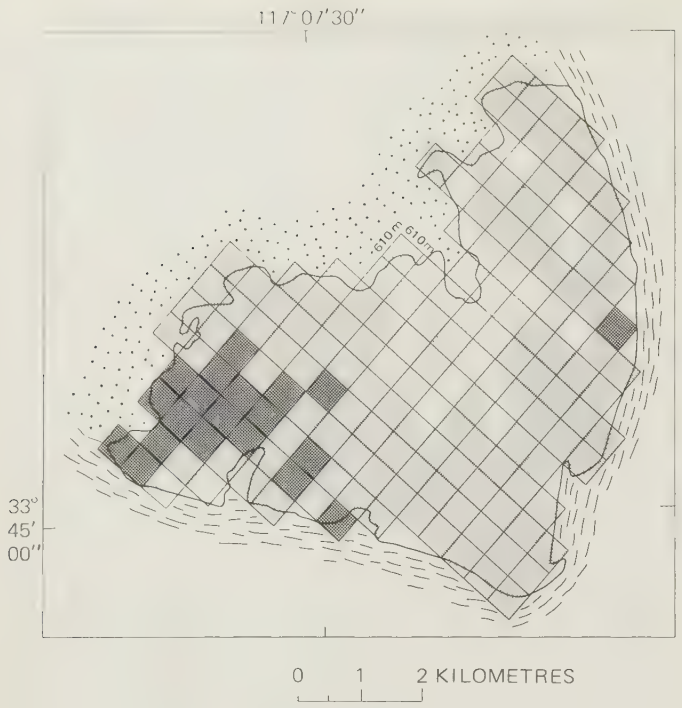

FIGURE 3.—Composition loadings on the second principal-components axis, Lakeview Mountains pluton, southern California. Table 2 shows composition scores on this axis. Geology from Morton (1969); grid points sampled by Morton, Baird, and Baird (1969) are at the centers of cell squares of this map.

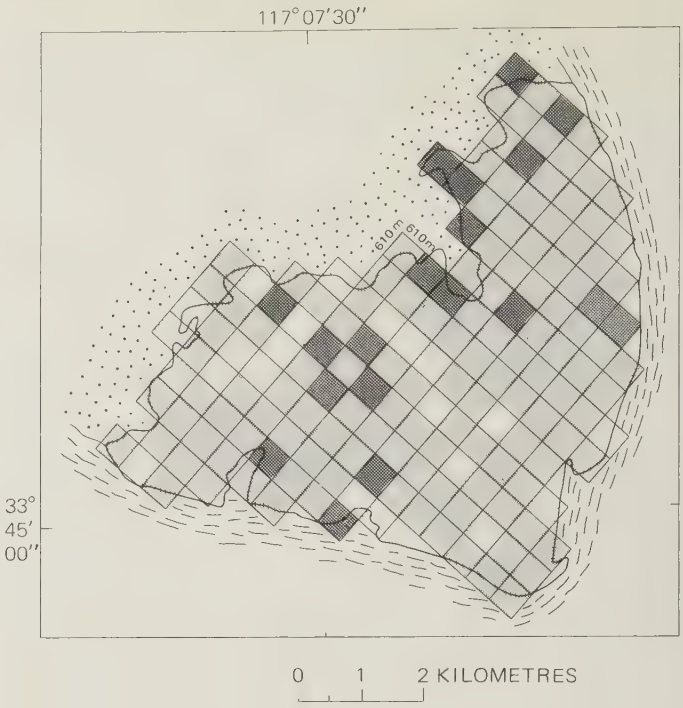

FIGURE 4.—Composition loadings on the third principal-components axis, Lakeview Mountains pluton, southern California. Table 2 shows composition scores on this axis. Geology from Morton (1969); grid points sampled by Morton, Baird, and Baird (1969) are at the centers of cell squares of this map.

schlieren was for sample BG4, and the highest for the leucocratic schlieren was for sample BG7 (Morton and others, 1969). Because the communalities of these vectors were not precisely unity, the vectors represent compositions close to but different from the original compositions of the corresponding samples. The original compositions and the compositions recomputed after projection are given in table 3. The projected vectors are represented in figure 6 (labeled MS, LS, and INC).

Using the method of oblique projection originally given by Imbrie (1963), the loadings of the sample vectors on vectors MS, LS, and INC were determined. These initial loadings were then transformed to composition loadings (see Miesch, 1976a, b) which can be interpreted as proportions of the three end members in each sample. The mixtures for each 20th sample of Morton, Baird, and Baird (1969, app. B) are given in table 4 where they are compared with the original sample compositions.

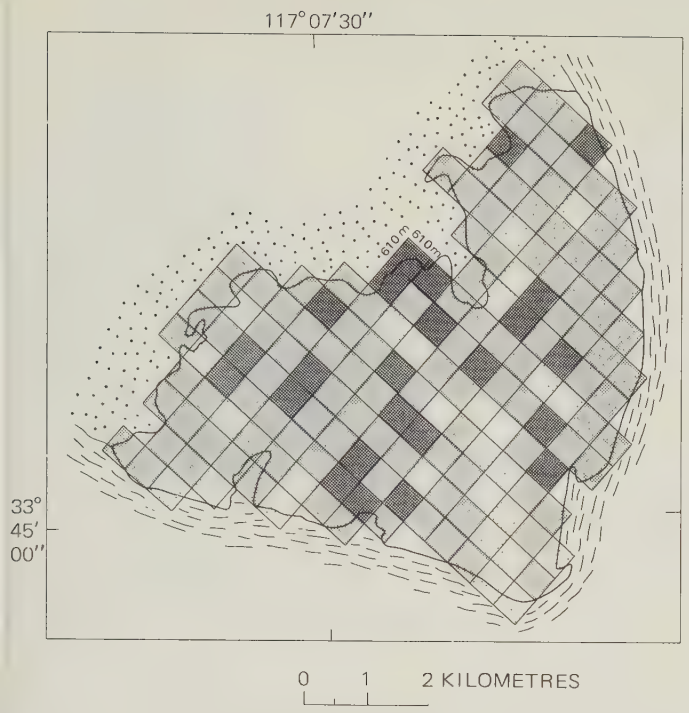

EXPLANATION

- Alluvium
- Metamorphic country rock
- Exposed part of pluton
- Contact between alluvium and country rock

Composition loadings (mixing proportions)

- >0.01
- -0.01—0.01
- <-0.01
- Not sampled

FIGURE 5.—Composition loadings on the fourth principal-components axis, Lakeview Mountains pluton, southern California. Table 2 shows composition scores on this axis. Geology from Morton (1969); grid points sampled by Morton, Baird, and Baird (1969) are at the centers of cell squares of this map.

A statistical summary of the composition loadings (mixing proportions) for all 162 samples, on end-members MS, LS, and INC, is given in table 5. It shows that the average sample from the pluton is close in composition to a mixture of equal parts of melanocratic schlieren and leucocratic schlieren from which 0.355 part of a material compositionally similar to the inclusions has been separated.

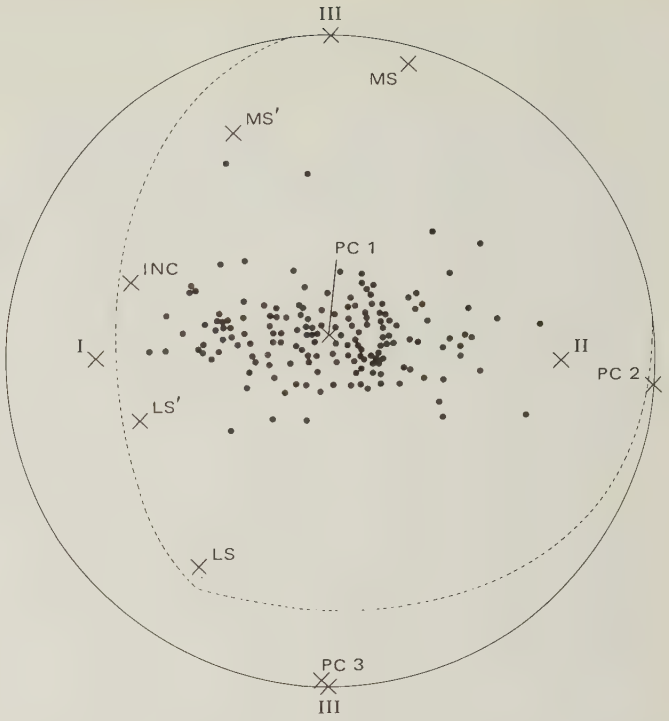

FIGURE 6.—Stereogram showing the three-dimensional vector system for the Lakeview Mountains pluton, southern California. Vectors have been restored to unit length after varimax projection. Average sample vector communality before restoration was 0.9874. Dots represent 162 sample vectors. Vectors I, II, and III are the varimax reference axes. Vectors MS′ and LS′ represent some alternative end mem-components reference axes. Vectors MS, LS, and INC represent, respectively, the approximate compositions of melanocratic schlieren, leucocratic schlieren, and inclusions. Vectors MS′ and LS′ represent some alternative end members. Vectors that plot within the area enclosed by the dotted line represent compositions that are entirely nonnegative. Compositions represented by the labeled vectors are in tables 2, 3, and 6.

PETROGENETIC IMPLICATIONS

The extended Q-mode factor model employing, as reference axes, vectors representing the compositions of the two types of schlieren (MS and LS) and the inclusions (INC) may be viewed as a descriptive one that merely expresses most of the chemical variation in the pluton in terms of these three components. The fact that the compositional variation, in large part, can be accounted for in this manner could be ascribed to chance, to indirect reasons, or directly to the process by which the pluton formed.

A map of the composition loadings (mixing proportions) for the sample vectors on the inclusion end member (INC) is given in figure 7 and shows essentially the same pattern as the loadings on David and Dagbert's (1975) factor 1. The pattern is also essentially

the same as that on the map of composition loadings on the second principal-components axis, figure 3. (Although the values represented in figures 3 and 7 are antipathetic to each other, comparison of the composition scores for the respective end members, given in tables 2 and 3, shows that the patterns reflect the same type of compositional variability.) The similarities among all three maps suggest that the principal-components axes, derived through both correspondence analysis and extended Q-mode factor analysis, reflect the effects of the inclusions, but this was not recognized until a reference axis representing the composition of the inclusions was deliberately employed in the model.

Two striking features of the map are shown in figure 7. One of these is the concentration of highly negative (<—0.7) loadings in the southwest part of the pluton, and the other is the concentration of positive loadings near the pluton's inferred center. The area in the southwest coincides with the area considered to be the site of very early magma emplacement (Morton, 1966, p. 119–121; Morton, 1969, p. 1548). The area near the center of the pluton is where most of the pegmatites occur (Morton, 1969, pl. 1) and is regarded as the part of the pluton that was last to crystallize (Morton, 1969, p. 1550). The composition loadings on vector INC (fig. 7), together with the composition scores for this vector (table 3), indicate that the early formed part of the pluton in the southwest is the most felsic and that the late-formed part near the center is the most mafic.

TABLE 3.—*Original compositions of selected samples of melanocratic schlieren, leucocractic schlieren, and inclusions and of recomputed (end-member) compositions represented by vectors projected into three-dimensional vector system*

A. Original compositions, in weight percent

Sample Number [1] / Constituent	BG4 Melanocractic schlieren	BG7 Leucocratic schlieren	RG2 Inclusion
SiO_2	55.66	60.21	51.90
Al_2O_3	11.27	25.63	20.40
FeO	14.45	.86	9.11
MgO	8.66	.65	5.57
CaO	5.82	8.48	9.77
Na_2O	1.96	3.79	2.91
K_2O	2.17	.37	.35

B. Recomputed compositions, in weight percent

Vector	MS [2]	LS [3]	INC [4]
SiO_2	57.01	60.05	54.05
Al_2O_3	11.79	25.59	19.51
FeO	12.49	1.96	8.80
MgO	7.47	.48	5.07
CaO	7.50	7.90	9.48
Na_2O	1.77	3.69	2.90
K_2O	1.96	.33	.19

[1] Sample numbers from Morton and others (1969, app. B). Data converted to oxides and adjusted to sum to 100.
[2] Position of vector shown in figure 6. Communality =0.9462.
[3] Position of vector shown in figure 6. Communality =0.9943.
[4] Position of vector shown in figure 6. Communality =0.9870.

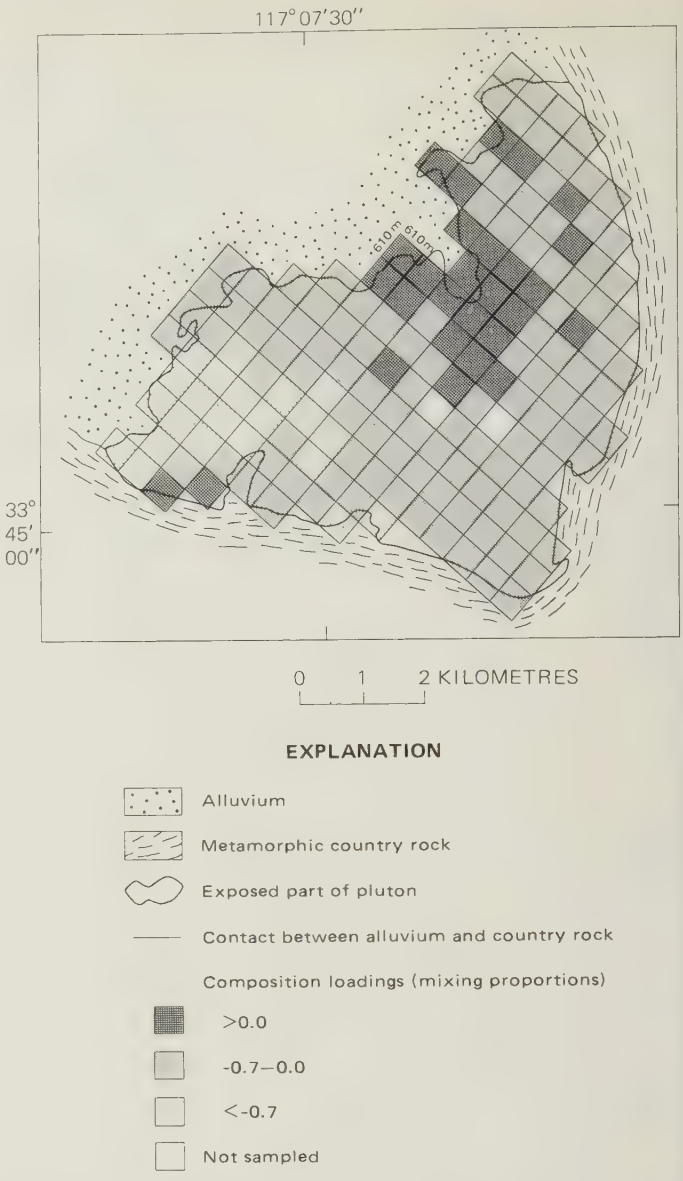

FIGURE 7.—Composition loadings on vector INC (fig. 6) representing the composition of inclusions (table 3) in the Lakeview Mountains pluton, southern California. The other two end members are represented by vectors MS and LS (fig. 6 and table 3). Geology from Morton (1969); grid points sampled by Morton, Baird, and Baird (1969) are at the centers of cell squares of this map.

The composition loadings on the inclusion end member (vector INC) range from —1.353 to 0.600 (table 5), implying that the inclusions have been both subtracted from and added to the other end members during the pluton's formation. Nearly all the positive loadings (indicating addition) are for samples from near the center of the pluton (fig. 7) where most of the pegmatites occur. The presence of pegmatites implies that volatiles were concentrated in this part of the magma, and these might have promoted partial

TABLE 4.—*Mixing proportions, original data, and corresponding data recomputed from the model for selected samples*

[Original data given as percentage of elements, from Morton and others (1969, app. B), were converted to oxides and adjusted to sum to 100; all oxide data are given in weight percent]

Sample	Mixing proportions[1]			SiO_2		Al_2O_3		FeO		MgO		CaO		Na_2O		K_2O	
	MS	LS	INC	Original	Recomputed	Original	Recomputed	Original	Recomputed	Original	Recomputed	Original	Recomputed	Original	Recomputed	Original	Recomputed
LV20	0.6185	0.5957	—0.2141	59.95	59.46	18.29	18.36	6.75	7.01	3.68	3.82	7.45	7.31	2.62	2.67	1.26	1.37
LV40	.7550	.7777	—.5328	60.30	60.95	18.66	18.41	6.48	6.27	3.35	3.31	6.74	6.76	2.68	2.66	1.79	1.64
LV60	.4067	.4814	.1119	58.10	58.14	19.23	19.30	7.13	7.01	3.70	3.84	8.00	7.91	2.83	2.82	1.00	.98
LV80	.5638	.5536	—.1175	59.44	59.04	18.36	18.52	7.06	7.09	3.73	3.88	7.52	7.49	2.69	2.70	1.20	1.27
LV100	.6821	.6181	—.3002	59.42	59.78	18.39	18.00	7.15	7.09	3.83	3.87	7.15	7.15	2.56	2.62	1.50	1.48
LV120	.8158	.8011	—.6169	60.52	61.27	18.44	18.08	6.74	6.33	3.19	3.35	6.61	6.60	2.60	2.61	1.90	1.75
LV140	.8983	.8244	—.7226	61.38	61.66	17.81	17.59	6.52	6.48	3.53	3.44	6.31	6.40	2.52	2.54	1.93	1.90
LV160	.3488	.3975	.2537	56.61	57.47	19.82	19.23	6.57	7.37	4.74	4.08	8.50	8.16	2.78	2.82	.97	.86

[1] See table 3*B* for compositions of end-members MS, LS, and INC.

melting of the inclusions or reaction with the silicate liquid phase, resulting in redistribution of their mineral constitutents in this part of the magma. Elsewhere in the magma, constituents of the inclusions might have been subtracted from the magma by fractional crystallization.

TABLE 5.—*Summary statistics for mixing proportions*

End member	MS	LS	INC
Mean	0.679	0.676	—0.355
Standard deviation	.193	.172	.358
Maximum	1.198	1.188	.600
Minimum	.131	.085	—1.353

The composition loadings (mixing proportions) of the samples on the axes representing the melanocratic and leucocratic schlieren (table 5) merely describe the compositional variations in the magma brought about by processes unrelated to the inclusions. A map of the ratios of the two (fig. 8) shows that, with the effect of the inclusions removed, the pluton tends to be more leucocratic near its center, as is commonly the situation for granitic plutons in the Sierra Nevada batholith (Bateman and others, 1963, p. 30–32; Moore, 1963, p. 115–116). The map also shows that, with the effect of the inclusions removed, the area in the southwest part of the pluton, considered to be the earliest-formed part, is more mafic than the late-formed central part. These observations provide strong support for the interpretation that the reversed type of zoning in the Lakeview Mountains pluton is related to the presence and origin of the inclusions.

The model was used to recompute an estimate of the entire data matrix (given partly in table 4) and the estimated matrix was then subtracted from the original data matrix to give the model residuals. The residuals for some of the oxide constituents show weak east-west trends across the pluton but most appear to be randomly distributed. The residuals for MgO (fig. 9), however, tend to be positive near the marginal parts of the pluton, indicating that the pluton, in these parts, contains more MgO than called for by the model. The positive MgO residuals indicate that MgO is more highly concentrated near the pluton's margins than can be accounted for by either the effects of the inclusions or the relative proportions of melanocratic and leucocratic schlieren.

Although the process of reincorporation of the inclusions into the magma in and near its central part would account for the positive signs on some of the composition loadings on the inclusion end member, any hypothesis stating that this actually occurred rests on the assumption that the composition of the magma, before separation of the inclusions, was either intermediate to the compositions of the two types of schlieren or not a great deal more mafic. On the other hand, if the composition of the magma, before the separation of the inclusions, was intermediate between the compositions represented by vectors MS′ and LS′ in figure 6 (table 6), the reincorporation of the inclusions is not required in order to explain the pluton's mafic core. This is shown by derivation of the composition loadings with respect to end-member vectors MS′, LS′, and INC (fig. 6); a statistical summary of these loadings is given in table 7. The summary shows that all loadings on end-member INC are negative, indicating that if the parent-magma composition was intermediate to the compositions represented by vectors MS′ and LS′ (table 6), the inclusions must have been subtracted from the magma in order to account for each of the sample compositions. The composition loadings for this alternative model are linearly related, in a positive way, to those derived using end-members MS, LS, and INC. Hence, the patterns of the maps (figs. 7 and 8) constructed from the loadings for the two models are precisely the same, even though the

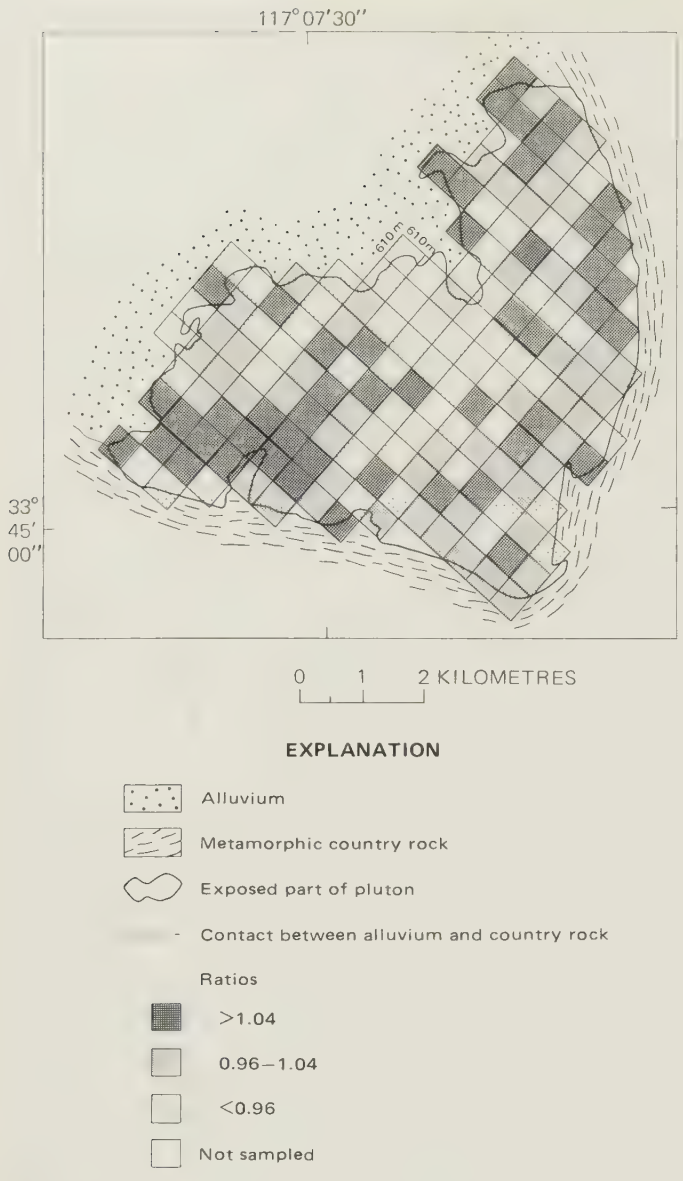

FIGURE 8.—Ratios of the composition loading on vector MS to the composition loading on vector LS (fig. 6), Lakeview Mountains pluton, southern California. Table 3 shows composition scores on these vectors. Geology from Morton (1969); grid points sampled by Morton, Baird, and Baird (1969) are at the centers of cell squares of this map.

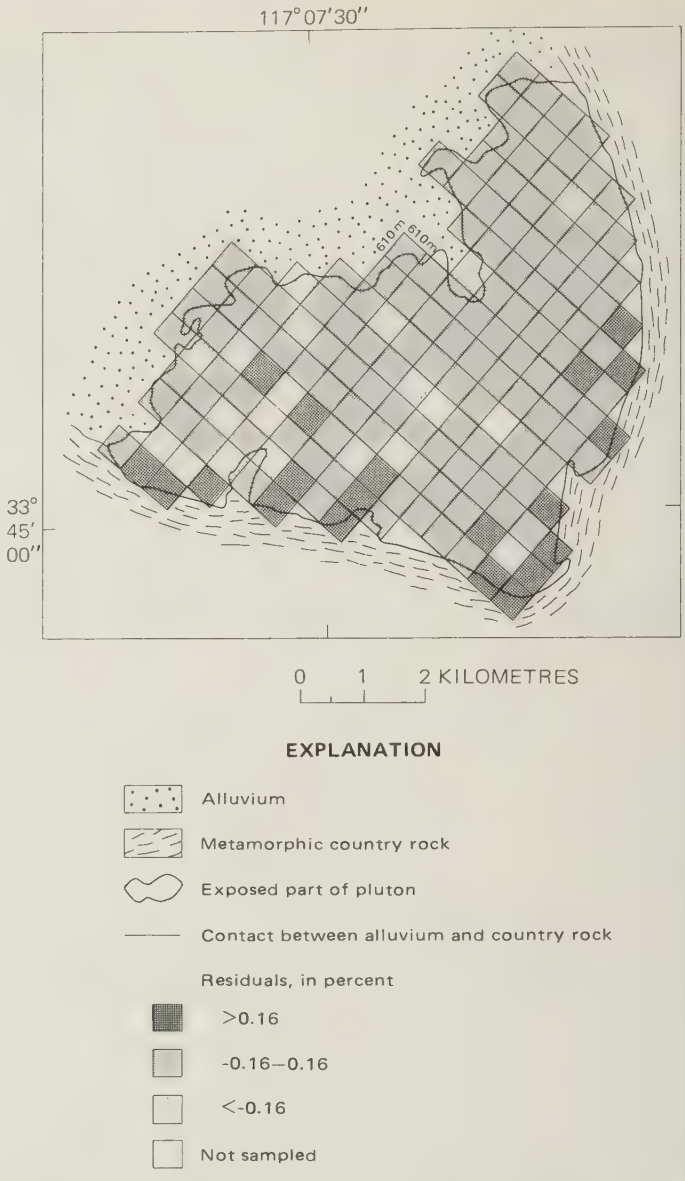

FIGURE 9.—MgO residuals from the factor models for the Lakeview Mountains pluton, southern California. Geology from Morton (1969); grid points sampled by Morton, Baird, and Baird (1969) are at the centers of cell squares of this map.

absolute values indicated by the symbols differ.[2] The alternative model leads to precisely the same reproduced data as represented in table 4; consequently, the map of MgO residuals (fig. 9) is unchanged.

According to either model, the major part of the compositional variation within the pluton is explained as having resulted from the formation of an early cumulant phase which separated from the magma and subsequently formed the widespread inclusions. Both models also show the marginal parts of the pluton as having been more greatly modified by the separation of the cumulant phase than was the central part (fig. 7). The required amounts of cumulant phase separated depend on the composition assumed for the parent magma. If this assumed composition is intermediate to the compositions represented by vectors MS′ and LS′ in figure 6, each of the 162 sample compositions is approximated by subtraction of the inclusions (table 7). However, if the composition assumed for the parent

[2] The map symbols in figure 7 define ranges of values bounded by the limits —0.7 and 0.0. For the alternative model, these limits are —3.7 and —1.8, respectively. The map symbols in figure 8 define ranges bounded by the limits 0.96 and 1.04. For the alternative model, these limits are 0.88 and 0.96, respectively.

magma is intermediate between the compositions represented by vectors MS and LS in figure 6, the compositions of most samples from the central part of the pluton can be approximated only by addition of the inclusions.

TABLE 6.—*Composition, in weight percent, represented by vectors MS′ and LS′ in figure 6*

Constituent	MS′	LS′
SiO_2	55.16	56.12
Al_2O_3	16.63	21.60
FeO	10.18	6.44
MgO	5.97	3.49
CaO	8.74	8.94
Na_2O	2.48	3.17
K_2O	.85	.24

TABLE 7.—*Summary statistics for mixing proportions of the alternative model*

End member	MS′	LS′	INC
Mean	1.817	1.965	—2.782
Standard deviation	.519	.501	1.000
Maximum	3.204	3.452	—.133
Minimum	.351	.246	—5.567

Field evidence for the disintegration of the inclusions and the redistribution of their constituents in the magma is lacking; therefore the model employing vectors MS and LS as end members cannot be supported by existing data. There are, however, some arguments for its plausibility. Theoretical considerations by Bowen (1928, p. 197–198) led him to suggest that inclusions more mafic than the enclosing melt may be disintegrated and dispersed by reaction with the silicate liquid. Also, because of the presence of pegmatites in the central part of the pluton, the role of water and other volatiles in lowering the temperature of melting (Tuttle and Bowen, 1958, p. 121–122) should be considered. Bateman and others (1963, p. D42) suggested that in the Sierra Nevada batholith, volatiles were responsible for contamination of granitic magmas by mafic inclusions.

The alternative model, employing vectors MS′, LS′, and INC as end members, calls for separation of the cumulant phase from all parts of the magma represented by the samples, but for the separation of lesser amounts from the central part than from those parts near the margins. This is in accord with a temperature gradient decreasing outward from the center of the magma toward its contacts with the wallrocks.

CONCLUSIONS

In petrologic applications of conventional Q-mode factor analysis, one may use the principal-components, varimax, or other mathematically determined reference axes and obtain a good notion of the compositions they represent by scanning the compositions represented by sample vectors that load high on them. Alternatively, one may use the oblique projection method of Imbrie (1963), which uses vectors representing selected samples of known composition as the reference axes. Also, both factor analysis and correspondence analysis can be used to derive the loadings of the variables on the reference axes. The method of extended Q-mode factor analysis, however, can be used where the original data on each observation sum to a constant, and the compositions represented by the reference axes are determined directly. The method shows that many of the mathematically derived reference axes determined for compositional data represent compositions that are partly negative. This is especially true of all but the first principal-components axis derived in the conventional Q-mode analysis, and probably true of all the principal-components axes from correspondence analysis. Partly negative compositions may be entirely satisfactory where the only purpose of the model is to provide a parsimonious description of the compositional variability, but not where it is to be used as a basis for a petrogenetic model.

The extended Q-mode method has the additional advantage of allowing one to test specific compositions for their suitabilities as end-member compositions in the m-dimensional compositional system. This is done by representing the composition as a vector in the M-dimensional space and then projecting it into the m-dimensional vector system. If the projected vector communality is large, the composition is compatible with the compositional series formed by the samples, and the composition represented by the projected vector will be close to that of the original composition tested. In this situation, the projected vector may serve as a reference axis(and the composition may be an end-member composition) for the extended Q-mode model.

It was possible to describe a major part of the compositional variability in the Lakeview Mountains pluton in terms of three selected compositions: (1) melanocratic schlieren, (2) leucocratic schlieren, and (3) inclusions, all of which are widespread throughout the pluton. The model may be viewed as merely descriptive, but it appears to have genetic implications. If the effect of the inclusions is removed, the compositional zoning in the pluton conforms to the zoning that is expected on the basis of what has been found in otherwise similar plutons of the Sierra Nevada.

Both models developed from the extended Q-mode technique explain the marginal parts of the pluton as having resulted from the separation of a cumulant

phase, having a composition like that of the inclusions, from a parent magma. According to one model, disintegration and dispersion of the inclusions caused the center of the pluton to be more mafic than the marginal parts. The disintegration of the inclusions may have been brought about by the concentration of volatiles, as evidenced by the presence of pegmatites. The alternative model explains the more mafic center of the pluton as the result of less extensive separation of the cumulant phase.

REFERENCES CITED

Baird, A. K., McIntyre, D. B., Welday, E. E., and Morton, D. M., 1967, A test of chemical variability and field sampling methods, Lakeview Mountain tonalite, Lakeview Mountains, southern California batholith: California Div. Mines and Geology Spec. Rept. 92, p. 11–19.

Bateman, P. C., Clark, L. D., Huber, N. K., Moore, J. G., and Rinehart, C. D., 1963, The Sierra Nevada batholith—A synthesis of recent work across the central part: U.S. Geol. Survey Prof. Paper 414–D, 46 p.

Bowen, N. L., 1928, The evolution of the igneous rocks: Princeton, N. J., Princeton University Press, 334 p.

David, Michel, and Dagbert, Michel, 1975, Lakeview revisited—Variograms and correspondence analysis—New tools for the understanding of geochemical data, in Ellicott, I. L., and Fletcher, W. K., eds., Geochemical Exploration 1974, Developments in economic geology [v.] 1: Internat. Geochem. Explor. Symposium, 5th, Vancouver, British Columbia, Canada 1974, Proc., p. 163–181.

David, Michel, Campiglio, Carlo, and Darling, Richard, 1974a, Progresses in *R*- and *Q*-mode analysis—Correspondence analysis and its application to the study of geological processes: Canadian Jour. Earth Sci., v. 11, no. 1, p. 131–146.

——— 1974b, Progresses in *R*- and *Q*-mode analysis—Correspondence analysis and its application to the study of geological processes—Reply: Canadian Jour. Earth Sci., v. 11, no. 10, p. 1497–1499.

Imbrie, John, 1963, Factor and vector analysis programs for analyzing geologic data: U.S. Office Naval Research, Geog. Branch, ONR Task No. 389–135, Contract Nonr 1228(26), Tech. Rept. 6, 83 p.

Klovan, J. E., and Imbrie, John, 1971, An algorithm and FORTAN–IV program for large-scale *Q*-mode factor analysis and calculation of factor scores: Internat. Assoc. Math. Geology Jour., v. 3, no. 1, p. 61–77.

Klovan, J. E., and Miesch, A. T., 1976, Extended CABFAC and *Q*MODEL computer programs for *Q*-mode factor analysis of compositional data: Computers & Geosciences, v. 1, no. 3, p. 161–178.

May, R. W., 1974, Progresses in R- and Q-mode analysis—Correspondence analysis and its application to the study of geologic processes—Discussion: Canadian Jour. Earth Sci., v. 11, no. 10, p. 1494–1497.

Miesch, A. T., 1976a, *Q*-mode factor analysis of compositional data: Computers & Geosciences, v. 1, no. 3, p. 147–159.

——— 1976b, *Q*-mode factor analysis of geochemical and petrologic data matrices with constant row-sums: U.S. Geol. Survey Prof. Paper 574–G (In press.)

Moore, J. G., 1963, Geology of the Mount Pinchot quadrangle, southern Sierra Nevada, California: U.S. Geol. Survey Bull. 1130, 152 p.

Morton, D. M., 1966, Petrology of the Lakeview Mountains pluton and adjacent area, Riverside County, California [California Univ., Los Angeles, Ph. D. thesis]: Ann Arbor, Mich., University Microfilms, Inc.

——— 1969, The Lakeview Mountains pluton, southern California batholith—Pt. 1, Petrology and structure: Geol. Soc. America Bull., v. 80, no. 8, pp 1539–1551.

Morton, D. M., Baird, A. K., and Baird, K. W., 1969, The Lakeview Mountains pluton, southern California batholith—Pt. 2, Chemical composition and variation: Geol. Soc. America Bull., v. 80, no. 8, p. 1553–1563.

Tuttle, O. F., and Bowen, N. L., 1958, Origin of granite in the light of experimental studies in the system $NaAlSi_3O_8$–$KAlSi_3O_8$–SiO_2–H_2O; Geol. Soc. America Mem. 74, 153 p.

Jour. Research U.S. Geol. Survey
Vol. 5, No. 1, Jan.–Feb. 1977, p. 117–124

SURFACE DEFORMATION IN PART OF THE SAN JACINTO VALLEY, SOUTHERN CALIFORNIA

By DOUGLAS M. MORTON, Menlo Park, Calif.

Abstract.—Ground fissuring and subsidence occur in a deep alluvium-filled graben between the Casa Loma and San Jacinto faults, San Jacinto Valley, southern California. These processes are attributed chiefly to compaction due to withdrawal of ground water. Subsidence due to compaction is estimated to be a maximum of 3.5 centimetres per year; tectonic subsidence of the graben is estimated to be from 0.3 to 0.6 cm per year. Ground fissuring occurs primarily on the west side of a closed depression in the graben. The area of ground fissures has expanded from 1 square kilometre in 1953 to 12 km² in 1974 and could grow even more. Individual fissures have attained lengths of 850 metres.

Subsidence and associated surface deformation have been documented for parts of the San Jacinto Valley by Fett, Hamilton, and Fleming (1967), Morton (1972), Lofgren and Rubin (1975), and Lofgren (1976). The most spectacular surface features are widespread ground fissures which presently occur over an area of 12 square kilometres in the northern part of the valley. This report summarizes, through the use of aerial photographs, the areal development of the ground fissures between 1953 and 1974.

Acknowledgments.—R. A. Nelson, Riverside County Flood Control District and Water Conservation District, kindly provided data on the high-water marks of the 1938 and 1965 lake level. W. H. Young, of the same organization, made available the 1962 and 1966 aerial photographs. R. K. Morton, Eastern Municipal Water District, provided wood sample d, dated by Teledyne Isotopes.

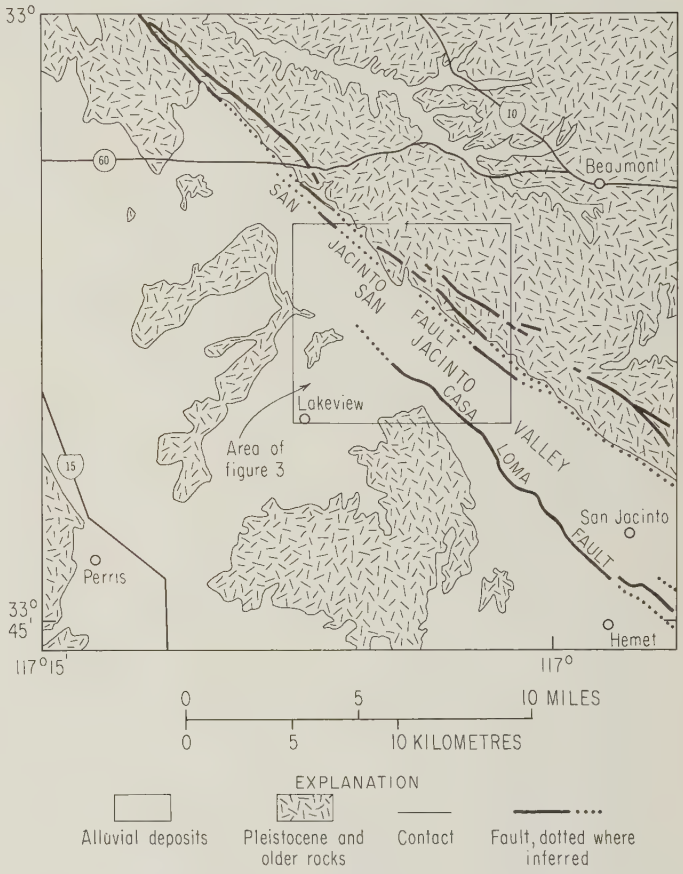

FIGURE 1.—General setting of the northern part of the San Jacinto Valley area (modified from Rogers, 1965).

GEOLOGIC SETTING

The San Jacinto Valley, part of the northern Peninsular Ranges province of southern California, is located over a deep alluvium-filled graben within the San Jacinto fault zone (fig. 1). The graben ranges in width from 3 to 4 kilometres and is bounded on the west by the Casa Loma fault and on the east by the San Jacinto fault (for example, Rogers, 1965; fig. 1). Seismic and gravity surveys indicate that 2,000 to 2,400 metres of sediment overlie the basement floor of the graben (Fett, 1968). East of the graben the basement surface occurs at variable depths beneath the sediment cover at the northern part of the valley and rises to 1,200 m above the valley to the south. West of the graben the basement is located generally at depths of 100 to 200 m (Woodford and others, 1971). Alluvium in the upper 100 m is composed chiefly of sand and sandy silt and less commonly of silt and clayey silt. Surface and near-surface alluvium locally is of low density and subject to hydrocompaction (Fett, 1968). Fine-grained alluvium predominates in the area of ground fissures, whereas coarser grained alluvium constitutes an alluvial fan deposit to the east. Beds rich in organic material and

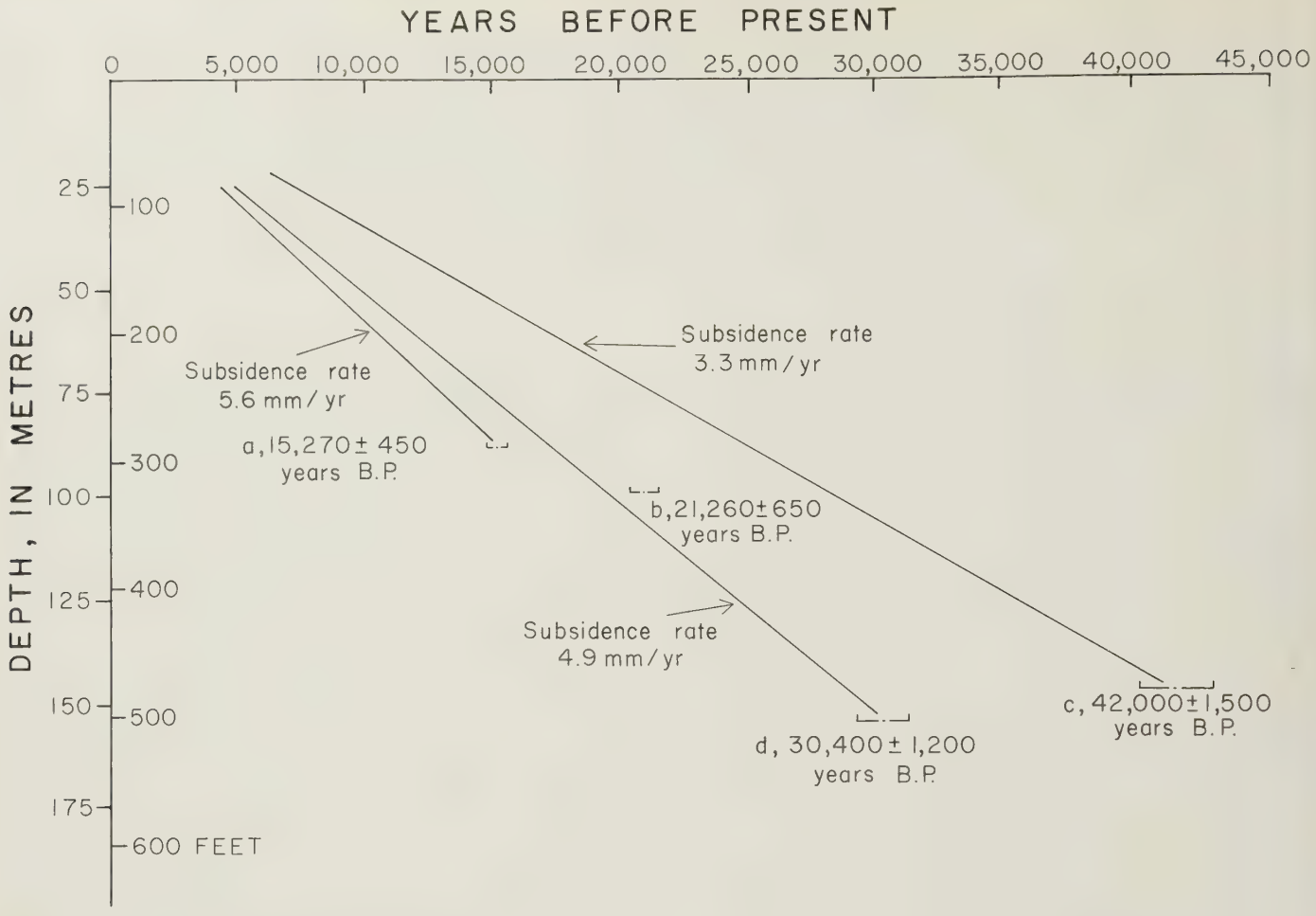

FIGURE 2.—Subsidence rates for the San Jacinto Valley. Samples a, b, and c are from Lofgren and Rubin (1975); sample d, dated by Teledyne Isotopes.

occasional logs are commonly found during drilling of water wells.

The San Jacinto fault consists of multiple south-facing scarps over a width up to 1.5 km (Sharp, 1972); individual fault segments dip northeastward at moderate-to-steep angles (Morton, 1972; Henderson, 1939).

Through much of its length within the valley, the Casa Loma fault is well marked by a sinuous north-facing scarp (Sharp, 1972; Morton, unpub. data, 1976). Where observed in trenches, the fault dips 60° to 70° to the northeast (Proctor, 1962; Morton, unpub. data, 1976).

TECTONIC SUBSIDENCE

Carbon-14 ages of wood samples recovered from depths of 88 to 150 m in drill holes indicate that tectonic subsidence of the northern part of the graben with respect to the area west of the graben occurred at an apparent rate of between 3 and 5.6 millimetres per year for the past 15,000 to 40,000 years (fig. 2). Assuming this rate to have been uniform, extrapolation for the total column of sediment gives an age of 400,000 to 700,000 years B.P. (before present) for the inception of sedimentation in the graben.

Measurements made on a deformed aqueduct pipe that crosses the Casa Loma fault suggest a right-lateral displacement rate of 0.23 centimetre per year from 1958 to 1973. This figure is the same as that obtained by repeated surveys across the fault reported by Proctor (1974).

The northern part of the San Jacinto Valley contains an elongate closed depression that periodically fills and forms a shallow lake. This ephemeral lake existed before 1895, prior to extensive water-well development; the closed depression is thus basically of tectonic origin. The apparent high-water marks identified with the 1938 and 1965 floods were determined by the Riverside County Flood Control District from aerial photographs taken after the respective floods. A comparison between the size of the lake formed during

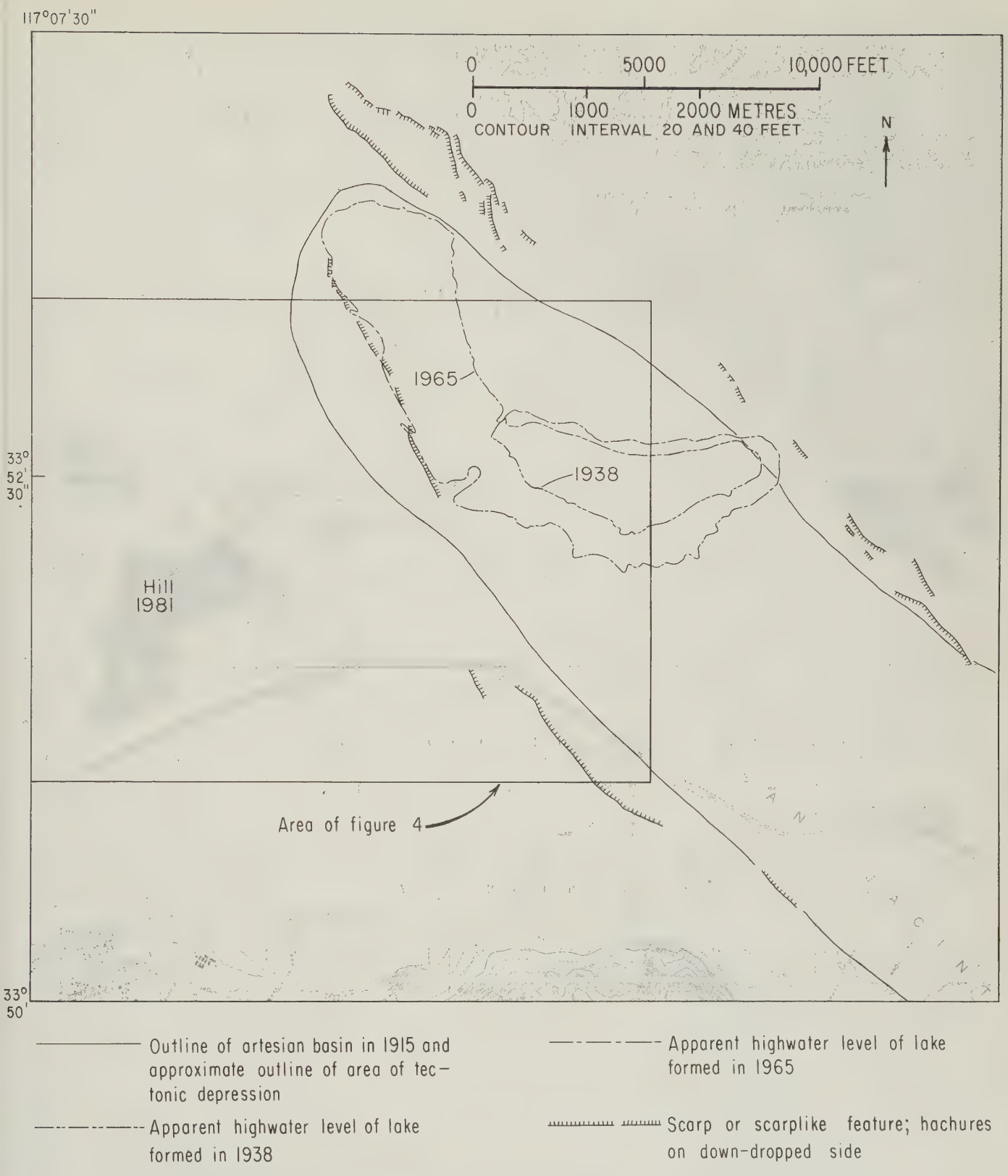

FIGURE 3.—Outline of former artesian basin and major physiographic features in the northern part of the San Jacinto Valley. Base from U.S. Geological Survey, 1:24,000 topographic quadrangle maps, El Casco and Lakeview, 1967.

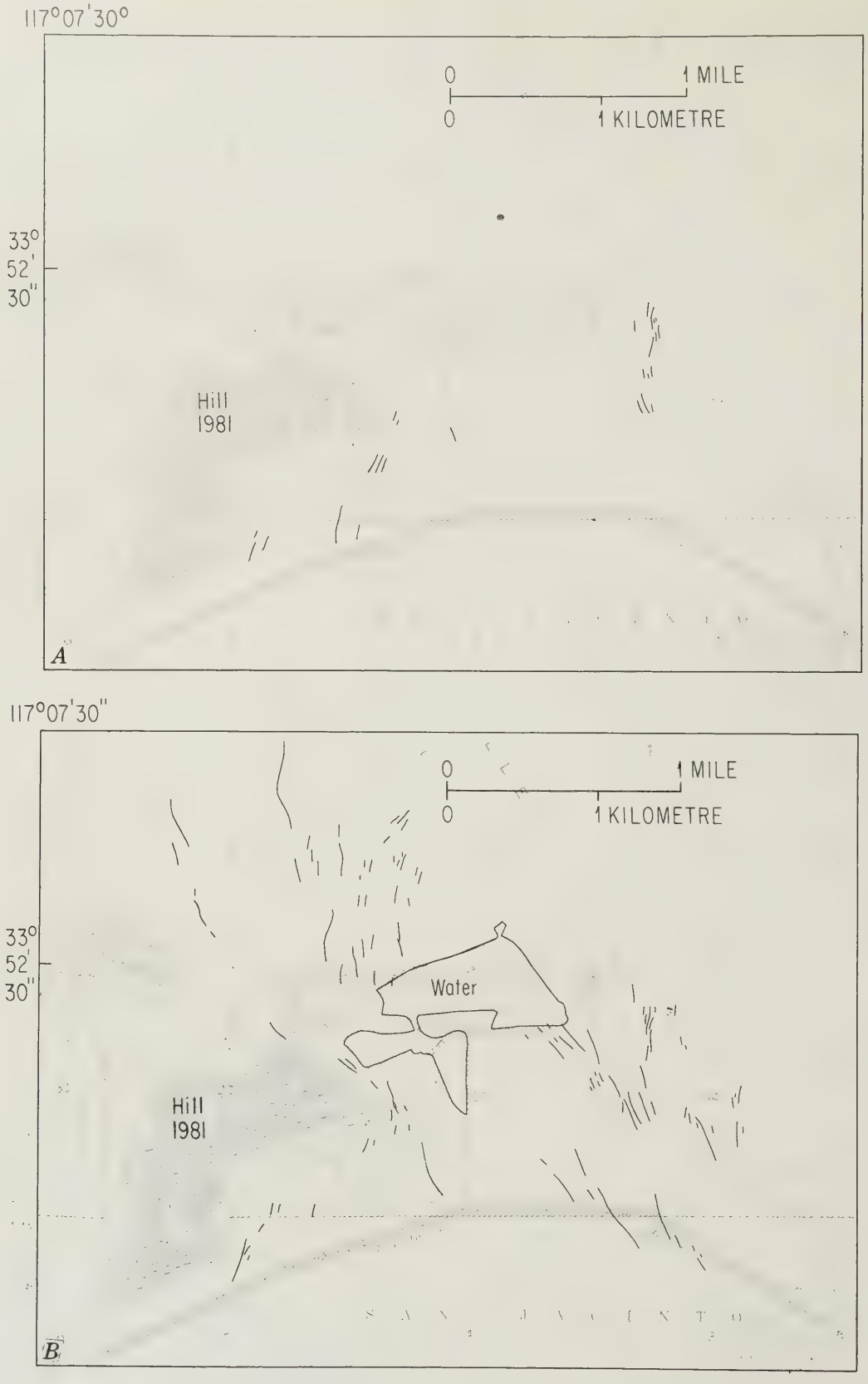

FIGURE 4.—Distribution of ground fissures. *A*, 1953; *B*, 1962; *C*, 1966; *D*, 1974.

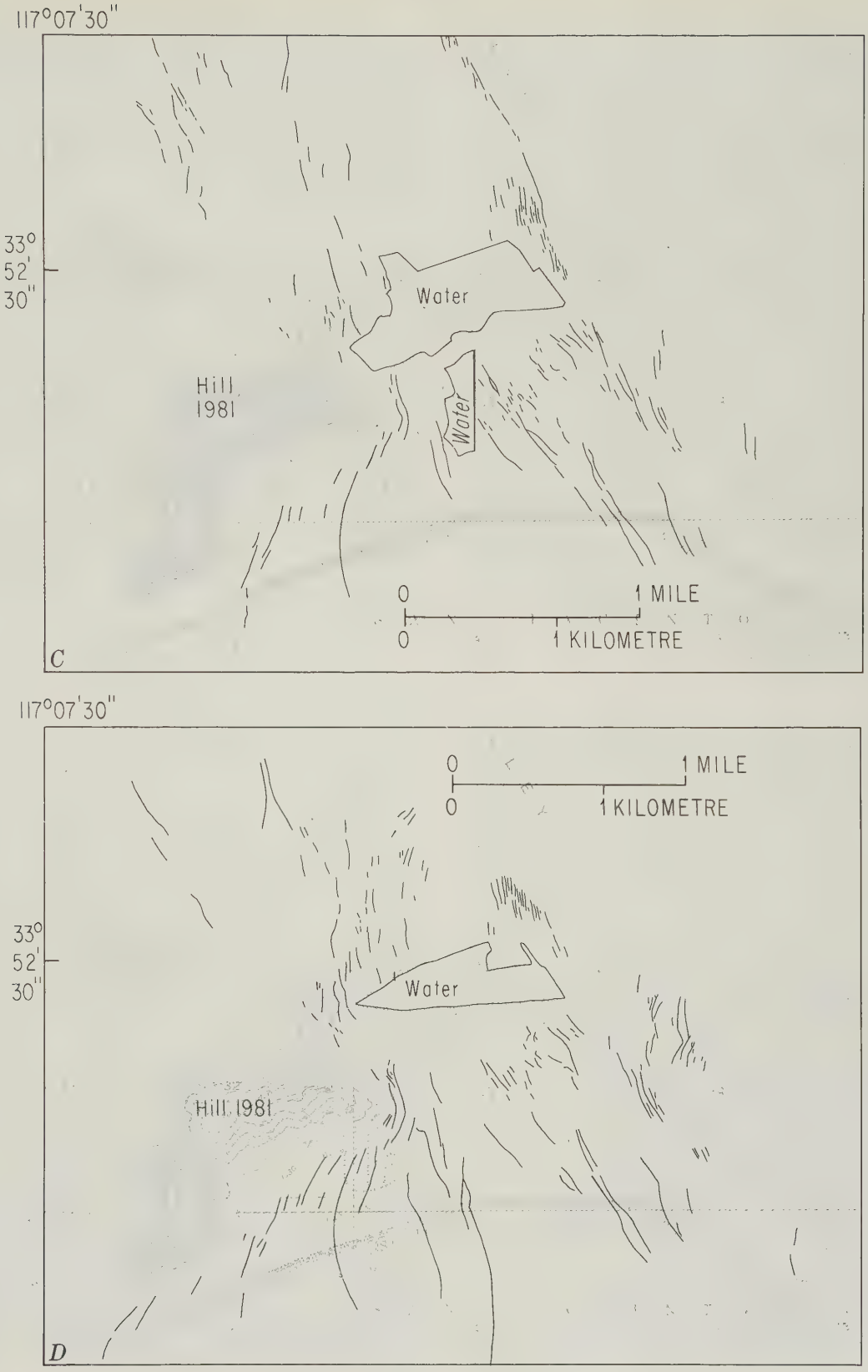

FIGURE 4.—Continued

A

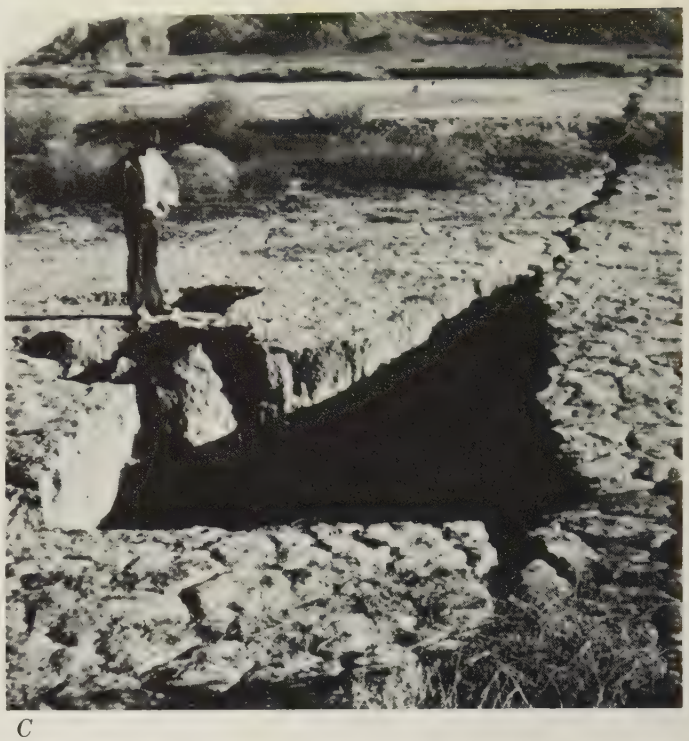

C

B

D

FIGURE 5.—Ground fissures in northwest part of San Jacinto Valley. *A*, Collapse hole along a partly developed fissure. Note the bridging alluvium (arrow) on left side of the hole. *B*, Newly formed fissure showing collapsed surface alluvium at bottom. *C*, Collapse hole along a newly formed fissure. *D*, Newly formed fissure. *E*, Slightly modified fissure of several years age. *F*, Highly modified older fissure.

E

F

FIGURE 5.—Continued

1965 and that formed during 1938 suggests a considerable increase in the size of the closed depression during the 27-year period. Although the enlargement of the topographic basin is coincident with ground-water development in the San Jacinto Valley, few producing water wells exist near the depression, which suggests that the apparent growth of this feature has been in large part tectonic or that a considerable volume of ground water has moved laterally from the vicinity of the depression to allow for the growth.

INDUCED SUBSIDENCE

Much of the graben area contained water under an artesian head of about 3 m at the time of settlement. Figure 3 gives the general outline of the northern part of the artesian basin in 1915 as shown by Waring (1919). By the early 1970's ground-water withdrawal had reduced the level to between 24 and 30 m below the ground surface.

Considerable subsidence due to sediment compaction apparently accompanied the lowering of the water table and appears to be greatest near the west side of the graben (Lofgren, 1976, p. 13). Releveling between 1939 and 1959 suggests an average maximum annual rate of subsidence of about 3.6 cm (Proctor, 1962). At the Casa Loma fault, an aqueduct pipe was vertically deformed at a rate of about 4 cm per year between its placement in 1958 and its repair in 1973 (D. M. Morton, unpub. data, 1976).

Assuming the tectonic subsidence of the graben to be between 0.3 and 0.6 cm per year on the basis of the dated wood samples, the subsidence resulting from compaction due to ground-water withdrawal currently is about a maximum of 3.5 cm per year. For a further treatment of the subsidence, see Lofgren (1976).

GROUND FISSURING

Ground fissuring, generally in marginal parts of the San Jacinto Valley adjacent to the San Jacinto and Casa Loma faults, has been attributed to subsidence (Fett and others, 1967). The most spectacular ground fissures are located in the northwestern part of the valley adjacent to and immediately west of the Casa Loma fault, 1.5 to 5 km north and northwest of Lakeview (figs. 1, 3). Most fissures are linear and oriented parallel or subparallel to the Casa Loma fault (fig. 4). However, the fissures near hill 1981 are arcuate, and those nearest to the hill conform to the contact between alluvium and basement around the hill.

Fissures of considerable length (700 m) apparently open to the surface very rapidly. The precursor to the surface opening of a fissure is usually a slight, elongate

depression and (or) a series of small (30–60 cm in diameter) holes that merge at depth into a continuous covered fissure. These covered fissures commonly open to the surface after rains, perhaps in response to the added weight on the bridging alluvium, piping, solution, and (or) to the lubricating effects of the water (fig. 5). Downdropped bridging alluvium may rest 0.3 to 1 m below the valley (fig. 5*B*, *C*). Newly opened fissures are as much as 700 m long and 3 m wide (fig. 5*C*, *D*). Over a period of years, some of the larger ones have progressively lengthened (fig. 4). Most of the fissures have been modified through time by partial infilling by alluvium and windblown vegetation (fig. 5*E*, *F*). Vegetation tends to grow more densely in the fissures than in adjacent areas because more water is available in the fissures. After partial infilling, fissures commonly reopen. Repeated plowing in farmed areas obliterates the narrower fissures but accommodates the wider ones (fig. 5*F*).

No fissure examined showed any evidence of lateral displacement. Most of the fissures with apparent vertical displacements of the walls are near or coincident with the Casa Loma fault; these fissures consistently have their east-facing side down.

Several southwest-facing scarps and one northeast-facing scarp occur along the San Jacinto fault on the east side of the valley (fig. 3). To what extent these scarps owe their origin to tectonic displacement is not known.

A series of aerial photographs taken between 1953 and 1974 documents the areal development of the ground fissures through time. Photographs taken in 1953 show the fissures to be limited to an area 2 km east of hill 1981 and an area immediately east and south of hill 1981 (fig. 4*A*); the total area of ground fissuring is only about 1 km². By 1962 the fissures extended over an area of 9 km² (fig. 4*B*), and both the number and the length of individual fissures had increased dramatically. Some of the longer ones had passed under the levees of the San Jacinto River. By 1966 the fissures covered an area of 11 km² and were as much as 850 m long (fig. 4*C*). Since 1966 the area subject to fissuring has continued to grow, reaching 12 km² by 1974 (fig. 4*D*). Also by this time the first fissures had developed on the east side of this part of the valley. The ultimate extent of the area subject to ground fissuring cannot be predicted.

REFERENCES CITED

Fett, J. D., 1968, Geophysical investigation of the San Jacinto Valley, Riverside County, California: Riverside, California Univ., M.A. thesis, 87 p.

Fett, J. D., Hamilton, D. H., and Fleming, F. A., 1967, Continuing surface displacement along the Casa Loma and San Jacinto faults in San Jacinto Valley, Riverside County, California: Eng. Geology, v. 4, p. 22–32.

Henderson, L. H., 1939, Detailed geological mapping and fault studies of the San Jacinto tunnel line and vicinity: Jour. Geology, v. 47, p. 314–324.

Lofgren, B. E., 1976, Land subsidence and aquifer-system compaction in the San Jacinto Valley, Riverside County, California: U.S. Geol. Survey Jour. Research, v. 4, no. 1, p. 9–18.

Lofgren, B. E., and Rubin, Meyer, 1975, Radiocarbon dates indicate rates of graben downfaulting, San Jacinto Valley, California: U.S. Geol. Survey Jour. Research, v. 3, no. 1, p. 45–46.

Morton, D. M., 1972, Geology of the Lakeview and Perris (7½′) quadrangles, Riverside County, California: California Div. Mines and Geology Map Sheet 19.

Proctor, R. J., 1962, Geologic features of a section across the Casa Loma fault, exposed in an aqueduct trench near San Jacinto, California: Geol. Soc. America Bull., v. 73, p. 1293–1296.

——— 1974, New localities for fault creep in southern California—Raymond and Casa Loma faults: Geol. Soc. America Abs. with Programs, v. 6, no. 3, p. 238.

Rogers, T. H., compiler, 1965, Geologic map of California, Olaf P. Jenkins edition—Santa Ana sheet: California Div. Mines and Geology, scale 1:250,000.

Sharp, R. V., 1972, Map showing recently active breaks along the San Jacinto fault zone between the San Bernardino area and Borrego Valley: U.S. Geol. Survey Misc. Geol. Inv. Map I–675.

Waring, G. A., 1919, Ground water in the San Jacinto and Temecula basins, California: U.S. Geol. Survey Water-Supply Paper 429, 113 p.

Woodford, A. O., Shelton, J. S., Doehring, D. O., and Morton, R. K., 1971, Pliocene-Pleistocene history of the Perris block, southern California: Geol. Soc. America Bull., v. 82, p. 3421–3448.

Jour. Research U.S. Geol. Survey
Vol. 5, No. 1, Jan.–Feb. 1977, p. 125–133

RADIATE SHELL STRUCTURES IN PALEOZOIC MYODOCOPID AND PALAEOCOPID OSTRACODES ARE EPIGENETIC

By I. G. SOHN, Washington, D.C.

Abstract.—The radiate structures in the shell of Paleozoic ostracodes are interpreted to be epigenetic in origin. On the basis of this interpretation, the genus *Radiicypridina* Bless, 1973, is a junior synonym of *Eocypridina* Kesling and Ploch, 1960. The type-series of *Eocypridina radiata* (Jones, Kirkby, and Brady, 1874), from the Coal Measures of Scotland, is illustrated, and a lectotype is designated. *Eocypridina aciculata* (Scott and Summerson, 1943) is a valid species, but the more elongated specimens they identified as *Cypridina radiata* Jones, Kirkby, and Brady, 1874, from the same collection, belong in *E. aciculata*. The variation in lateral outline of specimens in the Hance Formation of Kentucky is due to the orientation of the valves in the rock.

Radiate structures on fossil ostracodes have been used in their classification; it is, therefore, important to determine whether or not these structures were formed by the animals. This paper discusses and illustrates the evidence for an epigenetic origin of radiate structures.

On July 7, 1967, I examined collections of fossil myodocopids in the British Museum of Natural History B. M., London, and found only one specimen, the holotype of *Philomedes elongatus* Jones, Kirkby, and Brady, 1884, from the base of the Middle Coal Measures, Derbyshire, that has radiating structures (B. M. I–758). Dr. M. A. Calver, Institute of Geological Sciences at Leeds, showed me a specimen of *Cypridina phillipsiana* Jones, 1870, from the Mansfield Marine Band at 515.5 ft (157 metres) in the Shilling Hill borehole, 1 mile (1.6 kilometres) south of the Ferrybridge Station, Yorkshire, that has radiate structures.

Dr. C. E. Palmar, Curator, Department of Natural History, Glasgow Museums and Art Galleries, Scotland, loaned me and permitted me to photograph (letter of Sept. 21, 1967) slide 01–53 mt, representing the type-series of *Cypridina radiata* Jones, Kirkby, and Brady, 1874. The slide contains seven pieces of shale on two pieces of cardboard (fig. 2*e*, *f*); it is labeled "Airdrie Blackband coll. J. T. Tullis Young 1868" and includes the specimens illustrated by Jones, Kirkby, and Brady (1874, pl. 5, figs. 6*a–f*). Some of these specimens show the radiate markings discussed in this paper.

In September 1967, I collected with Prof. C. H. Summerson, Ohio State University, specimens of myodocopid ostracodes that have radiate markings from the Hance Formation (Lower and Middle Pennsylvanian) at Scott and Summerson's type-locality in Kentucky (USGS colln. 12902–PC). We also collected from a second locality (USGS collns. 12889–PC, 12-903–PC, and 12904–PC), the location of which I obtained from Dr. R. N. C. Eagar, Keeper of Geology, Manchester Museum. Bless (1973) described the ostracodes previously collected by Dr. Eagar. Preliminary study indicated that the radiate markings are not diagnostic and should not be used in classification (Sohn, 1968). The present paper is the result of a detailed study of these collections.

Acknowledgments.—I wish to thank all the individuals mentioned in the text for their contributions; Dr. L. S. Kornicker, National Museum of Natural History, for profitable discussions; Dr. G. A. Cooper, National Museum of Natural History, for making the photographs for figures 1*d* and 1*e* of a specimen loaned by R. H. Bate, British Museum of Natural History; and M. J. Mann and Donna Peace, National Museum of Natural History, for making the scanning electron micrographs.

PREVIOUS WORK

Jones, Kirkby, and Brady (1874, p. 14, pl. 5, figs. 6a–f) discussed and illustrated radiate structures on the shells of the Carboniferous myodocopid species *Cypridina radiata* Jones, Kirkby, and Brady, 1874. They (1874, p. 14) diagnosed *C. radiata* as having "* * * peculiar star-like vascular patches * * *." This species was later identified and illustrated by Pruvost (1911, p. 73, pl. 2, figs. 15*a*, *b*; 1919, p. 46, pl. 24, figs. 14–19) in France, and by Scott and Summerson (1943, p. 673, pl. 2, fig. 2) from the Hance Formation (Lower and Middle Pennsylvanian) of Kentucky.

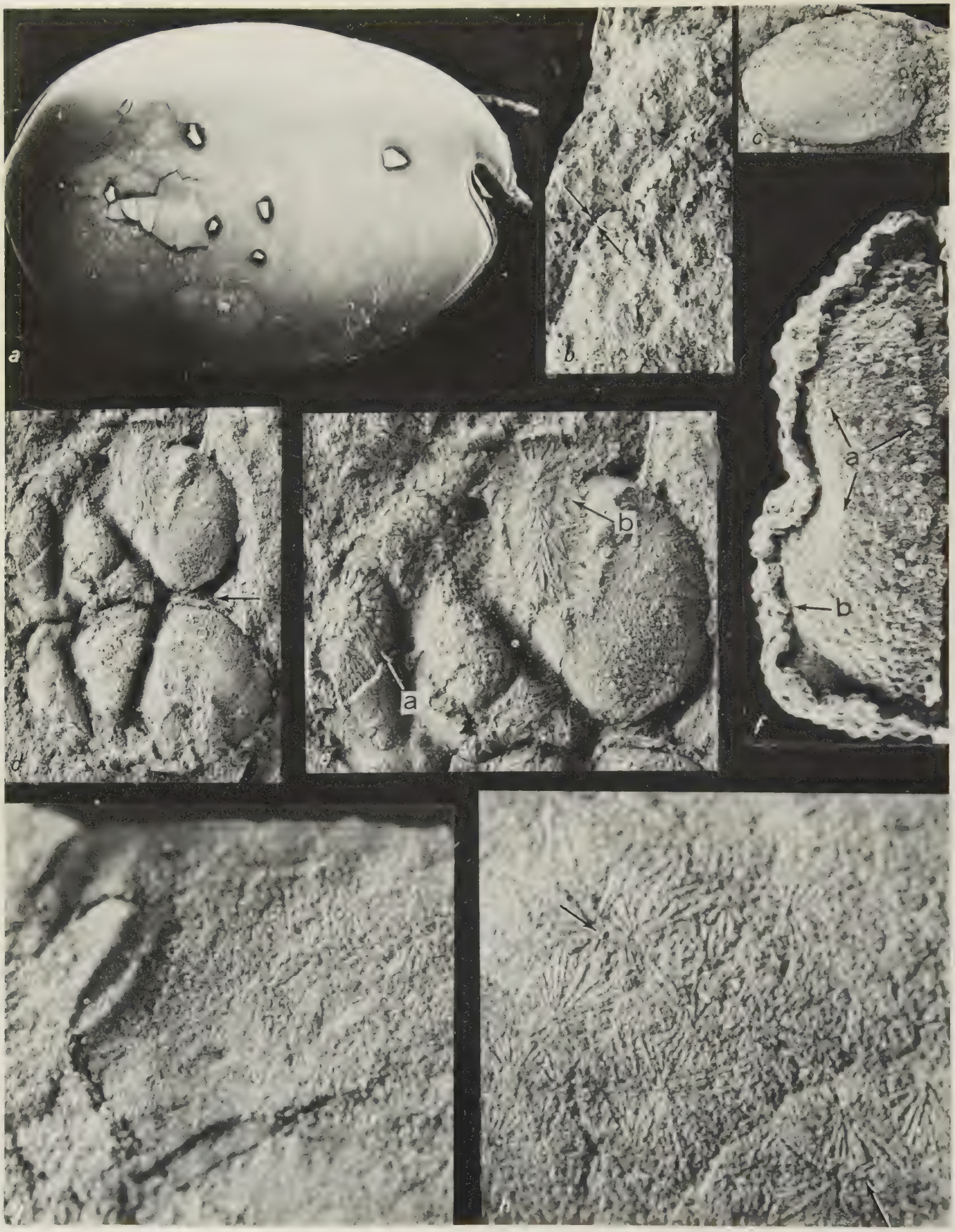
a
b
c
a
b
d
b
a
a
b

Scott and Summerson (1943, p. 674, pl. 2, figs. 1, 3) based, in part, their new species *C. aciculata*, which they found associated with *C. radiata*, on the ovate to subcircular lateral outline, and "* * * a complex set of acicular radii* * *" on the inner surface of the shell.

Leperditia radiata Ulrich, 1879, from the Utica Shale (Ordovician) of Ohio, was described as having a radiate surface. These structures (fig. 2*a*) were later illustrated by Ruedemann (1926, p. 144, pl. 23, fig. 16) on a specimen of *Elpe radiata* (Ulrich), from the Deer River Shale (Middle Ordovician), New York. The type-series labeled "Cotypes" consists of four shale fragments (USNM 41711) on which the valves have radiate markings (fig. 2*a*). In addition, a specimen labeled "*Elpe radiata* (Ulrich), Cincinnatian (Eden), Covington, Ky." (USNM 41715) is a partly exfoliated valve on shale that has faint and rather unconvincing radiating structures on the inside of the valve. A third collection of "*Elpe radiata*" (USNM 41712) consists of three pieces of shale with paper labels glued to each. Two of the pieces are marked "*Elpe radiata* Ulrich, Utica Shale, Georgian Bay, Canada, Coll. by A. W. Vogdes, September 1889," and each has two poorly preserved and partly exfoliated valves that have radiate markings. The third piece of shale has a pencilled note attached that reads "*Elpe radiata* Ulrich, 460A Southgate Member, Eden, Swatara Gap, Pa." This specimen has two valves that have beautifully developed radiate markings (fig. 2*b*).

A restudy of "*Elpe radiata*" is beyond the scope of this paper, but a statement as to the nomenclature is pertinent. According to P. C. Sylvester-Bradley (in Moore, 1961, p. Q396) *Elpe* Barrande, 1872, non Robineau-Desvoidy, 1863, was renamed *Elpozoe* Pribyl, 1950. The genus is classified in the Entomoconchacea, a superfamily in the Myodocopida that has a stratigraphic range of Devonian–Carboniferous. The type-series of the Middle Ordovician *Leperitia radiata* (fig. 2*a*), though poorly preserved, does not have myodocopid characters. The specimen in USNM colln. 41712 from Swatara Gap, Pa. (fig. 2*b*) may have had a dorsal sulcus similar to the Devonian *Cyprosina whidbornei* Jones, 1881, as illustrated by Kornicker and Sohn (1976, text fig. 93), and is not conspecific with the types of *Elpozoe radiata* (Ulrich, 1879). *Cyprosina* Jones, 1881, may be a myodocopid.

FIGURE 1.—*Vargula*, *Eocypridina*, and *Beyrichiana*.

a. *Vargula hilgendorfii* (Müller, 1890).
Right side of carapace, SEM (scanning electron micrograph) approximately × 33. Figured specimen USNM (Crustacea) 152734. Collected alive, September 1954 at Zushi Beach, Kanagawa, Japan, by Dr. Y. Haneda, Yokosuka City Museum. Illustrated to show similarity of incisure to that of *Eocypridna* shown in figures 1*a*, 1*g*, and 2*m*.

b, *c*, *g*, *h*. *Eocypridina aciculata* (Scott and Summerson, 1943).
b, *c*. Cast of right valve, SEM enlargement (*b*) dorsanterior approximately × 18; arrows show outer layer continuing into matrix. Partly exposed valve (*c*) approximately × 5. Figured specimen USNM 168202. Pennsylvanian. Hance Formation (Westphalian A), Balkan quadrangle, Bell County, Ky. USGS loc. 12889–PC.
g, *h*. Mold and cast of parts left valve approximately × 25. Arrow in lower right of figure 1*h* points to radiate needles used in X-ray determination. Figured specimen USNM 168188. Same collection as above.

d, *e*. *Beyrichiana gigantea* (Jones, Kirkby, and Brady, 1874).
d. Open carapace, lateral view, anterior towards left, approximately × 6.
e. Enlargement of right valve, arrows show radiate structures on valve below outer layer, and also one extending into matrix. Figured specimen B.M. I–6219. Lower Carboniferous shale from Eskdale, Dumfriesshire, Scotland.

f. *Beyrichiana* sp.
Ventral view of a silicified right valve, approximately × 100. Figured specimen USNM 168187. Permian, southeastern side of Idhra, just off the Argolian coast of Greece. USNM loc. 9260, collected July 4, 1974, by R. E. Grant and R. A. Doescher, Smithsonian Institution.

PRESENT STUDY

Jones, Kirkby, and Brady (1884, p. 88) stated that radiate structures are present on *Beyrichia gigantea* Jones, Kirkby, and Brady, 1874 (=*Beyrichiana* Kellet, 1933), from black Lower Carboniferous shale at Eskdale, Dumfriesshire, and cited *Leperditia radiata* Ulrich, 1879, as an example of similar radiate structures. I borrowed a specimen of *Beyrichia gigantea* (=*Beyrichiana*) from the British Museum which I am illustrating (fig. 1*d*, *e*). This is a palaeocopid ostracode carapace with open valves joined along the hinge. The photograph shows a clump of radiate crystals on the inner layer of the shell (arrow a in fig. 1*e*) below the broken part of the shell, and one clump that extends into the matrix (arrow b in fig. 1*e*). In order to explain this specimen, I am including an illustration (fig. 1*f*) of an as yet undescribed species of *Beyrichiana* from the Permian of Greece that was dissolved from limestone by means of hydrochloric acid. Because of incomplete replacement, only parts of the outer layer and of the inner layer were silicified; consequently, the carbonate filling between these two layers was removed by acid. It is the space between

the outer and inner layer of the shell in which the radiate structures developed in *B. gigantea*. The fact that the one clump appears to extend into the matrix indicates that the radiate structures in this specimen are a postmortem development, and not anatomical in origin.

C. primaeva (McCoy, 1844) is a Carboniferous species recorded from Great Britain. A collection (USNM 157829) labeled "*Cypridina primaeva* (McCoy) sp., T. Rupert Jones, Beals' Col., Sedgley, England," consists of two split concretions with many valves and fragments of myodocopid ostracodes that have radiate structures. A few of these colorless radiating crystals were identified by M. E. Mrose as siderite ($FeCO_3$), plus a trace of kaolinite (Branch of Experimental Geochemistry and Mineralogy report WX–3069, film 20305, Dec. 19, 1966).

Post-mortem recrystallization is not unusual in mineralized arthropodan cuticle. Sohn and Kornicker (1969) produced in the laboratory variously shaped artifacts in the calcareous layer by soaking in water the valves of *Vargula hilgendorfi* (Müller, 1890) collected alive at Zushi Beach, Kanagawa, Japan, and then macerating them in Clorox. They cited published records of similar artifacts. Those artifacts are not similar to the radiating crystals in *C. radiata* and other fossil specimens. The radiate structures on the fossils could not be of anatomical origin because some of the crystals interfere with the growth of the neighboring crystals as shown by the arrows on figure 1*h*. The center and radiating needles to the left of the bottom right arrow were later removed for Cu$K\alpha$ X-radiation analysis after photography of the specimen. Mr. P. J. Dunn, Department of Mineral Sciences, Smithsonian Institution, using a Gandolfi powder camera, determined on Aug. 8, 1974, that the crystals are an unidentifiable micaceous mineral. A similar determination by Mr. Dunn on Apr. 14, 1975, of crystals from a specimen (USNM 168190) from USGS loc. 12889–PC, indicated gypsum.

Oppenlander (1968, figs. 2, 6) illustrated artificial spherulites in crystalline polymers, and Digby (1967a, 1967b, 1968) illustrated calcifications produced in the cuticle of the shore crab *Carcinus maenas* (Linné, 1758) that resemble the radiate structures in the fossils. Bless (1973, p. 249) reported that the size of the radiate structures varies from 0.1 mm to more than 3 mm in diameter, and that some specimens have both large and small rosettes, whereas other specimens have only large or only small rosettes. I have not been able to ascertain any regular pattern in the distribution of the nodules in the valves of living and radiate structures in fossil specimens of myodocopids. In a biological system, the size and location of each rosette would be expected to be genetically fixed within the shell wall.

EVIDENCE FOR EPIGENETIC ORIGIN OF RADIATE STRUCTURES

Nodules of monohydrocalcite ($CaCO_3.H_2O$) and calcite were formed in the laboratory in the calcareous layer of valves of the living myodocopid *Vargula hilgendorfii* (Müller, 1890) by Sohn and Kornicker (1969), and siderite ($FeCO_3$) was determined by X-ray analysis of needles from radiating structures on a myodocopid specimen of "*Cypridina primaeva* McCoy, 1844." Epigenetic radiating structures between the outer and inner walls of the palaeocopid *Beyrichiana gigantea* (Jones, Kirkby, and Brady, 1874) are illustrated (fig. 1*d*, *e*). The radiate structures on specimens from the Hance Formation, Kentucky (fig. 1*g*, *h*; fig. 2*c*, *d*, *g–r*) are gypsum or an unidentifiable micaceous mineral, and they do not have a pattern of distribution compatible with a physiological process.

In view of the above evidence, I suggest the following interpretation of the origin of radiate structures in fossil ostracodes. When geochemical conditions were suitable, the carbonate in the calcareous layer of the ostracode was rearranged post mortem into acicular crystals. In certain instances, the radiate structures were replaced by gypsum, siderite, and possibly other minerals to form pseudomorphs. Occasionally, the geochemical regime was favorable to the formation of similar crystals in the matrix near the ostracode (arrow in fig. 1*d* and arrows a and b in fig. 1*e*).

The evidence against a physiological origin of the radiate structures warrants the revision of the classification of the Paleozoic Cypridininae.

COLLECTION LOCALITIES

USGS loc. No.	*Field No.*	*Description of locality, stratigraphic position, collector, and date*
12889–PC	9/12/3/67	Bell County, Ky., Balkan quadrangle, 0.75 mile (1.2 km) N. of Cardinal, 600 yards (549 m) NNW of bench mark 1099, in cut to straighten U.S. Route 119. Hance Formation (Westphalian A), about 8 feet (2.4 m) below sand, about 1 foot (0.30 m) composite sample of brown-stained gray mudstone and gypsum. Collected by I. G. Sohn and C. H. Summerson, Sept. 12, 1967. Equivalent to Bless (1973) locality, about 130 feet (39.6 m) above the Naese Sandstone Member of the Lee Formation.
12902–PC	9/12/5/67	Harlan County, Ky., Wallins Creek quadrangle, north side U.S. Route 119, west bend of road, about 0.55 mile (0.89 km) by road west of county

USGS loc. No.	Field No.	Description of locality, stratigraphic position, collector, and date
		line, about 330 yards (302 m) N. 10° W. of Molus. Hance Formation (Westphalian A), brown-stained gray mudstone and gypsum, 18 feet (5.5 m) below sandstone. Collected by I. G. Sohn and C. H. Summerson, Sept. 12, 1967. Equivalent to loc. 7 of Scott and Summerson (1943, p. 662) which is about 125 feet (38 m) above the Naese Sandstone Member of the Lee Formation.
12903–PC	9/12/1/67	Same locality and lithology as loc. 12889–PC. Composite sample of about 1 foot (0.30 m), collected about 2 feet (0.6 m) below sand, and about 6 feet (1.8 m) above Field No. 9/12/3/67. Collected by I. G. Sohn and C. H. Summerson, Sept. 12, 1967.
12904–PC	9/12/4/67	Same locality and lithology as loc. 12889–PC. Composite sample about 1 foot (0.30 m), collected 1 foot (0.30 m) below loc. 12889–PC. Collected by I. G. Sohn and C. H. Summerson, Sept. 12, 1967.

CLASSIFICATION

Class OSTRACODA, Latriel, 1802 [1804]

Superorder MYODOCOPA Sars, 1866

A phylogenetic scheme for the Myodocopa is proposed by Kornicker and Sohn (1976, fig. 2).

Order MYODOCOPIDA Sars, 1866

Suborder MYODOCOPINA Sars, 1866

Superfamily CYPIRDINACEA Baird, 1850

Family CYPRIDINIDAE Baird, 1850

At present, the family contains the following subfamilies: Cypridininae Baird, 1850, Azygocypridininae Kornicker, 1970.

Subfamily CYPRIDINIAE Baird, 1850

Hartmann and Puri (1974, p. 11) relegated the Azygocypridinina Kornicker, 1970, to tribe Azygocypridini in the Cypridininae together with the tribes Gigantocypridini Hartmann "(in press)" and Cypridinini Baird, 1850. They listed the following living genera and subgenera in the Cypridinini: *Amphisiphonostra* Paulsen, 1962; *Bathyvargula* Poulsen, 1962; *Codonocera* Brady, 1902; *Cypridina* Milne-Edwards, 1840; *Doloria* Skogsberg, 1920; *Hadacypridina* Poulsen, 1962; *Heterodesmus* Brady, 1865; *Macrocypridina* Skogsberg, 1920; *Melavargula* Poulsen, 1962; *Metavargula* Kornicker, 1970; *Monopia* Claus, 1873 (with *Monopia* and *Cypridinodes* Brady, 1902); *Paracypridina* Poulsen, 1962; *Paradoloria* Poulsen, 1962; *Paravargula* Poulsen, 1962; *Pterocypridina* Poulsen, 1962; *Sheina* Harding, 1966; *Siphonostra* Skogsberg, 1920; *Skogsbergia* Poulsen, 1962; *Vargula* Skogsberg, 1920, and the fossil genus *Cyprosis* Jones, 1881.

Future study will determine whether this classification is valid. However, the fossil genera *Eocypridina* Kesling and Ploch, 1960 and *Radiicypridina* Bless, 1973, were described in the Cypridininae. The similarity of the fossils in lateral outline and in type of incisure (fig. 1*g*) to *Vargula* Skogsberg, 1920 (fig. 1*a*) indicate that the subfamily began in the Devonian.

Genus *EOCYPRIDINA* Kesling and Ploch, 1960

Type-species (original designation).—*Eocypridina campbelli* Kesling and Ploch., 1960, Michigan Univ., Mus. Paleontology, Contr., v. 15, no. 12, p. 284. Upper Devonian, Indiana.

Eocypridina Kesling and Ploch, 1960, Michigan Univ., Contr. Mus. Paleontology, v. 15, no. 12, p. 283; Samoylova, 1967, Paleont. Zhur., no. 1, p. 145; Buschmina, 1970, Akad. Nauk SSSR, Sibirsk. Otdeleniye., Inst. Geologii i Geofiziki Trudy, vyp. 71, p. 76.

Radiicypridina Bless, 1973, Rev. Española Micropaleontología, v. 5, no. 2, p. 248.

Cypridina Milne-Edwards, 1840 (part) authors of Paleozoic species.

Discussions.—*Eocypridina* was adequately described and illustrated by Kesling and Ploch (1960, p. 284) as follows:

> Carapace large, ovate, nearly equivalved. Rostrum of each valve sharply acuminate and hooklike (as in *Cypridina* H. Milne-Edwards, 1840, p. 409), not bluntly truncate (as in *Philomedes* Lilljeborg, 1853, p. 175). Upper border of rostral notch not folded over lower (as in *Cylindroleberis* Brady, 1868, p. 127). No posteroventral siphon (as in *Gigantocypris* Müller, 1895, p. 164). Adductor-muscle scars arranged in an oval, consisting of a posterior area with nearly horizontal, slightly curved bars, an anterodorsal area with radiating bars, and an anteroventral area with peripheral spots.

Bless diagnosed *Radiicypridina* (1973, p. 248) as follows [italics added]:

> Carapace subovate to subcircular in lateral view. Valves evenly convex. Rostrum hook-like, downcurved and overhanging anterior incisure. Carapace three-layered. Inner and outer layer may appear smooth or with blebby reticulations. They are occasionally preserved, and were presumably not calcified. The calcareous layer is thick and *consists of several to numerous rosettes of acicular radi. The size of these rosettes may vary, even in one individual.* The muscle scar pattern is complex and consists of an oval cluster of adductor muscle scars and several additional scars posteroventrally and posterodorsally of the adductor scars.

Because "rosettes of acicular radii" are not of anatomical origin, and are present also in palaeocopid fossils, this character is not a valid generic criterion. The difference between *Eocypridina* and *Radiicypridina* depends on the adductor attachment muscle-scar

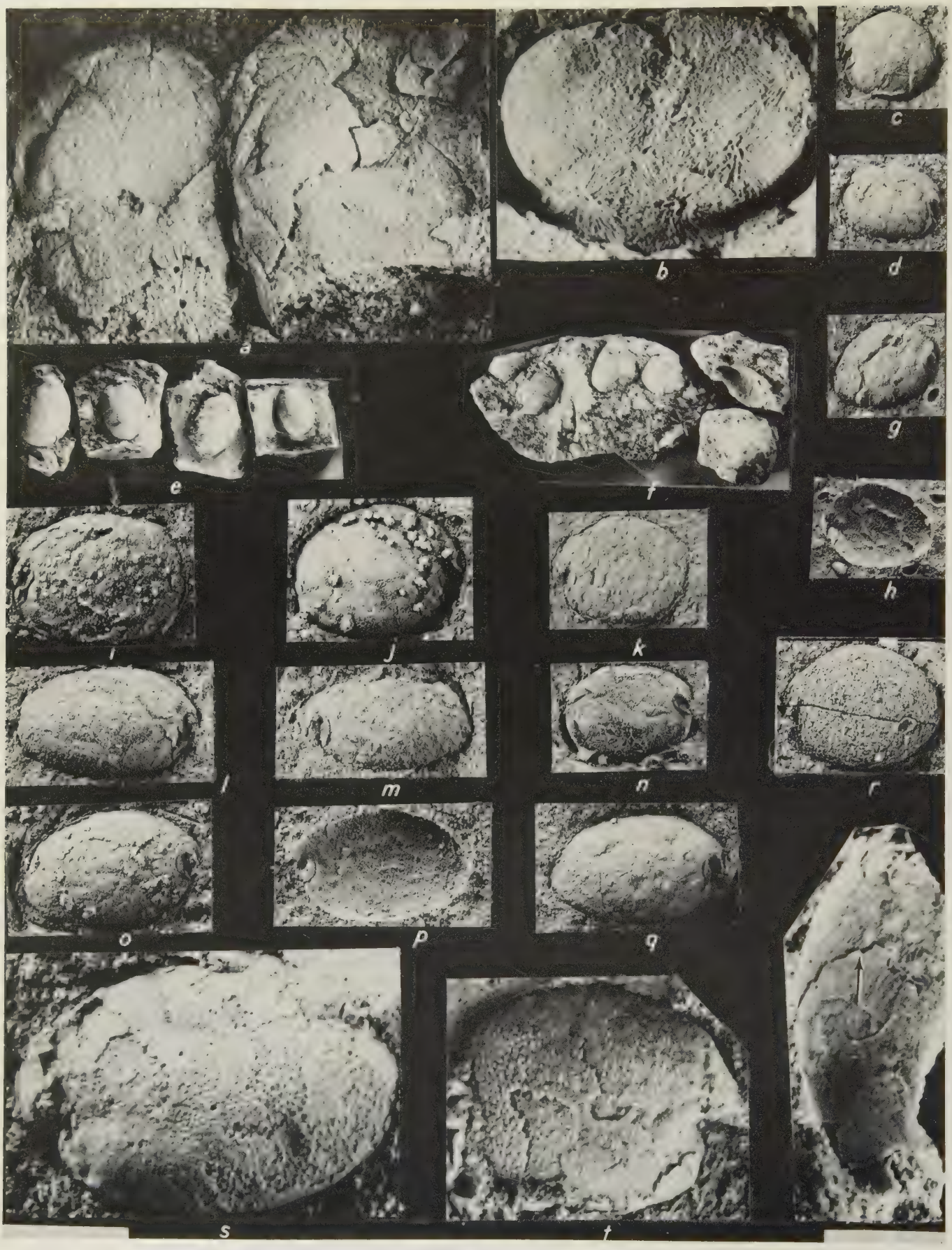
a
b
c
d
e
f
g
h
i
j
k
l
m
n
r
o
p
q
s
t

FIGURE 2.—"*Elpe*" and *Eocypridina*.

a, b. "*Elpe radiata*" (Ulrich, 1879).

a. Two valves showing radiate structures approximately × 12. Cotypes, USNM 41711. Eden Formation, Fulton Shale, First Ward, Cincinnati, Ohio.

b. Lateral view of left valve approximately × 12. Figured specimen USNM 41712. Southgate Member of Eden Formation, Swatara Gap, Pa.

c, d. *Eocypridina aciculata* (Scott and Summerson, 1943). Casts of left and right valves, juveniles, approximately × 5. Figured specimens USNM 168191, 168192. Pennsylvanian Hance Formation (=Westphalian A), Balkan quadrangle, Bell County, Ky. USGS locs. 12904–PC and 12889–PC, respectively.

e, f. *Eocypridina radiata* (Jones, Kirkby, and Brady, 1874). Type series, approximately × 2½, on slide 01–53mt, Glasgow Museums and Art Galleries, Scotland. "Upper Coal-measures" Airdrie Blackbank Ironstone, Glasgow district, Scotland.

g–r. *Eocypridina aciculata* (Scott and Summerson, 1943).

g, h. Cast and mold of the anterior part of a right valve approximately × 5. Figured specimen USNM 168193. Pennsylvanian, Hance Formation (=Westphalian A), Wallis Creek quadrangle, Harlan County, Ky. USGS loc. 12902–PC.

i–k. Casts of left, right, and juvenile left valves approximately × 5. Note variation in dorsal margin. Figured specimens USNM 168194–168196. Pennsylvanian, Hance Formation (=Westphalian A), Balkan quadrangle, Bell County, Ky. USGS loc. 12903–PC.

l, m. Casts of right and left valves approximately × 5, showing rim on incisure and false lateral outline. Figured specimens USNM 168199, 168200. Pennsylvanian. Hance Formation (=Westphalian A), Balkan quadrangle, Bell County, Ky. USGS loc. 12904–PC.

n. Cast of right valve approximately × 5. Figured specimen USNM 168198. Pennsylvanian, Hance Formation (=Westphalian A), Wallis Creek quadrangle, Harlan County, Ky. USGS loc. 12902–PC.

o–q. Cast and mold of right valve and cast of right valve approximately × 5. Note the thickness of outer shell layer along dorsal margin (fig. 2*p*) where it is broken, and note the same thickness on dorsoposterior (fig. 2*o*). Figured specimens USNM 168200, 168201. Pennsylvanian, Hance Formation (=Westphalian A), Balkan quadrangle, Bell County, Ky. USGS loc. 12889–PC.

r. Cast of left valve, approximately × 5. Figured specimen USNM 128197. Pennsylvanian, Hance Formation (=Westphalian A), Balkan quadrangle, Ky. USGS loc. 12903–PC.

s–u. *Eocypridina radiata* (Jones, Kirkby, and Brady, 1874).

s. Left valve approximately × 15. Lectotype, same specimen as second from left in figure *e*. Illustrated by Jones, Kirkby, and Brady (1874, pl. 5, figs. 6*a–c*).

t. Right valve approximately × 15. Paralectotype, same specimen as on left in figure *f*. Illustrated by Jones, Kirkby, and Brady (1874, pl. 5, figs. 6*e, f*, area of fig. 6*e* shown by arrow).

u. Cast approximately × 15. Same specimen as as upper right in figure *f*. Illustrated by Jones, Kirkby, and Brady (1874, pl. 5, fig. 6*d*, area of 6*d* shown by arrow).

pattern. My colleague and frequent collaborator, Dr. L. S. Kornicker, Smithsonian Institution, informed me that the adductor attachment muscle scar is variable within genera in the cypridinids. The differences between the scars in *Eocypridina* as illustrated by Kesling and Ploch (1960, fig. 1, pls. 2, 3) and those of *Radiicypridina* illustrated by Bless (1973, text fig. 1) are not sufficient to discriminate between the two genera.

Although Kesling and Ploch (1960) did not categorically state that they transferred previously described species into *Eocypridina*, they implied that the species discussed in the following statement were considered by them to be congeneric with the type-species of *Eocypridina* (p. 287):

Eocypridina campbelli, sp. nov., differs from most previously described species of Paleozoic cypridinids in having a hook-like rostrum. Other species with similar rostra are *Cypridina fallax* Kegel (1926, p. 7, pl. 1, fig. 3), *C. grossartiana* Jones and Kirkby, (1867, p. 218), *C. radiata* Jones, Kirkby, and Brady (1874, p. 14, pl. 5, figs. 6*a–f*), *C. subovata* Ulrich and Bassler (1906, p. 162, pl. II, figs. 23–26), and *C. tonkinensis* Patte (1926, p. 218, pl. 8, figs. 28–30; pl. 9, fig. 1).

Because most of the species that have been referred to *Eocypridina* are based on poorly preserved specimens, it is not warranted to redescribe and properly diagnose them. Until such time as better preserved topotypic specimens are found, many should be considered as nomina dubia. Description in this paper is confined to the type-series of *Eocypridina radiata* (Jones, Kirkby, and Brady, 1874), and the species from the Hance Formation, Kentucky.

Stratigraphic range.—Devonian-Lower Triassic.

Eocypridinia radiata (Jones, Kirkby, and Brady, 1874)

Figures 2*e, f, s–u*

Cypridina radiata Jones, Kirkby, and Brady, 1874, Palaeontographical Soc., Mon. p. 14, pl. 5, figs. 6*a–f*.

not *Cypridina radiata* Jones, Kirkby, and Brady. Scott and Summerson, 1943, p. 673, pl. 2, fig. 2=*Eocypridina aciculata* (Scott and Summerson, 1943).

not *Radiicypridina radiata* (Jones and Kirkby [*sic*]). Bless, 1973, p. 250, text fig. 1=*Eocypridina aciculata* (Scott and Summerson, 1943).

Diagnosis.—Subovate, incisure somewhat below greatest height.

Discussion.—I have examined the type-series of this species which I am illustrating in figure 2*e*, *f*, *s–u*. The original figure 2*s* is here designated as the lectotype because it is the best preserved specimen. Figure 2*t* was originally illustrated by Jones, Kirkby, and Brady (1874) as figures 6*e*, *f*, and the area of figure 6*e* is shown by an arrow on the specimen illustrated as figure 2*t*. The arrow in figure 2*u* shows the area originally illustrated as figure 6*d*. The only available criterion discriminating this species is the lateral outline and the position of the incisure in relation to the greatest height as shown in figures 2*s*, *t*. All the specimens with radiate structures subsequently identified in Europe as *E. radiata* should be reevaluated.

Scott and Summerson (1943, p. 674) based their identification of this species on three internal molds collected from the Hance Formation of Kentucky. Bless (1973) also studied specimens from Kentucky. Because the specimens from Kentucky are not conspecific with the type-series, I am referring them to *Eocypridina aciculata* (Scott and Summerson, 1943).

Stratigraphic range.—Known only from the "Upper Coal-measures" Airdrie Blackbank Ironstone, Glasgow district, Scotland.

***Eocypridina aciculata* (Scott and Summerson, 1943)**

Figures 1*b*, *c*, *g*, *h*; figures 2*c*, *d*, *g–r*.

Cypridina aciculata Scott and Summerson, 1943, Am. Jour. Sci., v. 241, p. 674, pl. 2, figs. 1, 3.

Cypridina radiata Jones, Kirkby, and Brady. Scott and Summerson, 1943, Am. Jour. Sci., v. 241, p. 673, pl. 2, fig. 2.

Radiicypridina radata (Jones and Kirkby). Bless, 1973, Rev. Española de Micropaleontología, v. 5, no. 2, p. 250, text fig. 1.

not *Cypridina radiata* Jones, Kirkby, and Brady, 1874, Palaeontographical Soc., Mon., p. 14, pl. 5, figs. 6*a–f*.

Diagnosis.—Subovate, large, greatest length to more than 7 mm, dorsal part of rostral incisure well above midheight.

Description.—The carapace is very large, to 7 mm in greatest length; the dorsal margin is strongly arched, the ventral margin is more gently arched; the posterior margin is convex and extends with uniform curvature into the dorsal and ventral margins; the anterior margin has a rostral incisure that starts well above midheight and is bordered by a rim similar to that in *Vargula* as shown in figure 1*g*; the anterior margin, including the rostrum, is convex and extends with uniform curvature into the dorsal and ventral margins. The dorsal and end outlines are probably evenly curved, not very wide.

Discussion.—Scott and Summerson (1943) included the radiate structures in their diagnosis of this species, a character considered by me to be of no diagnostic value. The ostracodes occur as casts and molds of brown, probably limonitic, clay in a mudstone; consequently, the lateral outlines of many of the specimens are geometric artifacts formed by the intersection of the plane of cleavage in the mudstone with the relatively shallowly curved valves. I have attempted to prepare with a needle the outlines of selected specimens, but because the specimens are as soft, if not softer than the matrix, it was impossible to do so. The cast and mold of the specimen illustrated in figures 2*o* and *p* show where the cleavage plane broke through the specimen; the dorsoanterior part of the shell of figure 2*p* clearly continues into the matrix of figure 2*o*. Figures 2*g* and *h* illustrate the counterparts of a specimen of which the cleavage plane cuts diagonally across the valve. Figures 2*c*, *d*, and *n* are of juveniles because the end margins are exposed. The remaining illustrations show either the radiate structures, or the variation in outline. Figure 2*l* illustrates one of the largest specimens in my collections, it is about 7 mm in greatest length as compared with the recorded length of 5.3 mm by Scott and Summerson (1943, p. 674). Bless (1973, p. 252, fig. 1) measured larger specimens.

Although I have been unable to examine the holotype of this species (letters to Scott, June 17, 1966; May 16, 1975), the illustration of the holotype (Scott and Summerson, 1943, fig. 2*a*) indicates that the rostral incisure is missing, and that the dorsal and posterior parts of the valve extend into the matrix. Precise measurement of the specimens would not yield any meaningful information because they are incomplete.

In addition to the illustrated specimens, I have 11 specimens from the type-locality, USGS loc. 12902–PC and 25 specimens from USGS locs. 126889–PC, 12903–PC, and 12904–PC. Although in the explanations to the figures, I refer to the fossils as either casts or molds, most of the fossils are not casts or molds. The "casts" are in fact the impression of the reorganized and replaced middle calcareous layer that is analogous to the surface shown in figure 1*f* by the three radiating arrows, whereas the molds represent the counterpart of the impression, analogous to the inside of the surface shown on the left side of figure 1*f* by arrow b.

Stratigraphic range.—Known only from the Hance Formation (Early and Middle Pennsylvanian) of Kentucky.

REFERENCES CITED

Bless, M. J. M., 1973, Radiicypridina, a new cypridinid ostracode genus from the Upper Carboniferous: Rev. Española Micropaleontología, v. 5, no. 2, 247–252, 1 text fig.

Digby, P. S. B., 1967a, Calcification and its mechanism in the shore-crab *Carcinus maenas* (L.): Linnean Soc., London Proc., v. 178, pt. 2, p. 129–146, 2 pls.

——— 1967b, Lime deposition and the template theory in calcification of crustacean cuticle: Anatomical Soc. Great Britain and Ireland Proc., v. 101, pt. 3, p. 611–612.

——— 1968, Mobility and crystalline form of the lime in the cuticle of the shore crab, *Carcinus maenas*: Zool. Soc. London, Jour, Zoology, v. 154, pt. 3, p. 273–286, 4 pls.

Hartmann, Gerd, and Puri, H. S., 1974, Summary of neontological and paleontological classification of Ostracoda: Mitt. Hamburg. Zool. Mus. Inst., v. 70, p. 7–73.

Jones, T. R., Kirkby, J W, and Brady, G. S., 1874–84, A monograph of the British fossil bivalved Entomostraca from the Carboniferous formations. Part 1. The Cypridinidae and their allies: London, Palaeontographical Soc., 92 p. 7 pls.

Kesling, R. V., and Ploch, R. A., 1960, New Upper Devonian cypridinacean ostracod from southern Indiana: Michigan Univ. Mus. Paleontology Contr., v. 15, no. 12, p. 281–292, 3 pls.

Kornicker, L. S., and Sohn, I. G., 1976, Phylogeny, ontogeny, and morphology of living and fossil Thaumatocypridacea (Myodocopa, Ostracoda): Smithsonian Contr. Zoology, no. 219 (In press.)

Moore, R. C., ed., 1961, Treatise on invertebrate paleontology; Pt. Q, Arthropoda 3, Ostracoda: New York and Lawrence, Kans., Geol. Soc. America and Univ. Kansas Press, 442 p., 344 figs.

Oppenlander, G. C., 1968, Structure and properties of crystalline polymers: Science, v. 159, no. 3821, p. 1311–1319, 11 figs.

Pruvost, Pierre, 1911, Note sur les Entomostracés bivalves du terrain houiller du Nord de la France: Soc. Géol. Nord Annales, v. 40, p. 60–80, 2 pls.

——— 1919, La faune continentale du terrain houiller du Nord de la France, *in* Introduction a l'étude du terrain houiller du Nord et du Pas-de-Calais: France Service Carte Géol. Mém., 584 p., 29 pls.

Ruedemann, Rudolf, 1926, The Utica and Lorraine formations of New York; pt. 2, Systematic paleontology; No. 2, Mollusks, crustaceans and euripterids: New York State Mus. Bull. 272, p. 137–145, pl. 23.

Scott, H. W., and Summerson, C. H., 1943, Non-marine Ostracoda from the Lower Pennsylvanian in the southern Appalachians, and their bearing on intercontinental correlation: Am. Jour. Sci. v. 241, no. 11, p. 654–675, 2 pls.

Sohn, I. G., 1968, New light on some myodocopid ostracodes, *in* Geological Survey research 1968: U.S. Geol. Survey Prof. Paper 600–A, p. A117.

Sohn, I. G., and Kornicker, L. S., 1969, Significance of calcareous nodules in myodocopid ostracod carapaces, *in* Neale, J. W., ed., The taxonomy, morphology, and ecology of Recent Ostracoda: Edinburgh, Scotland, Oliver and Boyd, p. 99–108, 3 pls.

Ulrich, E. O., 1879, Descriptions of new genera and species of fossils from the Lower Silurian about Cincinnati: Cincinnati Soc. Nat. History, Jour., v. 2, p. 8–12, pl. 7.

Jour. Research U.S. Geol. Survey
Vol. 5, No. 1, Jan.–Feb. 1977, p. 135–141

MUSCLE SCARS OF LATE PALEOZOIC FRESHWATER OSTRACODES FROM WEST VIRGINIA

By I. G. SOHN, Washington, D.C.

Abstract.—Different adductor muscle attachment scar patterns of the three ostracode genera *Darwinula* Brady and Robertson, 1885, *Gutschickia* Scott, 1944, and *Whipplella* Holland, 1934, from Pennsylvanian and Permian rocks of West Virginia are illustrated for the first time. *Gutschickia* and *Whipplella* have been considered as junior synonyms of *Carbonita* Strand, 1928, and the oldest darwinulid scar pattern previously known was from the Upper Triassic of Germany. The different patterns document the presence of *Darwinula* in the Pennsylvanian of the United States and indicate that *Whipplella* and *Gutschickia* are valid genera. The use of ostracodes in discriminating between Carboniferous and Permian continental sedimentary rocks should be based on restudy of the species in these genera.

This is a progress report on my study of the nonmarine Pennsylvanian and Permian ostracodes from the Eastern United States. The first papers (Sohn, 1972; 1975b) evaluated the published record and concluded that the nonmarine ostracodes have been inadequately studied. Specimens are either on pieces of shale as crushed specimens, partly exfoliated valves, and casts (steinkerns), or, when disaggregated from shales and crushed from limestone, they occur as rare closed carapaces, but mostly as steinkerns. The detailed shell structure was not known for any of the described species. All the described Pennsylvanian and Permian freshwater ostracode species in the United States have been referred to the following genera: *Candona* Baird, 1845; *Carbonita* Strand, 1928; *Cypridopsis* Brady, 1867; *Darwinula* Brady and Robertson, 1885; *Gutschickia* Scott, 1944; *Hilboldtina* Scott and Summerson, 1943; *Pruvostina* Scott and Summerson, 1943; and *Whipplella* Holland, 1934.

The genera *Candona*, *Cypridopsis*, and *Darwinula* are based on living type-species, whereas the other five genera have Paleozoic type-species. Table 1 is a revision of a similar table (Sohn, 1975b, p. 266) showing the diagnostic features of each of the freshwater genera to which Pennsylvanian and Permian species in the United States have been assigned. The table is based on published information except for *Candona*, *Cypridopsis*, *Darwinula*, *Gutschickia*, and *Whipplella*. I have examined living material of species of *Candona*, *Cypridopsis*, and *Darwinula*, and the types of the type species of *Gutschickia* and *Whipplella*. Four genera: *Gutschickia*, *Hilboldtina*, *Pruvostina*, and *Whipplella* were considered to be synonyms of *Carbonita* by Anderson (1970, p. 74), who assigned 17 species and the single variety of the 26 species described in the United States as junior synonyms of 6 species in *Carbonita*.

Bless and Pollard (1972, p. 9) accepted Anderson's (1970, p. 74) synonymy of the American genera, stating that

> Our interpretation of this genus is wider than many previous authors whose genera we have included in the above synonymy. We regard such genera as based on characters not worthy of generic rank as we believe they are variable even within species e.g. *Whipplella*, marginal overlap, *Hilboldtina*, surface ornament, *Pruvostina*, *Gutschickia*, size and surface ornament.

Sohn (1975b, p. 265–280, figs. 1–6) showed that the stratigraphic ranges of the American freshwater ostra-

TABLE 1.—*Criteria for discriminating between late Paleozoic freshwater ostracode genera, on the basis of the type-species*

Genus	Hinge	Overlap	Muscle scar
Candona	Not impressed	Left/right	Cyprid (fig. 1*a*).
Carbonita	do	Right/left	Modified healdiid (fig. 1*b*).
Cypridopsis	do	Left/right	Cyprid (fig. 1*c*).
Darwinula	do	Right/left	Darwinulid (fig. 1*d*; fig. 3*o*, *q*, *u*, *v*, *x*).
Gutschickia	Impressed	Right/left ventral; left raised above hinge	Modified healdiid (fig. 1*e*; fig. 2*c*).
Hilboldtina	Not impressed	Left/right dorsal; right/left ventral	Unknown.
Pruvostina	Impressed	Right/left or left/right	Do.
Whipplella	Slightly impressed	Right/left	Modified suchonellid (fig. 1*f*; fig. 2*b*, *h*, *k*).

FIGURE 1.—Adductor muscle attachment scars of the freshwater genera identified in the upper Paleozoic.

a. Candona candida (O. F. Müller, 1776), Holocene, from van Morkhoven (1962, fig. 44).

b. Carbonita Strand, 1928, Late Carboniferous, from Anderson (1970, fig. 1).

c. Cypridopsis vidua (O. F. Müller, 1776), Holocene, from Kesling (1951, fig. 1).

d. Darwinula stevensoni (Brady and Robertson, 1870), Holocene, showing 12 individual spots, from Sohn (1976).

e. Gutschickia sp., Pennsylvanian, drawn from figure 2*c*.

f. Whipplella sp., Permian, drawn from figure 2*k*.

g. Suchonella Spizharsky, 1937, Permian, from Mischina (1972, fig. 4).

code species are not the same as the range of the European species to which Anderson assigned them as synonyms. Their stratigraphic ranges are so great that they are of no use in discriminating between Pennsylvanian and Permian rocks in the United States. Some of the American species may not be synonymous with those in Europe.

With the exception of the adductor muscle attachment scar of the European genera *Carbonita* Strand, 1928, illustrated by Anderson (1970, fig. 1), of *Suchonella* Spizharsky, 1937, illustrated by Mischina (1972, fig. 4), and of *Vymella* Kalis and Mischina, 1975 (in Mischina and Kalis, 1975, fig. 1b; pl. 9, fig. 4*b*), the muscle-scar patterns of the freshwater genera restricted to the Paleozoic have not been described. Without this information the American species could not be assigned with any degree of certainty to their proper genera.

I have examined Holland's (1934) types, and Cooper's (1946) types and duplicates. Mischina (1972, p. 47) determined the scar pattern of *Suchonella* by tracing the scars on more than 150 photographic enlargements; I used steinkerns for scanning electron micrography. Because this study is based on steinkerns, the specific identity of the specimens used has not yet been determined, although the generic designations are fairly certain.

Genus *WHIPPLELLA* Holland, 1934

Figure 2*a*, *b*, *h–k*

Type-species (*original designation*).—*Whipplella cuneiformis* Holland, 1934, p. 344, pl. 25, figures 5*a–c*. Nineveh Limestone Member of Greene Formation (Permian), Limestone Hill, West Virginia.

Anderson (1970, p. 85) placed this species in synonymy with *Carbonita inflata* (Jones and Kirkby, 1879), a species having the recorded stratigraphic range in Europe of Westphalian B to Westphalian C. Bless (1973, p. 11) tentatively extended the range of *C. inflata* to include the base of the Namurian (Namurian A) through Stephanian B. Because Holland (1934, pl. 25, figures 18–20) illustrated *W. cuneiformis* by drawings, Scott (1944, pl. 24, figs. 18–20) reillustrated the holotype with photographs of the right, dorsal, and ventral views.

Holland (1934) described and illustrated by drawings seven Permian species of *Whipplella*. To date, the following species have been recorded in the genus:

Whipplella carbonaria Scott, 1944, Pennsylvanian, Illinois.
cenisa Kremp and Grebe, 1955, Westphalian, Germany.
cuneiformis Holland, 1934, Permian, West Virginia.
deltoidea Holland, 1934. See *Gutschickia*.
depressa Holland, 1934, Permian, West Virginia.
magnitata Holland, 1934, Permian, Pennsylvania.
ninevehensis Holland, 1934. See *Gutschickia*.
ovata Holland, 1934, Permian, Pennsylvania.
parvula Holland, 1934, Permian, Pennsylvania and West Virginia.
rhenana (Kummerow, 1949). Kremp and Grebe, 1955, Westphalian, Germany.

Scott (1944) transferred *Whipplella ovata* Holland, 1934, and *W. parvula* Holland, 1934, to *Cypridopsis*, and *W. magnitata* Holland, 1934, to *Candona*. Vangerow (1957) identified and illustrated *W. cenisa* (p.

464, pl. 20, figs. 15, 17–19) and *W. rhenana* (p. 463, pl. 20, figs. 14, 16, 20) from the Upper Carboniferous of Aachen, Germany. Bless (1967, p. 162) identified *W. cenisa* and *W. rhenana* from the Westphalian of the Netherlands, and later (Bless and Pollard, 1972, p. 17) considered both species as synonyms of *Carbonita humilis* (Jones and Kirkby, 1879). This leaves a current record of only the Permian *W. cuneiformis*, *W. depressa*, and *W. ovata* in America.

Two collections, one from the so-called "Upper Rockport Limestone Member" of the Greene Formation, more than 200 feet stratigraphically above the Nineveh Limestone Member (USGS colln. 12901–PC), the other from the younger so-called "Windy Gap Limestone Member" (USGS Colln. 12905–PC), contain steinkerns that show the adductor muscle attachment scar (fig. 2*a*, *b*, *h–k*). The American genus that most closely resembles the steinkerns is *Whipplella*. The scar pattern differs from that of Carbonita; it resembles more that of *Suchonella* Spizharsky, 1937, as illustrated by Mischina (1972, fig. 4). The steinkerns differ from *Suchonella* in lacking evidence for a posterior septum and in having 11 spots instead of 9 spots that make up the adductor muscle attachment scar pattern in the Russian genus.

Genus *DARWINULA* Brady and Robertson, 1885

Figure 3*o–x*

Type-species (*monotypy*). — *Polycheles stevensoni* Brady and Robertson, 1870. Living, worldwide.

Sohn (1974; 1976) showed that the adductor muscle attachment scar in the type-species on specimens obtained from a culture varies in number, shape, and disposition of individual scars. This variation is independent of ontogenetic growth. The number of individual scars may be 9 to 12 fig. 1*d*; fig. 3*o*, *q*) and may differ between the valves of the same individual (fig. 3*u*, *v*). More than 250 named species, which range in age from the Pennsylvanian to the present, have been either originally assigned or later transferred to *Darwinula*.

Previously, the oldest darwinulid adductor muscle attachment scar pattern was illustrated by Beutler and Gründel (1963, pl. 6a, fig. 3) on the Late Triassic (Keuper) *Darwinula liassica* (Brodie, 1843) (=*Darwinula* sp. Sohn, 1968). Scott (1944, p. 146, pl. 24, figs. 6–8) described *D. hollandi* from the Permian Nineveh Limestone Member of the Greene Formation, Pennsylvania, as the first Paleozoic species in the United States. This species was considered by Cooper (1946, p. 78) as an immature molt of *Darwinula pungens* (Jones and Kirkby, 1879) that he identified and illustrated from the Pennsylvanian of Knox County, Ill. Anderson (1970, p. 98) assigned *D. pungens* to *Carbonita* and removed Cooper's specimens from the synonymy because the Pennsylvanian specimen has a typically darwinulid overlap. Steinkerns from the Monongahela Formation (Upper Pennsylvanian) of West Virginia (USGS colln. 12899–PC) show the typical darwinulid adductor muscle attachment scar pattern, and one of them has eight individual spots on the left valve and nine on the right (fig. 3*u*, *v*). These steinkerns confirm the presence of *Darwinula* as far back as the Pennsylvanian.

Genus *GUTSCHICKIA* Scott, 1944

Figures 2*c–g*; 3*a–n*

Type-species (original designation): *Whipplella ninevehensis* Holland, 1934. Permian, Pennsylvania.

Scott (1944, pl. 23, figs. 5–8) reillustrated the holotype of *G. ninevehensis* because the original illustrations were by drawings. To date, the following species have been either described in or transferred to *Gutschickia*:

Gutschickia bretonensis Copeland, 1957, Carboniferous, Canada.
convexa Tasch, 1963, Permian, Kansas.
deltoidea (Holland, 1934), Permian, Pennsylvania.
fameniana Rozhdestvenskaja, 1972, Late Devonian, Early Carboniferous(?), U.S.S.R.
levis Cooper, 1946, Pennsylvanian, Illinois.
ninevehensis (Holland, 1934), Permian, Pennsylvania.
ovata Cooper, 1946, Pennsylvanian, Illinois.
subangulata (Jones and Kirkby, 1879). Cooper, 1946. Pennsylvanian, Illinois; Permian, West Virginia.
triangulata Rozhdestvenskaja, 1972, Late Devonian, Early Carboniferous, U.S.S.R.
wellingtonensis Tasch, 1963, Permian, Kansas.

An internal cast of a left valve on shale from the Monongahela Formation (Upper Pennsylvanian) of West Virginia (USGS colln. 12899–PC) has a muscle scar (fig. 2*c*) that is similar in outline and in the configuration of individual spots to *Carbonita* Strand, 1928. Although the valve is not as convex in dorsal outline (fig. 2*d*) as the types of *Gutschickia* (fig. 3*a–e*), associated better preserved specimens indicate that it belongs to this genus. It is as yet an undescribed species of *Gutschickia* (fig. 2*f*, *g*; fig. 3*h–n*).

The documentation of three distinct adductor muscle attachment scars in freshwater Pennsylvanian and Permian ostracodes in the United States indicates that the assignment of species to Paleozoic freshwater genera was solely on the basis of shape and size. The identification or transfer of American species to European genera and species may be unwarranted.

Rozhdestvenskaja (1972, p. 113, 114, pl. 40, figs. 1–3) illustrated three Late Devonian (Famennian) ostracodes that have an overlap similar to that of *Carbonita* and also to that of *Rishona* Sohn, 1961, a marine genus.

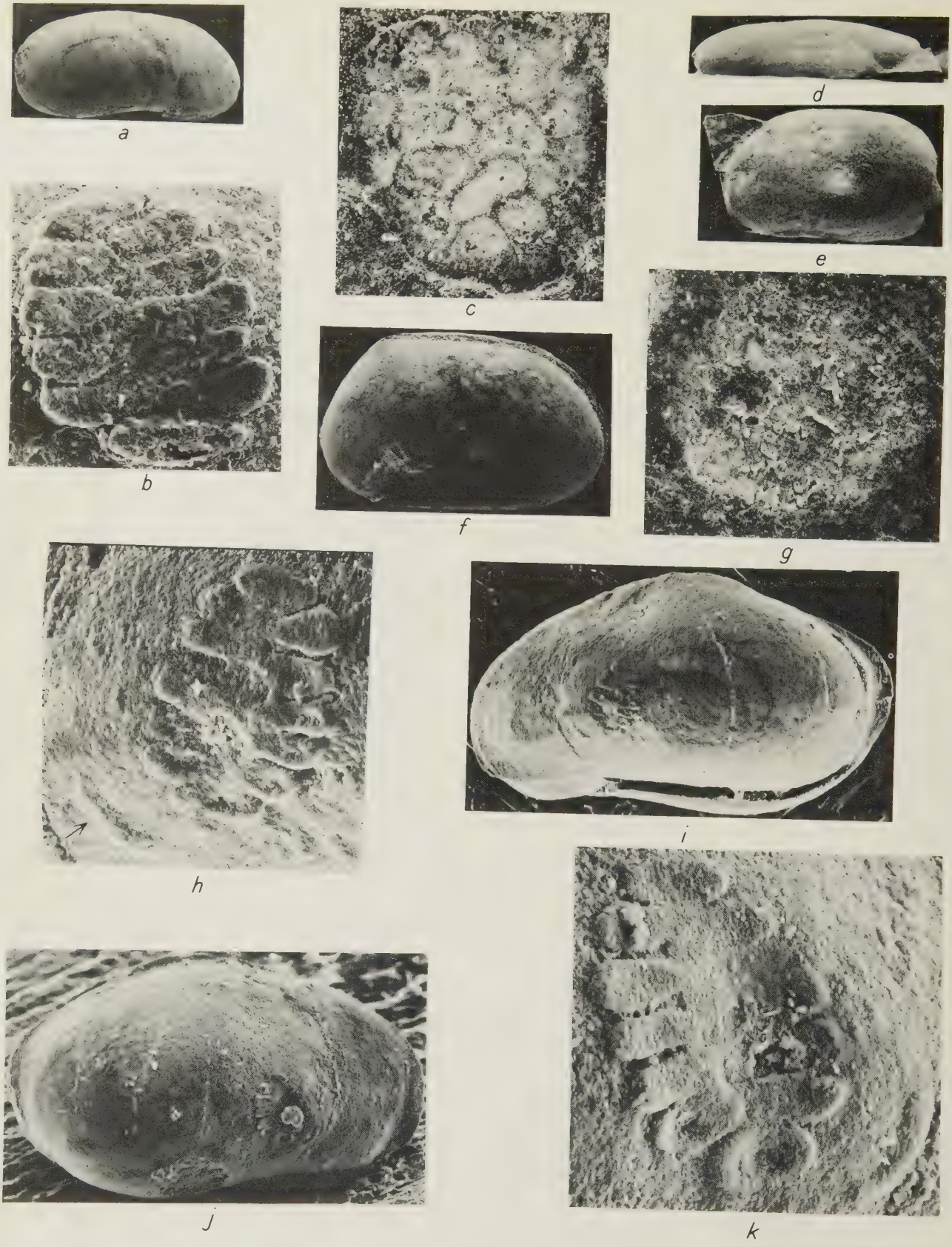

FIGURE 2.—*Whipplella* and *Gutschickia*.

Associated ostracodes belong to *Acratia* Delo, 1930, *Bairdia* McCoy, 1844, *Bairdiocypris* Kegel, 1932, *Cavellina* Coryell, 1928, and more than a dozen typically marine genera. *Gutschickia* has the left valve raised above the hinge but does not overlap the right; consequently, the two Russian species probably do not belong to the Pennsylvanian and Permian genus *Gutschickia.*

Interpretation of muscle-scar patterns on fossil ostracodes, especially on steinkerns, is subject to error because of possible artifacts. I am confident that my interpretation is correct for the following reasons: The *Darwinula* pattern is present on more than one specimen (fig. 3*u*, *v*, *x*), and it resembles that of living *Darwinula* here illustrated for comparison (fig. 3*o–q*); the *Gutschickia* pattern is also present on other specimens, albeit on a second specimen the pattern is not as clear as that on the first (fig. 3*g*); and the *Whipplella* scar is so well preserved that there is no doubt as to its authenticity. The fact that similar general patterns were illustrated for *Suchonella* Spizharsky, 1937, and *Vymella* Kalis and Mischina, 1975, adds credence to my interpretation.

FIGURE 2.—Continued

a, b. Whipplella sp.

a. Right lateral view of steinkern approximately × 50. Note accessory scar anterior to adductor muscle attachment scar not shown in figure *b.*

b. Adductor muscle attachment scar approximately × 600. Figured specimen USNM 168121, Permian, so-called "Upper Rockport Limestone Member" of Greene Formation, Wetzel County, W. Va., USGS colln. 12901–PC.

c–e. Gutschickia sp.

c. Adductor muscle attachment scar approximately × 425.

d, e. Dorsal and left views of internal cast on shale approximately × 34. Figured specimen USNM 168122, Pennsylvania Monongahela Formation, Monongalia County, W. Va., USGS colln. 12899–PC.

f, g. Gutschickia sp.

f. Right view of corroded carapace approximately × 65.

g. Poorly preserved adductor muscle attachment scar approximately × 445. Figured specimen USNM 168123, same collection as above.

h–k. Whipplella sp.

h. Adductor and accessory (shown by arrow) attachment muscle scars of left valve approximately × 400.

i, j. Left and right views of abraded carapace approximately × 100.

k. Adductor and accessory (shown by arrow) attachment muscles scars of right valve approximately × 500. Figured specimen USNM 168002, Permian, so-called "Windy Gap Limestone Member" of Greene Formaton, Wetzel County, W. Va., USGS colln. 12905–PC.

The adductor muscle attachment scar pattern has been one of the primary criteria for family classification in both living and fossil ostracodes (Schweyer, 1939, p. 93; von Morkhoven, 1962, p. 47). It is, therefore, significant that there are at least three distinct adductor muscle-scar patterns in the freshwater Paleozoic ostracodes. They prove that not only three distinct genera but also three different families were present.

Species of these genera occur both in Carboniferous and Permian sediments of nonmarine origin; consequently, the use of these ostracodes in discrimination between the two systems must be based on species rather than on genera. For example, Cooper (1946, p. 68, pl. 8, figs. 36–39) illustrated a specimen from the Virgilian (Upper Pennsylvanian) of Illinois that he identified as *Gutschickia ninevehensis* (Holland, 1934). Holland's species is from the Lower Permian and was designated by Scott (1944, p. 146) as the type-species of *Gutschickia;* consequently, according to the published record, the species crosses the Pennsylvanian-Permian boundary. The specimen from the Pennsylvanian (fig. 3*f*, *g*), however, differs in lateral outline from the holotype (fig. 3*c–e*), and the two specimens are probably not conspecific. Research in progress on the Pennsylvanian and Permian nonmarine ostracodes of the Appalachian region may aid in the boundary problem.

Acknowledgments.—I thank Dr. M. J. Copeland, Geological Survey of Canada, for the negatives of Cooper's (1946) types that he had rephotographed; Dr. L. S. Kent, Illinois State Geological Survey, for lending Cooper's specimens; Dr. M. R. Dawson, Carnegie Museum, for lending Holland's (1934) types; and Dr. Ruth Seggev-Lerner, The Israel Institute of Petroleum, Israel, for preserved specimens from Lake Tiberias. R. R. Larson, U.S. Geological Survey, and W. R. Brown and M. J. Mann, Smithsonian Institution, made the scanning electron micrographs.

I thank Dr. S. V. Meyen, Secretary General, 8th International Congress of Carboniferous Stratigraphy and Geology, Moscow, September 1975, for his letter (June 11, 1975) informing me that an expanded abstract of this paper is included in the program for the Congress (Sohn, 1975a).

REFERENCES CITED

Anderson, F. W., 1970, Carboniferous Ostracoda—the genus *Carbonita* Strand: Great Britain Geol. Survey Bull. 32, p. 69–121, pls. 12–18, 1 text fig.

Beutler, G., and Gründel, J., 1963, Die Ostracoden des Unteren Keupers im Bereich des Thüringer Beckens: Freiberger Forschungshefte, no. C–164, p. 33–92, 9 pls., 4 text figs.

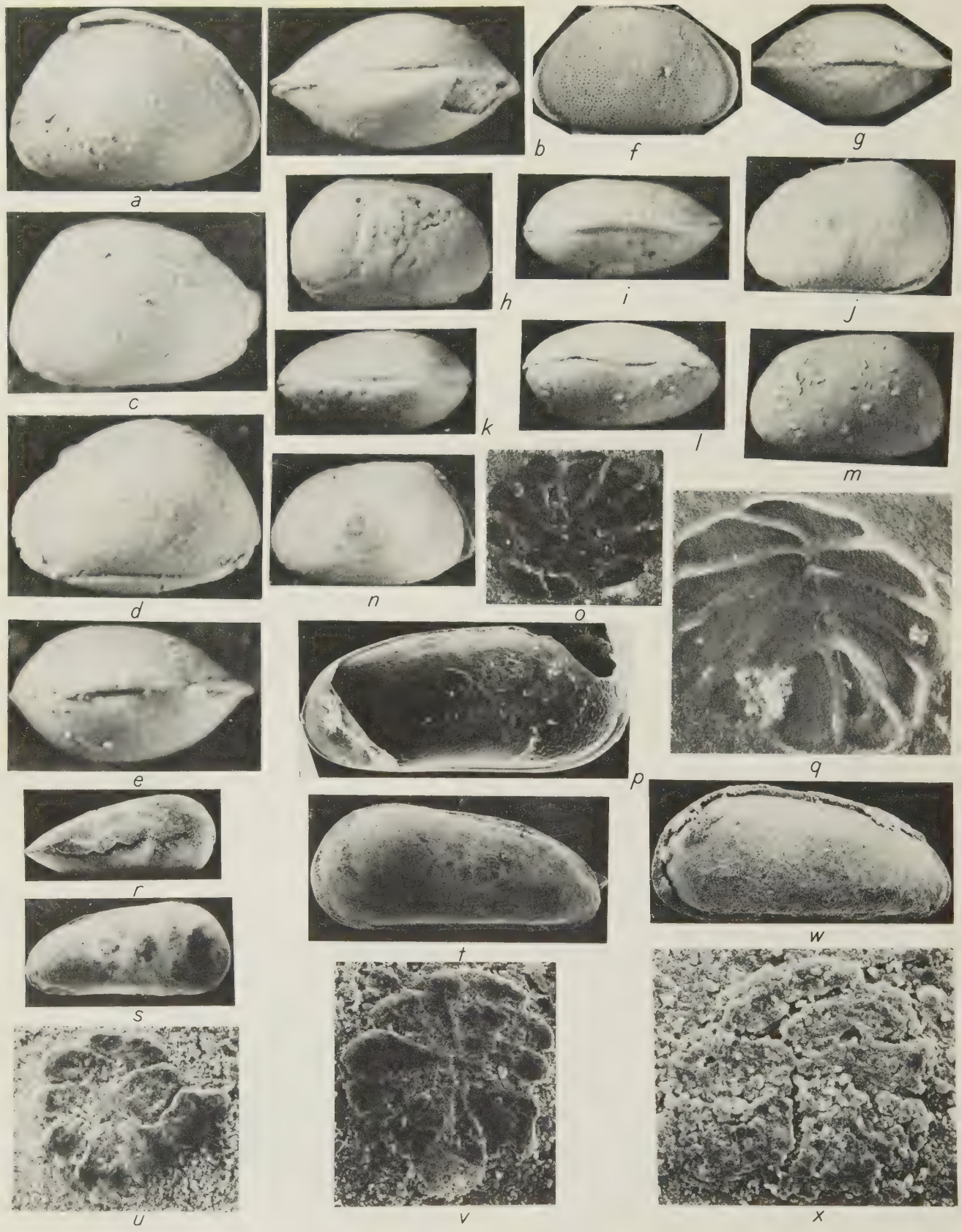

FIGURE 3.—*Gutschickia* and *Darwinula*.

Bless, M. J. M., 1967, Ostracoden aus dem Limburgkarbon (Niederlande): Freiberger Forschungshefte, no. C–213, p. 159–164, 2 pls.

——— 1973, Derzeitlinger Stand der Kenntnisse über die Ostracoden-Stratigraphie in Karbon Westeuropas: Freiberger Forschungshefte, no. C–282, p. 5–21, 8 pls.

Bless, M. J. M., and Pollard, J. E., 1972, Paleoecology and Ostracode faunas of Westphalian Ostracode Bands from Limburg, The Netherlands, and Lancashire, Great Britain: [Netherlands] Rijks. Geol. Dienst Meded., new ser., v. 24, 32 p., 5 pls. (also pub. in 1973 as: [Netherlands] Rijks. Geol. Dienst Meded., new ser., no. 24, p. 21–53).

Cooper, C. L., 1946, Pennsylvanian ostracodes of Illinois: Illinois State Geol. Survey Bull. 70, 177 p., 21 pls.

Holland, W. C., 1934, The ostracods of the Nineveh limestones of Pennsylvania and West Virginia: Carnegie Mus. Annals, v. 22, nos. 2–4, p. 343–350, pl. 25.

Kesling, R. V., 1951, The morphology of ostracod molt stages: Illinois Biol. Mon., v. 21, nos. 1–3, 324 p., 96 pls., 36 text figs., 5 charts.

Mischina, E. M., 1972, O sistematike iskopaemykh darwinulid (ostrakody): Paleont. Sbornik, vyp. 1, no. 9, p. 44–51, 6 text figs.

Mischina, E. M., and Kalis, A. E., 1975, A new ostracod genus of northeastern part of the Russian platform: Akad. Nauk SSSR, Paleont. Zhur., 1975, no. 1, p. 76–81, pl. 9, 1 text fig.

Morkhoven, F. P. C. M. van, 1962, Post-Paleozoic Ostracoda, v. 1: Amsterdam, Elsevier Pub. Co., 204 p., 79 text figs.

Rozhdestvenskaja, A. A., 1972, Ostrakody Verkhnego Devona Bashkirii: Akad. Nauk SSSR, Bashkirskii Filial, Inst. Geol. Moscow, Izdat. "Nauka", 193 p., 40 pls.

Schweyer, A. V., 1939, The results of the study of Mesozoic and Cainozoic Ostracoda of the U.S.S.R.: Petroleum Geol.-Prospecting Inst., Trans., ser. A, no. 116, p. 93–103 [in Russian].

Scott, H. W., 1944, Permian and Pennsylvanian fresh-water ostracodes: Jour. Paleontology, v. 18, no. 2, p. 141–147, pls. 23, 24.

Sohn, I. G., 1972, Dunkard Ostracoda—an evaluation [abs.], *in* First I. C. White Memorial Symposium, The age of the Dunkard, Abstracts and Reference Papers: Morgantown, West Virginia Geol. Survey, p. 30–31.

——— 1974, Antiquity of the adductor muscle attachment scar in *Darwinula* Brady and Robertson, 1885 [abs.]: International Symposium on evolution of post-Paleozoic Ostracoda, Hamburg, 18–25 August [p. 30].

——— 1975a, Adductor muscle attachment scars of the ostracodes *Darwinula* and *Gutschickia* from Upper Pennsylvanian rocks and of *Whipplella* from Permian rocks in West Virginia [abs.]: Internat. Cong. Carboniferous Stratigraphy and Geology, 8th, Moscow, Sept. 1975, Abs. of Papers, p. 268–269.

——— 1975b, Dunkard Ostracoda—an evaluation, *in* Barlow, J. A., ed., Proceedings of the First I. C. White Memorial Symposium, The age of the Dunkard: Morgantown, West Virginia Geol. Survey, p. 265–280.

——— 1976, Antiquity of the adductor muscle attachment scar in *Darwinula* Brady and Robertson, 1885, *in* Hartmann, G., ed., International symposium on evolution of post-Paleozoic Ostracoda: Mitt. Hamburg. Zool. Mus. Inst. [In press.]

Vangerow, E. F., 1958, Mikropaläontologische Untersuchungen in den Kohlscheider Schichten im Wurmrevier Bei Aachen: Geol. Jahrb. 1957, v. 73, p. 457–497, pls. 20–23.

FIGURE 3.—Continued

a–e. Gutschickia ninevehensis (Holland, 1934).

a, b. Right and dorsal views of *Whipplella ninevehensis* approximately × 30. Paratype, Carnegie Museum 6464. Permian, Nineveh Limestone Member of Greene Formation, Pennsylvania.

c–e. Right, left and dorsal views of *Whipplella ninevehensis* approximately × 30. Holotype, Carnegie Museum 6483. Permian, same collection as above.

f, g. Gutschickia sp.

f, g. Right and dorsal views of *G. ninevehensis* (Holland) identified and illustrated by Cooper, 1946, approximately × 30. Compare dorsal overlap on figure *g* with figures *b* and *c*. Illinois State Geol. Survey 44P137. Pennsylvanian, shales in Cohn cyclothem, Clark County, Ill.

h–n. Gutschickia sp.

h–j. Right dorsal and left views of carapace approximately × 30. Fgured specimen USNM 168124. Pennsylvanian, Monogahela Formation, Monongalia County, W. Va., USGS colln. 12899–PC.

k–m. Dorsal, ventral and right views of well-preserved carapace approximately × 30. Figured specimen USNM 168125, same collection as above.

n. Right view of corroded carapace showing adductor muscle attachment scar approximately × 30. Compare with figures 2*c* and *e*. Figured specimen USNM 168126, same collection as above.

o–q. Darwinula stevensoni (Brady and Robertson, 1870).

o. Adductor muscle attachment scar inside of left valve showing nine individual spots approximately × 330. Figured specimen USNM (Crustacea) 151956, collected alive in Lake Tiberias, Israel, by Dr. Ruth Seggev, Bar-Ilan University, Israel.

p, q. Inside of right valve approximately × 100, and detail of adductor muscle attachment scar showing 10 individual spots approximately × 800. Figured specimen lost, same collection as above.

r–x. Darwinula sp.

r, s. Ventral and left views of corroded carapace approximately × 60.

t. Right view of same carapace approximately × 80.

u. Adductor muscle attachment scar with eight individual spots, left valve, approximately × 600.

v. Adductor muscle attachment scar with nine individual spots, right valve, approximately × 600. Figured specimen USNM 16827, Pennsylvanian, Monongahela Formation, Monongalia County, W. Va., USGS colln. 12899–PC.

w, x. Right side of steinkern approximately × 80, and detail of adductor muscle attachment scar showing seven individual spots approximately × 790. Figured specimen lost, same collection as above.

RECENT PUBLICATIONS OF THE U.S. GEOLOGICAL SURVEY

(The following books may be ordered from the Branch of Distribution, U.S. Geological Survey, 1200 South Eads Street, Arlington, VA 22202 (an authorized agent of the Superintendent of Documents, Government Printing Office). Prepayment is required. Remittances should be sent by check or money order payable to U.S. Geological Survey. Give series designation and number, such as Bulletin 1368–A, and the full title. Prices of Government publications are subject to change. Increases in costs make it necessary for the Superintendent of Documents to increase the selling prices of many publications offered. As it is not feasible for the Superintendent of Documents to correct the prices manually in all the previous announcements and publications stocked, the prices charged on your order may differ from the prices printed in the announcements and publications)

Professional Papers

P 655–L. Accuracy of evapotranspiration rates determined by the water-budget method, Gila River flood plain, southeastern Arizona, by R. L. Hanson and D. E. Dawdy. 1976. p. L1–L35. $1.05.

P 743–F. Microfossil correlation of California lower Tertiary sections: A comparison, by R. Z. Poore. 1976. p. F1–F8; plates in pocket. $1.75.

P 869. Noncystimorph colonial rugose corals of the Onesquethaw and lower Cazenovia Stages (Lower and Middle Devonian) in New York and adjacent areas, by W. A. Oliver, Jr. 1976. 156 p.; 108 plates. $4.30.

P 872. Geology of the Golden quadrangle, Colorado, by Richard Van Horn. 1976. 116 p. $3.65.

P 903. The Paleozoic and Mesozoic rocks; a discussion to accompany the geologic map of the United States, by P. B. King and H. M. Beikman. 1976. 76 p. $1.90.

P 909. Boundaries of the United States and the several States, by F. K. Van Zandt, 1975. 191 p. $5.20.

P 923. Stratigraphy of the north half of the western Sierra Nevada metamorphic belt, California, by L. D. Clark. 1976. 26 p., plate in pocket. 75¢.

P 929. ERTS–1, a new window on our planet, edited by R. S. Williams, Jr., and W. D. Carter. 362 p. $13.

P 936. Alteration and geochemistry of Tertiary volcanic rocks in parts of the Virginia City quadrangle, Nevada, by D. H. Whitebread. 1976. 43 p.; plate in pocket. $1.15.

P 954–C. Elemental composition of selected native plants and associated soils from major vegetation-type areas in Missouri, by J. A. Erdman, H. T. Shacklette, and J. R. Keith. 1976. p. C1–C87. $2.10.

P 955. Mineralogy and geology of the wagnerite occurrence on Santa Fe Mountain, Front Range, Colorado, by D. M. Sheridan, S. P. Marsh, M. E. Mrose, and R. B. Taylor. 1976. 23 p. 75¢.

P 959–G. Rutile in Precambrian sillimanite-quartz gneiss and related rocks, east-central Front Range, Colorado, by S. P. Marsh and D. M. Sheridan. 1976. p. G1–G17. 55¢.

P 962. The North Pacific Miocene record of *Mytilus* (*Plicatomytilus*), a new subgenus of Bivalvia, by R. C. Allison and W. O. Addicott. 1976. 22 p; 3 plates. 95¢

P 963. Displacement of the south flank of Kilauea Volcano: the result of forceful intrusion of magma into the rift zones, by D. A. Swanson, W. A. Duffield, and R. S. Fiske. 1976. 39 p. $1.15.

P 964. A land use and land cover classification system for use with remote sensor data, by J. R. Anderson, E. E. Hardy, J. T. Roach, and R. E. Witmer. 1976. 28 p. 75¢.

P 968. The paleontology of rostroconch mollusks and the early history of the Phylum Mollusca, by John Pojeta, Jr., and Bruce Runnegar. 1976. 88 p.; 54 plates. $3.40.

P 970. Mineral resources of the Illinois-Kentucky mining district, by D. M. Pinckney. 1976. 15 p. 45¢.

P 998. Floods of March-April 1973 in Southeastern United States, by G. W. Edelen, Jr., and J. F. Miller. 1976. 283 p. $4.50.

P 1002. The Guatemalan earthquake of February 4, 1976, A preliminary report, by A. F. Espinosa, editor. 1976. 90 p. $2.20.

Bulletins

B 1399. Geology of the Rockland and Arbon quadrangles, Power County, Idaho, by D. E. Trimble and W. J. Carr. 1976. 115 p.; plate in pocket. $1.70.

B 1402. Bedrock geology of the Conconully quadrangle, Okanogan County, Washington, by C. D. Rinehart and K. F. Fox, Jr. 1976. 58 p.; plate in pocket. $2.30.

B 1405–G. Upper Cambrian Orr Formation: Its subdivisions and correlatives in western Utah, by L. F. Hintze and A. R. Palmer. 1976. p. G1–G25. 55¢.

B 1406. Reconnaissance geology of the Upper St. John and Allagash River basins, Maine, by E. L. Boudette, N. L. Hatch, Jr., and D. S. Harwood. 1976. 37 p.; plates in pocket. 70¢

B 1407. Geology of the Precambrian W (Lower Precambrian) rocks in western Gogebic County, Michigan, by R. G. Schmidt. 1976. 40 p.; plate in pocket. 80¢.

B 1410. Structural dislocations in eastern Massachusetts, by R. O. Castle, H. R. Dixon, E. S. Grew, Andrew Griscom, and Isidore Zietz. 1976. 39 p.; plate in pocket. $1.35.

B 1415. Marine gold placers along the Gulf of Alaska margin, by Erk Reimnitz and George Plafker. 1976. 16 p.; plate in pocket. $1.45.

B 1428. Directory to U.S. Geological Survey program activities in coastal areas, 1974–76, edited by P. A. Marcus. 1976. 154 p. $1.75.

Water-Supply Papers

W 2102. Surface-water supply of the United States, 1966–70—Part 1, North Atlantic slope basins—Volume 2, Basins from New York to Delaware. 1976. 985 p. $7.

W 2103. Surface-water supply of the United States, 1966–70—Part 1, North Atlantic slope basins—Volume 3, Basins from Maryland to York River. 1976. 971 p. $7.

W 2112. Surface-water supply of the United States, 1966–70—Part 4, St. Lawrence River basin—Volume 2, St. Lawrence River basin below Lake Huron. 1976. 738 p. $5.50.

W 2129. Surface-water supply of the United States, 1966–70—Part 11, Pacific slope basins in California—Volume 2, Basins from Arroyo Grande to Oregon State line except Central Valley. 1976. 678 p. $5.55.

W 2131. Surface-water supply of the United States, 1966–70—Part 11, Pacific slope basins in California—Volume 4, Northern Central Valley basins. 1976. 747 p. $5.85.

W 2172. Ground-water levels in the United States, 1970–74, South-Central States. 1976. 172 p. $2.50.

U.S. GOVERNMENT
PRINTING OFFICE
PUBLIC DOCUMENTS DEPARTMENT
WASHINGTON, D C 20402

OFFICIAL BUSINESS
PENALTY FOR PRIVATE USE $300

POSTAGE AND FEES PAID
U.S. DEPARTMENT OF THE INTERIOR
INT 413

U.S.MAIL

Special
fourth-class
rate books